Novel Non-Equilibrium Steady States and Phases in Periodically Driven and Measured Quantum Systems

Matthew Benjamin Wampler
Nokesville, VA, USA

B.S. Bridgewater College, 2017

A Dissertation presented to the Graduate Faculty of the University of Virginia in Candidacy for the degree of Doctor of Philosophy

Department of Physics

UNIVERSITY OF VIRGINIA

May, 2023

Committee Members:
Israel Klich
Olivier Pfister
Eugene Kolomeisky
John Imbrie

Abstract

The advent of phases of matter which are inherently and explicitly quantum mechanical has made it possible to create devices with exciting capabilities that would otherwise be completely impossible. Recently, experimental advancements are beginning to make it feasible to not just create such quantum materials, but actually manipulate microscopic details in these systems to engineer their properties on demand. Furthermore, by externally interacting with quantum systems, it is possible to induce phases of matter (such as time crystals and materials exhibiting anomalous topological properties) that are forbidden for isolated systems in equilibrium. In this dissertation, we introduce a variety of new classes of physically realizable, non-equilibrium models with a focus on systems which are periodically driven or subjected to a periodic protocol of quantum measurements. We leverage this driving and these quantum measurements to induce non-trivial steady states and phases of matter with surprising and appealing novel properties.

We first examine free fermionic lattice systems subject to quantum measurements (as well as other quantum operations such as particle injection). For example, we consider the effect of a measurement device (along with a variety of other kinds of disturbances) which is dragged through a Fermi sea. The device induces a wake pattern (in analogy with a boat moving through water) which is characterized by the speed at which the probe is moved through the system and its direction with respect to the lattice. Furthermore, stark contrasts emerge between the wake geometry of a quantum disturbance (such as a measurement) and classical disturbances (such as a potential). These effects are especially prominent at half-filling where the the density wake due to measurements disappears and the wake from a moving particle extractor is temperature invariant.

We also introduce a model where lattice fermions are subjected to a periodic sequence of measurements which break the time reversal symmetry of the original free hopping evolution. We show that this protocol induces chiral edge transport in the system that is protected against perturbations and deformations of the boundary at high measurement rates. This model shows that it is possible to induce chiral edge modes in an analogous way to those in anomalous Floquet topological insulators via measurements alone. On the other hand, the measurement-induced model also exhibits novel, distinct features due to the non-unitary nature of the evolution.

Finally, we turn to consider exotic non-equilibrium dynamics which may be induced via a combination of periodic driving and interactions, instead of through a protocol of measurements. Namely, we introduce a broad class of interacting Floquet models which exhibit special points in parameter space where the dynamics becomes exactly solvable. Additionally, at other interaction strengths and driving frequencies, we show that the system exhibits Hilbert space fragmentation with some subspaces corresponding to a (complex) permutation of number states while others may be non-integrable and thermalize. When disorder is added to the system, it is shown that this dynamics is stabilized within finite regions of parameters space (thereby corresponding to true dynamical phases of matter) instead of just at finely tuned parameter values. Importantly, the phases realizable in this fashion include many of the uniquely non-equilibrium materials which are currently the focus of active interest including, for example, time crystals and anomalous Floquet topological insulators. In this way, we show how our introduction and analysis of this broad class of interacting Floquet models allows for new insights into these non-equilibrium phases as well as provides a framework upon which to systematically search for and examine other completely novel non-equilibrium steady states.

List of Publications

1. **Wampler, M.**, Schauss, P., Kolomeisky, E., Klich, I., Quantum Wakes in Lattice Fermions. **Phys. Rev. Research** 3, 033112, **2021** [1]

2. **Wampler, M.**, Khor, B., Refael, G., Klich, I., Stirring by Staring: Measurement Induced Chirality. **Phys. Rev. X** 12, 031031, **2022** [2]

3. **Wampler, M.**, Klich, I., Arrested Development and Fragmentation in Strongly-Interacting Floquet Systems. Accepted at **SciPost Physics**: scipost_202210_00045v2, **2023** [3]

4. **Wampler, M.**, Klich, I., Fragmentation and Novel Prethermal Dynamical Phases in Disordered, Strongly-Interacting Floquet Systems. **Preprint**: arXiv:2212.09678, **2023** [4]

Acknowledgements

My life has been filled with many incredible role models, mentors, collaborators, advocates, and friends. Much of who I am as a physicist — and who I am as a human being — is due to the guidance and support of these wonderful people.

First, I'd like to thank my advisor Israel Klich. Working with Israel has been one of the great joys of my graduate school career. I am constantly amazed by the ease at which he cuts past superfluous complexities in a problem to get to the core of the issue. I have learned so much from both his direct instruction, our general discussions, and indirectly from just following his thought process as we work together to make theoretical progress. It has completely transformed the way I attack problems and how I think about physics as a whole. It is also a pleasure to share not only physics with Israel, but a love of music as well. I'm one of a lucky few PhD students who can honestly say that they could not have asked for a better advisor. I feel so honored to be able to call him both a mentor and a friend.

Second, I'd like to thank my defense committee as well as my yearly research review committee. Your questions and feedback have helped tremendously to continually sharpen my theoretical arguments as well as significantly broaden my understanding of our fields to help better put my work into context. I'd also like to thank my collaborators who have so patiently described the relevant aspects of their field and areas of expertise which I am unfamiliar, who have intently and eagerly considered my ideas, and who have made beautiful insights into our shared work.

To all my former professors and teachers. Thank you for guiding me, kindly answering all my dumb questions, being flexible and encouraging me to follow my academic interests wherever they took me, and for providing the perfect role model for everything a great teacher and researcher should be. I hope I can make even some small fraction of the impact in other's lives as you have made in mine.

Importantly, I'd also like to thank all my fellow grad students and friends. Your support and camaraderie has turned the tougher aspects of graduate school into not just a survivable, but even an enjoyable endeavor. Whether we climbed together, skied together, played volleyball together, played frisbee together, played music together, played games together, hiked together, or simply loved hanging out together doing absolutely nothing at all — my life, both inside and outside of physics, has been incalculably improved by your presence in it. My friends (and family) are my whole world

— thank you for filling that world with such pure joy.

Finally, to my family. Without the help of many of the people I have listed before this, I could not be *where* I am today. Any successes I have had have been, in a large part, due to them. This is certainly true of you too, but — more importantly — without you I would not be *who* I am today. It is your model of kindness, forgiveness, curiosity, and love which I (imperfectly) strive to mimic every day. I cannot put into words what your unconditional love and support means to me. All I can say is: thank you, thank you, thank you — I love y'all so much.

Contents

Dedicated to J. Paul Wampler,

I daily strive to achieve the same thoughtfulness, playfulness, humility, drive to work hard (especially when helping others), and — above all — sincere kindness and generosity which made you such a positive force for good in this world and in the lives of everyone you met.

I love you grandaddy

Chapter 1

Introduction

1.1 Quantum Engineering

Over the past half-century, there has been an explosion of new discoveries regarding materials or phases of matter with exciting properties that are manifestly quantum mechanical. These systems, such as high-temperature superconductors [5], Bose-Einstein condensates [6], and topological quantum phases [7, 8], promise to (or already have) bring about technological revolutions across a wide variety of fields. Furthermore, investigations into their properties have led to new theoretical intuition and powerful mathematical and experimental tools ([9] for example) which may be leveraged to help understand emergent phenomena in other systems and beyond. With these new tools, it is beginning to be possible to not just manufacture quantum phases of matter, but actually externally control their microscopic properties. This suggests the possibility to engineer desired quantum behavior and then adapt it on command.

Understanding (and taking advantage of) the effects of this external manipulation of the microscopic details of quantum systems, however, poses theoretical challenges. Many of the conventional tools used to describe collective behavior in quantum materials are restricted to isolated, time independent systems that are at (or near) equilibrium [10]. New methods must be developed in order to gain insights into these now manifestly open and time-dependent contexts far from equilibrium. Extensive theoretical effort has been focused on developing such methods over the past 15 years especially following discoveries that non-equilibrium systems are not only useful for imitating exotic equilibrium dynamics in a tunable fashion, but may also support phases of matter which are forbidden in equilibrium [11]. Two prominent examples are Time Crystals

[12, 13] and anomalous Floquet topological insulators [14, 15] (also, see section 1.3). Excitement surrounding the development of better analytical tools for out of equilibrium systems is further fueled by the desire to better understand the dynamics of quantum circuits and to improve upon existing quantum computing platforms [16].

In this dissertation, we focus on several examples of novel, exotic dynamics in the non-equilibrium setting. In this chapter, we provide a pedagogical introduction to the theoretical tools which will be necessary to investigate such non-equilibrium dynamics, making reference to more standard, familiar tools from equilibrium or open systems whenever useful. We will also present simple toy models which illustrate how behavior in non-equilibrium systems can arise which is impossible in equilibrium. These toy models additionally provide a convenient point of reference for the rest of the models introduced in this work.

In chapter 2, we consider the effects of local disturbances (such as a potential, particle density measurement device, or extractor which pulls particles out of the system) as it is dragged through a sea of lattice fermions which are initially at equilibrium. In analogy to the wake pattern left behind a boat moving through water, the local disturbance will create a characteristic wake pattern in the fermion density. The shape and properties of this wake pattern may be analyzed, with stark contrasts appearing between the wake patterns of different kinds of local disturbances. For weak disturbances and for lattice sites far from the location of the disturbance, the change in particle density from its equilibrium value is small and, therefore, the system may be accurately described by linear response. This means that, on top of the interest of the wake dynamics in its own right, the system also provides a convenient platform to gain intuition and develop tools which will be useful in the analysis of systems far from equilibrium while still working in a near-equilibrium setting. We also provide a description of how to realize this dynamics in cold-atom systems.

We leave the near-equilibrium setting in chapter 3 and consider the effects of a protocol of measurements which when applied to lattice fermions induces protected chiral transport along the edge of the system while the bulk exhibits no transport. This measurement induced chirality is reminiscent of similar behavior in anomalous Floquet topological insulators (see section 1.3), where the protected chiral edge transport is realized by periodic driving instead of by a periodic sequence of measurements. Despite these similarities, however, the two systems also exhibit many distinct features due to the contrast between the unitary evolution in the periodically driven case versus the

manifestly non-unitary dynamics of the measurements.

Chapter 4 introduces a class of interacting, periodically driven models whose properties may be studied in a general fashion. Specifically, it is shown that at special driving frequencies and interaction strengths the dynamics is exactly solvable. At other special points in parameter space, the Hilbert space fragments into an exponential number of subspaces. The dynamics in some of these subspaces is integrable and described exactly in our framework, while other subspaces may thermalize. Chapter 5 considers the same class of models except with added disorder. In this case, many of the finely tuned properties found in chapter 4 are shown to be stabilized within finite regions of parameter space to create true non-equilibrium phases of matter. This stabilization is achieved through mechanisms referred to as many-body localization and prethermalization (background on these phenomena is given in Sec. 1.4).

For ease of presentation, each chapter contains the main results and ideas in its body with many of the technical details included in a corresponding appendix.

The rest of this introduction will be focused on providing theoretical background and further context on non-equilibrium dynamics. We begin with a brief introduction of the theoretical tools necessary to describe periodically driven (also called Floquet) systems.

1.2 Floquet Theory

One possible route towards driving a system out of equilibrium is to introduce time-dependence into the system parameters. Through the careful control of this time-dependence, one may hope to engineer interesting dynamics and phases of matter in a tunable fashion. In general, the dynamics of a quantum wave function is described by the time-dependent schrödinger equation

$$i\hbar \frac{d}{dt}\Psi(t) = \mathcal{H}(t)\Psi(t). \tag{1.1}$$

with the general solution

$$\Psi(t) = \mathcal{U}(t)\Psi(t=0) \tag{1.2}$$

$$\mathcal{U}(t) = \mathcal{T}e^{-\frac{i}{\hbar}\int_0^t \mathcal{H}(s)ds}. \tag{1.3}$$

In the rest of this work, we set $\hbar = 1$ for brevity unless otherwise noted.

It is not possible, in general, to write the evolution operator $\mathcal{U}(t)$ in closed form. Therefore, it is prudent to focus on regimes where $\mathcal{U}(t)$ becomes more tractable. One possibility is to consider only systems where the Hamiltonian is periodic in time, with some period T, i.e.

$$\mathcal{H}(t+T) = \mathcal{H}(t). \tag{1.4}$$

According to Floquet's theorem [17], solutions to the time-dependent schrödinger equation, when the Hamiltonian is of the form (1.4), may be written

$$\Psi(t) = e^{-i\epsilon t}\Phi(t) \quad \text{s.t.} \quad \Phi(t+T) = \Phi(t). \tag{1.5}$$

In other words, the eigenstates of the evolution are given by a wavefunction with the same periodicity as the Hamiltonian times a time-dependent phase which is characterized by the "quasi-energy" ϵ[1]. The time-dependence of a Floquet (i.e. periodically driven) system implies that energy is not conserved. However, as we will see shortly, the quasi-energy plays a somewhat analogous role which allows for the continued use of typical tools from static systems, such as band theory, up to slight adjustments.

In order to see how this is the case, it is convenient to consider the stroboscopic evolution, i.e. only consider the evolution after time intervals given by integer multiples of the period T. The relevant operator of interest is the evolution of a single period given by

[1] This result is directly analogous to Bloch's theorem for systems with spatially periodic lattice potentials. See (1.10)

$$U(T) = \mathcal{T} e^{-i\int_0^T \mathcal{H}(s)ds} \equiv e^{-i\mathcal{H}_F T} \tag{1.6}$$

where we have defined the Floquet Hamiltonian, $\mathcal{H}_F$, above. The unitarity of $U(T)$ guarantees that $\mathcal{H}_F$ is hermitian. In practice, we note that it is often helpful to write $\mathcal{H}_F$ explicitly in terms of a series expansion in $\mathcal{H}(t)$. A common choice is the Floquet-Magnus expansion [18] where the first few terms are given by

$$\mathcal{H}_F = \int_0^T H(t)dt - \frac{i}{2}\int_0^T dt_1 \int_0^{t_1} dt_2 \left[\mathcal{H}(t_1), \mathcal{H}(t_2)\right] + ... \tag{1.7}$$

Intuitively, this expansion may be interpreted as a continuous generalization of the Baker–Campbell–Hausdorff formula [19].

Now, note that the stroboscopic evolution of the Floquet states (1.5) is given by

$$e^{-i\mathcal{H}_F T}\Psi(0) = U(T)\Psi(0) = \Psi(T) = e^{-i\epsilon T}\Psi(0) \tag{1.8}$$

where we have used the periodicity of $\Phi(t)$ in the final equality. Eq. (1.8) is the characteristic eigenvalue equation for the stroboscopic evolution and we compare and contrast it with the eigenvalue equation for a static Hamiltonian $H\Psi = E\Psi \implies e^{-iHT}\Psi = e^{-iET}\Psi$. It is due to this analogy that we refer to ϵ as the "quasi-energy" and we may use it in a way that is much analogous to eigenenergies in time-independent systems. However, there are two key differences:

1. Eq (1.8) is only an eigenvalue equation at stroboscopic times (since we had to use the time periodicity of $\Phi(t)$ in the final equality).
2. The quasi-energy is periodic in intervals of $\frac{2\pi}{T}$ (since Eq. (1.8) is invariant under the transformation $\epsilon \to \epsilon + \frac{2\pi m}{T}$ for any integer m).

Much of the original excitement of Floquet theory was on carefully choosing $\mathcal{H}(t)$ such that the corresponding $\mathcal{H}_F$ was an important, static Hamiltonian of interest [11]. This would then allow for the realization and study of these time-independent Hamiltonians in a highly controllable fashion. However, the past decade has seen an explosion in interest of leveraging the above two differences with static systems to realize

novel states of matter not possible in equilibrium [13, 14]. In the next section, we describe a Floquet model (first introduced by Rudner et. al. [20]) which achieves just this.

1.3 Topology in Physical Systems

Topology is the study of geometrical properties of an object which are invariant under continuous deformations. Physical systems which exhibit properties that correspond to such a topological invariant may often present interesting and surprising dynamics which find applications in a broad range of contexts [7]. This is because the invariant continuous deformations could correspond to typical noise, errors, or perturbations in the system, allowing topological properties to be much more robust than phenomena in topologically trivial systems. Famous examples include, for instance, quantized conductance in quantum hall systems [21] and systems with long-range topological order such as the Toric code [22].

In this section, we first give a brief review of the relevant features of topology and how it enters into band theory of time-independent systems. For a more thorough introduction, see [23]. We then discuss how the periodicity of the quasi-energy allows for the emergence of new topological invariants and phases which are impossible for the time-independent systems.

1.3.1 Topology of Tight-Binding Models in Equilibrium

We focus on tight-binding lattice systems. Lattice systems are spatially periodic by displacements of a set of lattice vectors $\mathbf{R} = \{\mathbf{R_m}\}$ with $\mathbf{R_m} = \sum_i m_i \mathbf{a}_i$ where $\mathbf{m} = \{m_i\}$ are a set of integers and $\mathbf{a}_i$ is a set of basis vectors. In other words, for some Hamiltonian $\mathcal{H}(\mathbf{r})$, we have

$$\mathcal{H}(\mathbf{r}) = \mathcal{H}(\mathbf{r} + \mathbf{R}). \tag{1.9}$$

By Bloch's theorem, we have that eigenstates of such a Hamiltonian have the form

$$\Psi(\mathbf{r}) = e^{i\mathbf{k}\cdot\mathbf{r}}u(\mathbf{r}) \tag{1.10}$$

This is directly analogous to Floquet's theorem (1.5) where here $u(\mathbf{r}+\mathbf{R}) = u(\mathbf{r})$ and $\mathbf{k}$ is the quasi-momentum. A lattice system is tight-binding if there are a finite number M of internal degrees of freedom (such as lattice sites, spin, etc.) within each unit cell[2] of the lattice. In this case, the Schrödinger equation will have a solution (of the form (1.10)) pertaining to each of the M internal degrees of freedom of the unit cell which are labeled by the "band index"[3] $\alpha \in \{1, ..., M\}$.

An example of a topological invariant in two dimensions (which will be relevant for discussions related to an example non-equilibrium system later in this chapter) is the Chern number, given by

$$\mathcal{C}_\alpha = \frac{1}{2\pi}\int_{BZ} d^2k\Omega_\alpha(\mathbf{k}) \tag{1.11}$$

where

$$\Omega_\alpha(\mathbf{k}) = [\nabla_\mathbf{k} \times \mathbf{A}_\alpha(\mathbf{k})]_z \tag{1.12}$$

$$\mathbf{A}_\alpha(\mathbf{k}) = i\langle u_\alpha|\nabla_\mathbf{k}|u_\alpha\rangle. \tag{1.13}$$

In the above, $\Omega_\alpha(\mathbf{k})$ is known as the Berry curvature and $\mathbf{A}_\alpha(\mathbf{k})$ the Berry connection. As can be seen from the definition (1.11), the Chern number is related to the flux of the Berry curvature through the Brillouin zone and may only take integer values.

A Chern number may be defined for any non-degenerate band α in the system and will remain invariant under perturbations which do not make energy bands touch (thereby making the band degenerate at some quasi-momentum). Furthermore, the

[2] for example, the Wigner-Seitz unit cell defined as the locus of points which are closer to a given lattice vector $\mathbf{R}$ than to any other $\mathbf{R}'$

[3] We will assume familiarity with the basics of band theory throughout the rest of this dissertation. We direct the unfamiliar reader to one of the many introductory textbooks on the subject. For example, [24]

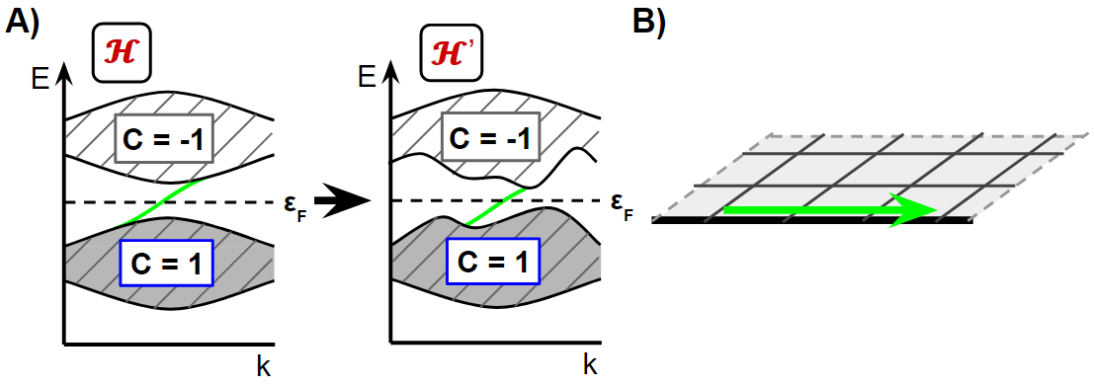

FIGURE 1.1: A two-band model exhibiting topological band structure and chiral edge modes in an equilibrium context. A) Since the fermi energy ε_F is in a band gap, it takes a large amount of energy to induce higher energy excitations in the system making it a band insulator. However, the filled band has non-zero chern number, so an edge band corresponding to a chiral mode on the boundary of the system (shown in green) will connect the bulk bands. If the Hamiltonian of the system $\mathcal{H}$ is continuously deformed into a new Hamiltonian $\mathcal{H}'$ in such a way that the band gap does not close, the chern number (and therefore the edge mode) is preserved. B) The chiral transport in the system which is protected under the transformation $\mathcal{H} \rightarrow \mathcal{H}'$.

Chern number is intimately linked to the dynamics at the boundary of a lattice system. A non-zero Chern number corresponds to the emergence of chiral modes that propogate along the edge of the system. In fact, the number of edge modes is given by summing the Chern numbers of the filled bands. These chiral edge modes will, therefore, be robust to any perturbations which leave the Chern number invariant. The band structure of such a system is schematically represented in Fig. 1.1.

1.3.2 Anomalous Floquet Topology

We saw in Sec. 1.2 that, since evolution in periodically driven systems may be linked to evolution of an effective static Hamiltonian, it is still possible to use band theory in Floquet systems. This comes with the important caveats, however, that the Floquet Hamiltonian only describes the dynamics at stroboscopic times and that energy is replaced by quasi-energy.

A Chern number may be defined for bands in Floquet systems in a directly analagous way to time-independent systems. Specifically, we use Bloch's theorem to write the

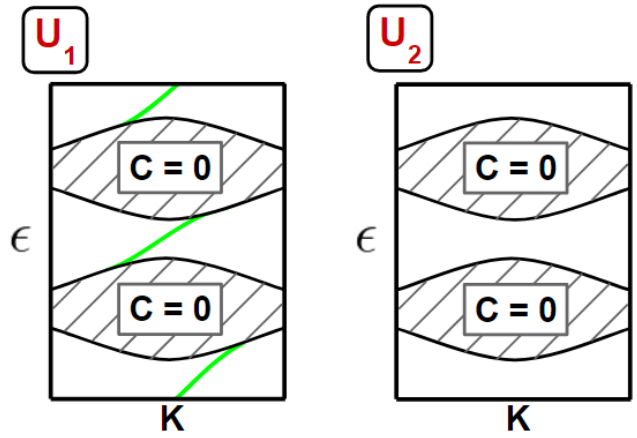

FIGURE 1.2: Two-band Floquet models exhibiting anomalous topology and trivial topology respectively. In both systems, the chern number of both bands is 0, but nonetheless there are still edge modes for U_1. This is only possible due to the periodicity of the quasi-energy ϵ which allows for edge bands to wind around from the top of each bulk band to the bottom of the other bulk band. Therefore, the chern number alone cannot distinguish between the topology of U_1 versus U_2.

Floquet eigenstate at stroboscopic times $\Psi(0)$ in the form (1.10) and then calculate the Chern number using (1.11). Naively, one might guess that the Floquet-Chern number completely characterizes the topology of the system as it does for Chern insulators. However, this is not the case. Consider the band structure shown in Fig. 1.2. Here, the Chern number for every band in the system evolving under U_1 is 0, but nonetheless the system still exhibits chiral edge modes. Such behavior is only possible due to the periodicity of the quasi-energy and cannot be realized in time-independent systems. Edge modes of this type are referred to as "anomalous" since they appear despite having 0 Chern number.

In order to see how such anomalous band structure can emerge, we consider an example model from Rudner, Lindner, Berg, and Levin (RLBL) [20]. The drive consists of a 4-step procedure for spinless Fermions on a square lattice. During step m, the system is evolved by the Hamiltonian

$$\mathcal{H}_m = -t_{hop} \sum_{(i,j)\in A_m} (a_i^\dagger a_j + h.c.) \tag{1.14}$$

for a time $\tau = \frac{T}{4}$, i.e. particles are only allowed to hop between sites connected by A_m as shown in Fig. 1.3A.

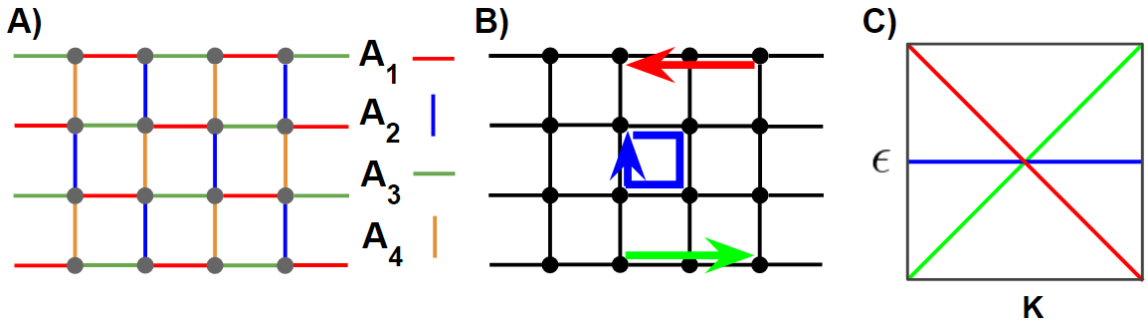

FIGURE 1.3: The Rudner-Lindner-Berg-Levin (RLBL) model exhibiting anomalous topology. A) The model consists of 4 steps with fermions hopping freely between sites connected by A_m during step m, with each step lasting for a time τ. B) When $\tau = \frac{\pi}{2t_{\text{hop}}}$, the evolution exactly swaps particle densities between sites connected by A_m. In this case, a particle in the bulk of the system traces out a closed trajectory shown in blue. Particles on the edge of the system, however, exhibit chiral transport after each period T. C) Energy bands for the RLBL model. Evolution of bulk particles is the identity after each period T, so quasi-energy bands are 0. The chiral edge modes correspond to edge bands with constant slope that wind around the quasi-energy.

The simplest case to consider is when $\tau = \frac{\pi}{2t_{hop}}$. Here, each step of the drive acts as a tensor product of swap gates between each edge A_m in the system, i.e.

$$e^{-i\mathcal{H}_m\tau} = \bigotimes_{(i,j)\in A_m} X_{(i,j)} \tag{1.15}$$

with $X_{(i,j)}$ the pauli X operator between sites i and j. Under this evolution, any particle injected into the bulk of the system will exhibit a closed loop trajectory after every period T (see Fig. 1.3B). Stroboscopically, this evolution corresponds to the identity and, therefore, a flat band of $\epsilon = 0$. On the other hand, a particle injected onto the edge of the system exhibits a chiral trajectory along the boundary. This leads to the Floquet band structure shown in Fig. 1.3C. Note that these edge modes are anomalous as they wrap all the way around the quasi-energy spectrum and correspond to a Chern number 0.

Since the Chern number does not accurately represent the topology of this system, it is important to come up with a new topological invariant that does [14]. A first

possibility is to simply count the number of times the edge modes wind around the quasi-energy spectrum. In a 2D system with translational invariance in the direction perpendicular to the boundary, for example, this may be done by averaging the slope of the quasi-energies for each band α around the closed loop of the quasi-momentum $k_\perp$ for the translationally invariant direction. Namely, the quasi-energy winding ν is given by

$$\nu = \frac{T}{2\pi} \sum_\alpha \int_{-\pi}^{\pi} dk_\perp \partial_{k_\perp} \epsilon_{k_\perp,\alpha} \tag{1.16}$$

It is also possible to write ν directly in terms of the stroboscopic evolution operator (1.6) in Fourier space $U_{k_\perp}(T)$,

$$\nu = \frac{i}{2\pi} \int_{-\pi}^{\pi} dk_\perp \, \mathrm{Tr} \left[U_{k_\perp}^{-1}(T) \partial_{k_\perp} U_{k_\perp}(T) \right]. \tag{1.17}$$

Since the group velocity of a given mode is $\partial_{k_\perp} \epsilon_{k_\perp,\alpha}$, ν directly corresponds to the total particle transport along the boundary. Furthermore, ν is quantized and protected against continuous deformations of $\epsilon_{k_\perp,\alpha}$.

However, ν is still not completely satisfactory as a topological invariant. This is because it depends explicitly on the geometry of the boundary. However, in analogy with time-independent systems, it is expected that the quantization of the transport on the edge of the system should not depend on this edge geometry and may be described completely in terms of the bulk properties of the system, i.e. there is a bulk-boundary correspondence. This is exemplified by the Chern number which is determined completely in terms of the translationally invariant bulk, but still describes the quantized boundary transport if an edge is added.

From the RLBL model when $\tau = \frac{\pi}{2t_{hop}}$, it is clear that considering only the stroboscopic evolution will not be sufficient to calculate such an invariant. This is because, in the bulk of the system, $U_{\text{bulk}}(T) = \mathbb{I}$ and is thus indistinguishable from a topologically trivial system with identity evolution. We must, therefore, not just consider the Floquet Hamiltonian and quasi-energies (which are defined at stroboscopic times), but instead consider the "micromotion" of the periodic drive, i.e. consider properties of the system during times within the driving period. In [20], the authors construct a winding

number $\mathcal{W}[U]$[4] from the bulk properties of the system

$$\mathcal{W}[U] = \frac{1}{8\pi^2}\int dt d^2k \,\mathrm{Tr}\left\{U^{-1}\partial_t U\left[U^{-1}\partial_{k_x}U, U^{-1}\partial_{k_y}U\right]\right\} \tag{1.18}$$

Here, the winding number is integrated over all 3 of the parameters over which U is periodic[5] and, in fact, corresponds precisely to the number n_{edge} of chiral edge modes

$$n_{\text{edge}} = \mathcal{W}[U]. \tag{1.19}$$

The winding number (1.18) therefore shows the bulk-boundary correspondence for periodically driven systems and generalizes the topological classification achieved by the Chern number in time-independent systems.

1.4 Floquet Thermalization

Up to this point, we have been ignoring a significant problem that has been lurking in the shadows for realizing anomalous, non-equilibrium phases of matter. Any system which is being driven (resonantly) may absorb energy from the drive. This seems to imply that, in the long time limit, the absorbed energy may completely scramble any of the carefully-induced, exotic, non-equilibrium dynamics[6]. In this case, the sole steady state of the driven system would be a featureless, spatially uniform, "infinite temperature" state, thereby making the discussions from the previous sections obsolete.

Thankfully, there exist mechanisms to prevent this runaway heating, allowing non-equilibrium steady states (such as those with anomalous winding as discussed in

[4]This form of $\mathcal{W}[U]$ is technically just for the case where $U_{\text{bulk}}(T) = \mathbb{I}$. For more general $U_{\text{bulk}}(T)$, the winding $\mathcal{W}_\epsilon[U]$ depends explicitly on the quasi-energy ϵ. In this more general case, there exists a nice relationship between the winding number and the Floquet-Chern number, $\mathcal{C}_{\epsilon\epsilon'} = \mathcal{W}_{\epsilon'}[U] - \mathcal{W}_\epsilon[U]$ where $\mathcal{C}_{\epsilon\epsilon'}$ is the sum of chern numbers for bands between ϵ and ϵ'. See [20] for details

[5]In fact, the winding number comes from a general topological classification of maps from $S^1 \times S^1 \times S^1 \to U(N)$ [25]

[6]This problem was really hiding within our discussion all along. For example, we made no effort to show that the Floquet-Magnus expansion (1.7) converges, and in fact its divergence is intimately linked to the infinite heating of Floquet systems [26].

the previous section) to be created in real, physical systems. Specifically, the heating may be prevented by adding disorder to the system which may prevent thermalization through a mechanism referred to as many-body localization [27], by considering "prethermal" systems in which the heating is slow compared to the non-equilibrium dynamics of interest [28], or by coupling the system to the environment (which acts in a somewhat analogous way to a heat sink to prevent runaway heating in the system itself) [29].

When disorder is added to a Floquet system (such as a disordered on-site potential), in certain cases the disorder may slow the absorption of energy from the drive and prevent its spread throughout the system. This mechanism prevents thermalization and is, in general, known as Many-body localization (MBL) [27]. The phenomena of localization by disorder was first investigated by Anderson [30] in a time-independent, non-interacting context to study metal-insulator transitions. There, it was shown that wavepackets (with wavelengths larger than the lattice spacing) within a disordered media may exhibit an interference effect which keeps the wavefunction localized instead of spreading diffusively as classical particles within a similar system would (this localization prevents conduction in the system leading to a transition from metal to insulator in dirty, i.e. disordered, materials). Since Anderson's seminal paper, many works have argued whether Anderson localization could be generalized to interacting (many-body) systems (e.g. [31–34]), culminating in a rigorous proof of its existence in 1D systems (with a physically reasonable assumption of limited level attraction) by Imbrie [35] in 2016. However, this work is not easily generalized to higher dimensions and there is reason to believe that MBL is, in fact, ruined for dimensions 2 and larger [36, 37]. Subsequent work has showed that MBL could, however, be extended to Floquet systems for weak, high-frequency drives [38].

We refrain from providing a full mathematically rigorous description of MBL in this introduction, but will instead focus on motivating (via perturbation theory) the basic physical intuition behind MBL and, additionally, through what mechanisms it might fail. Consider a lattice system with an added random on-site potential. The Hamiltonian of such a system is given by

$$\mathcal{H} = \sum_i v_i n_i + H \tag{1.20}$$

where i is a combined index for all lattice sites and internal degrees of freedom, v_i is uniformly distributed between $[-W, W]$ for some disorder strength $W \in \mathbb{R}$, and H is the Hamiltonian for the clean lattice system. If W is large, we might hope to describe the system via perturbation theory. To do this, we first split H into a term H_0 which commutes with the disorder term $[H_0, n_i] = 0$ and a term $\mathcal{V}$ which does not. Then, we rewrite the full Hamiltonian as

$$\mathcal{H} = \sum_i v_i n_i + H_0 + \mathcal{V} \tag{1.21}$$

$$\equiv \mathcal{D} + \mathcal{V} \tag{1.22}$$

where we have defined $\mathcal{D}$ in the second line. Denote the eigenstates and eigenvalues of $\mathcal{D}$ as $\mathcal{D}|\mathbf{n}\rangle = E_{\mathbf{n}}|\mathbf{n}\rangle$, a perturbative expansion for the eigenstates of $\mathcal{H}$ is then given by

$$|\mathbf{n}\rangle + \sum_{\mathbf{m}} \frac{\langle \mathbf{m}|\mathcal{V}|\mathbf{n}\rangle}{E_{\mathbf{n}} - E_{\mathbf{m}}}|\mathbf{m}\rangle + \text{ Higher Orders .} \tag{1.23}$$

Note that since $[\mathcal{D}, n_i] = 0$, its eigenstates are number states (product states with a well-defined number of particles at each i) and in this sense evolution under $\mathcal{D}$ is localized. Intuitively, if the eigensystem of $\mathcal{H}$ is well described as a local, weak perturbation of that of $\mathcal{D}$, then one might hope to argue that evolution under $\mathcal{H}$ is similarly localized. More concretely, we focus on the case where $\mathcal{V}$ is a sum of local terms where the norm of each local term is small compared with the disorder strength, i.e.

$$\mathcal{V} = \sum_i V_i \; ; \; ||V_i||_{HS} \sim g \ll W \tag{1.24}$$

where V_i is given only by terms which act within a finite region of lattice site i and $|| \cdot ||_{HS}$ is the Hilbert-Schmidt norm. The locality of $\mathcal{V}$ guarantees that the matrix elements $\langle \mathbf{m}|\mathcal{V}|\mathbf{n}\rangle$ are only non-zero between number states which are local transformations of each other. Furthermore, since the spectrum $E_{\mathbf{n}}$ is a random distribution set in part by the disorder strength W and since $g \ll W$, the factor $\frac{\langle \mathbf{m}|\mathcal{V}|\mathbf{n}\rangle}{E_{\mathbf{n}} - E_{\mathbf{m}}}$ will be small for almost all $\mathbf{m}$. However, there will be rare cases where the random statistics of the on-site disorder

happens to create a degeneracy (resonance) $E_{\mathbf{n}} - E_{\mathbf{m}} \approx 0$.

If the rare resonant factors $\frac{\langle \mathbf{m}|\mathcal{V}|\mathbf{n}\rangle}{E_{\mathbf{n}}-E_{\mathbf{m}}}$ were not present, then we would have that evolution under $\mathcal{H}$ is localized. In particular, the eigenstates of $\mathcal{H}$ (1.23) would be given by number states with small corrections that decay rapidly as they become less local (i.e. for higher and higher orders of perturbation theory). The crux of showing MBL occurs is therefore to focus on the effects of the rare resonances and show that they do not ruin localization. It is these resonances that are argued to ruin localization in dimensions $d > 1$, but they may be rigorously handled in 1D [37].

An exciting application of MBL to Floquet systems is in cases where it is possible to continuously deform a clean Floquet unitary evolution operator into a disordered Floquet unitary exhibiting MBL in such a way that preserves the topology of the system. This allows for the possibility to truly realize phases of matter with the anomalous topological features discussed in Section 1.3 by preventing the runaway heating in the system. However, the attentive reader may note a difficulty on this front. Many models which realize anomalous topology, including the example RLBL model discussed in Section 1.3, are in 2 or higher dimensions where MBL has been argued to fail. There are a few ways around this problem. First, one may consider systems where the rare resonances do not appear. This may be done, for example, by trying to switch the random on-site potential to a quasi-periodic (pseudo-random) potential in such a way that the energy degeneracy is removed [39]. Another possibility is to consider systems with a finite number of particles. In the thermodynamic limit, the probability of resonances appearing in such a system goes to zero leading to so called K-body localization [40]. On the other hand, even when resonances do ruin localization, this may take an exponentially long time [36, 41] (in some large parameter for the system such as $\frac{W}{g}$ from (1.24)). In this case, for any relevant experimental or numerical time scales, the dynamics will be indistinguishable from a system which is MBL. Any system such as this which takes an exponentially long time to thermalize is referred to as prethermal. An active area of research is focused on creating prethermal non-equilibrium phases which do eventually thermalize, but may exhibit exotic quasi-conserved properties (such as anomalous topology) on all experimentally relevant time scales (e.g. [42, 43]).

Another mechanism to prevent heating is to connect the Floquet system to a reservoir. When an open system is driven, dissipation from the environment may prevent runaway heating in the system and allow for non-trivial non-equilibrium steady states to still be realized. Determining in what physical scenarios this prevention of infinite

heating occurs and, when it does, finding ways to control the environmental coupling and drive to achieve interesting steady states is an active area of research [29, 44–49].

Additionally, some degree of coupling to the environment is inevitable for many physical platforms, and so understanding the effects of dissipation on Floquet dynamics is important on a practical front. Considering open systems is further interesting as it allows for the possibility of non-unitary evolution; it is an interesting question to consider if novel dynamics may be realized with periodic, non-unitary evolution. For example, in chapter 3, we introduce a lattice system which undergoes free-hopping evolution interspersed with a periodic series of measurements. This system is somewhat analagous to a non-unitary version of the RLBL model discussed in Section 1.3 (including, for example, exhibiting protected chiral edge transport), but also exhibits interesting differences due to the dissapative nature of the system. We now turn to review some of the theoretical tools needed to describe open systems.

1.5 Open Quantum Systems

The general state of an open quantum system is described by its density matrix ρ. General evolution of density matrices may be written using the Kraus operator formalism given by

$$\rho \longrightarrow \mathcal{L}(\rho) = \sum_{\nu} A_\nu \rho A_\nu^\dagger \, ; \, \sum_{\nu} A_\nu^\dagger A_\nu = 1. \tag{1.25}$$

This form ensures that ρ remains non-negative and the normalization condition on the Kraus operators A_ν preserves $\mathrm{Tr}\{\rho\} = 1$.[7]

While explicitly working in the general Kraus operator formalism is useful in some contexts, it is often fruitful to focus on certain restricted or approximation regimes where $\mathcal{L}$ is especially tractable. For example, one popular choice is to use the Lindblad formalism. Here, it is assumed that the system of interest is weakly coupled to a bath and that the time scales for dynamics in the bath and the bath-system coupling are both much faster than typical time scales for evolution in the system itself. Under these

[7] For more in depth discussions of Kraus operators (and open systems in general) that are beyond the scope of this introduction, the interested reader may consult [50] or other similar introductory texts with chapters on the subject.

conditions, it is possible to make a few approximations (namely the Markovian and Secular approximations) which simplify the Kraus map on ρ into the Lindblad form (for details, see for example Preskill's lecture notes [51]). The main mathematical benefit of this set of approximations is that it implies the density matrix at a given time $\rho(t+dt)$ can be written completely in terms of the density matrix at the previous time step $\rho(t)$, i.e. the system is Markovian and has no memory of the state of the system from further in the past. This allows for the evolution of the density matrix to be written as a first order differential equation (known as the Lindblad master equation) with respect to t.

In this dissertation, however, we will take a different approach. Instead of considering a set of (physically resonable) approximations, we restrict to a class of Kraus operators where dynamics is more tractable but still exact. In order to motivate what class of dynamics we wish to investigate, consider the evolution of a general correlation function

$$\left\langle a^\dagger_{i_1}...a^\dagger_{i_{\ell_1}} a_{i_{(\ell_1+1)}}...a_{i_{(\ell_1+\ell_2)}} \right\rangle = \mathrm{Tr}\left\{ \rho a^\dagger_{i_1}...a^\dagger_{i_{\ell_1}} a_{i_{(\ell_1+1)}}...a_{i_{(\ell_1+\ell_2)}} \right\} \tag{1.26}$$

given by

$$\begin{aligned} \left\langle a^\dagger_{i_1}...a^\dagger_{i_{\ell_1}} a_{i_{(\ell_1+1)}}...a_{i_{(\ell_1+\ell_2)}} \right\rangle \longrightarrow & \left\langle a^\dagger_{i_1}...a^\dagger_{i_{\ell_1}} a_{i_{(\ell_1+1)}}...a_{i_{(\ell_1+\ell_2)}} \right\rangle \\ & + \sum_\nu \mathrm{Tr}\left\{ \rho A^\dagger_\nu \left[a^\dagger_{i_1}...a^\dagger_{i_{\ell_1}} a_{i_{(\ell_1+1)}}...a_{i_{(\ell_1+\ell_2)}}, A_\nu \right] \right\} \end{aligned} \tag{1.27}$$

where we have used the normalization condition of A_ν. Note, the $\ell_1 + \ell_2$ correlation function is, in general, taken to a higher order correlation function leading to a hierarchy of equations which quickly becomes intractable. However, a subset of this general evolution can be found by taking just the two-point function $G_{ij} \equiv \langle a^\dagger_i a_j \rangle$, and asking under what set of Krauss operators does the hierarchy close, i.e. what set of Kraus operators map two-point functions to two-point (and not higher) correlation functions $G \to G' = \mathcal{K}(G)$.

In [52], it is shown that, for fermions on a lattice, the following Krauss operators form a set of possible operations that close the hierarchy on the two point function

level:

$$\text{Non-interacting Evolution:} \quad \mathcal{L}_u(\rho) = \mathcal{U}\rho\mathcal{U}^\dagger \tag{1.28a}$$

$$\text{Particle Detection:} \quad \mathcal{L}_{D,i}(\rho) = n_i\rho n_i + (1-n_i)\rho(1-n_i) \tag{1.28b}$$

$$\text{Soft Particle Injection:} \quad \mathcal{L}_{in,i,\epsilon}(\rho) = \epsilon(2-\epsilon)a_i^\dagger\rho a_i + (1-\epsilon(1-n_i))\rho(1-\epsilon(1-n_i)) \tag{1.28c}$$

$$\text{Soft Particle Extraction:} \quad \mathcal{L}_{out,i,\epsilon}(\rho) = \epsilon(2-\epsilon)a_i\rho a_i^\dagger + (1-\epsilon n_i)\rho(1-\epsilon n_i) \tag{1.28d}$$

Here, ϵ is a real number between 0 and 1 and $\mathcal{U}$ is assumed to describe non-interacting evolution under which fermion operators transform as $\mathcal{U}^\dagger a_i^\dagger \mathcal{U} = U_{ij}a_j^\dagger$, where U is called a single-particle evolution. It is then a straight-forward task of applying the anti-commutation relations of $a^\dagger, a$ to find the corresponding transformations on the two point function:

$$\text{Non-interacting Evolution:} \quad \mathcal{K}_U(G)_{ij} = (UGU^\dagger)_{ij} \tag{1.29a}$$

$$\text{Particle Detection:} \quad \mathcal{K}_{D,i}(G) = P_iGP_i + (1-P_i)G(1-P_i) \tag{1.29b}$$

$$\text{Soft Particle Injection:} \quad \mathcal{K}_{in,i,\epsilon}(G) = (1-P_i)G(1-P_i) + (1-\epsilon)P_iG(1-P_i) + (1-\epsilon)(1-P_i)GP_i + (1-\epsilon)^2P_iGP_i + \epsilon(2-\epsilon)P_i \tag{1.29c}$$

$$\text{Soft Particle Extraction:} \quad \mathcal{K}_{out,i,\epsilon}(G) = \mathcal{K}_{in,i,\epsilon}(G) - \epsilon(2-\epsilon)P_i \tag{1.29d}$$

Here, $P_i = |i\rangle\langle i|$ is the (single particle) projector onto site i.

We emphasize that no approximations are used in the derivation of Eq. (1.29). The resulting simplicity arises completely from the restricted set of allowed Kraus operations. If we are only interested in transport or particle density properties of a system which may be written completely in terms of the two-point function, the closed-hierarchy formalism thus allows for the exact solution of the dynamics via a function which scales polynomially (the two-point function) instead of a function which scales exponentially (the density matrix) in system size. We will first use the closed hierarchy formalism in the next chapter in the context of linear response where the system will be near-equilibrium and so many of the tools from time-independent systems may still be applied. In chapter 3, however, we will push far away from equilibrium and consider a periodic application of closed-hierarchy Kraus operators where it will be somewhat

fruitful to make analogies with Floquet systems.

Chapter 2

Quantum Wakes in Lattice Fermions

2.1 Introduction

Many signature effects of classical hydrodynamics have counterparts in quantum systems and serve to provide intuition as well as a spectacular source for interesting new physical situations. Due to the absence of internal scale in hydrodynamics, it can be applied for physical scenarios of vastly different scales. For example, relativistic hydrodynamics has been successfully used to explain collective effects in heavy-ion collisions at RHIC and LHC [53]. On the other hand, studies of hydrodynamic-like effects in strongly interacting electron systems show unexpected effects due to their similarity to viscous fluids. For example, ref. [54] shows that in certain situations, conductance may exceed Landauer's ballistic limit due to viscous effects, while ref. [55] demonstrates that slow "swimming" in a Fermi gas is of a topological nature, and can be fine-tuned to be done without dissipation.

Another interesting example of a hydrodynamics inspired study is the investigation of wake waves produced as a response to a moving potential interacting with a two-dimensional electron gas, recently described by Kolomeisky and Straley in [56]. There, it was pointed out that the pattern formed is determined by a Mach number and has similarities to Kelvin wakes in water and to Mach shock waves following a supersonic projectile. This behavior can be traced to the coherent interference between plasma excitations in the medium, with a dispersion which is water-like $(\omega(q)^2 \propto q)$ at long wavelengths. A related effect, Cerenkov radiation due to a moving charge in a dielectric has also been studied extensively, most recently in photonic crystals where a host of new variations on the effect have been uncovered where, for example, the direction of radiated energy can be flipped see e.g. [57, 58].

Here, we consider an altogether different system and, with it, a new set of non-equilibrium problems. We examine the discrete-time steady-state generated by the interaction of different types of disturbances, as described below, with fermions on a lattice, as the disturbances move from site to site. Thus, the discrete time, the lattice and the many-body nature of the system play essential roles in the definition of our model. We find that non-classical disturbances may yield a drastically different response. The case in point is that of a moving quantum particle detector, which in this context has no classical counterpart. In addition, we study a moving particle extraction site, in which particles can be ejected out of the system. These two types of disturbances are compared with results we obtain for a moving potential. We note that in recent years, there have been many investigations of measurement-induced dynamics in many-body systems [59–64]. Measurement induced dynamics has been also observed in experiments [65–67]. Moving detectors have been considered before as well, most notably in describing the Unruh effect [68], where a uniformly accelerated detector observes a thermal radiation in vacuum. However, the question we consider here is, to the best of our knowledge, completely new: what type of a steady state density pattern will a moving detector leave behind when measuring particle densities in a Fermi sea.

The recent progress of quantum simulation with ultracold atoms [69] makes them an ideal platform for studying these effects. Here, we focus on cold Fermi gases which became a valuable tool in recent years to study non-equilibrium dynamics in analogy to electronic systems. Indeed, recently, increasingly sophisticated techniques became accessible leading to the measurement of spin dynamics [70–72] and charge transport [73–75]. In particular, it also became possible to observe spin charge separation in one-dimensional lattice systems [76] and to study spin- and charge transport in the two-dimensional Fermi-Hubbard model in the regime of low temperatures and strong correlations that challenge current theory calculations [77, 78]. These experiments demonstrate that ultracold fermionic atoms are an effective platform for quantum simulation of non-equilibrium phenomena even beyond the capabilities of exact calculations.

Classically, the universality of wakes following moving ships has been characterized by Kelvin's seminal result, that a (gravity) wake behind a moving ship in water is delimited within a constant angle 39°, irrespective of the ship's velocity [79]. Recent results emphasize finite-size effects [80] through the dependence on the Froude number $v/\sqrt{gL}$ of a moving pressure source traveling at velocity v of length L, where g is the gravitational acceleration constant [81]. Here, we study wakes created by point disturbances moving through a Fermi lattice gas including the quantum effects (Fig.

2.1). Our results depend on both the velocity and the angle with respect to the Bravais lattice directions, as well as on the type of disturbance. Concretely, we consider a tip traveling through a lattice of cold fermionic atoms, interacting with an atom on a lattice site, and then during a time τ moving on to the next site.

We find several unexpected results. For example, we observe a dramatic difference between the wakes of a moving particle detector and a traveling potential disturbance. In particular, on the square lattice at half filling the detector wake vanishes identically due to particle hole symmetry at any temperature. Another surprising result is that, at half-filling, the wake formed by a "particle" extractor is independent of temperature. To find an analytic form for the wake left behind a moving potential we use a co-moving steady-state equation and employ a strategy of identifying nodal lines where the (co-moving) disturbance is exactly zero, in contrast to most treatments of water wakes, which seek for extrema, i.e. troughs and crests. Due to the scale inherent in the lattice structure, our wakes depend explicitly on the time τ characterizing the effective speed of the moving tip, compared to the hopping energy t_{hop} of the fermions in a tight-binding lattice.

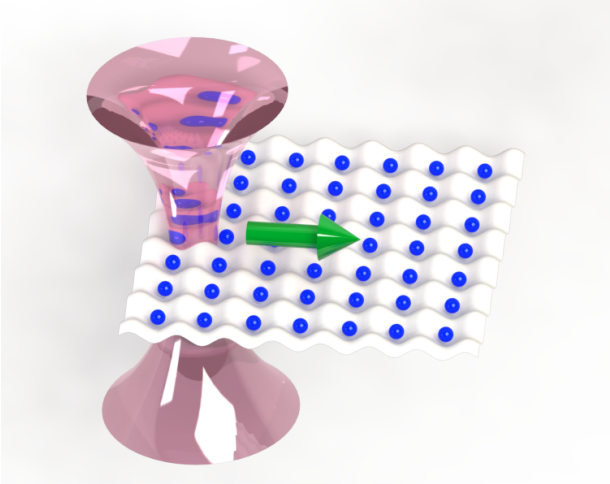

FIGURE 2.1: A lattice of cold atoms interacting with a moving disturbance. The disturbance can be an applied potential, a detector or an extractor. The blue dots represent the fermionic atoms and the red focussed laser beam illustrates the disturbance moving into the direction of the green arrow.

To describe these effects of dynamics in many-particle quantum systems we use the non-equilibrium framework derived in [52]. This framework allows for the study of a variety of non-equilibrium problems including particle detection and injection/extraction. It was shown in [52] that in certain statistical mechanics problems, which we detail in

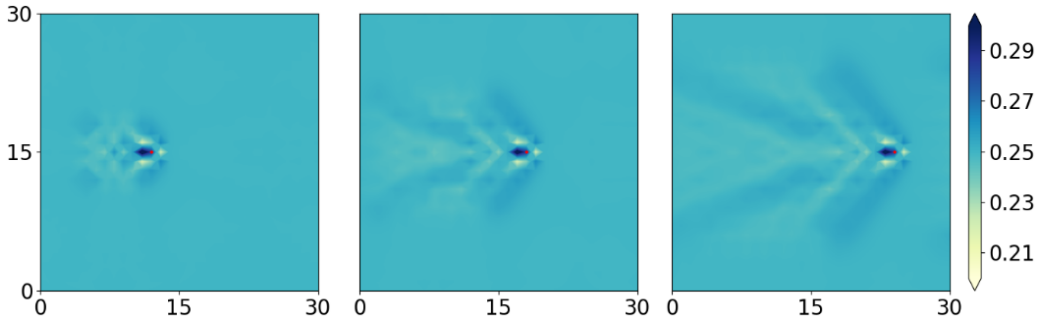

FIGURE 2.2: Snapshots of the wake developing following a moving particle detector at quarter filling. Plotted are the local particle densities of each lattice site as given by the color bar on the right. The location of the disturbance is marked by a red dot. The simulations are done by iteration of free evolution (Eq. (2.4)) interspersed with interactions with a particle detector (Eq. (2.6)) beginning from the ground state of free fermions on a 30×30 lattice. The detector was initialized at position $(8, 15)$ and moves horizontally to the next site during time $1/(3.4\, t_{hop})$, where t_{hop} is the hopping parameter of the free evolution.

the Formalism section, it is possible to make a systematic connection between the evolution of n body density functions with $n+1$ density functions, similar in spirit to the Bogoliubov-Born-Green-Kirkwood-Yvon (BBKGY) hierarchy, which is the essential structure leading to the Boltzmann equation for single particle densities from higher order correlation functions (see, e.g. [82]). This approach allows the buildup of tractable non-equilibrium problems utilizing combinations of four elementary operations: detection, particle injection, particle extraction and free evolution. While some of these ideas have been applied to problems in 1D (e.g. driven and dissipative XX spin chains [83] and steady states of a driven hopping model [52]), here we study an essential 2D problem: the emergence of wakes behind moving objects interacting with a Fermi sea. In particular, we discuss the difference between the motion of a detector, particle extractor, and a potential in detail. The approach of [52] allows for an efficient numerical calculation of the dynamics in such problems. An example of the development of a wake a moving detector is described in Fig. 2.2, while a comparison between a moving detector and potential is provided in Fig. 2.3 at different filling fractions of a Fermi sea in a 2d hopping model.

The structure of the paper is as follows. We start by briefly introducing the formalism of [52]. Next we study the effect of a potential hopping from site to site, solving for the characteristic angles of the traveling pattern. We then continue to study the motion of a detector and the motion of a particle extractor and compare these with our

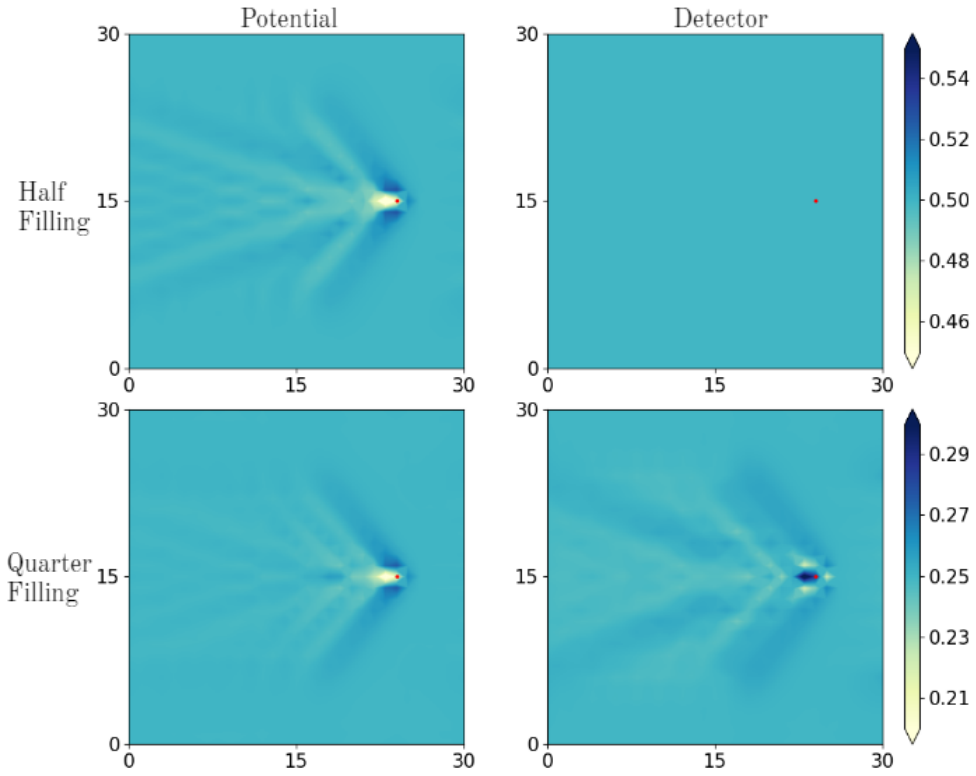

FIGURE 2.3: Comparison of density plots for wakes of a moving point potential (left) with a moving detector (right). The detector/point potential was initialized at position $(8, 15)$ and moves horizontally to the next site during time $1/(3.4\ t_{hop})$, where t_{hop} is the hopping parameter of the free evolution. Snapshots are taken after 18 time steps, when the full wake pattern has been sufficiently developed. At half filling the difference is most dramatic (top) but differences remain at quarter filling (bottom).

results for the moving potential. Finally, we suggest an experimental setup to directly observe the wake patterns.

2.2 Formalism

First, we provide a formal description of the system depicted in figure 2.1. We will denote by $a_{\mathbf{r}}$ the annihilation operator for a fermion at lattice site $\mathbf{r}$. To describe the density distribution we will focus on the two point function, defined as:

$$G_{\mathbf{r}\mathbf{r}'}(t) = Tr\rho(t)a^{\dagger}_{\mathbf{r}}a_{\mathbf{r}'} \tag{2.1}$$

where $\rho(t)$ is the density matrix at time t. The evolution of $G_{\mathbf{r}\mathbf{r}'}$ depends on the problem at hand. Due to the discrete nature of the lattice, we find it natural to consider the time evolution in discrete time steps τ, pertaining to the time disturbance moves from site to site. After a step in the evolution process, $G(t) \to \mathcal{K}(G) \equiv G(t+\tau)$, where $\mathcal{K}(G)$ is specified for various processes below.

In general, if the system undergoes Hamiltonian evolution during a time τ, we have

$$\rho(t+\tau) = \mathcal{U}\rho(t)\mathcal{U}^{\dagger} \tag{2.2}$$

where $\mathcal{U} = \mathcal{T}e^{-\frac{i}{\hbar}\int_t^{t+\tau}\mathcal{H}(s)ds}$ is the many-body evolution. For a general interacting Hamiltonian, $G_{\mathbf{r}\mathbf{r}'}(t+\tau)$ is not determined by $G(t)$ alone and would depend on all higher order correlation functions.

For a non-interacting Hamiltonian, however, the evolution of G does not depend on high order correlations. Let us take the Hamiltonian to be $\mathcal{H}(t) = \sum_{\mathbf{r}\mathbf{r}'} H_{\mathbf{r}\mathbf{r}'}(t)a^{\dagger}_{\mathbf{r}}a_{\mathbf{r}'}$, where H is an $N \times N$ matrix if there are N fermion sites. The evolution of G from time t to time $t+\tau$ is simplified by the fact that for such a Hamiltonian,

$$\mathcal{U}^{\dagger}a^{\dagger}_{\mathbf{q}}\mathcal{U} = U_{\mathbf{q}\mathbf{q}'}a^{\dagger}_{\mathbf{q}'}. \tag{2.3}$$

where $U_{\mathbf{q}\mathbf{q}'} = [\mathcal{T} e^{\frac{i}{\hbar}\int_t^{t+\tau} H^T(s)ds}]_{\mathbf{q}\mathbf{q}'}$ is an $N \times N$ single particle evolution operator [1]. We therefore find for G:

$$\begin{aligned} G_{\mathbf{r}\mathbf{r}'}(t+\tau) &= Tr\mathcal{U}\rho(t)\mathcal{U}^\dagger a_{\mathbf{r}}^\dagger a_{\mathbf{r}'} = Tr\rho(t)\mathcal{U}^\dagger a_{\mathbf{r}}^\dagger a_{\mathbf{r}'}\mathcal{U} \\ &= [UG(t)U^\dagger]_{\mathbf{r}\mathbf{r}'} \equiv [\mathcal{K}_U(G)]_{\mathbf{r}\mathbf{r}'} \,. \end{aligned} \tag{2.4}$$

In other words, the matrix G undergoes the evolution $G(t) \to UG(t)U^\dagger$, independent of higher correlation functions. A few other operations that yield a closed equation for G are possible and described in detail in [52].

We will use two of the aforementioned operations. We start with the elementary particle detection measurement at a site $\mathbf{r}$. It is described by the following Krauss map of the many body density matrix:

$$\rho \to \hat{n}_{\mathbf{r}}\rho\hat{n}_{\mathbf{r}} + (1-\hat{n}_{\mathbf{r}})\rho(1-\hat{n}_{\mathbf{r}}) \tag{2.5}$$

where $\hat{n}_{\mathbf{r}} = a_{\mathbf{r}}^\dagger a_{\mathbf{r}}$ is the number operator associated with site $\mathbf{r}$. Note that for fermions, $\hat{n}_{\mathbf{r}}$ is a projection operator, and the Krauss map (2.5) describes complete decoherence between the number on the site $\mathbf{r}$ and other sites. Substituting (2.5) in Eq. (2.1), fermion detection induces the following map on G:

$$G \to \mathcal{K}_{detect.\,r}(G) = P_{\mathbf{r}}^\perp G P_{\mathbf{r}}^\perp + P_{\mathbf{r}} G P_{\mathbf{r}} \,. \tag{2.6}$$

where $P_{\mathbf{r}} = |\mathbf{r}\rangle\langle\mathbf{r}|$ is the (single-particle) projector on site $\mathbf{r}$ and $P_{\mathbf{r}}^\perp = I - P_{\mathbf{r}}$. An additional operation is an extraction event of a particle at site $\mathbf{r}$. Such an operation can be described by the Krauss map

$$\rho \to \epsilon(2-\epsilon)a_{\mathbf{r}}\rho a_{\mathbf{r}}^\dagger + (1-\epsilon\hat{n}_{\mathbf{r}})\rho(1-\epsilon\hat{n}_{\mathbf{r}}). \tag{2.7}$$

where $0 \leq \epsilon \leq 1$ describes the efficiency of the extraction procedure. Again, substituting this map in the definition (2.1) we obtain

$$\begin{aligned} G \to \mathcal{K}_{extr.\,r}(G) = P_{\mathbf{r}}^\perp G P_{\mathbf{r}}^\perp + \\ (1-\epsilon)P_{\mathbf{r}} G P_{\mathbf{r}}^\perp + (1-\epsilon)P_{\mathbf{r}}^\perp G P_{\mathbf{r}} + (1-\epsilon)^2 P_{\mathbf{r}} G P_{\mathbf{r}}. \end{aligned} \tag{2.8}$$

[1] Throughout the rest of the paper we will use units where $\hbar = 1$.

In this paper, we combine the three types of maps above to represent the dynamics of a disturbance interacting with a lattice as it moves from site to site. We prepare the system at an initial state, with a two point function $G(t=0) = G_0$. The disturbance will interact with the system at position $\mathbf{r} = 0$, and moves to act on an adjacent point $a\mathbf{w}$, where it acts again after which it moves to $2a\mathbf{w}$ and so on, with the disturbance at the nth step acting at position $\mathbf{r} = na\mathbf{w}$. We only consider motion at angles where the tip hits the actual lattice sites, i.e. the direction of motion $\mathbf{w}$ needs to be a lattice vector.

The evolution of the correlation matrix G between successive time steps is described by the maps given in Eqs (2.4), (2.6), or (2.8)—as elaborated in detail in each section. Let the evolution from time τn to $\tau(n+1)$ be given by $\mathcal{K}_n$ (for example, detection at point $\mathbf{r} = na\mathbf{w}$ using (2.6), followed by non-interacting evolution for a time τ using (2.4)). The evolved system at time $n\tau$ will therefore have the correlation matrix:

$$G(n\tau) = \mathcal{K}_n(\mathcal{K}_{n-1}(....\mathcal{K}_1(G_0)....)), \tag{2.9}$$

and in particular, the local density change compared to the initial density is

$$\delta G_{\mathbf{rr}} \equiv Tr(\rho(n\tau)a^\dagger_{\mathbf{r}}a_{\mathbf{r}}) - Tr(\rho(0)a^\dagger_{\mathbf{r}}a_{\mathbf{r}}) = G_{\mathbf{rr}}(n\tau) - G_{\mathbf{rr}}(0) \tag{2.10}$$

we follow these dynamics numerically, explicitly affecting the iteration procedure for each of the cases, as explained below, and compare the results to the co-moving steady state which we now define.

For a moving disturbance, a steady state can only be formed in the co-moving frame. Consider an elementary operation $G \to \mathcal{K}(G)$ (for example detection, followed by non-interacting evolution for a time τ), which is then repeated, but shifted in space by the vector $a\mathbf{w}$. Let S be the translation operator along the direction of motion $\mathbf{w}$, via $S^\dagger\,\mathbf{r} = \mathbf{r} + a\mathbf{w}$. We then define a steady state for the correlation matrix in the co-moving frame via the requirement that

$$G_{steady} = S^\dagger \mathcal{K}(G_{steady})S, \tag{2.11}$$

namely G_{steady} is invariant under the combination of the operation $\mathcal{K}$ and moving to the next site. To identify relevant steady states, we will seek solutions to (2.11) in the vicinity of states associated with an unperturbed system. Indeed, as we shall see, the nature of the steady states depends both on the form of the dynamics $\mathcal{K}$ as well as on

the initial background state (for example, a Fermi gas at different filling fractions).

We note that, for simplicity, we focus here on initial states suitable for non-interacting systems. We emphasize that the formalism is valid also for systems prepared in an interacting state as long as the subsequent dynamics is well approximated by non-interacting evolution.

2.3 A Moving Potential

Consider a tip traveling along the lattice, in a direction $\mathbf{w}$ taking a time τ to move between two sites. We approximate this process as a discrete process, where a potential V hops from site to site, remaining a time unit τ at each site. For the purposes of this paper, we will focus on the simplest case of a square lattice with nearest neighbor hopping as the free evolution, i.e. $\mathcal{H}_0 = -t_{hop} \sum_{\langle \mathbf{r},\mathbf{r}' \rangle} a^\dagger_{\mathbf{r}} a_{\mathbf{r}'}$ with single particle energies $\varepsilon(k) = -2t_{hop} \left[\cos(k_x a) + \cos(k_y a)\right]$ where a is the lattice spacing. We will take the tip potential at a fixed reference point $\mathbf{r}_0$ to be $\mathcal{V} = V a^\dagger_{\mathbf{r}_0} a_{\mathbf{r}_0}$. We will mostly concentrate on half filling in this section.

We describe below the wake formed behind a point potential moving at a general speed and angle with respect to the lattice. We begin by summarizing the main results of this section before providing full derivations. Fig. 2.4 shows the simulation of the wake pattern formed by evolving the system in real time following a successive application of the tip along a horizontal line moving at various speeds. Fig. 2.5 represents the simulation of the wake formed by similarly evolving the system in real time except with the tip moving at several different angles with respect to the lattice. Denoting

$$\alpha = \frac{1}{2\tau t_{hop}} \tag{2.12}$$

we use Eq. (2.11) to find that the angles of lines of zero disturbance are described by

$$\frac{r_y}{r_x} = \frac{1 + w_y \alpha}{\pm 1 + w_x \alpha} \;\; ; \;\; \frac{r_y}{r_x} = \frac{-1 + w_y \alpha}{\pm 1 + w_x \alpha} \tag{2.13}$$

These "zero disturbance" lines are represented as red lines in the figures, and delineate the shape of the wake openings. As expected, since we are not in a Kelvin regime,

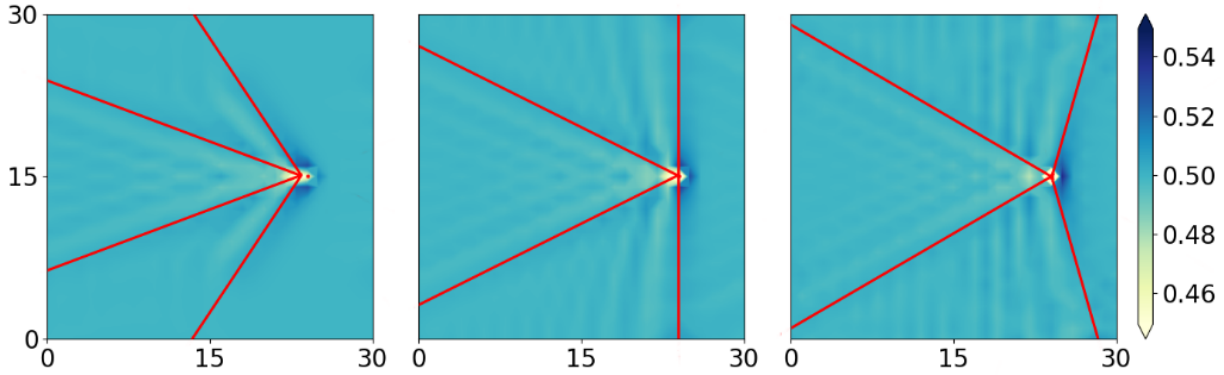

FIGURE 2.4: Density plots for varying velocities of a moving potential. From left to right, velocities $\alpha = 1.7$, 1.0, and 0.7. Red lines represent the angles given by Eq. (2.35). Each line corresponds to the solution for a given quadrant in Fig. 2.6. Note the forward pointing cone is a result of a forward d-wave radiation when the source is moving slowly.

the angle depends on the speed of the disturbance and is discussed below. Note, in contrast to the classic Kelvin wakes and potential wakes in a two-dimensional electron gas [56], here the lattice breaks rotational symmetry and the wake pattern changes as the potential path rotates with respect to the lattice.

Before moving on to the derivation, let us comment briefly on the limiting behavior of Eq. (2.13). Note, that as $\alpha \to 0$, we find $\frac{r_y}{r_x} \to \pm 1$, i.e. the two main diagonal directions. This result is consistent with the expectation that as the velocity vanishes, the moving potential is almost static and will radiate via the underlying D-wave symmetry of the lattice.

As $\alpha \to \infty$, i.e. the limit of an extremely fast moving tip, we find that $\frac{r_y}{r_x} \to \frac{w_y}{w_x}$, in other words, the wake converges onto a line following the disturbance, as any disturbance would not have time to disperse. Hence, Eq. (2.13) implies that the wake will essentially vanish for a potential moving at $\alpha \to \infty$.

The co-moving steady state to be found for our system is described by, Eq. (2.11), where $\mathcal{K}(G) = e^{i\tau(H_0+V)} G e^{-i\tau(H_0+V)}$ where $H_0 = -t_{hop} \sum_{\langle \mathbf{r},\mathbf{r}' \rangle} |\mathbf{r}\rangle \langle \mathbf{r}'|$ is the unperturbed single particle Hamiltonian and $V = V |\mathbf{r_0}\rangle \langle \mathbf{r_0}|$ is the tip potential at some initial reference point $\mathbf{r}_0$. Namely:

$$S^\dagger e^{i\tau(H_0+V)} G e^{-i\tau(H_0+V)} S = G \tag{2.14}$$

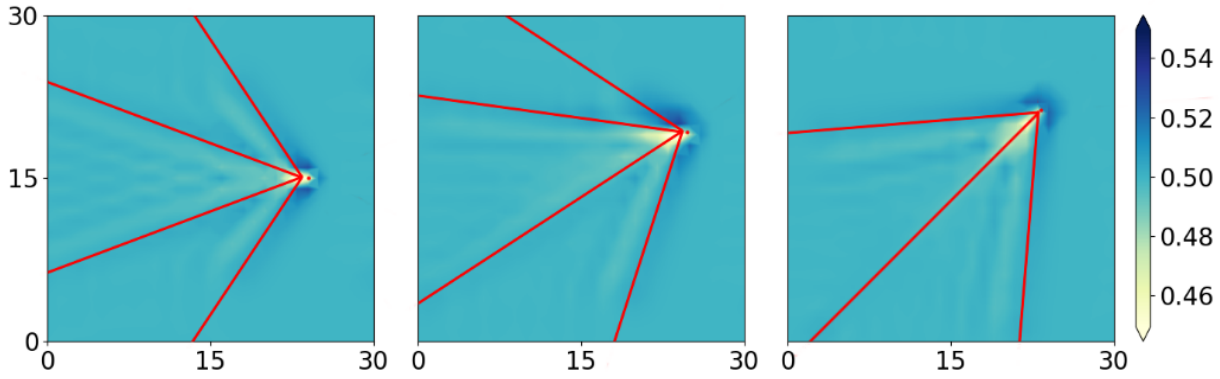

FIGURE 2.5: Density plots for varying the angle of a moving potential compared to the lattice vectors. A potential moving at 0, 23, and 45 degrees with respect to the lattice. Here, $\alpha = 1.7$. A smeared potential (Gaussian with half a lattice spacing width) is used instead of a point potential to include effects when the tip is not precisely on a lattice site. It is argued in the appendix that the wake geometry is unaffected by this change away from a point potential. Red lines represent the angles given by Eq. (2.35). Note that for motion at 45 degrees the angles for quadrants 1 and 4 in Eq. (2.35) coincide reducing the number of lines to 3.

In general, equation (2.14) admits infinitely many solutions for G. In particular, any correlation matrix G that satisfies:

$$[G, S^\dagger e^{i\tau(H_0+V)}] = 0 \tag{2.15}$$

will automatically be a co-moving non-equilibrium steady state. In the physical scenario we are interested in, however, we have an initial reference state, the correlation matrix G_0 of the unperturbed Fermi system, and in the following we consider the wake as a weak perturbation on this state, allowing us to analytically establish the dominant behavior of the wake pattern.

Since we are only perturbing the free evolution by a small potential, we can assume the steady state G will be close to the steady state of free evolution, G_0, where $G_{0\mathbf{r}\mathbf{r}'} = \langle a^\dagger_{\mathbf{r}} a_{\mathbf{r}'} \rangle_{equilibrium}$. Thus, we write $G = G_0 + \delta G$ where δG is assumed a small perturbation. Since H_0 is translation-invariant, we write the co-moving non-equilibrium steady state equation in momentum space as:

$$e^{ia\mathbf{w}\cdot(\mathbf{k}-\mathbf{k}')} \langle \mathbf{k}| e^{i\tau(H_0+V)}(G_0 + \delta G) e^{-i\tau(H_0+V)} |\mathbf{k}'\rangle = \langle \mathbf{k}| G_0 + \delta G |\mathbf{k}'\rangle$$

Substituting lowest order perturbation theory, keeping terms up to linear order in V and δG, we find that the real space density disturbance, at zero temperature is given by:

$$\langle \mathbf{r}|\delta G|\mathbf{r}\rangle = \frac{V\tau a^4}{(2\pi)^4}\int\int_{-\frac{\pi}{a}}^{\frac{\pi}{a}} d\mathbf{k}d\mathbf{k}' A(\mathbf{k},\mathbf{k}')R(\mathbf{k},\mathbf{k}',\mathbf{w}) \\ e^{i(\mathbf{r}_0-\mathbf{r})\cdot(\mathbf{k}-\mathbf{k}')}\left[\Theta(\varepsilon_f-\varepsilon(\mathbf{k}))-\Theta(\varepsilon_f-\varepsilon(\mathbf{k}'))\right] \tag{2.16}$$

where:

$$A(\mathbf{k},\mathbf{k}') = \frac{e^{i\tau[\varepsilon(\mathbf{k})-\varepsilon(\mathbf{k}')]}-1}{\tau(\varepsilon(\mathbf{k})-\varepsilon(\mathbf{k}'))}, \tag{2.17}$$

$$R(\mathbf{k},\mathbf{k}',\mathbf{w}) = \frac{1}{1-e^{-ia\mathbf{w}\cdot(\mathbf{k}-\mathbf{k}')}e^{-i\tau[\varepsilon(\mathbf{k})-\varepsilon(\mathbf{k}')]}}, \tag{2.18}$$

and ε_f is the Fermi energy. Derivation details can be found in the appendix.

Our main objective now is to compute the large-scale features of the resulting pattern, namely the typical angle that appears in the wake pattern. As in the case of the original Kelvin wake, which is typically derived by a stationary phase method, the present treatment requires careful consideration of the dominant contribution to the density variation [Eq. (2.16)]. The terms A and R in Eq. (2.16) will provide us with regions that are particularly important for the integral over $\mathbf{k}$ and $\mathbf{k}'$. Due to the Fermi functions, we can write Eq. (2.16) as:

$$\langle \mathbf{r}|\delta G|\mathbf{r}\rangle = \frac{2V\tau a^4}{(2\pi)^4}\int_{\varepsilon(\mathbf{k})>\varepsilon_f}\int_{\varepsilon(\mathbf{k}')<\varepsilon_f} d\mathbf{k}d\mathbf{k}' \\ \mathrm{Re}\Big\{A(\mathbf{k},\mathbf{k}')R(\mathbf{k},\mathbf{k}',\mathbf{w})e^{i(\mathbf{r}_0-\mathbf{r})\cdot(\mathbf{k}-\mathbf{k}')}\Big\} \tag{2.19}$$

Note that $|A(\mathbf{k},\mathbf{k}')| < 1$ (this follows from the inequality $|e^{i\theta}-1| \leq |\theta|$) and is dominated by $\mathbf{k}$,$\mathbf{k}'$ near $\varepsilon(\mathbf{k})-\varepsilon(\mathbf{k}') = 0$. We thus see that in contrast to the measurement and extraction wakes considered next, the integral is dominated by momenta near the Fermi surface since we can take such momenta to satisfy both conditions $\tau(\varepsilon(\mathbf{k})-\varepsilon(\mathbf{k}')) \ll 1$ and $\varepsilon(\mathbf{k}) > \varepsilon_f$ and $\varepsilon(\mathbf{k}') < \varepsilon_f$.

We will henceforth consider the situation at half filling. Looking at the Fermi surface for our system, we break up the expansion around the Fermi surface into four quadrants given in Fig. 2.6. Close to the Fermi lines, we will use the variables δ_y and

$\delta_{y'}$ instead of k_y, k'_y as the small shifts away from the Fermi surface. Explicitly,

Quadrant		
1	$k_y = \frac{\pi}{a} - k_x + \delta_y$	$k'_y = \frac{\pi}{a} - k'_x + \delta_{y'}$
2	$k_y = -\frac{\pi}{a} + k_x + \delta_y$	$k'_y = -\frac{\pi}{a} + k'_x + \delta_{y'}$
3	$k_y = \frac{\pi}{a} + k_x + \delta_y$	$k'_y = \frac{\pi}{a} + k'_x + \delta_{y'}$
4	$k_y = -\frac{\pi}{a} - k_x + \delta_y$	$k'_y = -\frac{\pi}{a} - k'_x + \delta_{y'}$

(2.20)

Let us now concentrate on R in Eq. (2.16). This term diverges when

$$\tau[\varepsilon(\mathbf{k}) - \varepsilon(\mathbf{k}')] + a\mathbf{w} \cdot (\mathbf{k} - \mathbf{k}') = 2\pi n \tag{2.21}$$

for n integer. Here we concentrate on the $n = 0$ contribution which already recovers some basic features of the wake pattern, and leave the analysis of $n \neq 0$ contributions for a future work. The equation can also be interpreted as a Mach-Cherenkov-Landau condition [84] for the momenta emitted by the wake due to creating a particle-hole excitation of momentum $\mathbf{K} = \mathbf{k} - \mathbf{k}'$. Perhaps a more familiar way to write the condition is:

$$\Omega(\mathbf{K}) + \mathbf{K} \cdot \mathbf{V} = 0 \tag{2.22}$$

where $V = \tau^{-1}\alpha a\mathbf{w}$, and $\Omega(K) = \nabla_{\mathbf{k}}\epsilon(\mathbf{k})|_{k_F} \cdot \mathbf{K}$.

For the square lattice, we have

$$\begin{gathered}\alpha a\mathbf{w} \cdot (\mathbf{k} - \mathbf{k}') = \\ \cos(k_x a) + \cos(k_y a) - \cos(k'_x a) - \cos(k'_y a)\end{gathered} \tag{2.23}$$

where α is defined by Eq. (2.12). Now, combining the restriction $\tau(\varepsilon(\mathbf{k}) - \varepsilon(\mathbf{k}')) \ll 1$ with Eq. (2.23), we find that

$$k'_x = k_x + w(k_y - k'_y) + \delta_x \tag{2.24}$$

where δ_x is given by $\delta_x \equiv \frac{\tau(\varepsilon(\mathbf{k}) - \varepsilon(\mathbf{k}'))}{aw_x}$ and where $w \equiv \frac{w_y}{w_x}$. Comparing to Eq. (2.20) we arrive at:

$$k_x = k'_x + \delta_{x'} \tag{2.25}$$

where $\delta_{x'} \equiv \frac{w(\delta_y - \delta_{y'}) + \delta_x}{1+(-1)^b w}$. Here, $b = 1$ for quadrant 1 and 4 (Fig. 2.6). Otherwise, $b = 0$. Note that our treatment of $\delta_{x'}$ as small breaks down when w is close to 1. Indeed, when $w_x = w_y$, the constraints on energy together with Eq. (2.23) are insufficient to force k and k' to be close, since $(k - k')$ can be large, with both k, k' close to the Fermi surface, and $(k - k')$ perpendicular to the **w** vector. While more refined analysis is needed to describe the special point $w_x = w_y$ exactly, here we simply observe numerically that our treatment works well for $w_x < w_y$ and $w_y > w_x$, and that the wake pattern change is continuous at $w_x = w_y$ and is well described by our Eq. (2.13).

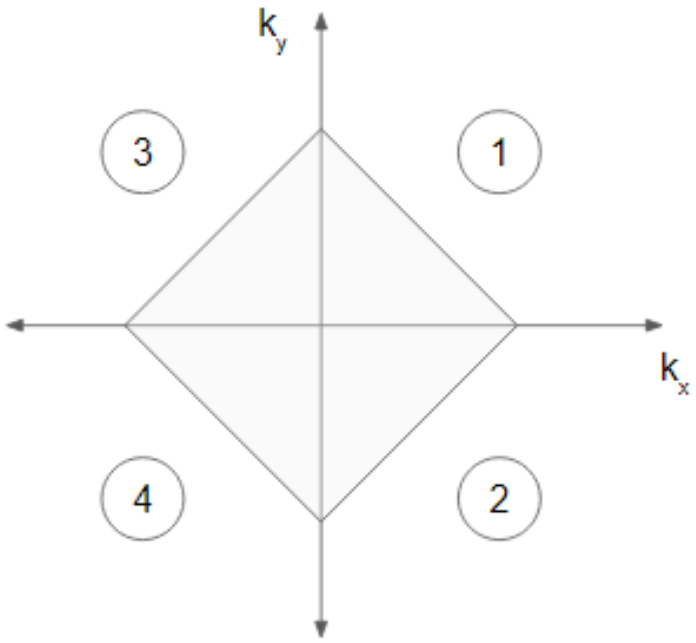

FIGURE 2.6: Fermi surface at half-filling. At half filling all states with momenta k_x and k_y within the diamond shape are occupied. For the calculation we consider the four quadrants separately.

We now combine Eqs. (2.25), (2.20), and (2.23), and expand in small $\delta_{x'}, \delta_y, \delta_{y'}$ to second order. Solving those, we can relate $\delta_{x'}$ and $\delta_{y'}$ to δ_y and solve for $k_x - k'_x$ and $k_y - k'_y$ as

$$k_x - k'_x = \frac{2(w_x\alpha + \sin(ak_x))(w_y\alpha + (-1)^{b+1}\sin ak_x)}{(w_x + (-1)^b w_y)\alpha\left[(w_x + (-1)^{b+1}w_y)\alpha + 2\sin(ak_x)\right]} \tag{2.26}$$

and

$$k_y - k'_y = \frac{2(w_x\alpha+\sin(ak_x))^2}{(w_x+(-1)^b w_y)\alpha\left[(w_x+(-1)^{b+1}w_y)\alpha+2\sin(ak_x)\right]} \tag{2.27}$$

If we assume our potential is at site $\mathbf{r}_0 = (0,0)$, the term $e^{i(\mathbf{r}_0-\mathbf{r})\cdot(\mathbf{k}-\mathbf{k}')}$ in Eq. (2.19) becomes

$$e^{i(\mathbf{r}_0-\mathbf{r})\cdot(\mathbf{k}-\mathbf{k}')} \to e^{-i\mathbf{r}\cdot(\mathbf{k}-\mathbf{k}')} = e^{-i\delta_y B} \tag{2.28}$$

where

$$B = \frac{2[w_x\alpha+\sin(ak_x)]}{(w_x+(-1)^b w_y)\alpha\left[(w_x+(-1)^{b+1}w_y)\alpha+2\sin(ak_x)\right]} \times \left[r_x(w_y\alpha+(-1)^{b+1}\sin ak_x)+r_y(w_x\alpha+\sin ak_x)\right] \tag{2.29}$$

greatly reducing our momentum space integral to two coordinates, k_x and δ_y. Note that when the denominators in A, R in Eq. (2.19) vanish, the leading behavior of the combination AR is real, we arrive at:

$$\langle \mathbf{r}|\delta G|\mathbf{r}\rangle \propto -\frac{2V\tau a^4}{(2\pi)^4}\sum_{\mathcal{Q}} \mathrm{Re}\left\{\iint_{\mathcal{Q}} dk_x d\delta_y e^{i\delta_y B}\right\}, \tag{2.30}$$

where $\mathcal{Q}$ is the set of four quadrants in Fig. 2.6. We have checked numerically that the integral (2.30) indeed captures the main wake pattern of the moving potential well. Our next task is to use Eq. (2.30) to find the main wake angles.

We now estimate analytically the main angles involved in the wake pattern left behind the moving potential. In the case of water wakes, we are interested in the wavefronts, which are lines of maximal disturbance. Here, we find that a more direct approach is to look instead for lines of zero disturbance, i.e. $\langle \mathbf{r}|\delta G|\mathbf{r}\rangle = 0$. We will begin by looking at the effects of individual quadrants in Eq. (2.30). Integrating over δ_y and looking first at quadrant 1, we find

$$\begin{aligned}\langle \mathbf{r}|\delta G|\mathbf{r}\rangle &\propto -\tfrac{2V\tau a^2}{(2\pi)^4}\,\mathrm{Re}\left\{\int_0^{\pi/a}\int_0^{k_x} dk_x d\delta_y e^{i\delta_y B}\right\} \\ &= \tfrac{2V\tau a^2}{(2\pi)^4}\,\mathrm{Im}\left\{\int_0^{\pi/a} dk_x \tfrac{e^{ik_x B}-1}{B}\right\}\end{aligned} \tag{2.31}$$

To find the characteristic wake lines, we now look for directions $\mathbf{r}$ such that Eq. (2.31) vanishes. Assuming that we could treat the equation by a stationary phase method, a condition for Eq. (2.31) vanishing would be that there exists a k_0 such that $k_x B \approx (k_x - k_0)^2$. In this case, using the stationary phase approximation around k_0 makes the dominant contribution to the integral in Eq. (2.31) real, and $\langle \mathbf{r}|\delta G|\mathbf{r}\rangle$ vanishes. Specifically, for this to happen, we need $B = 0$ and $\frac{d}{dk_x}B = 0$ when evaluated at k_0. Looking at $r_x, r_y \gg 1$, i.e. far away from the potential, the dominating behavior of B (Eq. (2.29)) comes from $r_x(w_y\alpha + (-1)^{b+1}\sin ak_x) + r_y(w_x\alpha + \sin ak_x)$. Hence, we find the equations:

$$r_x(w_y\alpha + (-1)^{b+1}\sin ak_x) + r_y(w_x\alpha + \sin ak_x) = 0, \tag{2.32}$$

and

$$(-1)^{b+1} r_x \cos ak_x + r_y \cos ak_x = 0. \tag{2.33}$$

Therefore, $\cos ak_x = 0$ implying $k_0 = \frac{\pi}{2a}$. Plugging this into Eq. (2.32) yields

$$\frac{r_y}{r_x} = \frac{1 + w_y\alpha}{1 + w_x\alpha}. \tag{2.34}$$

Repeating this calculation for the other three quadrants, we find

Quadrant	Line of $\langle \mathbf{r}\|\delta G\|\mathbf{r}\rangle = 0$
1	$\frac{r_y}{r_x} = \frac{1+w_y\alpha}{1+w_x\alpha}$
2	$\frac{r_y}{r_x} = \frac{-1+w_y\alpha}{1+w_x\alpha}$
3	$\frac{r_y}{r_x} = \frac{1+w_y\alpha}{-1+w_x\alpha}$
4	$\frac{r_y}{r_x} = \frac{-1+w_y\alpha}{-1+w_x\alpha}$

(2.35)

and hence our main result Eq. (2.13). Figures 2.4 and 2.5 show agreement between the simulations of the potential wakes and our Eq. (2.35). While the above treatment was perturbative in V, our analytical treatment for the angles should hold asymptotically at large distances from the source. This is because, in that regime, the response to the disturbance is weak regardless of the strength of the perturbation. Close to the source, the density profile will, in general, not be linear in the strength of the perturbing potential. In particular, at half filling, the requirement $\delta G \ll G_0$ implies that $\langle \mathbf{r}|\delta G|\mathbf{r}\rangle \ll \frac{1}{2}$. To see the range of validity of the description close to the source, let us consider $\langle \mathbf{r}|\delta G|\mathbf{r}\rangle$

as expressed in the integral (2.31). We note that B grows linearly in $|\mathbf{r}|$, and therefore, asymptotically $\langle \mathbf{r}|\delta G|\mathbf{r}\rangle$ oscillates and decays at least as fast as $|\mathbf{r}|^{-1}$ (consistent with the numerical observations). The expression (2.31) shows that the density profile will be perturbative when $\frac{V\tau a}{|\mathbf{r}|} \ll 1$, or, in other words at distances $\frac{|\mathbf{r}|}{a} \gg V\tau$.

2.4 Moving particle extractor and moving detectors

We proceed to consider a moving detector or particle extraction from the system. Note, that these processes are non-unitary. In this section we establish the co-moving steady-state for this problem. In particular, we show that in marked contrast with a moving potential, a moving detector at half filling does not generate a wake because of particle-hole symmetry.

We assume that the detection or extraction process is dominant when the tip is at a given site, but quickly weakens as the tip moves away from that site. It is therefore natural to discretize the process in such a way that we have a disturbance at a given site, followed by a free evolution of the system during a time τ that the tip is traveling to the next site on it's trajectory. The appropriate transformation rules $\mathcal{K}(G)$ for detection and extraction are given in Eq. (2.6) and (2.8) respectively. If we allow for pure detection to happen with probability p (associated with the efficiency of the detector) and similarly extraction protocol with probability q, we can combine them, together with the free evolution $U = e^{-i\tau H_0}$ into the general form

$$\begin{aligned} G \to \mathcal{K}(G) = \\ \mathcal{K}_U((1-p-q)G + p\mathcal{K}_{detect}(G) + q\mathcal{K}_{extract}(G))) \end{aligned} \tag{2.36}$$

which can be written as:

$$G \to \mathcal{K}(G) = U^\dagger \left[G - \gamma\{G,P\} + \xi PGP\right] U \tag{2.37}$$

where $\xi = 2p + \epsilon^2 q$, $\gamma = p + \epsilon q$, $\{G,P\} \equiv GP + PG$ indicates the anti-commutator, and P is the projection onto a site $\mathbf{r}_0$ where the tip acts. In particular, pure detection will be described by $q = 0$, hence $\gamma = p$ and $\xi = 2p$.

In the next sections we work under the assumption that $p, q \ll 1$ and hence $\gamma \ll 1$. The co-moving steady state equation (2.11) now reads:

$$\langle \mathbf{k} | S^\dagger U^\dagger \left[G - \gamma \{G, P\} + \xi PGP \right] US | \mathbf{k}' \rangle = \langle \mathbf{k} | G | \mathbf{k}' \rangle \tag{2.38}$$

Written explicitly in momentum space we have:

$$e^{ia\mathbf{w}\cdot(\mathbf{k}-\mathbf{k}')} e^{i\tau[\varepsilon(\mathbf{k})-\varepsilon(\mathbf{k}')]} \{ \langle k|G|k' \rangle - \gamma \langle \mathbf{k}|\{G,P\}|\mathbf{k}' \rangle + \xi \langle \mathbf{k}|PGP|\mathbf{k}' \rangle \} = \langle \mathbf{k}|G|\mathbf{k}' \rangle$$

Assuming that $\gamma \ll 1$, $G \approx G_0 + \delta G$, with δG being a small correction, and zero temperature, we find that the local density variation is given by:

$$\langle \mathbf{r}|\delta G|\mathbf{r} \rangle = \frac{\gamma a^4}{(2\pi)^4} \int\int_{-\pi/a}^{\pi/a} d\mathbf{k} d\mathbf{k}' R(\mathbf{k}, \mathbf{k}', \mathbf{w}) e^{i(\mathbf{r}_0 - \mathbf{r})\cdot(\mathbf{k}-\mathbf{k}')} \left[\frac{\xi \rho_f}{\gamma} - \Theta(\varepsilon_f - \varepsilon(\mathbf{k})) - \Theta(\varepsilon_f - \varepsilon(\mathbf{k}')) \right] \tag{2.39}$$

where ρ_f is the density of fermions in G_0 (i.e. the diagonal of the G_0 matrix). Note, that like in the potential case, the term R in Eq. (2.39) implies that Eq. (2.23) still characterizes a dominant region for the integral. However, Eq. (2.39) has two added difficulties when compared with the moving potential case Eq. (2.16). First, we no longer have the helpful constraint that $\tau \left[\varepsilon(\mathbf{k}) - \varepsilon(\mathbf{k}') \right] \approx 0$. Secondly, $\varepsilon(\mathbf{k})$ and $\varepsilon(\mathbf{k}')$ can now be on the same side of ε_f as well as on the opposite side. Nonetheless, in numerical experiments we have observed that the geometry for a moving potential, Eq. (2.35), does appear to also match with the wake patterns of a moving detector and extractor, as can be observed, e.g., by comparing the wake pattern Fig. 2.4 to the extractor pattern Fig. 2.8 .

By iterating the evolution equation for the two point function G, the wake pattern can be generated numerically. For the case of a particle removal site moving through a half-filled Fermi sea we obtain the images shown in Fig. 2.7 and 2.8. The geometry of the wake patterns is similar to the ones described for the moving potential Fig. 2.4, however the density variation is always negative due to the depleted particles.

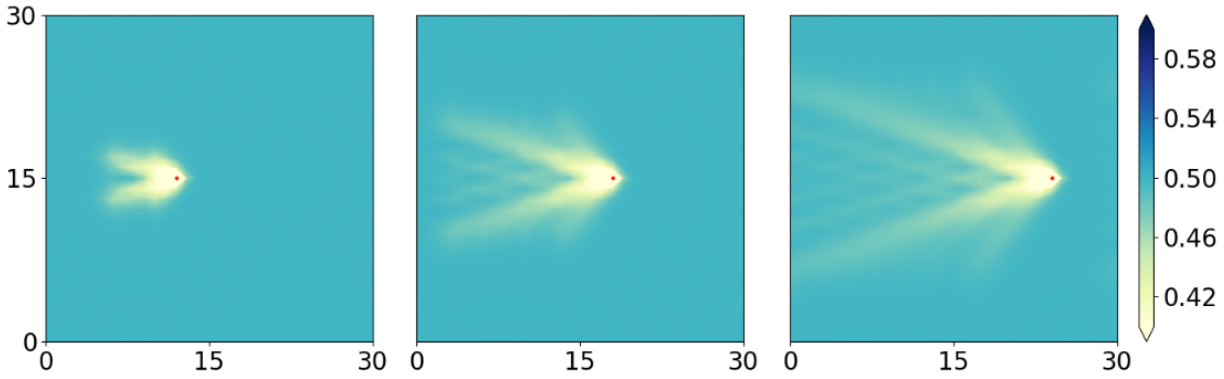

FIGURE 2.7: Density plot of a wake developing following a fermion extraction site moving at $\alpha = 1.7$. The pictures show a steady-state in the comoving frame.

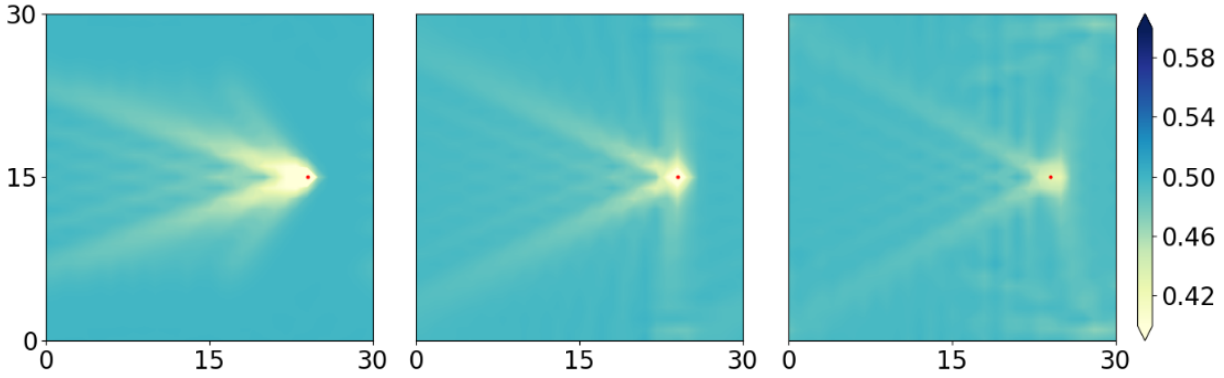

FIGURE 2.8: Density plot for varying speeds of a moving particle extractor at half-filling. From left to right, speed $\alpha = 1.7$, 1.0, and 0.7 respectively.

2.4.1 Moving detector at half filling

Particle detection at half filling shows marked contrast with the density wake due to a moving potential. Indeed, due to particle hole symmetry it leaves the average density profile, namely the diagonal of G unchanged. On the other hand, a potential perturbation breaks particle-hole symmetry and generates the density wake described above.

In fact, we can establish a stronger property, namely:

$$\langle \mathbf{r}|\delta G|\mathbf{r}\rangle_{\mu} + \langle \mathbf{r}|\delta G|\mathbf{r}\rangle_{-\mu} = 0 \tag{2.40}$$

where $\langle \mathbf{r}|\delta G|\mathbf{r}\rangle_{\mu}$ is obtained by successive applications of $\mathcal{K}$ from Eq. (2.36) on an initial state $G_0 = \frac{1}{1+e^{\beta(H-\mu)}}$, with $q = 0$, using an arbitrary choice of measuring site at each step, and in the end subtracting G_0. In other words, changing the sign of the chemical

potential changes the sign of the wake.

An immediate consequence of Eq. (2.40) is that at the point, where our many-body Hamiltonian has particle-hole symmetry, namely $\mu = 0$ i.e. at half filling:

$$\langle \mathbf{r}|\delta G|\mathbf{r}\rangle_{\mu=0} = 0, \tag{2.41}$$

i.e. there should be no wake pattern created by a moving detector. This is shown in Fig. 2.9 by comparing a detector moving through a half-filled versus a quarter-filled Fermi sea. The image also shows how the quarter filled wake is opposite in sign to the wake generated in the Fermi system at three quarter filling.

A full non-perturbative proof of the remarkable relation Eq. (2.40) is presented in the appendix. Here for simplicity we establish Eq. (2.40) starting from the (zero temperature) perturbative result Eq. (2.39) with $\epsilon_F = \mu$ and $\xi = 2\gamma$. Note that the sum $\langle \mathbf{r}|\delta G|\mathbf{r}\rangle_{\mu} + \langle \mathbf{r}|\delta G|\mathbf{r}\rangle_{-\mu}$ is given by Eq. (2.39) with the term in brackets replaced with

$$2 - \Theta(\mu - \varepsilon(\mathbf{k})) - \Theta(\mu - \varepsilon(\mathbf{k}')) - \Theta(-\mu - \varepsilon(\mathbf{k})) - \Theta(-\mu - \varepsilon(\mathbf{k}')) \tag{2.42}$$

where we used that $\rho_f(\epsilon_F) + \rho_f(-\epsilon_F) = 1$.

Now consider the following map reflecting points about the Fermi surface:

$$\mathbf{k} \to \mathcal{M}(\mathbf{k}) \equiv (-1^b, -1^{1+\mathcal{Q}})\frac{\pi}{a} - \mathbf{k} \tag{2.43}$$

where $\mathcal{Q}$ is the quadrant number and $b = 0$ if in quadrants 1 or 2 and $b = 1$ in quadrants 3,4. Note that $\epsilon(\mathcal{M}(\mathbf{k})) = -\epsilon(\mathbf{k})$, and that, $\exp[i\mathbf{r}\cdot(\mathcal{M}(\mathbf{k}) - \mathcal{M}(\mathbf{k}'))] = \exp[-i\mathbf{r}\cdot(\mathbf{k} - \mathbf{k}')]$ thus, the real part of $R(\mathbf{k}, \mathbf{k}', \mathbf{w})e^{i(\mathbf{r_0}-\mathbf{r})\cdot(\mathbf{k}-\mathbf{k}')}$ in Eq. (2.39) is symmetric under such a transformation. On the other hand, the bracket term Eq. (2.42) is anti-symmetric under the map $\mathcal{M}$. The result of k, k' integrations will therefore vanish, establishing Eq. (2.40).

2.4.2 A "fluctuation" wake

The above results suggest at first glance that there is no effect of the detector at half filling. In fact, this is not the case! While the moving detector does not affect the average density at half filling, it does perturb correlations, and thus may be observed through fluctuations. For example, such correlations may be observed by looking at

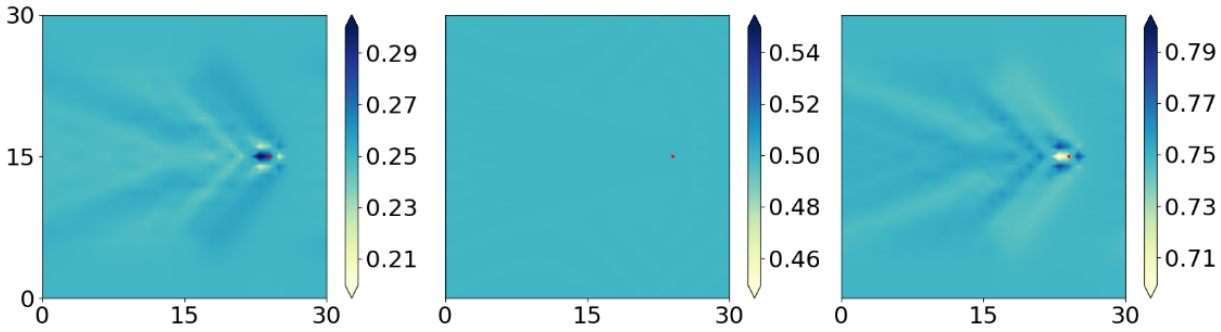

FIGURE 2.9: Density plots of a detector moving through a Fermi sea at several filling fractions. From left to right, the detector is moving at $\alpha = 1.7$ for quarter-filling, half-filling, and three-quarter-filling, respectively. The color bar has the same scale but different offset (centered around the initial filling fraction).

the number of particles in a mode $a^\dagger_{A(\mathbf{r})} \equiv \frac{1}{\sqrt{A}} \sum_{\mathbf{r}'-\mathbf{r}\in A} a^\dagger_{\mathbf{r}'}$, representing an equal weight superposition in a region lattice neighborhood A of a point $\mathbf{r}$. We have:

$$n_A(\mathbf{r}) \equiv \langle a^\dagger_{A(\mathbf{r})} a_{A(\mathbf{r})} \rangle = \frac{1}{|A|} \sum_{\mathbf{r}'\mathbf{r}''\in(A+\mathbf{r})} G_{\mathbf{r}'\mathbf{r}''} = \frac{1}{|A|} \sum_{\mathbf{r}''\mathbf{r}'\in(A+\mathbf{r})} G_{0\mathbf{r}'\mathbf{r}''} + \frac{1}{|A|} \sum_{\mathbf{r}'\mathbf{r}''\in(A+\mathbf{r})} \delta G_{\mathbf{r}'\mathbf{r}''} \tag{2.44}$$

We will focus on A being the set of nearest neighbors: an example of the wake in the density of the $n_A(\mathbf{r})$ is then shown in Fig. 2.10. That this wake may be non-zero can be observed by generalizing Eq. (2.39) for off-diagonal elements. In this case, the only change to (2.39) is that $e^{-i\mathbf{r}\cdot(\mathbf{k}-\mathbf{k}')} \to e^{-i(\mathbf{r}\cdot\mathbf{k}-\mathbf{r}'\cdot\mathbf{k}')}$. Now, combining Eqs. (2.39) and Eq. (2.44), we find

$$\begin{aligned} e^{-i(\mathbf{r}\cdot\mathbf{k}-\mathbf{r}'\cdot\mathbf{k}')} &\to e^{-i\mathbf{r}\cdot(\mathbf{k}-\mathbf{k}')} \sum_{q,q'\in\kappa} e^{-iqa+iq'a} \\ &= e^{-i\mathbf{r}\cdot(\mathbf{k}-\mathbf{k}')}(1-\tfrac{\varepsilon(\mathbf{k})}{t_{hop}})(1-\tfrac{\varepsilon(\mathbf{k}')}{t_{hop}}) \end{aligned} \tag{2.45}$$

where $\kappa = \{0, k_x, k_y, -k_x, -k_y\}$.

Note, Eq. (2.45) is not symmetric under a reflection of $\varepsilon(\mathbf{k})$,$\varepsilon(\mathbf{k}')$ about the Fermi energy. This implies that, unlike the diagonal of G_{rr}, the wake generated for the modes like A for a detector are non-zero.

A couple of remarks are in order.
(1) While we focused here on the density of the $a^\dagger_A$ modes as an indicator of correlations, a more natural quantity for an experimental consideration is density-density

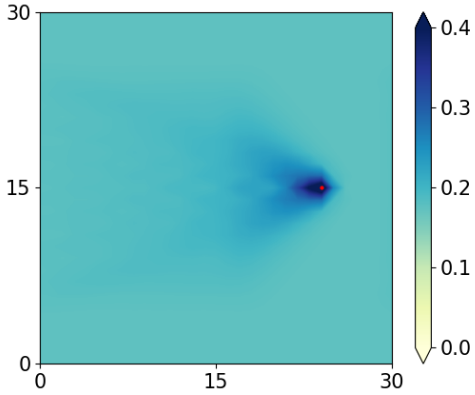

FIGURE 2.10: Density of particles in a spatially spread mode centered around each lattice site (given by $n_A(\mathbf{r})$ as defined in Eq. (2.44)) following a moving detector at half-filling. Here, $\alpha = 1.7$.

correlations, and number fluctuations in the region A. A preliminary check shows that such number fluctuations will also exhibit a wake, which can be studied by considering the four-fermi correlation generalization of Eq. (2.4) and (2.6), which give a closed hierarchy of 4 point functions. This calculation will be presented in a future work.
(2) A moving detector at half filling is an interesting example of a "hierarchy" of steady states. In this hierarchy, the local average density or "diagonal" of G at half filling is steady for any path a detector makes, and is thus in a steady state. However, the correlations depend on the trajectory of the detector and would, in general, not be in a steady state, moreover the many-body density matrix would not be in a steady state. It is not hard to construct examples where G is in a steady state, while the many body density matrix is time-dependent.

2.5 Finite temperature states

In this section we analyze the effect of a non-zero temperature of the system on our moving disturbances. We assume that the system is prepared initially at finite temperature, and we neglect thermal dissipation on the time scale of the motion of our disturbances. We find that at a generic filling the amplitude of the wakes are decreased, as may be expected on general grounds, i.e. with increased density fluctuations of the background. These results are shown in Figs. 2.11 and 2.12. Furthermore, we find

that, at $\rho_f = \frac{1}{2}$, a moving detector continues to produce no wake at finite temperature. Perhaps the most surprising effect we find is that the extractor wake at half filling is temperature independent. This behavior is striking when compared to the moving potential source, see Fig. 2.11.

At finite temperature, $\langle \mathbf{k}|G_0|\mathbf{k}'\rangle = \delta_{\mathbf{k}\mathbf{k}'}F(\varepsilon(\mathbf{k}))$ instead of $\delta_{\mathbf{k}\mathbf{k}'}\Theta(\varepsilon_f - \varepsilon(\mathbf{k}))$, where $F(\varepsilon(\mathbf{k}))$ is the Fermi-Dirac distribution. We find that the finite temperature steady states, are simply obtained by replacing the step functions in equations (2.16) and (2.39) by Fermi-Dirac functions $F(\varepsilon(\mathbf{k}))$.

Thus, the steady state of δG for a moving potential source, Eq. (2.16), becomes

$$\begin{aligned}\langle \mathbf{r}|\delta G|\mathbf{r}\rangle = \tfrac{V\tau a^4}{(2\pi)^4}\iint_{-\pi/a}^{\pi/a} d\mathbf{k}d\mathbf{k}' A(\mathbf{k},\mathbf{k}')R(\mathbf{k},\mathbf{k}',\mathbf{w}) \\ e^{i(\mathbf{r_0}-\mathbf{r})\cdot(\mathbf{k}-\mathbf{k}')}\left[F(\varepsilon(\mathbf{k})) - F(\varepsilon(\mathbf{k}'))\right]\end{aligned} \tag{2.46}$$

while for detection/extraction at finite temperature, Eq. (2.39) becomes

$$\begin{aligned}\langle \mathbf{r}|\delta G|\mathbf{r}\rangle = \tfrac{\gamma a^4}{(2\pi)^4}\iint_{-\pi/a}^{\pi/a} d\mathbf{k}d\mathbf{k}' R(\mathbf{k},\mathbf{k}',\mathbf{w})e^{i(\mathbf{r_0}-\mathbf{r})\cdot(\mathbf{k}-\mathbf{k}')} \\ \left[\tfrac{\xi\rho_f}{\gamma} - F(\varepsilon(\mathbf{k})) - F(\varepsilon(\mathbf{k}'))\right].\end{aligned} \tag{2.47}$$

We can understand the temperature independence of the moving extractor at half filling as follows. Consider the difference between the moving extractor and moving detector steady state equations (Eq. (2.47) with $\xi = 2\gamma$ and $\xi = \gamma$ respectively), we find:

$$\begin{aligned}\langle \mathbf{r}|\delta G_{det}|\mathbf{r}\rangle - \langle \mathbf{r}|\delta G_{extr}|\mathbf{r}\rangle = \\ \tfrac{\gamma a^4}{(2\pi)^4}\iint_{-\pi/a}^{\pi/a} d\mathbf{k}d\mathbf{k}' R(\mathbf{k},\mathbf{k}',\mathbf{w})e^{i(\mathbf{r_0}-\mathbf{r})\cdot(\mathbf{k}-\mathbf{k}')}\rho_f\end{aligned} \tag{2.48}$$

Note, Eq. (2.48) depends only on the density ρ_f. Therefore the difference Eq. (2.48) is independent of temperature if temperature is varied at a fixed density. Since detection creates no wake when $\rho_f = \frac{1}{2}$ at any temperature, this implies that a moving particle extractor is temperature independent at $\rho_f = \frac{1}{2}$. The result above, Eq. (2.48), that the difference between the detector and extractor wakes is temperature independent has been done perturbatively in δG for illustration purposes. In fact it is possible to establish that

$$\frac{d}{dT}\left(\langle \mathbf{r}|G_{det}|\mathbf{r}\rangle - \langle \mathbf{r}|G_{extr}|\mathbf{r}\rangle\right) = 0 \tag{2.49}$$

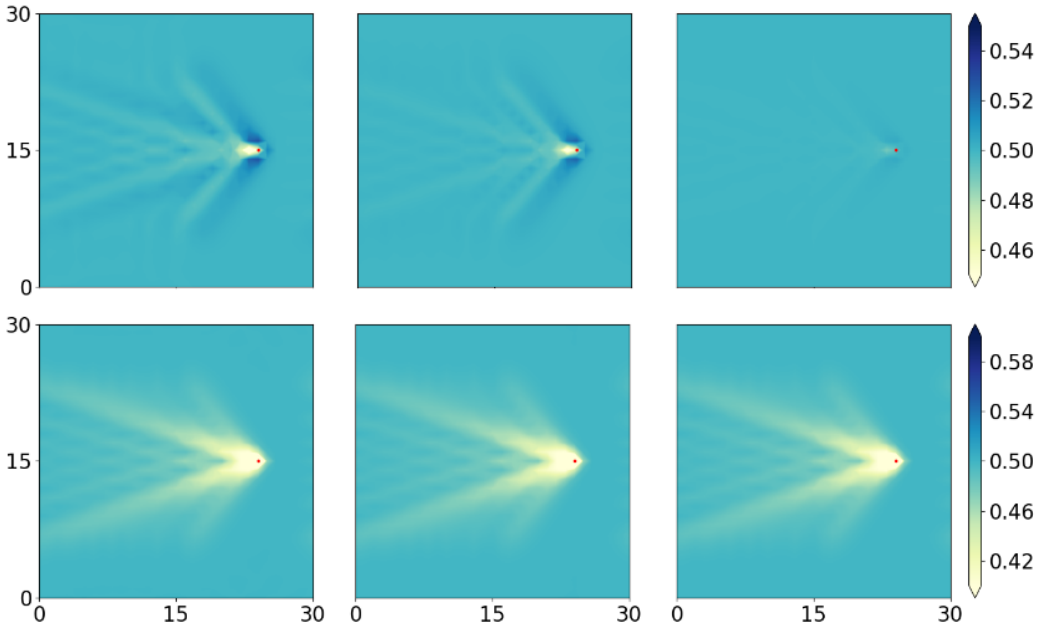

FIGURE 2.11: Density plots of potential (top) and extraction (bottom) wakes at half-filling over varying temperature. From left to right, $\frac{T}{t_{hop}} = 0$, 1, and 10.

where G_{det},G_{extr} are the non-perturbative steady states for a moving detector and extractor respectively, as derived in the appendix. This result matches simulations of the moving particle extractor as shown in Fig. 2.11. We note, in passing, that numerical checks show that the fluctuation wake is temperature dependent at half filling, even though there is no detector wake.

2.6 Discussion of experimental realizations

Here we consider a setup where the wakes may be explored in experiments with ultracold ^{6}Li fermions in optical lattices. Quantum gas microscopes with single-particle and single-site resolution can directly observe the wake structure, as follows. The disturbance can be created by a focused laser beam with a waist on the order of the lattice spacing by employing a high-resolution objective [85]. Experimental system sizes of more than 30x30 lattice sites have been realized for fermions [78]. We have checked by numerical simulations that using a Gaussian smeared potential instead of a point potential does not significantly alter wake geometry. Moreover, the wake pattern is not significantly changed if the initial Gaussian is not centered on a lattice site.

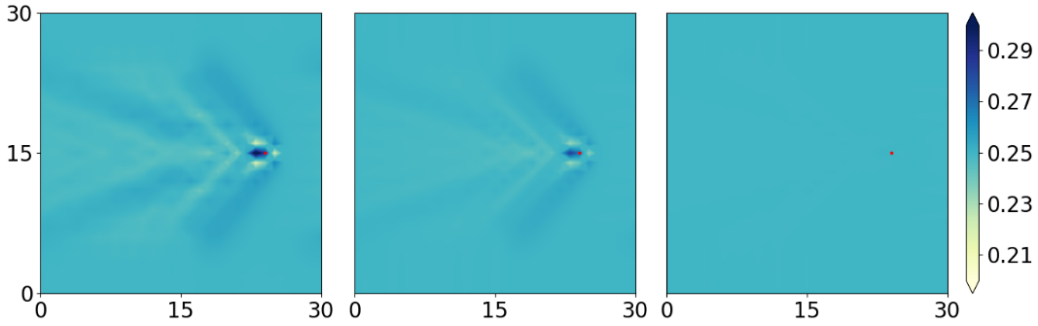

FIGURE 2.12: Density plots of detection wakes at quarter-filling and varying initial temperature. From left to right, $\frac{T}{t_{hop}} = 0$, 1, and 10.

Because of the light mass of ^{6}Li the timescales for Hubbard physics are still convenient for lattice spacing of approximately 1 μm [76] leading to moderate requirements of the objective (NA > 0.5). A dynamically movable disturbance can be implemented, for example, by piezo-actuated mirror mount or an acousto-optical deflector. An experimental run will then start with the preparation of a two-dimensional Fermi-Hubbard system and the movement of the focused laser beam through this system up to a certain position. Finally, the system is frozen by increasing the lattice depth and then imaged via fluorescence imaging. A single realization does not contain enough information to extract the details of the wake pattern. Reaching a density resolution of about 2% requires averaging about 2500 experimental realizations ($1/\sqrt{n}$) while keeping track of the final position of the disturbance. The required precision and amount of data is comparable to recent experiments at existing quantum gas microscopes [76, 85]. The parameter τ is proportional to the duration of beam motion, which should be compared to the hopping energy t_{hop}. It is possible to swipe the beam at different rates to obtain values of α spanning the full range from the slow-moving D-wave like wakes to the disappearance of the disturbance at high speeds. We remark that in a finite optical lattice setting, the large scale wake pattern may not have enough time to develop if the speed is such that the co-moving steady state cannot be effectively reached.

We note that all three types of disturbances can be implemented in experiments. A moving potential can be created by a far-detuned laser beam. A moving detector can be realized by a near-resonant laser beam. Scattering of photons at low intensity leads in good approximation to a measurement of the on-site particle density. Last, a particle extractor can be implemented via a defocussed red-detuned optical dipole trap. Caused by the out-of-plane minimum in the potential, atoms will be sucked out-of-plane and will be lost in the experiment.

Beyond cold atoms, we expect the effects we predict to also hold in other systems which can be well described by non-interacting fermions. We note that, for spin-polarized fermions contact-interactions are suppressed at low temperatures and dynamics is dominated by the effects of Pauli exclusion, making our approach particularly effective in this case. Moreover, we emphasize that our treatment is essentially exact, and thus can provide a benchmark for studies of the perturbative effect of interactions.

It is also important to note that while the present discussion is focused on non-interacting systems, the formalism presented in [52] is valid also for systems prepared in an interacting state, as long as the subsequent step of unitary evolution while the tip is traveling between sites is well approximated by non-interacting evolution. Thus, a system prepared in a strongly correlated state, such as a Mott insulator, for example, that undergoes a quantum quench where interactions are turned off will still be described by the current method.

Much (though not all) of the work in this chapter leveraged the fact that the local disturbances only made small corrections away from the equilibrium two-point function. In the next chapter, we will consider a system where this is not the case and see how interesting dynamics may emerge in this far-from-equilibrium setting.

Appendix

2.A The steady state Equations

(1) **Moving potential.** Here, we explain the iterative equations for the two point correlation functions and the density in the case of non-interacting evolution. We start with the case of a system interacting with an external potential, no measurements or change in particle number is involved and so the evolution is unitary. In this case, the evolution of the system's many body density matrix is driven by the Schrodinger equation:

$$\partial_t \rho(t) = -\frac{i}{\hbar}[\mathcal{H}(t), \rho(t)]. \tag{2.50}$$

where $\mathcal{H}(t)$ is the many body Hamiltonian. For the two point correlation function, defined as:

$$G_{\mathbf{r}\mathbf{r}'}(t) = \langle a^\dagger_{\mathbf{r}} a_{\mathbf{r}'} \rangle = Tr(\rho(t) a^\dagger_{\mathbf{r}} a_{\mathbf{r}'}) \tag{2.51}$$

it follows that

$$\partial_t G_{\mathbf{r}\mathbf{r}'}(t) = -\frac{i}{\hbar} Tr([\mathcal{H}(t), \rho(t)] a^\dagger_{\mathbf{r}} a_{\mathbf{r}'}) = -\frac{i}{\hbar} Tr \rho(t) [a^\dagger_{\mathbf{r}} a_{\mathbf{r}'}, \mathcal{H}(t)]). \tag{2.52}$$

For a general interacting Hamiltonian, the equation above is very complicated, and $\partial_t G_{\mathbf{r}\mathbf{r}'}(t)$ involves high order correlations through the right hand side of the equation, and we do not have a closed equation for the matrix G.

In the case where particles are non-interacting Fermions (for example neutral fermionic atoms, or when electron-electron interactions are screened), a closed equation for G is available. In such a situation, the Hamiltonian is quadratic in creation/annihilation operators, i.e. of the form $\mathcal{H}(t) = \sum_{\mathbf{x}\mathbf{y}} H_{\mathbf{x}\mathbf{y}}(t) a^\dagger_{\mathbf{x}} a_{\mathbf{y}}$. Using the cannonical anti-commutation relations $\{a^\dagger_{\mathbf{x}}, a_{\mathbf{y}}\} = \delta_{\mathbf{x}\mathbf{y}}$ and $\{a_{\mathbf{x}}, a_{\mathbf{y}}\} = 0$, the commutator in the equation of motion for

G is of the form

$$[\mathcal{H}(t), a^\dagger_{\mathbf{r}} a_{\mathbf{r}'}] = \sum_{\mathbf{xy}} H_{\mathbf{xy}}(t)[a^\dagger_{\mathbf{x}} a_{\mathbf{y}}, a^\dagger_{\mathbf{r}} a_{\mathbf{r}'}] = \sum_{\mathbf{xy}} H_{\mathbf{xy}}(t)(\delta_{\mathbf{yr}} a^\dagger_{\mathbf{x}} a_{\mathbf{r}'} - \delta_{\mathbf{xr}'} a^\dagger_{\mathbf{r}} a_{\mathbf{y}}) \tag{2.53}$$

leading to:

$$\begin{aligned} \partial_t G_{\mathbf{rr}'}(t) &= \tfrac{i}{\hbar} Tr\rho(t)[\mathcal{H}(t), a^\dagger_{\mathbf{r}} a_{\mathbf{r}'}]) \\ = \tfrac{i}{\hbar} \textstyle\sum_{\mathbf{x}} H_{\mathbf{xr}}(t) Tr\rho(t)(a^\dagger_{\mathbf{x}} a_{\mathbf{r}'}) - \tfrac{i}{\hbar} \textstyle\sum_{\mathbf{y}} H_{\mathbf{r}'\mathbf{y}}(t) Tr\rho(t)(a^\dagger_{\mathbf{r}} a_{\mathbf{y}})) \\ = \tfrac{i}{\hbar} \textstyle\sum_{\mathbf{x}} H_{\mathbf{xr}}(t) G_{\mathbf{xr}'}(t) - \tfrac{i}{\hbar} \textstyle\sum_{\mathbf{y}} H_{\mathbf{r}'\mathbf{y}}(t) G_{\mathbf{ry}}(t) \\ = \tfrac{i}{\hbar}([H^T(t), G(t)])_{\mathbf{rr}'} \end{aligned} \tag{2.54}$$

yielding a closed equation for G. In particular, the local density at point $\mathbf{r}$ which is $G_{\mathbf{rr}}(t)$ evolves as:

$$\partial_t G_{\mathbf{rr}}(t) = \tfrac{i}{\hbar}([H^T(t), G(t)])_{\mathbf{rr}}. \tag{2.55}$$

It is important to note, that this equation is not a closed equation for the density, since it involves off diagonal terms in G, thus to find the evolution of the density, the full Eq (2.54) must be solved. For a *real* Hamiltonian, as discussed in this paper, this equation is solved, for any time τ by

$$G(t+\tau) = \mathcal{T} e^{\frac{i}{\hbar}\int_t^{t+\tau} H(s)ds} G (\mathcal{T} e^{\frac{i}{\hbar}\int_t^{t+\tau} H(s)ds})^\dagger = K_U(G) \tag{2.56}$$

as described in Eq. (2.4).

The discrete-time co-moving steady state equation on the lattice $G = S^\dagger \mathcal{K}(G) S$, Eq. (2.11), states that as the potential (or another type of disturbance) moves to the next lattice site, G remains invariant, up to a shift of the coordinates co-moving with the disturbance. Written explicitly in coordinate representation, Eq. (2.11) reads $G_{\mathbf{rr}'} = [S^\dagger \mathcal{K}(G) S]_{\mathbf{rr}'}$, or, equivalently, using that for momentum states, $S|\mathbf{k}\rangle = e^{-ia\mathbf{w}\cdot\mathbf{k}}|\mathbf{k}\rangle$, we have

$$G_{\mathbf{kk}'} = [S^\dagger \mathcal{K}(G) S]_{\mathbf{kk}'} = e^{ia\mathbf{w}\cdot(\mathbf{k}-\mathbf{k}')} [\mathcal{K}(G)]_{\mathbf{kk}'} \tag{2.57}$$

Let us write $G = G_0 + \delta G$, where G_0 is the initial steady state before turning on the traveling perturbation. Using the form (2.56), taking the Hamiltonian H between

steps to be of the form $H_0 + V$, the steady state equation (2.57) is explicitly given by:

$$e^{ia\mathbf{w}\cdot(\mathbf{k}-\mathbf{k}')} \left\langle \mathbf{k} \right| e^{i\tau(H_0+V)}(G_0 + \delta G)e^{-i\tau(H_0+V)} \left| \mathbf{k}' \right\rangle = \left\langle \mathbf{k} \right| G_0 + \delta G \left| \mathbf{k}' \right\rangle \tag{2.58}$$

Note that at this no approximation has been made up to this point. Since we are only perturbing the free evolution by a local potential, we can assume the steady state G will be close to the steady state of free evolution, G_0, and thus δG is assumed a small perturbation. To proceed, we now use perturbation theory in Eq. (2.58), by expanding to lowest order in V. Namely, we use the expansion :

$$e^{-i\tau(H_0+V)} \approx e^{-i\tau H_0} + ie^{-i\tau H_0} \int_0^\tau ds e^{isH_0} V e^{-isH_0} \tag{2.59}$$

and keep terms up to linear order in V and in δG. The resulting equation is:

$$\begin{aligned} e^{ia\mathbf{w}\cdot(\mathbf{k}-\mathbf{k}')} \Big\{ &\left\langle \mathbf{k} \right| G_0 \left| \mathbf{k}' \right\rangle + \left\langle \mathbf{k} \right| e^{i\tau H_0} \delta G e^{-i\tau H_0} \left| \mathbf{k}' \right\rangle \\ &+ \left\langle \mathbf{k} \right| e^{i\tau H_0} \left(i \int_0^\tau ds e^{isH_0} [G_0, V] e^{-isH_0} \right) e^{-i\tau H_0} \left| \mathbf{k}' \right\rangle \Big\} \\ &= \left\langle \mathbf{k} \right| G_0 \left| \mathbf{k}' \right\rangle + \left\langle \mathbf{k} \right| \delta G \left| \mathbf{k}' \right\rangle . \end{aligned} \tag{2.60}$$

Next we note that without the perturbation, G_0 is assumed to be a steady state of free evolution. Since H is transnational invariant, G_0 can be taken to be diagonal in momentum space, therefore we can set $\left(e^{ia\mathbf{w}\cdot(\mathbf{k}-\mathbf{k}')} - 1 \right) \left\langle \mathbf{k} \right| G_0 \left| \mathbf{k}' \right\rangle = 0$. Doing the s integral,

$$i \int_0^\tau ds e^{is[\varepsilon(\mathbf{k})-\varepsilon(\mathbf{k}')]} = \frac{e^{i\tau[\varepsilon(\mathbf{k})-\varepsilon(\mathbf{k}')]} - 1}{\varepsilon(\mathbf{k}) - \varepsilon(\mathbf{k}')}$$

we find

$$\begin{aligned} &\left(e^{ia\mathbf{w}\cdot(\mathbf{k}-\mathbf{k}')} e^{i\tau[\varepsilon(\mathbf{k})-\varepsilon(\mathbf{k}')]} - 1 \right) \left\langle \mathbf{k} \right| \delta G \left| \mathbf{k}' \right\rangle \\ &= \frac{\left(e^{i\tau[\varepsilon(\mathbf{k})-\varepsilon(\mathbf{k}')]} - 1 \right) e^{ia\mathbf{w}\cdot(\mathbf{k}-\mathbf{k}')} e^{i\tau[\varepsilon(\mathbf{k})-\varepsilon(\mathbf{k}')]}}{\varepsilon(\mathbf{k}) - \varepsilon(\mathbf{k}')} \left\langle \mathbf{k} \right| [G_0, V] \left| \mathbf{k}' \right\rangle \end{aligned} \tag{2.61}$$

At zero temperature

$$\langle \mathbf{k}|G_0 V|\mathbf{k}'\rangle = G_0(\mathbf{k}) \langle \mathbf{k}|V|\mathbf{k}'\rangle = \Theta(\varepsilon_f - \varepsilon(\mathbf{k})) \textstyle\sum_{\mathbf{r}} \langle \mathbf{k}\rangle \, \mathbf{r} V(\mathbf{r}) \langle \mathbf{r}\rangle \, \mathbf{k}' \tag{2.62}$$

$$= \tfrac{V}{vol} \Theta(\varepsilon_f - \varepsilon(\mathbf{k})) e^{i\mathbf{r_0}\cdot(\mathbf{k}-\mathbf{k}')}, \tag{2.63}$$

where vol is the system volume. Thus,

$$\langle \mathbf{k}|\delta G|\mathbf{k}'\rangle = \frac{V\left(e^{i\tau[\varepsilon(\mathbf{k})-\varepsilon(\mathbf{k}')]}-1\right)e^{ia\mathbf{w}\cdot(\mathbf{k}-\mathbf{k}')}e^{i\tau[\varepsilon(\mathbf{k})-\varepsilon(\mathbf{k}')]}}{vol[\varepsilon(\mathbf{k})-\varepsilon(\mathbf{k}')]\left(e^{ia\mathbf{w}\cdot(\mathbf{k}-\mathbf{k}')}e^{i\tau[\varepsilon(\mathbf{k})-\varepsilon(\mathbf{k}')]}-1\right)} \times e^{i\mathbf{r_0}\cdot(\mathbf{k}-\mathbf{k}')}\left[\Theta(\varepsilon_f-\varepsilon(\mathbf{k}))-\Theta(\varepsilon_f-\varepsilon(\mathbf{k}'))\right] \tag{2.64}$$

Finally, density variation in the co-moving non-equilibrium steady state is given by Fourier transforming (2.A) back to real space and taking the diagonal element,

$$\langle \mathbf{r}|\delta G|\mathbf{r}\rangle = \frac{V\tau a^4}{(2\pi)^4}\iint_{-\pi/a}^{\pi/a} d\mathbf{k}d\mathbf{k}'\left[\frac{e^{i\tau[\varepsilon(\mathbf{k})-\varepsilon(\mathbf{k}')]}-1}{\tau(\varepsilon(\mathbf{k})-\varepsilon(\mathbf{k}'))}\right]\left[\frac{1}{1-e^{-ia\mathbf{w}\cdot(\mathbf{k}-\mathbf{k}')}e^{-i\tau[\varepsilon(\mathbf{k})-\varepsilon(\mathbf{k}')]}}\right] \times e^{i(\mathbf{r_0}-\mathbf{r})\cdot(\mathbf{k}-\mathbf{k}')}\left[\Theta(\varepsilon_f-\varepsilon(\mathbf{k}))-\Theta(\varepsilon_f-\varepsilon(\mathbf{k}'))\right] \tag{2.65}$$

In experiments the point potential may be realized by a broader beam. As we are looking for far field wake patterns, we do not expect local structure of the disturbance to have a significant effect. For example, if the point potential was instead Gaussian, the term $e^{i(\mathbf{r_0}-\mathbf{r})\cdot(\mathbf{k}-\mathbf{k}')}$ in Eq. (2.65) would be replaced by $e^{-\frac{\sigma^2}{2}|\mathbf{k}-\mathbf{k}'|^2+i(\mathbf{r_0}-\mathbf{r})\cdot(\mathbf{k}-\mathbf{k}')}$ where σ^2 is the variance of the Gaussian potential. Note, however, that when calculating the wake geometry we look far away from the potential source ($|\mathbf{r_0}-\mathbf{r}|$ large) and also need only to consider terms where $|\mathbf{k}-\mathbf{k}'|$ is small since these $\mathbf{k}$,$\mathbf{k}'$ dominate the integral. Hence, we can safely neglect the $e^{-\frac{\sigma^2}{2}|\mathbf{k}-\mathbf{k}'|^2}$ term so long as $|\mathbf{r_0}-\mathbf{r}| >> \sigma$ and thus find that the wake geometry of the Gaussian potential is equivalent to that of the point potential. In Figs. 2.B.1 and 2.B.2 we simulate potential wakes for a selection of Gaussian potentials and find that the wake geometry is indeed equivalent to that of the point potential.

(2) **Moving detection/extraction.** The co-moving steady state equation reads $G = S^\dagger\mathcal{K}(\mathcal{G})$. Written explicitly in momentum space, using (2.36), we have:

$$e^{ia\mathbf{w}\cdot(\mathbf{k}-\mathbf{k}')}e^{i\tau[\varepsilon(\mathbf{k})-\varepsilon(\mathbf{k}')]}\{\langle k|G|k'\rangle-\gamma\langle\mathbf{k}|\{G,P\}|\mathbf{k}'\rangle+\xi\langle\mathbf{k}|PGP|\mathbf{k}'\rangle\}=\langle\mathbf{k}|G|\mathbf{k}'\rangle \tag{2.66}$$

Assuming that $\gamma \ll 1$, $G \approx G_0 + \delta G$, and zero temperature,

$$\gamma\langle\mathbf{k}|GP|\mathbf{k}'\rangle \approx \gamma\langle\mathbf{k}|G_0P|\mathbf{k}'\rangle = \frac{\gamma}{vol}\Theta(\varepsilon_f-\varepsilon(\mathbf{k}))e^{i\mathbf{r_0}\cdot(\mathbf{k}-\mathbf{k}')} \tag{2.67}$$

Hence,

$$\gamma \left\langle \mathbf{k} \right| \{G, P\} \left| \mathbf{k}' \right\rangle \approx \frac{\gamma}{vol} e^{i\mathbf{r}_0 \cdot (\mathbf{k}-\mathbf{k}')} \left[\Theta(\varepsilon_f - \varepsilon(\mathbf{k})) + \Theta(\varepsilon_f - \varepsilon(\mathbf{k}')) \right] . \tag{2.68}$$

Now turning to the PGP term,

$$\begin{aligned} \left\langle \mathbf{k} \right| PG_0P \left| \mathbf{k}' \right\rangle &= \frac{a^2 vol}{(2\pi)^2} \int d\mathbf{q} \Theta(\varepsilon_f - \varepsilon(\mathbf{q})) \left\langle \mathbf{k} \right| P \left| \mathbf{q} \right\rangle \left\langle \mathbf{q} \right| P \left| \mathbf{k}' \right\rangle \\ &= \frac{a^2 vol}{(2\pi)^2} e^{i\mathbf{r}_0 \cdot (\mathbf{k}-\mathbf{k}')} \int d\mathbf{q} \Theta(\varepsilon_f - \varepsilon(\mathbf{q})) = \frac{\rho_f}{vol} e^{i\mathbf{r}_0 \cdot (\mathbf{k}-\mathbf{k}')} . \end{aligned} \tag{2.69}$$

where ρ_f is the density of fermions for G_0.

Plugging Eqs. (2.68) and (2.A) into Eq. (2.66), we get

$$\begin{aligned} \left\langle \mathbf{k} \right| \delta G \left| \mathbf{k}' \right\rangle = \frac{\gamma}{vol} \left(\frac{e^{ia\mathbf{w} \cdot (\mathbf{k}-\mathbf{k}')} e^{i\tau[\varepsilon(\mathbf{k}) - \varepsilon(\mathbf{k}')]}}{e^{ia\mathbf{w} \cdot (\mathbf{k}-\mathbf{k}')} e^{i\tau[\varepsilon(\mathbf{k}) - \varepsilon(\mathbf{k}')]} - 1} \right) \\ \times \left[\frac{\xi \rho_f}{\gamma} - \Theta(\varepsilon_f - \varepsilon(\mathbf{k})) - \Theta(\varepsilon_f - \varepsilon(\mathbf{k}')) \right] e^{i\mathbf{r}_0 \cdot (\mathbf{k}-\mathbf{k}')} . \end{aligned} \tag{2.70}$$

Finally, the local density variation is given by:

$$\begin{aligned} \langle \mathbf{r} | \delta G | \mathbf{r} \rangle = \frac{\gamma a^4}{(2\pi)^4} \iint_{-\pi/a}^{\pi/a} d\mathbf{k} d\mathbf{k}' \left(\frac{1}{1 - e^{-ia\mathbf{w} \cdot (\mathbf{k}-\mathbf{k}')} e^{-i\tau[\varepsilon(\mathbf{k}) - \varepsilon(\mathbf{k}')]}} \right) \\ \times e^{i(\mathbf{r}_0 - \mathbf{r}) \cdot (\mathbf{k}-\mathbf{k}')} \left[\frac{\xi \rho_f}{\gamma} - \Theta(\varepsilon_f - \varepsilon(\mathbf{k})) - \Theta(\varepsilon_f - \varepsilon(\mathbf{k}')) \right] \end{aligned} \tag{2.71}$$

which is Eq. (2.39) in the main text.

2.B Non-perturbative Results

In this section, we show that no detection wake is created at $\rho_f = \frac{1}{2}$ and that the difference between detection and extraction is temperature independent even non-perturbatively.

We start by looking at a series of non-perturbative detections on G_0. A single detection at site r and evolution for time τ is

$$G = UP_rG_0P_rU^\dagger + UP_r^\perp G_0P_r^\perp U^\dagger \equiv \sum_{a=\{0,1\}} P_r^a(\tau)G_0P_r^a(\tau) \tag{2.72}$$

since $[U, G_0] = 0$ and where $P^0 \equiv P$, $P^1 \equiv P^\perp$, and $UPU^\dagger \equiv P(\tau)$.

Hence, after doing a series of m measurements, we have

$$G = \sum_{a_1,a_2,\ldots,a_m} \left\{ \left[\prod_{n=m,m-1,\ldots,1} P_{r_n}^{a_n}((m-n+1)\tau) \right] G_0 \left[\prod_{n=1,2,\ldots,m} P_{r_n}^{a_n}((m-n+1)\tau) \right] \right\} \tag{2.73}$$

Looking at the diagonal of G in real space and inserting a resolution of identity, $\int d\mathbf{q_n}\,|\mathbf{q_n}\rangle\langle\mathbf{q_n}|$, to the right of every $P_{r_n}^{a_n}$ sitting in the first term in brackets in Eq. (2.73) and inserting $\int d\mathbf{q'_n}\,|\mathbf{q'_n}\rangle\langle\mathbf{q'_n}|$ to the left of every $P_{r_n}^{a_n}$ sitting in the second bracketed term in Eq. (2.73) we find

$$\begin{aligned} \langle\mathbf{r}|G|\mathbf{r}\rangle \equiv \zeta_m(\mu) = \int d\mathbf{k}d\mathbf{k}'e^{-i\mathbf{r}\cdot(\mathbf{k}-\mathbf{k}')} \int dQdQ' \sum_{a_1,a_2,\ldots,a_m} \\ \times \left\{ \langle\mathbf{k}|P_{r_m}^{a_m}(\tau)|\mathbf{q_m}\rangle \, \langle\mathbf{q_m}|P_{r_{m-1}}^{a_{m-1}}(2\tau)|\mathbf{q_{m-1}}\rangle \ldots \right. \\ \left. \times \, \langle\mathbf{q_2}|P_{r_1}^{a_1}(m\tau)|\mathbf{q_1}\rangle \, \langle\mathbf{q_1}|G_0|\mathbf{q'_1}\rangle \, \langle\mathbf{q'_1}|P_{r_1}^{a_1}(m\tau)|\mathbf{q'_2}\rangle \ldots \langle\mathbf{q'_m}|P_{r_m}^{a_m}(\tau)|\mathbf{k}'\rangle \right\} \end{aligned} \tag{2.74}$$

where μ is the chemical potential. Now, focusing on only terms directly dependent on $\mathbf{q_1}$,$\mathbf{q'_1}$ and denoting all other terms by B, we find

$$\begin{aligned} \zeta_m(\mu) &= B\int d\mathbf{q_1}d\mathbf{q'_1} \sum_{a_1} \langle\mathbf{q_2}|P_{r_1}^{a_1}(m\tau)|\mathbf{q_1}\rangle \, \langle\mathbf{q_1}|G_0|\mathbf{q'_1}\rangle \, \langle\mathbf{q'_1}|P_{r_1}^{a_1}(m\tau)|\mathbf{q'_2}\rangle \\ &= B\int d\mathbf{q_1} \sum_{a_1} \langle\mathbf{q_2}|P_{r_1}^{a_1}(m\tau)|\mathbf{q_1}\rangle \, F_\mu(\varepsilon(\mathbf{q_1})) \, \langle\mathbf{q_1}|P_{r_1}^{a_1}(m\tau)|\mathbf{q'_2}\rangle \\ &= B\int d\mathbf{q_1}e^{im\tau[\varepsilon(\mathbf{q_2})-\varepsilon(\mathbf{q'_2})]}F_\mu(\varepsilon(\mathbf{q_1})) \left[\delta_{\mathbf{q_1}\mathbf{q_2}}\delta_{\mathbf{q_1}\mathbf{q'_2}} + e^{i\mathbf{r_1}\cdot(\mathbf{q_2}-\mathbf{q'_2})} \left(2 - \delta_{\mathbf{q_1}\mathbf{q_2}} - \delta_{\mathbf{q_1}\mathbf{q'_2}} \right) \right] \\ &= \zeta_{m-1}(\mu) + B\int d\mathbf{q_1}e^{im\tau[\varepsilon(\mathbf{q_2})-\varepsilon(\mathbf{q'_2})]}F_\mu(\varepsilon(\mathbf{q_1}))e^{i\mathbf{r_1}\cdot(\mathbf{q_2}-\mathbf{q'_2})} \left(2 - \delta_{\mathbf{q_1}\mathbf{q_2}} - \delta_{\mathbf{q_1}\mathbf{q'_2}} \right) \\ &= \zeta_{m-1}(\mu) + Be^{im\tau[\varepsilon(\mathbf{q_2})-\varepsilon(\mathbf{q'_2})]}e^{i\mathbf{r_1}\cdot(\mathbf{q_2}-\mathbf{q'_2})} \left(2\rho_f - F_\mu(\varepsilon(\mathbf{q_2})) - F_\mu(\varepsilon(\mathbf{q'_2})) \right) \end{aligned} \tag{2.75}$$

Now, we look at $\zeta_m(\mu)+\zeta_m(-\mu)$ in a way analogous to Eq. (2.42) in the main text. Here, we find

$$\zeta_m(\mu)+\zeta_m(-\mu)=\zeta_{m-1}(\mu)+\zeta_{m-1}(-\mu) \tag{2.76}$$
$$+B\left\{e^{im\tau[\varepsilon(\mathbf{q_2})-\varepsilon(\mathbf{q_2'})]}e^{i\mathbf{r_1}\cdot(\mathbf{q_2}-\mathbf{q_2'})}\left(2-F_\mu(\varepsilon(\mathbf{q_2}))-F_\mu(\varepsilon(\mathbf{q_2'}))-F_{-\mu}(\varepsilon(\mathbf{q_2}))-F_{-\mu}(\varepsilon(\mathbf{q_2'}))\right)\right\}$$

Note, the real part of the term in braces in Eq. (2.76) is anti-symmetric under the transformation $\mathbf{q}\to m(\mathbf{q})$, where $\mathbf{q}$ here represents all $\mathbf{q_n}$, $\mathbf{q_n'}$, $\mathbf{k}$, and $\mathbf{k}'$. Let us now look at the term B. Note, explicitly,

$$B=\int dQ_1dQ_1'e^{-i\mathbf{r}\cdot(\mathbf{q_{m+1}}-\mathbf{q_{m+1}'})}\sum_{a_2,\ldots,a_m}\prod_{n=m+1,m,\ldots,2}$$
$$\times\langle\mathbf{q_n}|P^{a_{n-1}}_{r_{n-1}}((m-n+2)\tau)|\mathbf{q_{n-1}}\rangle\ \langle\mathbf{q_{n-1}'}|P^{a_n}_{r_{n-1}}((m-n+2)\tau)|\mathbf{q_n'}\rangle \tag{2.77}$$

where dQ_1 and dQ_1' are defined by $\prod_{n=2,\ldots,m+1}d\mathbf{q_n}$ and $\prod_{n=2,\ldots,m+1}d\mathbf{q_n'}$ respectively. Also, here we define $\mathbf{q_{m+1}}\equiv\mathbf{k}$ and $\mathbf{q_{m+1}'}\equiv\mathbf{k}'$.

Simplifying B, we find

$$B=\int dQ_1dQ_1'e^{-i\mathbf{r}\cdot(\mathbf{q_{m+1}}-\mathbf{q_{m+1}'})}\prod_{n=m+1,m,\ldots,2}e^{i(m-n+2)\tau\left[\varepsilon(\mathbf{q_n})-\varepsilon(\mathbf{q_{n-1}})+\varepsilon(\mathbf{q_{n-1}'})-\varepsilon(\mathbf{q_n'})\right]} \tag{2.78}$$
$$\times\Big[\delta_{\mathbf{q_nq_{n-1}}}\delta_{\mathbf{q_n'q_{n-1}'}}-e^{i\mathbf{r_{n-1}}\cdot(\mathbf{q_n}-\mathbf{q_{n-1}})}\delta_{\mathbf{q_n'q_{n-1}'}}$$
$$-e^{i\mathbf{r_{n-1}}\cdot(\mathbf{q_{n-1}'}-\mathbf{q_n'})}\delta_{\mathbf{q_nq_{n-1}}}+2e^{i\mathbf{r_{n-1}}\cdot(\mathbf{q_n}-\mathbf{q_{n-1}})}e^{i\mathbf{r_{n-1}}\cdot(\mathbf{q_{n-1}'}-\mathbf{q_n'})}\Big]$$

It can now be seen from Eq. (2.78) that B is symmetric under the transformation $\mathbf{q}\to m(\mathbf{q})$. Since B is symmetric and the term in braces in Eq. (2.76) is anti-symmetric, we find

$$\zeta_m(\mu)+\zeta_m(-\mu)=\zeta_{m-1}(\mu)+\zeta_{m-1}(-\mu) \tag{2.79}$$

Thus, $\zeta_m(\mu)+\zeta_m(-\mu)=\zeta_0(\mu)+\zeta_0(-\mu)=1$ and

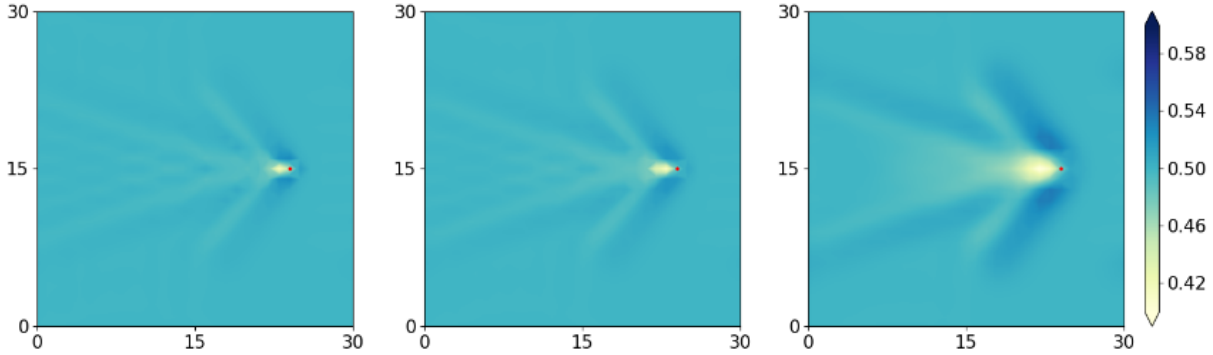

FIGURE 2.B.1: A Gaussian potential at half-filling and $\alpha = 1.7$. From left to right, the standard deviation of the Gaussian in terms of lattice spacing, a, is point potential, $0.5a$, and a.

$$\langle \mathbf{r}|G|\mathbf{r}\rangle_{\mu} = 1 - \langle \mathbf{r}|G|\mathbf{r}\rangle_{-\mu} \tag{2.80}$$

i.e. the detection wake for a chemical potential of μ is one minus the detection wake for a chemical potential of $-\mu$. Hence, when $\mu = 0$ there is no detection wake. We emphasize that this result assumed no particular path for the moving detector.

Turning to a moving extractor, note that for the difference between the extractor and detector wake, we get Eq. (2.73) where we set $a_1, a_2, ..., a_m = 0$. Thus, Eq. (2.76) becomes

$$\begin{aligned}\zeta_m &= B \int d\mathbf{q_1} e^{im\tau[\varepsilon(\mathbf{q_2})-\varepsilon(\mathbf{q}_2')]} \delta_{\mathbf{q_1}\mathbf{q}_1'} F(\varepsilon(\mathbf{q_1})) e^{i\mathbf{r_1}\cdot(\mathbf{q_2}-\mathbf{q}_2')} \\ &= B e^{im\tau[\varepsilon(\mathbf{q_2})-\varepsilon(\mathbf{q}_2')]} e^{i\mathbf{r_1}\cdot(\mathbf{q_2}-\mathbf{q}_2')} \rho_f \end{aligned} \tag{2.81}$$

Hence, the difference between a moving detector and moving extractor is temperature independent non-perturbatively. Similar to the perturbative case, this implies that a moving particle extractor at $\rho_f = \frac{1}{2}$ is temperature independent. Again, note that we have assumed no particular path for our moving particle extractor.

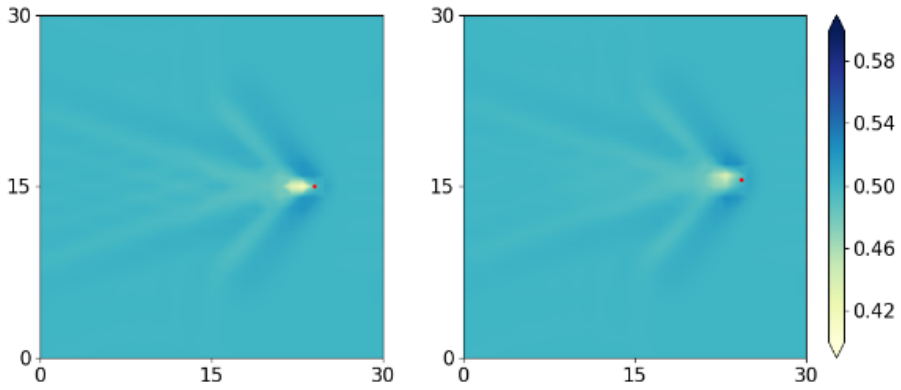

FIGURE 2.B.2: A Gaussian potential at half-filling, $\alpha = 1.7$, and $0.5a$ standard of deviation where a is the lattice spacing. Left is a Gaussian starting directly on lattice site (8,15). Right is a Gaussian starting in-between lattice sites at (8.3,15.6).

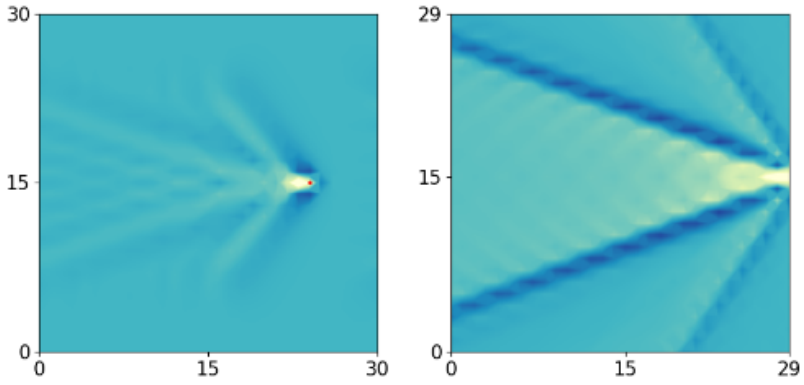

FIGURE 2.B.3: Comparison of potential wake at half-filling for $\alpha = 1.7$ for simulation (left) and numerical integration of Eq. (2.30) (right).

Chapter 3

Stirring By Staring: Measurement Induced Chirality

3.1 Introduction

One of the most exciting goals of the field of quantum dynamics is to be able to control the microscopic motion of particles in a reliable and universal way. Floquet engineering, coupled with our knowledge of topological quantum phases, presented one such route and brought about new paradigms for the quantum control of atomic and electronic motion. A periodic modulation of the Hamiltonian was shown to induce Chern bands in non-topological semiconductors as well as graphene, and this remarkable feat was observed in a variety of solid state and atomic systems [86–88].

The range of drive-induced topological phases kept growing over the past decade to include states with no static analogs. A prominent example is the anomalous Floquet Anderson insulator [42, 89–91]. In this 2D phase, a chiral edge state emerges alongside completely trivial bulk bands in stark contrast to standard topological edge states which are spectrally connected to bulk bands. Thus, such an insulator avoids issues associated with Fermion anomalies. The trick behind this phase is a Floquet Hamiltonian modulation which alters the hopping along a square lattice in a sequence that stirs the particles [20] in such a way that bulk motion is cancelled and edge states emerge.

An additional tool for control, however, is measurement (e.g. [92, 93]). 'Dark state' engineering was explored as a means to stabilize a variety of phases through measurement or decay processes that eliminate unwanted elements in the wave function in order to stabilize a desired steady state [94–98]. The challenge in this approach is to engineer the necessary projectors. The combination of periodic driving and dissipation

has also been discussed [99, 100]. More recently, it was discovered that a combination of unitary evolution and measurement could actually induce a transition between highly entangled quantum states into low entanglement classical-looking states at high measurement frequency [101–108]. The study of the competing effects of projective measurement and unitary evolution has also been intensely researched in the context of quantum circuit models [95, 106, 109–121]. The physics of measurement-induced phase transitions has been studied in the context of measurement protected quantum orders [95], symmetry-protected topological (SPT) phases [113], geometric phase [122], many-body localization [123], and various aspects of entanglement measures [104, 109, 112, 114, 115, 117]. There are also recent works which study the entanglement transitions with measurement and unitary evolution for free fermions hopping on a 1D chain [102, 124, 125]. In [52] the competing effects of unitary evolution and measurements were studied using a closed hierarchy approach. This method was used to describe non-equilibrium steady states of current [52] as well as density fluctuations (quantum wakes) following a moving particle detector and other disturbances in Ch. 2 (see also [1]).

In this manuscript we combine these developments to show that measurements can stabilize protected edge transport. All that is needed is a sequence of local occupation measurements which serve to herd particles into circular orbits. These circular orbits then play a somewhat similar role to the semi-classical orbits used to illustrate the quantum hall effect [126, 127] where particles take closed trajectories in the bulk while the presence of an edge induces chiral motion via 'skipping orbits' [1]. The result, so called stirring by staring, combines the pioneering ideas of dark-state engineering with Floquet engineering to generate exotic protected edge dynamics. As a simple example, we show how this can be accomplished on a Lieb lattice where chirality is achieved via an 8-step measurement pattern.

We show that our measurement scheme, illustrated in Fig. 1 and explained in detail below, yields no net transport of particles in the bulk of the lattice. However, when the system has an edge, it will induce movement of particles along the edge, Fig. 2. We explore the evolution of particle density in the system using the closed hierarchy method [52] both by direct numerical simulation as well as by analytically studying the

[1]The analogy is incomplete, however, in the Zeno limit of rapid measurements where the measurement induced chirality is a completely classical effect (as opposed to the quantum hall effect where coherence plays a key role). The effect, however, does persist in the regime of less frequent measurements where the consequences of quantum coherence become important

Zeno limit of rapid measurements, where the transport can be conveniently described as a stochastic process, and corrections to this process in the near-Zeno limit. In this regime, we prove that the boundary transport is protected from a wide range of edge perturbations including random potentials, hopping energies, edge deformations, and site removal. It is critical to note that such protection cannot be achieved in a 1D system (with a strictly local Hamiltonian), where a removal of a small set of sites can simply disconnect the system into disjoint parts with no possibility of transport.

3.2 The protocol

The measurement cycle consists of 8 steps taking an overall time T. At each step, we take repeated snapshots of the presence of particles throughout a subset of the lattice, while the system is allowed to evolve freely between the measurements. We will denote the set of sites *not* being measured at step i by A_i as marked in figure 1, and enforce periodicity by setting $A_{i+8} = A_i$. Within each step, the following procedure is followed:

1. Particle densities at all sites in $(A_i \cap A_{i-1})^c$ are measured.
2. Free evolution under a free hopping Hamiltonian $\mathcal{H} = -t_{hop} \sum_{\langle \mathbf{r}\mathbf{r}' \rangle} a^\dagger_{\mathbf{r}} a_{\mathbf{r}'}$ for a time $\tau = \frac{T}{8n}$. Here n is an integer describing the measurement frequency.
3. Particle densities at all sites in A_i^c are measured.
4. Steps 2 and 3 are repeated n times.

For convenience, throughout the paper we will set $t_{hop} = 1$ and $\hbar = 1$. For clarity, we note here that in the rest of the manuscript we will refer to one complete iteration of the full 8 step procedure as a "full measurement cycle" or sometimes just "measurement cycle." On the other hand, each of the individual steps within the 8 step procedure will be referred to as a "measurement step."

The steps detailed above correspond to a sequence of maps on the density matrix ρ of the system. Two distinct elements are involved in the dynamics. First, the measurement of the presence of a particle at a lattice site $\mathbf{r}_i$ can be represented by the Krauss map $\rho \to n_i \rho n_i + (1 - n_i)\rho(1 - n_i)$, with $n_i = a_i^\dagger a_i$ the number operator for the site. In between such measurement steps we have unitary evolution, which is described, as usual, via $\rho \to \mathcal{U}\rho\mathcal{U}^\dagger$, where $\mathcal{U}$ is a many body evolution operator.

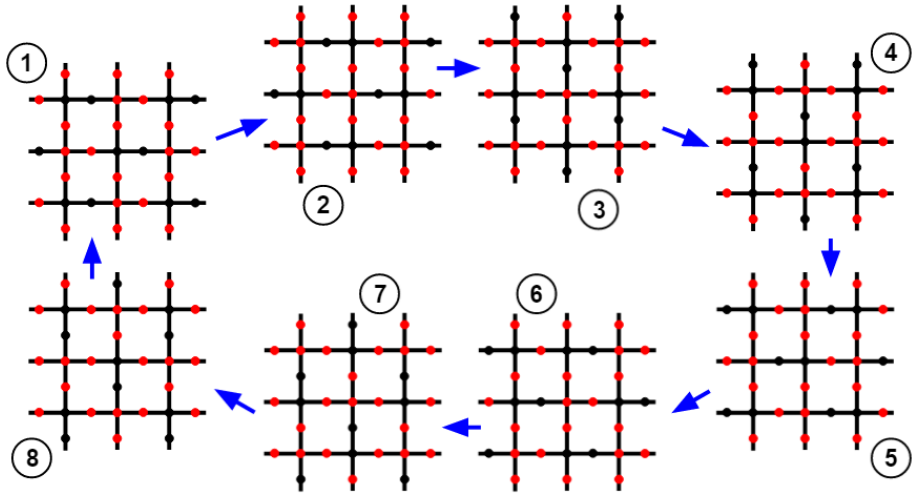

FIGURE 1: Measurement protocol. Red vertices indicate the set of repeatedly measured sites, while black sites are unmeasured (the free evolving sets, A_i). The adjacent pairs of black vertices trace out an inherently chiral (in this case clockwise) path along a decorated square inside the Lieb lattice. The path can be made counter-clockwise if the order of the 8 steps is reversed.

To describe the densities and correlations in the system, we concentrate on the iterative evaluation of two point correlation operators

$$G_{\mathbf{r}\mathbf{r}'}(t) = \mathrm{Tr}\Big(\rho(t) a^\dagger_{\mathbf{r}} a_{\mathbf{r}'}\Big). \tag{3.1}$$

The two point correlation has a closed evolution equation under particle density measurements and free evolution operations, as long as the free evolution is non-interacting [52]. The change in G due to the Krauss map associated with *single* site particle density measurement can be shown to imply eliminating correlations between the measured site and other sites [52]. Explicitly, one can check that the measurement of particle presence at a lattice site $\mathbf{r}$ is described by the map

$$G \to (1 - P_{\mathbf{r}})G(1 - P_{\mathbf{r}}) + P_{\mathbf{r}} G P_{\mathbf{r}} \tag{3.2}$$

where $P_{\mathbf{r}} = |\mathbf{r}\rangle\langle\mathbf{r}|$ is the (single-particle) projector onto site $\mathbf{r}$. For non-interacting evolution, fermion operators transform as $\mathcal{U}^\dagger a^\dagger_{\mathbf{q}} \mathcal{U} = U_{\mathbf{q}\mathbf{q}'} a^\dagger_{\mathbf{q}'}$, where U is called a single-particle evolution. In this case G transforms as

$$G \to U G U^\dagger. \tag{3.3}$$

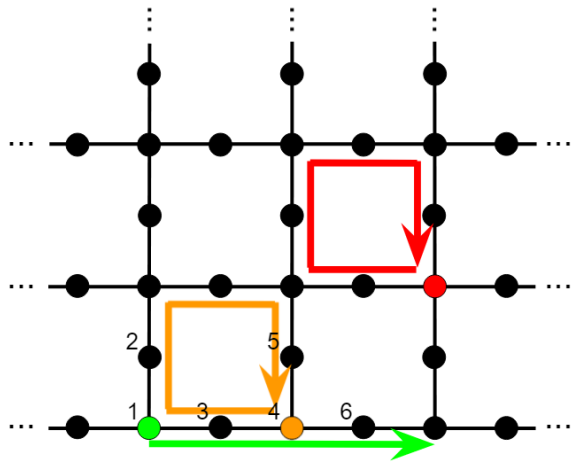

FIGURE 2: Particle trajectories on the Lieb lattice under the measurement protocol in the infinite measurement (Zeno) limit with the perfect switching cycle ($\frac{T}{8} = \frac{\pi}{2}$). In this regime, evolution becomes deterministic and particle trajectories can be seen explicitly. Particles localized in the bulk (Red) at the start of the protocol and particles initialized at sites of type 3 or 4 (orange) on the edge trace out a closed loop after no more than 5 measurement cycles. On the other hand, particles initialized at sites of type 1 (green) or 6 on the boundary at the beginning of the protocol propagate along the edge, shifting by 1 dynamical unit cell every 2 measurement cycles (see appendix 3.G for details).

In the case of interest for us here, we will take $U = e^{-i\tau H}$, where $H = \sum_{\langle \mathbf{r},\mathbf{r}' \rangle} |\mathbf{r}\rangle\langle\mathbf{r}'|$, describing free hopping of the fermions on the lattice.

To study the repeated application of these maps to G, it is convenient to view G as a vector in $\mathcal{H}_{double} = \mathbb{C}^{n^2}$ where n is the total number of fermion sites. We write $G = \sum_{\mathbf{r}\mathbf{r}'} G_{\mathbf{r}\mathbf{r}'} |\mathbf{r}\rangle\langle\mathbf{r}'| \rightarrow G = \sum_{\mathbf{r}\mathbf{r}'} G_{\mathbf{r}\mathbf{r}'} |\mathbf{r}\rangle \otimes |\mathbf{r}'\rangle$ and the evolution of G under the maps above can be notated as

$$G(t+T) = \Lambda G(t). \tag{3.4}$$

where Λ is the (super) operator acting on G corresponding to the 8 step measurement protocol given in the previous section. To construct Λ, we write the transformation associated with free evolution and with particle measurement, respectively, as

$$G \rightarrow (U \otimes \bar{U})\, G \tag{3.5}$$

$$G \rightarrow \pi_{\mathbf{r}} G \tag{3.6}$$

where $\pi_{\mathbf{r}} \equiv (1 - P_{\mathbf{r}}) \otimes (1 - P_{\mathbf{r}}) + P_{\mathbf{r}} \otimes P_{\mathbf{r}}$. If all the sites in a set A^c are measured simultaneously, we find (See appendix 3.C) that the combined operation on G becomes

$$\prod_{\mathbf{r}\in A^c} \pi_{\mathbf{r}} \equiv \Pi_A = \sum_{\mathbf{r}\in A^c} P_{\mathbf{r}} \otimes P_{\mathbf{r}} + P_A \otimes P_A \tag{3.7}$$

where

$$P_A \equiv \sum_{\mathbf{r}\in A} P_{\mathbf{r}}. \tag{3.8}$$

Note that $(\Pi_A G)_{\mathbf{r}\mathbf{r}'} = G_{\mathbf{r}\mathbf{r}'}$ if both sites $\mathbf{r}\mathbf{r}'$ are in the unmeasured set A, on the other hand if $\mathbf{r}$ or $\mathbf{r}'$ are in A^c we have $(\Pi_A G)_{\mathbf{r}\mathbf{r}'}\delta_{\mathbf{r}\mathbf{r}'}$. In other words, the correlations between the measured sites A^c and all other sites are destroyed while acting as an identity on the subspace A of unmeasured sites. It is important to note that Π_A is itself a projection operator on $\mathcal{H}_{double}$. To see this, note that the operators $\pi_{\mathbf{r}}$ form a set of commuting orthogonal projectors, and consequently their product is an orthogonal projector. Another useful property that follows is that

$$\Pi_B \Pi_A = \Pi_{A\cap B}. \tag{3.9}$$

We are now in position to write the evolution operator Λ describing a cycle of measurements and evolution as described by the measurement protocol above. Explicitly, after each cycle, which involves 8 steps each repeated n times, $G \to \Lambda G$ with

$$\begin{aligned} \Lambda = &\left[\Pi_{A_8}(U \otimes \bar{U})\Pi_{A_8}\right]^n \\ &\times \left[\Pi_{A_7}(U \otimes \bar{U})\Pi_{A_7}\right]^n \ldots \left[\Pi_{A_1}(U \otimes \bar{U})\Pi_{A_1}\right]^n \end{aligned} \tag{3.10}$$

We now turn to analyze the dynamics described by this operator.

3.3 The Zeno limit

We first study the operator Λ, of Eq. (3.10), in the limit of many measurements per cycle (i.e. $n \to \infty$). The dynamics under high frequency repeated measurements is known as the quantum Zeno limit. The signature characteristic of this regime is the

freezing of evolution in the subspace of measured sites. The Zeno effect (and the closely related anti-Zeno effect) has a long history [128] with broad applications including, for example, counterfactual quantum computing and communication [129, 130] and loss suppression in ultracold molecule experiments with strong, long-range dipolar interactions [131, 132]. Over the past 30 years, the Zeno and related effects have been observed experimentally across a variety of physical systems [133–139].

Let us first consider one of the eight steps in (3.10). Formally expanding in $\tau = \frac{T}{8n}$,we find that:

$$(\Pi_A(U \otimes \bar{U})\Pi_A)^n = \Pi_A \left(U_A^n \otimes \bar{U}_A^n\right) \Pi_A + O(\tau^2 n). \tag{3.11}$$

Here $U = e^{-i\tau H}$ and $U_A = e^{-i\tau H_A}$ where $H_A \equiv P_A H P_A$. To get Eq. (3.11), we first expand each measurement/evolution step in τ:

$$\begin{aligned} \Pi_A(U \otimes \bar{U})\Pi_A &= \Pi_A(I - i\tau\left[H \otimes I - I \otimes H\right])\Pi_A + O(\tau^2) \\ &= \Pi_A e^{-i\tau\Pi_A[H\otimes I - I\otimes H]\Pi_A}\Pi_A + O(\tau^2). \end{aligned} \tag{3.12}$$

A short calculation (see appendix 3.C) shows that

$$\Pi_A \left[H \otimes I - I \otimes H\right] \Pi_A = H_A \otimes P_A - P_A \otimes H_A \tag{3.13}$$

hence

$$\Pi_A(U \otimes \bar{U})\Pi_A = \Pi_A(U_A \otimes \bar{U}_A)\Pi_A + O(\tau^2) \tag{3.14}$$

which, using $[U_A \otimes \bar{U}_A, \Pi_A] = 0$, gives (3.11). The expression (3.11) shows that, in the Zeno limit, the average evolution is dominated by local evolution in the region A and suppresses hopping into the measured sites A^c. Finally, plugging Eq. (3.11) into Eq. (3.10), we find

$$\begin{aligned} \Lambda = \Pi_{A_8} \left(U_{A_8}^n \otimes \bar{U}_{A_8}^n\right) \Pi_{A_8 \cap A_7} \\ \times \left(U_{A_7}^n \otimes \bar{U}_{A_7}^n\right) ... \Pi_{A_2 \cap A_1} \left(U_{A_1}^n \otimes \bar{U}_{A_1}^n\right) \Pi_{A_1} + O(\tau^2 n). \end{aligned} \tag{3.15}$$

Next, we use this result to formally describe evolution for N cycles, when $N n \tau^2 \ll 1$, and $n\tau$ is kept constant.

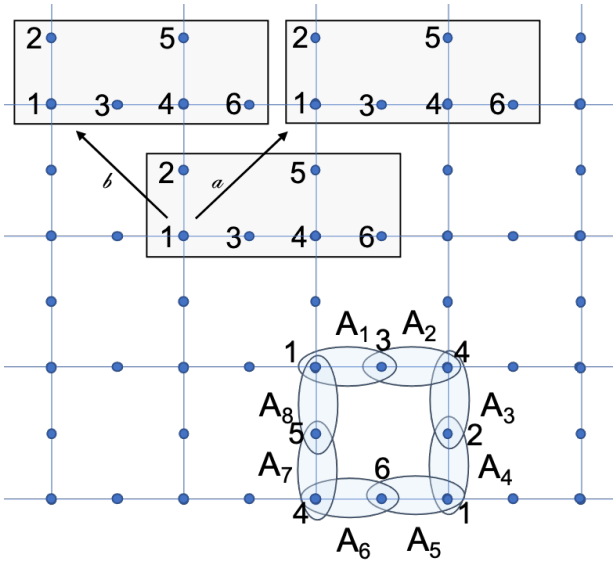

FIGURE 3: The unit cell for the measurement driven Lieb lattice dynamics consists of two Lieb lattice unit cells. A choice for such a dynamical unit cell is depicted.

3.4 Stochastic description of the Zeno limit

The local nature of the evolution in the Zeno limit (3.15) leads to a striking simplification that we now describe. We observe that, if one only follows the local particle density given by the diagonal elements $G_{\mathbf{rr}}$, the evolution is given by a periodic classical stochastic process. To see this, note that the evolution of G in the Zeno limit consists of steps of the form

$$G \to U_{A_i}^n G U_{A_i}^{n\dagger} \tag{3.16}$$

Each set A_i consists of the union of pairs of neighbouring sites, the black sites in Fig. 1. Since the pairs forming A_i are disjoint, the evolution U_{A_i}, can only develop non-trivial correlations between the sites of the same pair. Consider a pair of such sites. After the evolution, all sites are measured except for sites in $A_i \cap A_{i+1}$, which is a set of isolated points on the lattice, in particular, any correlations (non diagonal terms in G) developed between the pair of sites in A_i would be set to zero once the site in A_i but not in A_{i+1} is measured (long range correlations between sites in $A_i \cap A_{i+1}$ are not annihilated, but will be annihilated in the next step, and cannot be generated by any of the U_{A_i}). Thus, if we start with a diagonal G it will remain diagonal throughout the evolution. Moreover, even if we start with some non-zero off-diagonal terms, these will

be quickly annihilated by the measurements. Thus we should be able to describe the evolution, in the Zeno limit, just in terms of the dynamics of the diagonal of G. Indeed, note that $G_{\mathbf{rr}}$ are real non-negative numbers and the total number of particles $\sum_{\mathbf{r}} G_{\mathbf{rr}}$ is a constant of motion, and thus $G_{\mathbf{rr}}$ can be treated (up to normalization) as probabilities, and the process describing the evolution is a classic stochastic process.

Explicitly, if we represent the density at time t as a vector, $|g(t)\rangle$, defined via

$$[g(t)]_{\mathbf{r}} \equiv G_{\mathbf{rr}}(t), \tag{3.17}$$

then in the Zeno limit the density evolves via Markovian dynamics as

$$|g\rangle \longrightarrow R_{cyc}\,|g\rangle \tag{3.18}$$

where the transition matrix R_{cyc} consists of the 8 steps of our process, namely

$$R_{cyc} = R_8 R_7 R_6 R_5 R_4 R_3 R_2 R_1. \tag{3.19}$$

The transition matrices R_i are defined as follows. Each unmeasured set A_i is associated with two site types α, β that are not being measured, as described in Fig. 3 (e.g. A_1 is the union of all sites of types $1,3$; A_2 is the union of sites $3,4$; etc). The unitary evolution associated with a given unmeasured set A_i, breaks into a sum of pairs of nearest neighbours:

$$U_{A_i} = I_{A_i^c} \bigoplus_{\langle\alpha,\beta\rangle\in A_i} e^{i\tau n\sigma_x}. \tag{3.20}$$

Next, we apply the evolution (3.16) and then measure all sites except those in $A_i \cap A_{i+1}$, which has the effect of eliminating off-diagonal elements in G. Consider one of the pairs of sites $\langle\alpha,\beta\rangle \in A_i$ and an initially diagonal $G = diag(g_1, g_2)$. Applying the evolution (3.20) to get $e^{i\tau n\sigma_x} G e^{-i\tau n\sigma_x}$ and then setting the off diagonal elements to zero, we get a new diagonal matrix G with $G = diag(\cos^2(n\tau)g_1 + \sin^2(n\tau)g_2, \cos^2(n\tau)g_2 + \sin^2(n\tau)g_1)$. In other words, a particle located in one of the sites jumps to the other site with probability

$$p = \sin^2(n\tau) = \sin^2(\frac{T}{8}), \tag{3.21}$$

or stays with probability $1-p$. A particle in any other position will not move. Therefore:

$$R_i = \oplus_{\langle\alpha,\beta\rangle\in A_i} \begin{pmatrix} 1-p & p \\ p & 1-p \end{pmatrix} \oplus_{\text{other sites}} I \tag{3.22}$$

This defines a periodically driven random walk. We note that the transition matrices R_i are bi-stochastic matrices, and thus so is R_{cyc}.

A remark is in order here about Eq. (3.22). In a system with a boundary, a set A_i may include isolated sites that do not have an adjacent neighbour also in A_i. For example consider the boundary of the lattice in Fig. 3. The set A_3 as defined includes sites of type 4 and 2, however looking at the lower boundary, we see that sites of type 4 on the boundary do not have an adjacent site of type 2. Similarly to the measured sites, the dynamics for these isolated elements of A_i are frozen in the Zeno limit. In (3.22), the isolated elements of A_i are included in "other sites" since they are not part of an adjacent pair in A_i.

The particular choice $T = 4\pi$, leads to $p = 1$. We refer to this choice as "perfect switching". In this case, R_{cyc} is a permutation matrix, and the motion of particles is deterministic. Of course, on the other hand, when $T = 8\pi$, $p = 0$ and there is no evolution at all.

We now consider the counting statistics of transport to the right per cycle. To do so, we attach a counting field $e^{i\theta}$ to each horizontal link, by modifying the above transition matrices of R_1, R_2, R_5, R_6 to

$$R_i = \oplus_{\langle\alpha,\beta\rangle\in A_i} \begin{pmatrix} 1-p & e^{i\theta}p \\ e^{-i\theta}p & 1-p \end{pmatrix} \oplus_{\text{other sites}} I \tag{3.23}$$

whenever α, β are nearest neighbours on a horizontal line, such that α is to the left of β.

With the counting field present, we can introduce the moment generating function,

$$\begin{aligned} \chi_N(\theta) &\equiv \textstyle\sum_{ij} \sum_{w:i\to j} e^{i\theta l(w)} Prob_N(w) G_{ii}(0) \\ &= \textstyle\sum_{ij} [R_{cyc}(\theta)^N]_{ij} G_{ii}(0) = \langle I | R_{cyc}^N(\theta) \, |g_0\rangle \end{aligned} \tag{3.24}$$

where $w : i \to j$ is a sequence of hops from site i to site j, $Prob_N(w)$ is the probability for the path w after N measurement cycles using the transition matrix R_{cyc}, and $l(w)$

is the net number of hops in the x direction. In the next line, $|g_0\rangle$ is the initial density distribution at $t = 0$ and $|I\rangle$ is a vector whose elements are all 1 (corresponding to $G = I$).

We can use χ_N to compute quantities of interest, most important of which is the flow, defined as the total displacement per cycle, per unit length. The flow in the x direction is given by

$$F = \lim_{N\to\infty} F_N \tag{3.25}$$

where F_N is the average flow in the first N cycles,

$$F_N = \frac{1}{L_x}\frac{1}{N}\, i\partial_\theta \chi_N(\theta)|_{\theta=0} \tag{3.26}$$

with L_x the length in the x direction.

3.4.1 Absence of bulk transport.

In a translation invariant situation, it is convenient to work in momentum space. Here, we must use the "dynamical unit cel" where the periodic evolution happens, which is double the Lieb lattice's original unit cell (see Fig. 3).

The Bravais lattice for the dynamical unit cell is a rotated square lattice whose primitive Bravais vectors are marked as a, b in Fig. 3. Below, we use $\boldsymbol{n}, \boldsymbol{m}$ to denote the position of the unit cell and $\mu, \nu \in \{1, .., 6\}$ to denote the individual atom inside the cell. We can then write:

$$R_i(\boldsymbol{n}, \mu; \boldsymbol{m}, \nu) = \int \frac{d^2k}{2\pi} R_i(\boldsymbol{k}, \mu, \nu) e^{i\boldsymbol{k}\cdot(\boldsymbol{n}-\boldsymbol{m})}. \tag{3.27}$$

for example, R_5, is associated with A_5, which includes sites $1, 6$ in neighbouring dynamic unit cells, hence

$$R_5(k,\theta) = \begin{pmatrix} 1-p & 0 & 0 & 0 & 0 & pe^{-i(\theta+k\cdot(a-b))} \\ 0 & 1 & 0 & 0 & 0 & 0 \\ 0 & 0 & 1 & 0 & 0 & 0 \\ 0 & 0 & 0 & 1 & 0 & 0 \\ 0 & 0 & 0 & 0 & 1 & 0 \\ pe^{i(\theta+k\cdot(a-b))} & 0 & 0 & 0 & 0 & 1-p \end{pmatrix}.$$

In the deterministic case, $p = 1$, we find for the full cycle

$$R_{cyc}(k,\theta) = \begin{pmatrix} 1 & 0 & 0 & 0 & 0 & 0 \\ 0 & 0 & e^{i\theta} & 0 & 0 & 0 \\ 0 & 0 & 0 & e^{i\theta} & 0 & 0 \\ 0 & 0 & 0 & 0 & 1 & 0 \\ 0 & 0 & 0 & 0 & 0 & e^{ik\cdot b}e^{-i\theta} \\ 0 & e^{-ik\cdot b}e^{-i\theta} & 0 & 0 & 0 & 0 \end{pmatrix}. \tag{3.28}$$

It is possible to check that in this case, with $p = 1$, $R_{cyc}(k,\theta)^5 = I$. Therefore, the system returns to itself after 5 cycles without generating any transport at all. For $p \neq 1$, we find that $ReTrR_{cyc}(k,\theta)^n$ is a symmetric function of θ, and here too, there is no transport after an arbitrary number of cycles. To do so we computed the characteristic polynomial of the matrix $R_{cyc}(k,\theta)$ and found that it is equal to that of $R_{cyc}(-k,-\theta)$, implying equality of eigenvalues of the matrices.

It is also possible to check that for any $k_x, k_y \neq 0 \pmod{2\pi}$, $||R_{cyc}|| < 1$, which implies the long time behavior will be dominated only by the $k = 0$ component of the initial distribution. For $k_x = k_y = 0$ and $\theta = 0$ there is a single left and right eigenvector with eigenvalue 1, which is the uniform density state $|I\rangle$, implying that up to exponentially small corrections, the current density (3.26) vanishes.

3.4.2 Edge transport

We have concluded that there is no bulk transport associated with the stochastic process defined by R_{cyc}, for any p. In this section, we contrast the situation to when an edge is present. We implement the dynamics by removing all sites beyond the physical edges (e.g. sites with $y < 1$) and removing any transitions involving sites beyond the edges from the dynamics. We start with the deterministic case, namely $p = 1$. In Fig. 2, we exhibit a half plane with an edge. For $p = 1$, we can track the motion of each particle and conclude that bulk particles perform a closed loop. On the other hand, particles starting at the edge divide into two sets: some of the edge particles $(6,1)$ perform a motion along the edge, while some $(3,4)$ perform a closed loop. Thus, if we start from an initial state where particles are placed along the edge we will have particle transport along the edge (particles $6,1$ will move to the right). This behavior is clearly analogous to the familiar skipping orbits in the semi-classical description of the integer quantum Hall effect.

What will happen away from $p = 1$? Consider first the case of a strip with periodic boundary conditions in the long direction (say x) and open boundary conditions in the y direction with L_y dynamical unit cells in the y direction. Let us consider states that are translationally invariant in the x direction, allowing us to analyze the behavior in (3.26) in momentum space. For any momentum k_x, the transition operator R can then be written as a $6L_y \times 6L_y$ matrix and analyzed. For $0 < p < 1$, any initially positioned particle has a finite probability to get to any other site within a finite time and the only steady state distribution of R with eigenvalue 1 is that of uniform density (in contrast to the $p = 1$, where additional steady states are possible. This distribution will be approached exponentially fast, governed by ${\lambda_2}^N$ where λ_2 is the second largest eigenvalue of R. In the uniform density distribution, there is no net charge transfer. Indeed in that case, the charge transfer of the upper and lower edge is carried in opposite directions and cancels.

To get net transfer, we initially place particles only close to one of the edges. In a finite width system, away from the perfect switching cycle, we expect the charge transport to be transient: once the measuring protocol starts, it will transport a finite amount of particles while also spreading particles towards the second edge, rapidly approaching the uniform density state. Thus, to study the net particle flow associated with a given edge we must work in the thermodynamic limit ($L_y \to \infty$), or, more precisely, $L_y \gg T_w$ where T_w is the typical time it may take a particle to diffuse from the middle of the sample to one of the edges.

We now numerically compute the number of particles, F, that flow across a slice through the Lieb lattice during evolution (see figure 4). In other words, we compare the number of particles to the left of the slice before and after the application of Λ, computing:

$$F_{sim} \equiv \sum_{\mathbf{r} \text{ to the left of slice}} \big((\Lambda G)_{\mathbf{rr}} - G_{\mathbf{rr}}\big). \tag{3.29}$$

This is done by initiating the system at $G(t = 0) = G_0$ where G_0 is a diagonal matrix corresponding to particles placed on the bottom half of a square lattice, with open boundary conditions. We then iterate the map (3.10), computing $\Lambda^N G_0$, increasing N but being careful to limit the number of cycles to remain within the regime that no significant density has had time to build up close to the upper edge.

The combination of the Zeno limit with the perfect switching point $p = 1$ leads to a clearly quantized flow, as is clearly exhibited in Fig 5, and can be understood by tracking the trajectories of the particles (see Fig. 2 and appendix 3.G for details of the

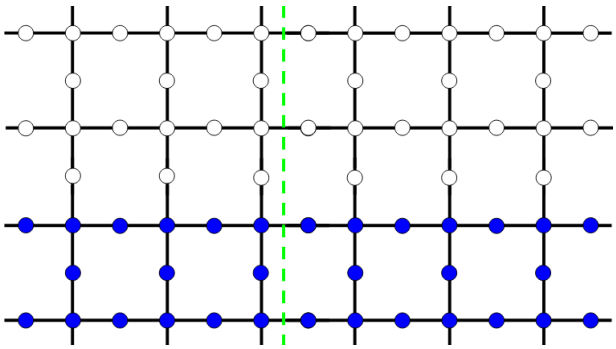

FIGURE 4: Lieb lattice with lower-half plane filled with particles (in blue). Trace is taken of the half plane to the right of the green dashed line. The flow across the barrier is then given by the difference between the right-half trace before and after evolution.

motion). Next we will consider both the cases of $p \neq 1$ as well as the non-Zeno limit.

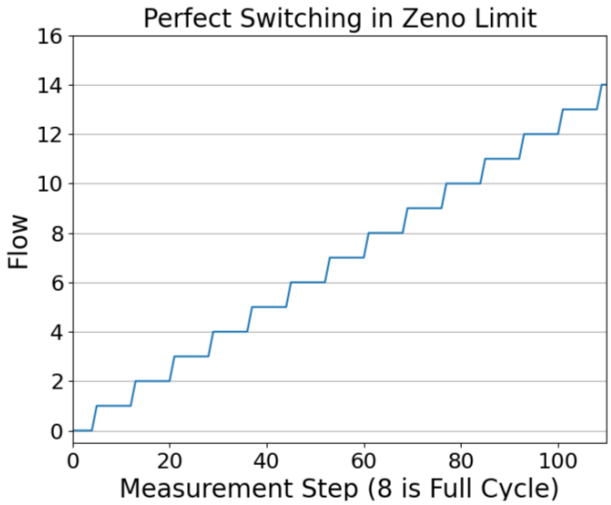

FIGURE 5: Charge transfer of the left-half filled plane in the Zeno limit with $\frac{T}{8} = \frac{\pi}{2}$, namely $p = 1$. In this section, the Lieb lattice size for all simulations is 33×33 unless otherwise stated. Here, precisely one particle is transported across the flow cut during the 8 step measurement cycle.

3.5 Charge Transport: Bulk-Edge Decomposition

We now turn to calculating the charge transport per measurement cycle in the Zeno limit with arbitrary p. The result is described in Fig. 6. Since the bulk transport vanishes for any p, the flow will be still completely localized near the edge. Below, we exhibit an analytical formula for the flow, Eq. (3.30), achieved using a bulk-boundary

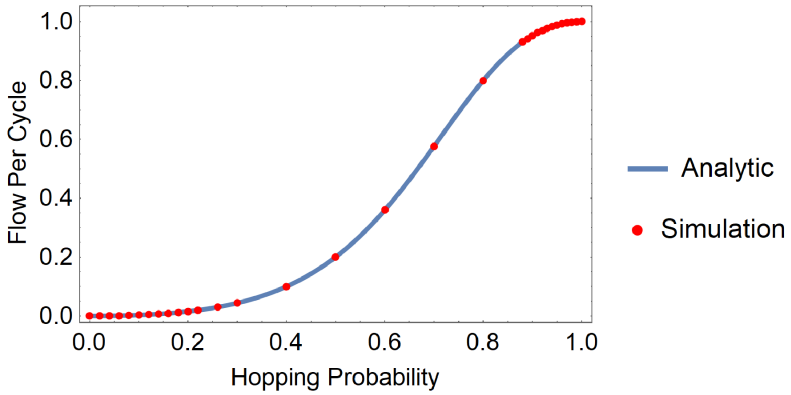

FIGURE 6: Charge transport per measurement cycle in the Zeno limit. The analytic formula given in Eq. (3.30) is compared with the transport found from direct simulation for a selection of hopping probabilities.

decomposition in the limit $L_y \to \infty$ (and verify it by direct numerical simulations of the dynamics on finite systems). The resulting dependence on p is shown in Fig. (6), exhibiting a crossover behavior ranging from the integer transport at $p = 1$ to no transport when $p = 0$ (where the dynamics is trivial, since all hopping is blocked).

We show how the edge flow can be written in terms of bulk operators. This correspondence between the bulk properties of the system and the charge transport on the edge provides both a direct, efficient method to calculate the flow as well as implies the robustness of the flow to any perturbations near the boundary of the system.

To observe the flow we imagine an infinite strip in the x direction. We partition the strip into 3 regions as shown in Fig. 7. The bottom region of the system (below height ℓ_1) is completely filled with particles, while the top (above ℓ_2) is empty. In-between ℓ_1 and ℓ_2, the particle density is left arbitrary and will have no effect on the particle transport. This choice isolates the flow along just the bottom edge of the system, removing the equal and opposite contribution from the flow along the top edge. Charge distributions of this type are analogously used as a tool to calculate charge flow along an edge in the context of Floquet topological insulators. See, for instance, [15]. In appendix 3.D we prove that

$$F = F_{bulk} + F_{edge} \tag{3.30}$$

where

$$F_{bulk} = i \sum_{\alpha\beta} [J_B(\mathbf{k}) \frac{1}{I - R_B(\mathbf{k})} \partial_{k_y} R_B(\mathbf{k})]_{\alpha\beta}|_{\mathbf{k}=0} \tag{3.31}$$

and

$$F_{edge} = \frac{1}{L_x} \langle \mathbf{I} | P_{y\leq 3} J P_{y\leq 2} | \mathbf{I} \rangle. \tag{3.32}$$

Here, R_B is a bulk transition operator, equal to R_{cyc} except with periodic instead of open boundary conditions to make it translational invariant. The transition operators R_B, R_{cyc} are used to define appropriate currents $J = -i\partial_\theta R_{cyc}(\theta)|_{\theta=0}$ and similarly $J_B = -i\partial_\theta R_B(\theta)|_{\theta=0}$. Above, for an operator A, translational invariant in x and y with respect to the unit cell of the dynamics and with matrix elements $A_{\alpha\beta}(\mathbf{r}, \mathbf{r}')$, we define $A(\mathbf{k})_{\alpha\beta}$ as in (3.27). In the edge contribution, $P_{y\leq 2}$ is a projection operator on sites with $y \leq 2$. The above expressions are proven starting from the expression Eq. (3.26) for the flow F_N after a finite number of cycles and then taking the limit of large N while maintaining $N \ll \ell_1$ and keeping $\ell_2 - \ell_1$ constant.

To compute F_{edge} we can write, explicitly

$$F_{edge} = \frac{1}{L_x} \sum_{\alpha\beta} \sum_{x,x'=1}^{L_x} \sum_{y'=1}^{2} \sum_{y=1}^{3} J_{\alpha\beta}(x, y; x', y'). \tag{3.33}$$

Calculating F_{edge} in this form we find with our measurement protocol

$$F_{edge} = p^2 + p^3 + p^4. \tag{3.34}$$

The contribution of F_{bulk} to the transport can also be evaluated readily, as it is made up of products and an inverse of 6×6 matrices and so can be easily computed for any p. In Fig 6, we combine these two terms and compare with direct simulations of the dynamics which exhibit excellent agreement.

We now make the following especially important remark that *both* F_{bulk} and F_{edge} depend only on the bulk properties of the system (assuming weak constraints to be described below). This implies that the flow is completely insensitive to the details of the structure of the edge or local perturbations. This can be argued in the following

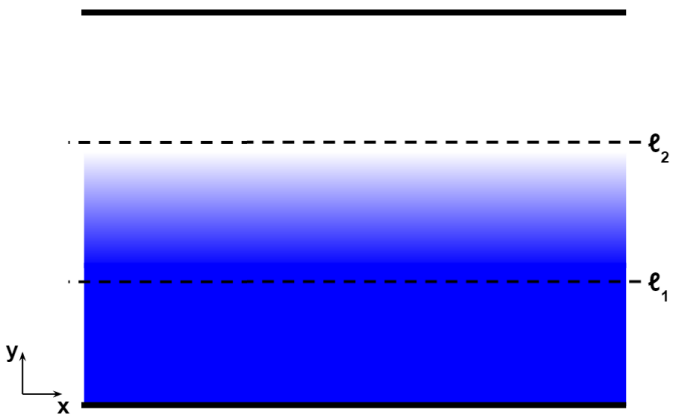

FIGURE 7: Initial particle density chosen for the flow analysis. All sites below the line $y = \ell_1$ are filled with particles (shown in blue). All sites above $y = \ell_2$ are empty. The probability of finding a particle at sites in-between $y = \ell_1$ and ℓ_2 is left arbitrary as the charge density in this region will not affect the flow.

way. We first note that

$$\langle \mathbf{I}|J|\mathbf{I}\rangle = 0 \tag{3.35}$$

i.e. there is zero total current in a uniform density system. Eq (3.35) can be seen from the form of the dynamics generated by our R matrices, (3.23), since

$$-i\partial_\theta|_{\theta=0} R_i|\mathbf{I}\rangle = \oplus_{\langle\alpha,\beta\rangle\in A_i} \begin{pmatrix} 0 & p \\ -p & 0 \end{pmatrix} \oplus_{\text{other sites}} I|\mathbf{I}\rangle = 0.$$

Now, consider a modification of the stochastic dynamics along the bottom edge of the system still obeying the no total current condition (3.35), and that there is no explicit bulk current introduced (the latter restriction of no added bulk currents may be removed upon closer analysis, see appendix 3.E). Assuming the current operator is short ranged (with range of at most one unit cell), one can rewrite the expression (3.32) as

$$F_{edge} = \frac{1}{L_x}\langle \mathbf{I}|JP_{y\leq 2}|\mathbf{I}\rangle = -\frac{1}{L_x}\langle \mathbf{I}|JP_{y>2}|\mathbf{I}\rangle \tag{3.36}$$

the expression on the right hand side for F_{edge} is independent of how we vary J on the lower boundary. In other words, the global zero current condition together with the fact that the two edges responsible for the transport are physically separated means that the contribution of F_{edge} to the flow must be protected. Together with the bulk nature of

F_{bulk}, we see indeed a protected flow. A more detailed proof can be constructed as follows (with details in the appendix): Consider the following matrix, describing the perturbed dynamics:

$$R_M(\mathbf{r},\mathbf{r}') = \begin{cases} \tilde{R} & r_y, r'_y \leq \ell_1 - (N+1) \\ R_{cyc} & \ell_1 - (N+1) \leq r_y, r'_y \leq \ell_2 + (N+1) \\ \tilde{R}' & r_y, r'_y \geq \ell_2 + (N+1) \\ 0 & \text{otherwise} \end{cases} \tag{3.37}$$

where $\tilde{R}, \tilde{R}'$ are real matrices such that R_M is doubly stochastic, i.e. R_M is identical to R_{cyc} in the bulk but modified near the boundary.

In appendix 3.E, we prove that the flow of R_M is equivalent to the flow of R_{cyc} assuming that

$$\langle \mathbf{I}| R_M(\theta=0) = \langle \mathbf{I}| \text{ and } R_M(\theta=0)\,|\mathbf{I}\rangle = |\mathbf{I}\rangle \tag{3.38}$$

$$\langle \mathbf{I}|J_M|\mathbf{I}\rangle = 0, \tag{3.39}$$

where J_M is the current operator associated with R_M. The first condition requires that R_M preserves particle number and that a uniform density is a steady state of the evolution; this implies that the transition matrix remains doubly stochastic. The second condition is the requirement that no net current can flow in the completely filled system. Note, the conditions (3.38) and (3.39) are certainly satisfied whenever R_M is a product of symmetric, doubly stochastic matrices which encapsulates a large class of physically relevant perturbations including, for example, local potentials, local variations of the hopping parameter, and removal of sites from the lattice. Indeed, repeating the argument leading to (3.21), including the presence of local potential terms (or variation in t_{hop}) in the local Hamiltonian will just locally change the hopping probability p, retaining the form of the dynamics as in (3.22) with modified ps (i.e. still made of doubly stochastic building blocks). Removal of sites can similarly be described by taking $p = 0$ for transitions to the removed site. Due to its stability, the flow may be viewed as a continuous topological invariant for the system. We emphasize that such protection cannot be achieved in 1D systems, which can be easily disconnected by the removal of a few sites.

A technical remark is in order here. The simulation result in Fig 6 was computed

using Eq (3.29) with the cut defined as shown in Fig. 5. Therefore, the quantity computed in the simulations, F_{sim} (Eq. (3.29)), is equivalent to placing the counting field θ only at a subset of the horizontal edges as opposed to placing θ on all horizontal edges as was used in defining $R_{cyc}(\theta)$ through Eq. (3.23). Accounting for the number of edges included in the simulations - these include 2 edges per two dynamical unit cells - and that each dynamical unit cell involves 4 edges and that no charge accumulation occurs, we find simply

$$F_{sim} = \frac{F}{4} \tag{3.40}$$

which was used in the comparison Fig. 6.

At this point, we wish to further discuss and clarify the nature of the protection of the flow in (3.30) and in what sense it is localized on the edge. In our set up, the charge density is constant in a thick neighbourhood of the edge. It is important to emphasize, however, that the protection is not simply due to Pauli blocking, but a feature of the classical stochastic dynamics. This is evident when we consider the flow when the density in the occupied (blue) region in Fig. 7 is uniformly reduced to a lower density $\rho < 1$. In this case (especially at low density), Pauli blocking is not important for the dynamics. However, the linearity of our stochastic dynamics shows that the new Flow will be $F(\rho) = \rho F(\rho = 1)$. Thus, the flow is protected (in the sense explained above) for any filling ρ, in sharp contrast with most topological insulators.

Another interesting feature of the charge transport here is that the flow we compute (for $p \neq 1$) is the result of the collective contribution of fermions that approach the edge, travel along it for a time, and then diffuse away, rather than the result of single wave packets traveling along the edge without dispersing. An alternative perspective that can help clarify the edge nature of the flow can be obtained by adding a particle sink/source where holes/particles can be injected/extracted from the system. In this case holes injected in the bulk will only contribute to charge flow (for a finite time) when they reach the edge. Note, the edge flow is due to unbound charges which are only a partial contribution to the local currents in the system. For example, in the completely filled system, since the density is uniform and the R matrices are symmetric there can be no current on any link in the system. The net zero current is the result of two different cancellations in the bulk and on the edges of the system. In the bulk, the zero current is the result of local current loops that give rise to a uniform magnetization and the net current is $\boldsymbol{\nabla} \times M = 0$. On the edge, the net current is zero as a result of cancellation between the bound currents, as in the bulk, and unbound currents that

exist only on the edge. The distinction, however, between charge transport (which is localized on the edge) and current (which is not localized on the edge) is largely independent of the present work and similar distinctions must be made, for example, in discussions of Floquet topological insulators [15].

For topological insulators, a bulk gap implies that small alterations to the bulk Hamiltonian will not destroy an edge mode so long as symmetries protecting the topological phase are preserved [7]. The actual value of the current will depend on the density and on the details of how the bands are filled. Similarly, here, small changes in the carrier density will lead to changes in the magnitude of the flow, but not its existence. Interestingly, unlike topological insulators, the existence of the flow and the protection we discuss are independent of the initial filling, which manifests itself in the off-diagonal part of G when the process starts.

On the other hand, while here the flow is robust (in the sense explained above) at any density, it's value is not in general robust to arbitrary global changes of the parameters. In our system, it is possible to continuously change the flow by small extensive perturbations, say, changing the total period T. However, as stated, the exact value for the flow of the system during N cycles is protected against even strong perturbations as long as these are far enough (i.e. within a distance at least N) from the interface with the region which is not of uniform density (see Appendix 3.E). Perturbations within the interface region may alter total charge transport values by inducing bulk currents in the system (see Fig. 3.E.1).

It is interesting to compare the behavior in the Zeno limit with a Floquet topological insulator evolution in our system which is equivalent to the one introduced in [20]. There, a periodic driving protocol is used as the source of chirality in the system, where hopping between neighbouring sites are sequentially turned on, but without any measurements. Explicitly, the analogous evolution for us, Λ_{Floq}, is:

$$\Lambda_{Floq} = \left(U^n_{A_8} \otimes \bar{U}^n_{A_8}\right)\left(U^n_{A_7} \otimes \bar{U}^n_{A_7}\right) ... \left(U^n_{A_1} \otimes \bar{U}^n_{A_1}\right) \tag{3.41}$$

where we have adapted the 5 step procedure on a square lattice of [20] to an analogous 8 step procedure on a Lieb lattice. To simplify the comparison, we have neglected the 5th "holding period" step and sublattice potentials in the original Rudner et. al. procedure [20].

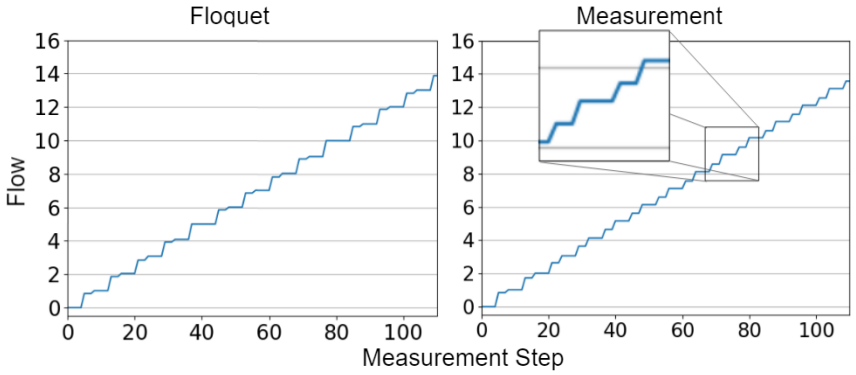

(A)

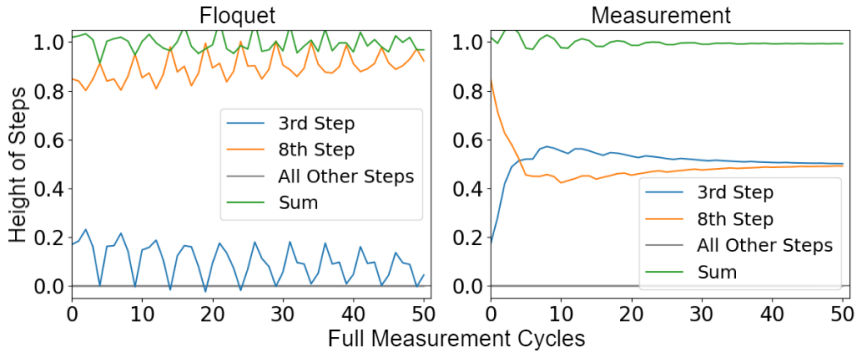

(B)

FIGURE 8: (a) Charge transfer for Floquet system (left) and measurement protocol in the Zeno limit (right) where, in both cases, the hopping probability $p = 0.96$. (b) Charge transfer after each measurement step for the Floquet system and measurement protocol with hopping probability $p = 0.96$. Note the convergence of the 3rd and 8th step to half the total flow per cycle.

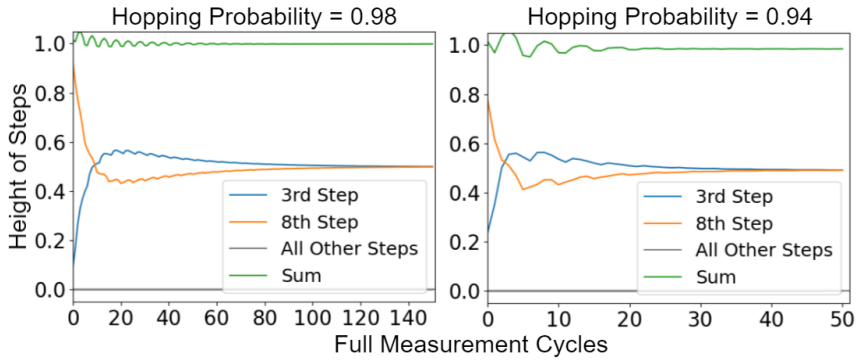

FIGURE 9: Flow after each measurement step for hopping probabilities $p = 0.98$ (left) and $p = 0.94$ (right). Note, in the long time limit, the 3rd and 8th measurement step of both hopping probabilities converge to half the total flow per measurement cycle.

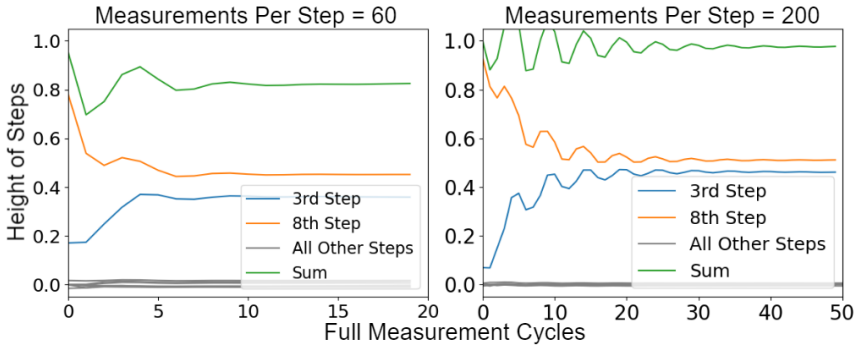

FIGURE 10: Flow after each measurement step for $n = 60$ and $n = 200$. For both, $\frac{T}{8} = \frac{\pi}{2}$.

Note the measurement protocol in the Zeno limit (Eq. 3.15) is precisely the Floquet evolution interspersed with measurements between each step. Markedly, when $p = 1$ the two evolutions are equivalent since the measurement projectors act trivially in the perfect switching case (when the initial G is diagonal).

We now turn to investigate the simulated dynamics in this regime. Away from the perfect switching cycle, $p = 1$, we find an interesting distinction between the Floquet evolution and the Zeno limit of the measurement/evolution cycle as shown in Fig. 8. Examining the charge transfer on the resolution of the 8 steps per cycle, we find a double step structure in the charge transfer which is not present in the corresponding Floquet evolution. Namely, the 3rd and 8th step of the measurement protocol each contribute half of the total flow per complete cycle. The reason for this double step structure is the following. The dynamics of particles in the lattice are governed by a classical, chiral random walk determined by R_{cyc}. The 3rd and the 8th step are the only two steps that cross the slice through the Lieb lattice, and thus all transport must occur within these 2 steps. For a particle starting far away from the slice, all information about whether the particle would cross the slice during the 3rd or 8th step in the deterministic $p = 1$ case is lost. Hence, in the long time dynamics, a particle is equally likely to cross the slice on either step leading to the observed double step structure. We emphasize that this double step structure holds for all $p \neq 1$ (see figure 9). However, similar to the Floquet evolution, the Flow per full measurement cycle decreases away from 1 for $p < 1$ as shown in figure 6.

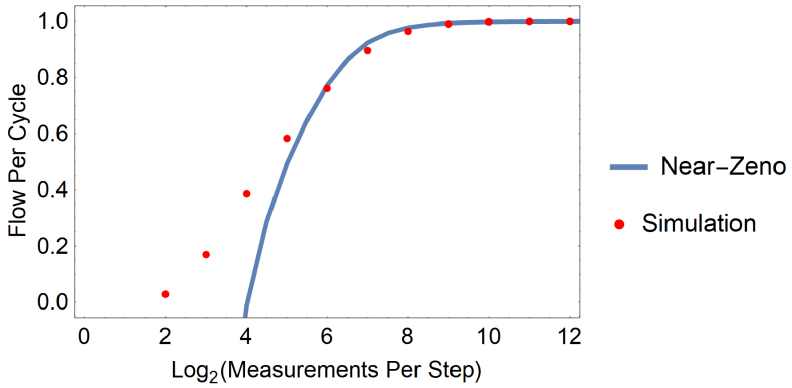

FIGURE 11: Flow per cycle as the measurements per step moves away from the Zeno limit. Compared are the values found from the near-Zeno limit approximation, Eq. (3.30) with the transformation Eq. (3.42), and the flow found from direct simulation. Both analytics and simulations are done in the perfect switching cycle, i.e. $\frac{T}{8} = \frac{\pi}{2}$.

3.6 Away from the Zeno limit

We now turn to consider the important question of whether the flow is still present when the frequency of measurements is reduced, i.e. we study the evolution under our measurement protocol away from the Zeno limit. In Fig. 11 we show the flow as function of $\log(n)$. We see that the flow is reduced, but still finite as the measurement frequency is reduced, crossing over from near constant behavior at high frequency, to roughly logarithmic behavior, $F \sim 0.2\log_2(n) - 0.4$ at low frequency n, with $F \sim 0.2$ particles per cycle at $n = 8$ measurements per step.

The blue line in Fig. 11 represents an analytic perturbative near-Zeno correction which fits the simulations remarkably well for $n > 64$. To arrive at it, we start with Eq. (3.15), now retaining terms up to and including order $O(n\tau^2)$. We prove in appendix 3.F that the resultant evolution, to order $O(n\tau^2)$, can still be completely described in terms of the dynamics of the diagonal of G, with the classically stochastic transfer matrices R_i replaced by the matrices $R_{nz,i}$ given by

$$R_{nz,i} = R_i - n\tau^2\tilde{R}_i \tag{3.42}$$

where $\tilde{R}_i$ is the near-Zeno correction to R_i. As in the Zeno case, we define

$$R_{nz} = R_{nz,8}R_{nz,7}R_{nz,6}R_{nz,5}R_{nz,4}R_{nz,3}R_{nz,2}R_{nz,1} \tag{3.43}$$

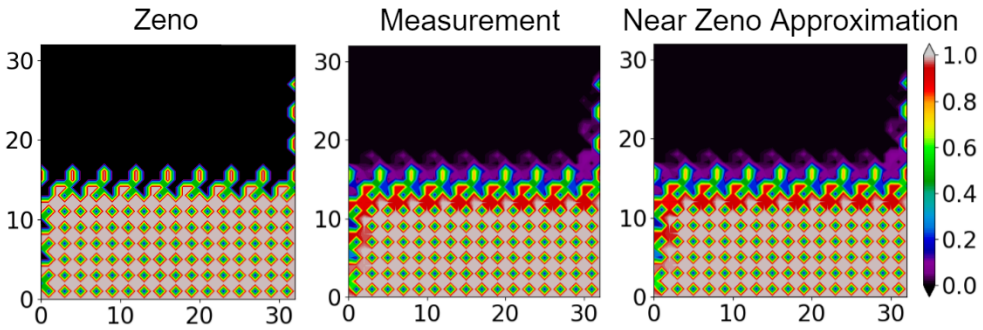

FIGURE 12: A comparison of, from left to right, the zeno limit, the full measurement protocol with 500 measurements per measurement step, and the near zeno approximation with 500 measurements per measurement step - all with $\frac{T}{8} = \frac{\pi}{2}$. Plotted are the local particle densities for a 33 by 33 site Lieb lattice after 51 measurement steps for the lower-half filled plane set up given in Fig. 4.

and, in treating R_{nz}, only terms up to $O(n\tau^2)$ are kept after combining equations (3.42) and (3.43). Finally, the blue line of Fig. 11 is obtained by substituting (3.43) into (3.30). In Appendix 3.F, we solve for (3.43) explicitly, but here we will focus only on the flow resulting from R_{nz}. We also note here that, similar to the Zeno limit case, the flow in the near-Zeno limit is protected to perturbations localized on the boundaries (see appendix 3.E). Furthermore, numerical simulations suggest that this protection persists even in the low frequency measurement regime. We leave a detailed investigation of this observation to future work.

In Fig 12 we show what the evolution of density in the system away from the Zeno limit looks like. The main feature is clearly the ability of particles to spread faster into the bulk, since the evolution is not confined as effectively to a sequence of two-site evolution steps as in the Zeno case. We emphasize, however, that there is still significant charge transport even far away from the Zeno regime (Fig. 11). On the other hand, the double step structure is broken with the 8th step in the measurement cycle providing an increasing percentage of the total flow per cycle as the number of measurements per measurement step is reduced. This is shown, for example, in Fig. 10. This is because particles on the edge are less affected by the move away from the Zeno limit (as they have fewer neighboring sites to spread too). Since the 8th measurement step hops across the Flow cut at the edge, a larger percentage of the Zeno limit flow is retained.

3.7 Concluding remarks

In this work we presented a framework for inducing edge modes via measurement protocols. Our work is complementary to the many recent advances in studying time periodic systems such as topological Floquet insulators [20, 86]. The resultant behavior is a remarkable demonstration of the role of an observer in quantum mechanics as fundamentally different from a classical observer.

Several remarks are in order regarding open problems. First, we emphasize that the behavior analyzed in this paper is that of the average transport and dynamics of densities over all possible measurement outcomes. While it is reasonable to expect that such an average would well represent the typical behavior of the system for a typical history of measurement outcomes (a"quantum trajectory"), it is of much interest to study how well this expectation holds by studying both fluctuations and the behavior of the quantum trajectories in our system.

While we have concentrated on the study of the two point function G, it would be also interesting to establish the limiting behavior of the many body density matrix ρ as the system is observed. In particular, this would allow us to study the development of entropy and non trivial correlation in the system. Indeed, in recent works, e.g. [104, 109, 116, 117], it has been shown that certain protocols of repeated measurements interspersed with free unitary evolution induce a phase transition in the Rényi entropy dependant on the rate of measurement. In our model, we have found that no two-point correlations are generated up to first order in the expansion away from the Zeno limit, keeping the system close to a product state at all times. However, for low measurement rates, these correlations are clearly generated. This suggests phase transitions of mutual information measures with the measurement rate may be present.

It is important to note that, while in this work we have focused mainly on the Lieb lattice, our procedure may be easily generalized to other lattices. For example, we provide a similar 8-step protocol on a square lattice and a 6-step protocol on a "modified" kagome lattice in appendix 3.B. Furthermore, we describe some restrictions on the kinds of protocols that can be implemented on a given lattice.

We note that while our dynamics is driven by non-interacting evolution, the formalism (see [52]) allows for an arbitrary initial state, including interesting highly correlated ones. Moreover, we expect that in the Zeno limit, the inclusion of certain interactions may be efficiently implemented with a proper modification of the current

treatment, which we leave for future work.

Finally, we suggest that a measurement protocol such as ours, while challenging, may be experimentally realizable. One possibility is the use of quantum dot arrays as the underlying lattice [140]. Another promising direction is quantum gas microscopes. Here, experiments working with ultracold ^{6}Li fermions have established the ability to resolve particle presence at single sites see e.g. [76, 78, 141].

Appendix

3.A Remarks about Steady States

What kind of steady states can we expect in a system like ours where evolution and density measurements are intertwined? Here it is convenient to look at the steady states of the correlation matrix G rather then the full density matrix ρ. Let us consider how the Hilbert-Schmidt norm of G changes under unitary evolution and measurements Eq. (1.29a, 1.29b) above. The Hilbert-Schmidt norm is defined as

$$\|G\|_{HS}^2 \equiv \mathrm{Tr}\Big\{G^\dagger G\Big\} = \sum_{ij} |G_{ij}|^2. \tag{3.44}$$

Clearly, $\|G\|_{HS}$, is invariant under unitary evolution of G. Particle measurements of G, as described by (3.2), on the other hand, set to zero some of the matrix elements of G and thus can only decrease $\|G\|_{HS}$. A necessary (though not sufficient) condition for some G_{steady} to be a steady state of some super-operator Λ, i.e. $\Lambda G_{steady} = G_{steady}$ is that the Hilbert-Schmidt norm remains constant. This provides a restriction on Λ. Any particle detection measurement contained in Λ must act trivially, i.e. not eliminate any matrix elements. Thus, without loss of generality writing $\Lambda \equiv \prod_i \Pi_i U_i$ we require that

$$\Lambda G_{steady} = \prod_i \Pi_i U_i G_{steady} = \prod_I U_i G_{steady} \tag{3.45}$$

Note, for our measurement procedure, this is clearly true for any scalar matrix G_{steady}. For a G_{steady} with a non-uniform diagonal (such as that of a single localized particle) to be a steady state of the measurement protocol, we can only satisfy Eq. (3.45) in the Zeno limit with $\frac{T}{8}$ fine tuned to $\frac{\pi}{2}$.

One possibility to find non-equilibrium steady states in the system, as well as offer an insight into larger systems is to use particle injection and removal as was previously done in [52]. To stabilize the system where the left half is filled with particles,

we may use a strip of width L, where we start where we constantly try to inject particles from the left, and extract any particle that arrives to the right of the sample.

In the context of the present paper, we instead look at the effective behavior of the system, when it is partially filled and evolve over times which are long, but short compared to the time it would take to arrive at the real uniform density steady state.

3.B The measurement protocol on other lattices

In this section we remark on lattices on which one can perform the measurement protocol outlined above. Our protocol is directly inspired by Floquet cycles where a collection of pairs of neighbouring sites are activated at any given step. To mimic this type of dynamics, we require the ability to isolate the activated pairs by performing rapid measurements on neighbouring sites. Thus, to apply our protocol directly, we require that there is no hopping amplitude to go between two distinct pairs. For a Hamiltonian describing nearest neighbour hopping on a lattice, this means that the edge distance between unmeasured pairs is at least two (see upper left figure in Figure 3.B.1).

This restriction then rules out the simple cycle on a square lattice originally introduced in [20], where individual squares are traced out in 4 steps, as in this case the edge distance between isolated pairs is only one. This does not, however, mean a measurement protocol cannot be implemented on a square lattice. A solution is to increase the size of the cycle to an 8 step process that traces out a path around clusters of 4 squares (see right figure in Figure 3.B.1). Here, the edge distance between activated pairs is 3, and thus they can be isolated using rapid measurements. Note, in this example protocol, there is a site at the center of the cycle that is never activated, i.e. always measured. If this site is removed, we find precisely the 8 step protocol on a Lieb lattice introduced in this paper. This choice was made to minimize the number of required measurements and to remove any spreading of particles through these unactivated sites away from the Zeno limit. We also here give an example of another measurement protocol with 6 measurement steps on a "Modified" Kagome Lattice, as opposed to the 8 steps for our protocol on a Lieb lattice, as shown in Fig. 3.B.2

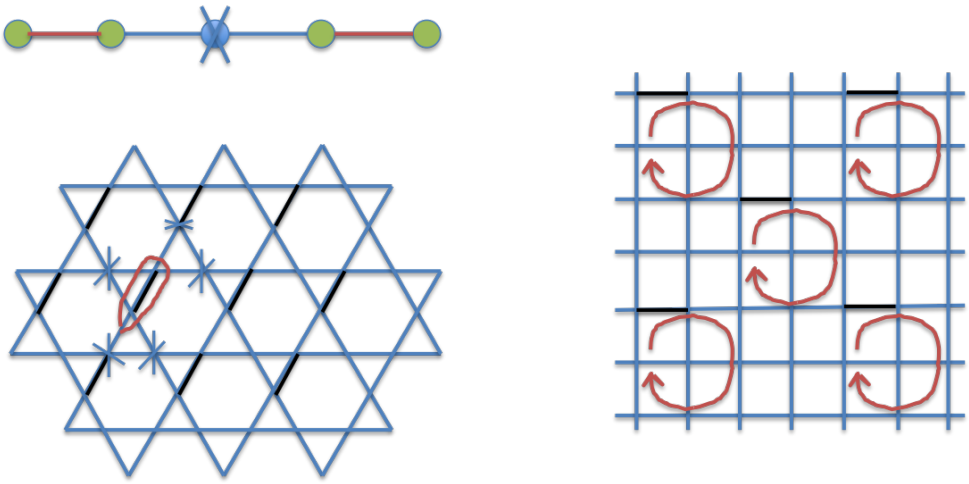

FIGURE 3.B.1: **Upper Left:** The measurement protocols require the bonds (red) between unmeasured sites (green) to be separated by at least two edges. This allows for at least one measured site (crossed) between them. **Lower Left:** The naive attempt to perform the measurement protocol on the Kagome lattice does not work because two of the surrounding measured sites around the unmeasured sites (circled with red) overlap with other unmeasured sites (denoted as the ends of black links). **Right:** An example of a measurement protocol on a square lattice that satisfies the requirement that the edge distance between unmeasured pairs must be at least 2. If the unactivated (always measured) sites in this protocol are removed, we have exactly the 8 step protocol on a Lieb lattice introduced in this paper.

3.C Some derivation details

In this section we supply a few more details about the formulas used in the main text.
I. Proof of Eq. (3.7):

$$\prod_{a\in A^c}\pi_a = \sum_{a\in A^c} P_a\otimes P_a + P_A\otimes P_A$$

We first note that: if $a\neq b$ then $p_a p_b = 0$, $p_a(1-p_b)=p_a$. Thus in the product

$$\prod_{a\in A^c}\pi_a = \prod_{a\in A^c}(P_a\otimes P_a + (1-P_a)\otimes(1-P_a)) \tag{3.46}$$

the term of the form $P_a\otimes P_a$ can only appear in a product of the form $(P_a\otimes P_a)\prod_{a'\in A^c;a'\neq a}(1-P_{a'})\otimes(1-P_{a'}) = P_a\otimes P_a$. Next note that: $\prod_{a\in A^c}(1-P_a) = \prod_{a\in A}P_a$. Therefore $\prod_{a\in A^c}(1-P_a)\otimes(1-P_a) = P_A\otimes P_A$. Combining these we get Eq. (3.7).

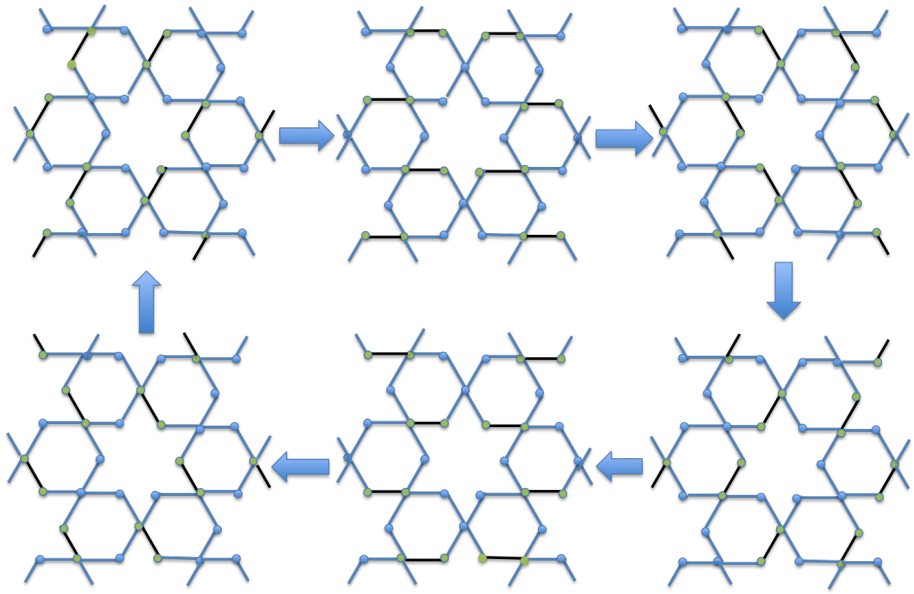

FIGURE 3.B.2: An example measurement protocol on a "Modified" Kagome lattice that utilizes 6 measurement steps (as opposed to the 8 step procedure used on the Lieb lattice). The black bonds indicate free hopping pairs and measurement is indicated by blue colored sites.

II. Derivation of equation (3.13):

$$\begin{aligned}
&\Pi_A \left[H \otimes I - I \otimes H\right] \Pi_A \\
&= \left(\textstyle\sum_{a\in A^c} P_a \otimes P_a + P_A \otimes P_A\right) \left[H \otimes I - I \otimes H\right] \left(\textstyle\sum_{b\in A^c} P_b \otimes P_b + P_A \otimes P_A\right) \\
&= \left(P_A \otimes P_A\right) \left[H \otimes I - I \otimes H\right] \left(P_A \otimes P_A\right) \\
&= H_A \otimes P_A - P_A \otimes H_A
\end{aligned} \tag{3.47}$$

where $H_A \equiv P_A H P_A$ and we used that if $a, b \in A^c$ then $P_A P_a = P_A P_b = 0$ and that $P_a P_b = \delta_{ab} P_a$.

3.D Bulk-Edge decomposition: Proof of formula (3.30).

Our starting point is Eq. (3.26). Taking the ∂_θ derivative and using the doubly-stochastic nature of R_{cyc} (when $\theta = 0$), i.e. $\langle \mathbf{I}| R_{cyc}(\theta = 0) = \langle \mathbf{I}|$ and $R_{cyc}(\theta = 0)\,|\mathbf{I}\rangle = |\mathbf{I}\rangle$, we find

$$\begin{aligned} F_N = \tfrac{1}{NL_x}\, i\partial_\theta \chi_N(\theta)|_{\theta=0} = \tfrac{1}{NL_x} i\partial_\theta \langle \mathbf{I}| R^N_{cyc}(\theta) G\,|\mathbf{I}\rangle\,|_{\theta=0} = \tfrac{1}{NL_x}\textstyle\sum_{m=0}^{N-1}\langle \mathbf{I}| J R^m_{cyc}(\theta=0) G|\mathbf{I}\rangle \\ = \tfrac{1}{NL_x}\textstyle\sum_{m=0}^{N-1}\langle \mathbf{I}| J\left[R^m_{cyc}(\theta=0), G\right]|\mathbf{I}\rangle + \tfrac{1}{L_x}\langle \mathbf{I}|JG|\mathbf{I}\rangle, \end{aligned} \tag{3.48}$$

where we have defined $J = -i\partial_\theta R_{cyc}(\theta)|_{\theta=0}$ and G is a diagonal matrix representing the initial density distribution, i.e., if written in matrix elements, $G_{\alpha,\beta}(\mathbf{r},\mathbf{r}') = \delta_{\alpha\beta}\delta_{\mathbf{r},\mathbf{r}'} g_\alpha(\mathbf{r})$ with $\mathbf{r} = (x, y)$ and $\mathbf{r}'$ coordinates of the unit cell, α, β internal sites, and $g_\alpha(\mathbf{r})$ the initial probability for a particle at a site indexed by $(\mathbf{r}, \alpha)$. Below we suppress the angle when describing $R_{cyc}(\theta = 0)$, and will just write R_{cyc}.

In our setup (see Fig. 7), we fill the system in such a way that $g_\alpha(\mathbf{r}) = 1$ for $y < \ell_1$ and $g_\alpha(\mathbf{r}) = 0$ for $y > \ell_2$. Let us define the set

$$S_m = \{\mathbf{r} : \ell_1 - m \le y \le \ell_2 + m\}. \tag{3.49}$$

The set S_m contains the interface between empty and full region, "thickened" by a height m below and above. Let also P_{S_m} be the projection on the set S_m defined as in (3.8). Explicitly:

$$P_{S_m,\alpha,\beta}(\mathbf{r},\mathbf{r}') = \delta_{\alpha\beta}\delta_{\mathbf{r},\mathbf{r}'} \begin{cases} 1 & \ell_1 - m \le y, y' \le \ell_2 + m \\ 0 & \text{otherwise} \end{cases}. \tag{3.50}$$

We now prove that we can freely move the projection P_{S_m} to either side of the commutator $\left[R^m_{cyc}, G\right]$, namely, taking the range of R_{cyc} to be short, $range(R_{cyc}) \le 1$, then

$$\left[R^m_{cyc}, G\right] = P_{S_m}\left[R^m_{cyc}, G\right] = \left[R^m_{cyc}, G\right] P_{S_m} = P_{S_m}\left[R^m_{cyc}, G\right] P_{S_m} \tag{3.51}$$

Proof: Consider the commutator $\left[R^m_{cyc}, G\right]$. Note that since $R_{\alpha\beta}(\mathbf{r},\mathbf{r}') = 0$ if $|\mathbf{r} - \mathbf{r}'| > 1$, we have $R^m_{\alpha\beta}(\mathbf{r},\mathbf{r}') = 0$ if $|\mathbf{r} - \mathbf{r}'| > m$. Therefore, looking at the matrix elements, we have $(\left[R^m_{cyc}, G\right])_{\alpha\beta}(\mathbf{r},\mathbf{r}') = R^m_{\alpha\beta}(\mathbf{r},\mathbf{r}')\left(g_\beta(\mathbf{r}') - g_\alpha(\mathbf{r})\right) = 0$ when $|\mathbf{r} - \mathbf{r}'| > m$ or $g_\beta(\mathbf{r}') - g_\alpha(\mathbf{r}) = 0$. Thus, the matrix elements of $\left[R^m_{cyc}, G\right]$ can only be non-zero when simultaneously $|\mathbf{r} - \mathbf{r}'| \le m$ and $g_\beta(\mathbf{r}') - g_\alpha(\mathbf{r}) \ne 0$. Let us check when the matrix elements can be non-vanishing.

Since the system is filled the system in such a way that $g_\alpha(\mathbf{r}) = 1$ for $y < \ell_1$, we see that if $y < \ell_1 - m$, the condition that $|\mathbf{r} - \mathbf{r}'| \leq m$ implies $y' \leq \ell_1$, and in particular $g_\beta(\mathbf{r}') = g_\alpha(\mathbf{r}) = 1$, making the commutator vanish. Similarly, the commutator will vanish if $y > \ell_2 + m$. And of course the same considerations can be applied to y'. We conclude that non-zero matrix elements are only possible if

$$\ell_1 - m \leq y, y' \leq \ell_2 + m \tag{3.52}$$

which implies (3.51). □

Since the boundaries of the system are not included in the S_m region, we may also replace the open boundary conditions of R^m_{cyc} with periodic ones, denoted by R^m_B, to get:

$$\left[R^m_{cyc}, G\right] = P_{S_m}\left[R^m_{cyc}, G\right] = \left[R^m_B, G\right] P_{S_m} \tag{3.53}$$

Similarly, since J is short ranged, far from the boundaries, the matrix elements of J are identical to those of $J_B \equiv -i\partial_\theta R_B(\theta)|_{\theta=0}$, namely $JP_{S_m} = J_B P_{S_m}$. This behavior holds when $m < min(\ell_1 - range(J), L_y - \ell_2 - range(J))$, which will always be assumed in the following treatment. Thus, we have:

$$\langle \mathbf{I}|J\left[R^m_{cyc}, G\right]|\mathbf{I}\rangle = \langle \mathbf{I}|JP_{S_m}\left[R^m_{cyc}, G\right]|\mathbf{I}\rangle = \langle \mathbf{I}|J_B P_{S_m}\left[R^m_B, G\right]|\mathbf{I}\rangle \tag{3.54}$$

Substituting in Eq. (3.48) we get

$$\begin{aligned} F_N &= \frac{1}{NL_x}\sum_{m=0}^{N-1}\langle \mathbf{I}|J_B P_{S_m}\left[R^m_B, G\right]|\mathbf{I}\rangle + \frac{1}{L_x}\langle \mathbf{I}|JG|\mathbf{I}\rangle \\ &= \frac{1}{NL_x}\sum_{m=0}^{N-1}\langle \mathbf{I}|J_B P_{S_m} R^m_B G|\mathbf{I}\rangle - \frac{1}{NL_x}\sum_{m=0}^{N-1}\langle \mathbf{I}|J_B P_{S_m} G|\mathbf{I}\rangle + \frac{1}{L_x}\langle \mathbf{I}|JG|\mathbf{I}\rangle \\ &= \frac{1}{NL_x}\sum_{m=0}^{N-1}\langle \mathbf{I}|J_B P_{S_m} R^m_B G|\mathbf{I}\rangle + \frac{1}{NL_x}\sum_{m=0}^{N-1}\langle \mathbf{I}|J(G - P_{S_m} G)|\mathbf{I}\rangle \end{aligned} \tag{3.55}$$

where in the last line we used that in the bulk $\langle \mathbf{I}|J_B P_{S_m} G|\mathbf{I}\rangle = \langle \mathbf{I}|JP_{S_m} G|\mathbf{I}\rangle$.

To proceed we note that

$$G - P_{S_m} G = (1 - P_{S_m})G = (P_{y<\ell_1 - m} + P_{y>\ell_2+m})G = P_{y<\ell_1-m} \tag{3.56}$$

where $P_{y<\ell_1-m}$, $P_{y>\ell_2+m}$ are projectors onto the regions with y below $y = \ell_1 - m$ and y above $y = \ell_2 + m$ respectively. Also, we used that: $P_{y<\ell_1-m}G = P_{y<\ell_1-m}$, and $P_{y<\ell_2+m}G = 0$, which follow immediately from the definition of G. Therefore:

$$F_N = \frac{1}{NL_x}\sum_{m=0}^{N-1}\langle \mathbf{I}|J_B P_{S_m} R_B^m G|\mathbf{I}\rangle + \frac{1}{NL_x}\sum_{m=0}^{N-1}\langle \mathbf{I}|JP_{y<\ell_1-m}|\mathbf{I}\rangle \tag{3.57}$$

We can further simplify as follows. Let us assume there is no bulk current per unit cell. Then, if averaged over a bulk strip whose width is a unit cell, we have $\langle \mathbf{I}|J(P_{y<\ell_1-m} - P_{y<\ell_1-(m-1)})|\mathbf{I}\rangle = 0$, which, finally, taking $range(J) = 1$, yields the form

$$\begin{aligned} F_N &= \frac{1}{NL_x}\sum_{m=0}^{N-1}\langle \mathbf{I}|J_B P_{S_m} R_B^m G|\mathbf{I}\rangle + \frac{1}{L_x}\langle \mathbf{I}|JP_{y\leq 2}|\mathbf{I}\rangle \\ &\equiv F_{bulk} + F_{edge}. \end{aligned} \tag{3.58}$$

In other words, we have split the charge transport into a term that depends only on the bulk properties of the system,

$$F_{bulk} = \frac{1}{NL_x}\sum_{m=0}^{N-1}\langle \mathbf{I}|J_B P_{S_m} R_B^m G|\mathbf{I}\rangle, \tag{3.59}$$

and a term that can be computed near the edge,

$$F_{edge} = \frac{1}{L_x}\langle \mathbf{I}|JP_{y\leq 2}|\mathbf{I}\rangle. \tag{3.60}$$

Let us consider the two terms separately.

The edge term. F_{edge} we can efficiently compute $\langle \mathbf{I}|JP_{y\leq 2}|\mathbf{I}\rangle$, which can be done explicitly by writing the transition matrix for a ladder geometry of small extension in the y direction. Note that due to the short-range nature of J, the edge expression can be further reduced to $\langle \mathbf{I}|P_{y\leq 3}JP_{y\leq 2}|\mathbf{I}\rangle$. Doing so for our system on Mathematica we find with our measurement protocol $F_{edge} = p^2 + p^3 + p^4$.

The bulk term F_{bulk}. Assuming the translational invariance of R_B, we can write F_{bulk} expressed in k-space by defining the momentum states

$$|\mathbf{k}\rangle_\alpha = \frac{1}{\sqrt{V}}\sum_{\mathbf{r}} e^{i\mathbf{k}\cdot\mathbf{r}}\,|\mathbf{r},\alpha\rangle \;,\; |\mathbf{r},\alpha\rangle = \int \frac{d^2k}{(2\pi)^2} e^{-i\mathbf{k}\cdot\mathbf{r}}\,|\mathbf{k}\rangle_\alpha \tag{3.61}$$

where $V = L_x L_y$ is the number of unit cells. To proceed, let us write the uniform density vector $|\mathbf{I}\rangle$ as

$$|\mathbf{I}\rangle = \sum_{\mathbf{r},\alpha} |\mathbf{r},\alpha\rangle = \sqrt{V} \sum_{\alpha} |\mathbf{k}=0\rangle_{\alpha} . \tag{3.62}$$

Therefore, using the momentum representation in (3.59) we arrive at

$$F_{bulk} = \frac{V}{NL_x} \sum_{m=0}^{N-1} \sum_{\alpha\beta} (J_B)_{\alpha\gamma} \left(\langle \mathbf{k}=0 | \, P_{S_m} R_B^m G \, |\mathbf{k}=0\rangle \right)_{\gamma\beta} \tag{3.63}$$

To evaluate this expression, we need, explicitly

$$\langle k_x = 0, k_y |_{\alpha} \, G \, |k'_x = 0, k'_y \rangle_{\beta} = \frac{\delta_{\alpha\beta}}{L_y} \sum_{y} g_{\alpha}(y) e^{-iy(k_y - k'_y)}. \tag{3.64}$$

where $g_\alpha(y) = L_x^{-1} \sum_x g_\alpha(\mathbf{r})$. For the evolution, let us write R_B^m in the form

$$\langle k_x = 0, k_y |_{\alpha} \, R_B^m \, |k'_x = 0, k'_y \rangle_{\beta} = \delta_{k_x k'_x} \delta_{k_y k'_y} \sum_{v=-m}^{m} C_{\alpha\beta m v} e^{ik_y v}. \tag{3.65}$$

where the coefficients $C_{\alpha\beta m v}$ depend on the model. The restriction $-m \leq v \leq m$ follow from the range of R_B^m being limited to m. Also note that:

$$\langle \mathbf{k} |_{\alpha} \, P_{S_m} \, |\mathbf{k}'\rangle_{\beta} = \frac{\delta_{\alpha\beta} \delta_{k_x k'_x}}{L_y} \sum_{\ell_1 - m \leq y \leq \ell_2 + m} e^{-iy(k_y - k'_y)}. \tag{3.66}$$

Putting these together we have

$$
\begin{aligned}
&\left(\langle \mathbf{k}=0|\, P_{S_m} R_B^m G\, |\mathbf{k}=0\rangle\right)_{\alpha\beta} \\
&= \frac{1}{L_y}\int \frac{dk'_y}{2\pi} \sum_{\ell_1-m\le y\le \ell_2+m} e^{ik'_y y} \sum_{v=-m}^{m} C_{\alpha\beta m v} e^{ik'_y v} \sum_{y'} g_\beta(y') e^{-ik'_y y'} \\
&= \frac{1}{L_y} \sum_{\ell_1-m\le y\le \ell_2+m} \sum_{y'} \sum_{v=-m}^{m} C_{\alpha\beta m v} \left(\int \frac{dk'_y}{2\pi} e^{ik'_y(y-y'+v)}\right) g_\beta(y') \\
&= \frac{1}{L_y} \sum_{v=-m}^{m} C_{\alpha\beta m v} \sum_{\ell_1-m\le y\le \ell_2+m} g_\beta(y+v) \\
&= \frac{1}{L_y} \sum_{v=-m}^{m} C_{\alpha\beta m v} \sum_{\ell_1-m+v\le y\le \ell_2+m+v} g_\beta(y) \\
&= \frac{1}{L_y} \sum_{v=-m}^{m} C_{\alpha\beta m v} \left[\left(\sum_{y=\ell_1}^{\ell_2} g_\beta(y) + m\right) - v\right] \\
&= \frac{1}{L_y}\left(i\partial_{k_y}[R_B^m(\mathbf{k})]_{\alpha\beta} + \left(\sum_{y=\ell_1}^{\ell_2} g_\beta(y) + m\right)[R_B^m(\mathbf{k})]_{\alpha\beta}\right)|_{\mathbf{k}=\mathbf{0}}.
\end{aligned}
\tag{3.67}
$$

Therefore, we have

$$
\begin{aligned}
F_{bulk} &= \frac{V}{NL_x} \sum_{m=0}^{N-1} \sum_{\alpha\beta\gamma} (J_B)_{\alpha\gamma} \left(\langle \mathbf{k}=0|\, P_{S_m} R_B^m G\, |\mathbf{k}=0\rangle\right)_{\gamma\beta} \\
&= \frac{1}{N} \sum_{m=0}^{N-1} \sum_{\alpha\beta} \left\{ i[J_B(\mathbf{k})\partial_{k_y}(R_B^m(\mathbf{k}))]_{\alpha\beta}|_{\mathbf{k}=0} + \left(\sum_{y=\ell_1}^{\ell_2} g_\beta(y) + m\right)[J_B(\mathbf{k})(R_B^m(\mathbf{k}))]_{\alpha\beta}|_{\mathbf{k}=0} \right\}
\end{aligned}
\tag{3.68}
$$

Next, we note that in Eq. (3.68) above, we can use

$$
\sum_{\alpha\beta} m[J_B(\mathbf{k})(R_B^m(\mathbf{k}))]_{\alpha\beta}|_{\mathbf{k}=0} = 0 \tag{3.69}
$$

This follows from the fact that R_B is a stochastic matrix, with $R_B\,|\mathbf{I}\rangle = |\mathbf{I}\rangle$, and the assumption that there is no net current in the uniform density system:

$$
0 = \langle \mathbf{I}|\, J_B\, |\mathbf{I}\rangle = \langle \mathbf{I}|\, J_B R_B^m\, |\mathbf{I}\rangle = V \sum_{\alpha\beta} [J_B(\mathbf{k})(R_B^m(\mathbf{k}))]_{\alpha\beta}|_{\mathbf{k}=0} = 0. \tag{3.70}
$$

Let us define $c_\alpha \equiv \sum_{y=\ell_1}^{\ell_2} g_\alpha(y)$. We then have:

$$F_{bulk} = \frac{1}{N}\sum_{m=0}^{N-1}\sum_{\alpha\beta}\Big\{i[J_B(\mathbf{k})\partial_{k_y}(R_B^m(\mathbf{k}))]_{\alpha\beta}|_{\mathbf{k}=0} + [J_B(\mathbf{k})(R_B^m(\mathbf{k}))]_{\alpha\beta}c_\beta|_{\mathbf{k}=0}\Big\} \tag{3.71}$$

Now, using repeatedly that $R_B\,|\mathbf{I}\rangle = |\mathbf{I}\rangle$, we write :

$$\begin{aligned}
&\frac{1}{N}\sum_{m=0}^{N-1}\sum_{\alpha\beta}\Big\{i[J_B(\mathbf{k})\partial_{k_y}(R_B^m(\mathbf{k}))]_{\alpha\beta}|_{\mathbf{k}=0} + [J_B(\mathbf{k})(R_B^m(\mathbf{k}))]_{\alpha\beta}c_\beta|_{\mathbf{k}=0}\Big\} \\
&= \frac{i}{N}\sum_{m=1}^{N-1}\sum_{\alpha\beta}\left\{[J_B(\mathbf{k})\sum_{q=0}^{m-1}R_B^q(\mathbf{k})\partial_{k_y}R_B(\mathbf{k})]_{\alpha\beta}|_{\mathbf{k}=0} + [J_B(\mathbf{k})\frac{R_B(\mathbf{k})^N - I}{R_B(\mathbf{k}) - I}]_{\alpha\beta}c_\beta|_{\mathbf{k}=0}\right\} \\
&= \frac{1}{N}\sum_{\alpha\beta}\left\{i[J_B(\mathbf{k})\Big(\frac{N[I - R_B(\mathbf{k})] + R_B^N(\mathbf{k}) - I}{[I - R_B(\mathbf{k})]^2}\Big)\partial_{k_y}R_B(\mathbf{k})]_{\alpha\beta}|_{\mathbf{k}=0}\right. \\
&\qquad\left. + [J_B(\mathbf{k})\frac{R_B(\mathbf{k})^N - I}{R_B(\mathbf{k}) - I}]_{\alpha\beta}c_\beta|_{\mathbf{k}=0}\right\}
\end{aligned} \tag{3.72}$$

We now consider the large N limit. If we assume that c_β doesn't scale with N, the dominant term becomes

$$F_{bulk} = i\sum_{\alpha\beta}[J_B(\mathbf{k})\frac{1}{I - R_B(\mathbf{k})}\partial_{k_y}R_B(\mathbf{k})]_{\alpha\beta}|_{\mathbf{k}=0}, \tag{3.73}$$

which is Eq. (3.31).

3.E Robustness of Flow

In this section, we show that the results of Appendix 3.D are robust to perturbations near the boundary (see Fig. 3.E.1). Consider a perturbation of our stochastic dynamics R_{cyc}, affecting regions away from the bulk of the sample where we have our interface between the occupied and unoccupied regions. Let us take it as described by a modified

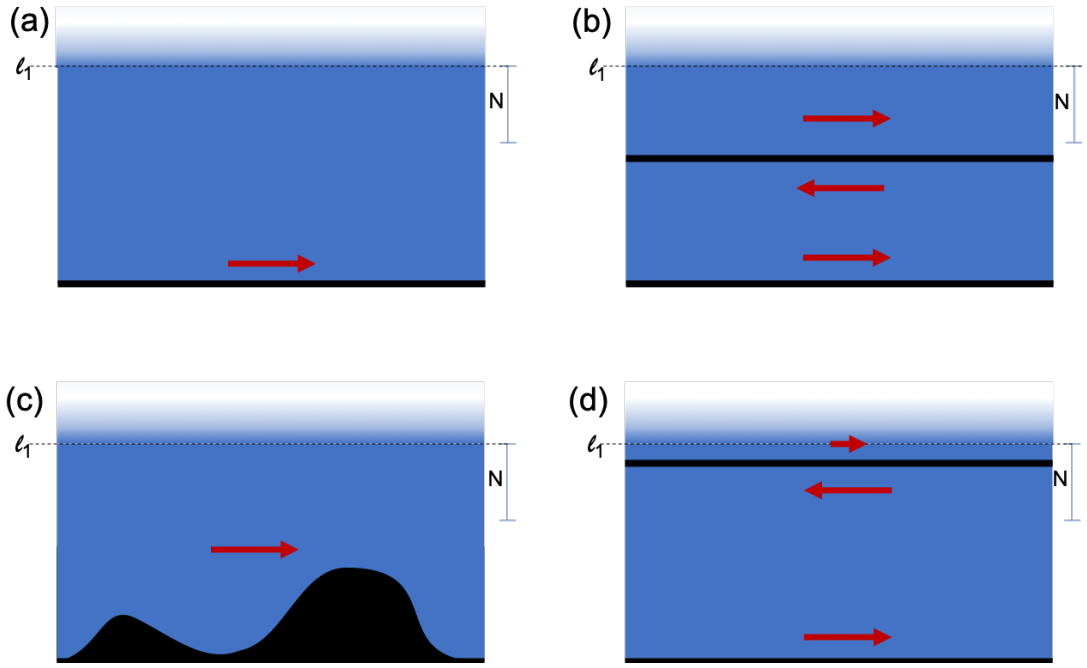

FIGURE 3.E.1: An illustration of the stability of the flow. When the initial state has uniform density below the line ℓ_1, our N cycle flow is only sensitive to perturbations occurring in the region above $\ell_1 - N$. For large N, the initial density configurations (a), (b), and (c) will have the same N cycle transport despite having drastic differences in R matrices (e.g. by introducing new edges in the system drawn in black above). On the other hand, panel (d) will have a reduced N cycle flow, since, in contrast with panel (b), the partially filled area on the upper part of the new edge will not be enough to cancel the flow below it.

dynamics given by R_M of the form:

$$R_M(\mathbf{r},\mathbf{r}') = \begin{cases} \tilde{R} & r_y, r_y' \leq \ell_1 - (N+1) \\ R_{cyc} & \ell_1 - (N+1) \leq r_y, r_y' \leq \ell_2 + (N+1) \\ \tilde{R}' & r_y, r_y' \geq \ell_2 + (N+1) \\ 0 & \text{otherwise} \end{cases} \tag{3.74}$$

where $\tilde{R}, \tilde{R}'$ are real matrices such that R_M is doubly stochastic, i.e. R_M is identical to R_{cyc} in the bulk but modified near the boundary. We now calculate the flow for this new matrix R_M and show it is equivalent to that of R_{cyc}. The situation is illustrated in figure 3.E.1.

Following Eq. 3.48, we find the flow for R_M is

$$F_N = \frac{1}{NL_x} i\partial_\theta \langle \mathbf{I}| R_M^N(\theta) G |\mathbf{I}\rangle \tag{3.75}$$

where we have added the counting field such that $[R_M(\theta)]_{\alpha\beta} = [R_M]_{\alpha\beta}\, e^{-i(\beta_x - \alpha_x)\theta}$ with $\alpha = (\alpha_x, \alpha_y)$ and $\beta = (\beta_x, \beta_y)$. Defining a matrix which is only modified in the bottom edge,

$$R_M'(\mathbf{r},\mathbf{r}') = \begin{cases} \tilde{R} & r_y, r_y' \leq \ell_1 - (N+1) \\ R_{cyc} & r_y, r_y' \geq \ell_1 - (N+1) \\ 0 & \text{otherwise} \end{cases} \tag{3.76}$$

we note that

$$R_M^N G = R_M'^N G \tag{3.77}$$

This is because the only non-zero contributions to $R_M^N G$ come from terms at $r_y, r_y' \leq \ell_2 + N$, hence we are free to replace $\tilde{R}' \to R_{cyc}$ in the region $r_y, r_y' > \ell_2 + N$ without changing the result. Combining eq. 3.75 with 3.77 and following the rest of the steps in eq. 3.48 we find

$$F_N = \frac{1}{NL_x} \sum_{m=0}^{N-1} \langle \mathbf{I}| J_M' \left[R_M'^m(\theta = 0), G \right] |\mathbf{I}\rangle + \frac{1}{L_x} \langle \mathbf{I}| J_M' G |\mathbf{I}\rangle \tag{3.78}$$

where $J_M^{'}$ is the current associated with $R_M^{'}$.

Similar to 3.51, we find

$$\left[R_M^{'m}(\theta=0), G\right] = \left[R_M^{'m}(\theta=0), G\right] P_{S_m}. \tag{3.79}$$

Note that in the region S_m, $R_M^{'}$ is identical to R_{cyc}. We therefore have

$$\left[R_M^{'m}(\theta=0), G\right] P_{S_m} = \left[R_{cyc}^{m}(\theta=0), G\right] P_{S_m} = \left[R_B^{m}(\theta=0), G\right] P_{S_m} \tag{3.80}$$

Repeating the steps that led to 3.57, we find

$$F_N = \frac{1}{NL_x}\sum_{m=0}^{N-1}\langle \mathbf{I}|J_B P_{S_m} R_B^m G|\mathbf{I}\rangle + \frac{1}{NL_x}\sum_{m=0}^{N-1}\langle \mathbf{I}|J_M^{'} P_{y<\ell_1-m}|\mathbf{I}\rangle \tag{3.81}$$

Note, the first term in 3.81 is equivalent to the F_{bulk} contribution for R_{cyc}. We will now show that $\frac{1}{NL_x}\sum_{m=0}^{N-1}\langle \mathbf{I}|J_M^{'} P_{y<\ell_1-m}|\mathbf{I}\rangle$ is equivalent to the F_{edge} contribution from R_{cyc}.

Note,

$$\begin{aligned}\frac{1}{NL_x}\sum_{m=0}^{N-1}\langle \mathbf{I}|J_M^{'} P_{y<\ell_1-m}|\mathbf{I}\rangle &= \frac{1}{NL_x}\sum_{m=0}^{N-1}\langle \mathbf{I}|J_M^{'} P_{\ell_1-N+m>y>\ell_1-N}|\mathbf{I}\rangle + \frac{1}{L_x}\langle \mathbf{I}|J_M^{'} P_{y<\ell_1-N}|\mathbf{I}\rangle \\ &= \frac{1}{NL_x}\sum_{m=0}^{N-1}\langle \mathbf{I}|J P_{\ell_1-N+m>y>\ell_1-N}|\mathbf{I}\rangle + \frac{1}{L_x}\langle \mathbf{I}|J_M^{'} P_{y<\ell_1-N}|\mathbf{I}\rangle \\ &= \frac{1}{L_x}\langle \mathbf{I}|J_M^{'} P_{y<\ell_1-N}|\mathbf{I}\rangle\end{aligned} \tag{3.82}$$

where in the second and third lines we have used the fact that $J_M^{'}$ is identical to J for $y > \ell_1 - N$ and that R_{cyc} has no bulk transport implies $\langle \mathbf{I}|J P_{\ell_1-N+m>y>\ell_1-N}|\mathbf{I}\rangle = 0$. Furthermore,

$$\frac{1}{L_x}\langle \mathbf{I}|J_M^{'} P_{y<\ell_1-N}|\mathbf{I}\rangle = \frac{1}{L_x}\langle \mathbf{I}|J_M^{'}\left(I - P_{y>\ell_1-N}\right)|\mathbf{I}\rangle \tag{3.83}$$

We now restrict ourselves to the case where $\langle \mathbf{I}|J_M^{'}|\mathbf{I}\rangle = 0$, i.e. no net current in the uniform density state. Note, this is the case when R is a product of bi-stochastic symmetric matrices, which includes many of the most natural perturbations near the

boundary (random potentials, removed sites, variation in hopping amplitude or measurement step timing, etc.). In this case, we find

$$\frac{1}{L_x}\langle \mathbf{I}|J_M^{'}\left(I-P_{y>\ell_1-N}\right)|\mathbf{I}\rangle = -\frac{1}{L_x}\langle \mathbf{I}|J_M^{'}P_{y>\ell_1-N}|\mathbf{I}\rangle = -\frac{1}{L_x}\langle \mathbf{I}|JP_{y>\ell_1-N}|\mathbf{I}\rangle \\ = \frac{1}{L_x}\langle \mathbf{I}|JP_{y\leq 2}|\mathbf{I}\rangle = F_{edge} \tag{3.84}$$

We thus have that flow is unaffected by arbitrary evolution near the boundary. It is only dependant on the bulk properties of the evolution. Note, this argument also holds if R_{cyc} is replaced by R_{nz}, the dynamics in the near Zeno case. In other words, transport is completely protected even (to first order) away from the Zeno limit. In fact, numerical simulations suggest that edge transport is unaffected by perturbations near the boundary even in the low frequency measurement regime. Proof of this, however, is still a work in progress.

3.F The Near-Zeno Approximation: Derivation of R_{nz}

Our starting point is Eq. (3.12). Let us now include terms of order up to $O(\tau^2)$, and rewrite it as

$$\Pi_{A_i}(U\otimes\bar{U})\Pi_{A_i} = \Pi_{A_i} - i\tau\left[H_{A_i}\otimes P_{A_i} - P_{A_i}\otimes H_{A_i}\right] \\ -\frac{\tau^2}{2}\Pi_{A_i}\left[H\otimes I - I\otimes H\right]^2\Pi_{A_i} + O(\tau^3) \\ = \Pi_{A_i}(U_{A_i}\otimes\bar{U}_{A_i})\Pi_{A_i} - \tau^2\zeta_{A_i}(H) + O(\tau^3) \tag{3.85}$$

where

$$\zeta_{A_i}(H) = \frac{1}{2}\Pi_{A_i}\left[H^2\otimes I + I\otimes H^2 - 2H\otimes H\right]\Pi_{A_i} \\ -\frac{1}{2}\left[H_{A_i}^2\otimes P_{A_i} + P_{A_i}\otimes H_{A_i}^2 - 2H_{A_i}\otimes H_{A_i}\right] \tag{3.86}$$

From this we find

$$\begin{aligned}
&\Pi_{A_{i+1}} \left(\Pi_{A_i}(U\otimes\bar{U})\Pi_{A_i}\right)^n \Pi_{A_{i-1}} \\
&= \Pi_{A_{i+1}} \left(\Pi_{A_i}(U_{A_i}\otimes\bar{U}_{A_i})\Pi_{A_i} - \tau^2\zeta_{A_i}(H)\right)^n \Pi_{A_{i-1}} + O(n\tau^3) \\
&= \Pi_{A_i\cap A_{i+1}}(U_{A_i}^n\otimes\bar{U}_{A_i}^n)\Pi_{A_i\cap A_{i-1}} \\
&-\tau^2\Pi_{A_i\cap A_{i+1}}\sum_{m=0}^{n-1}(U_{A_i}^m\otimes\bar{U}_{A_i}^m)\zeta_{A_i}(H)(U_{A_i}^{n-1-m}\otimes\bar{U}_{A_i}^{n-1-m})\Pi_{A_i\cap A_{i-1}} + O(\tau^3 n) \qquad (3.87)
\end{aligned}$$

The first term in (3.87) corresponds to the evolution in the Zeno limit and generates the operation R_i on the diagonal of G (as is explained in the Zeno Limit Section). The second term, as will be shown, corresponds to the $\tilde{R}_i$ operations on the diagonal of G.

To see this, we start by noting that the operator $\Pi_{A_i\cap A_{i+1}}$ kills the correlations between every pair of sites, unless both sites are within $A_i\cap A_{i+1}$. Hence, off-diagonal elements of G are only generated if $(U_{A_i}^m\otimes\bar{U}_{A_i}^m)\zeta_{A_i}(H)(U_{A_i}^{n-1-m}\otimes\bar{U}_{A_i}^{n-1-m})$ can generate correlations between the elements of $A_i\cap A_{i+1}$. The operators $(U_{A_i}\otimes\bar{U}_{A_i})$ can only generate correlations within the neighboring pairs inside of A_i. Now, note that the neighboring pairs within A_i are separated by at least 3 edges. Therefore, to generate correlations between the neighboring pairs using a power of H, i.e. H^ν, we must have at least $\nu\geq 3$. $\zeta_{A_i}(H)$, on the other hand, contains H with a power of at most 2. It follows then that neither $\zeta_{A_i}(H)$ nor $(U_{A_i}\otimes\bar{U}_{A_i})$ can generate correlations between the adjacent pairs in A_i. Hence, any correlations generated by $(U_{A_i}^m\otimes\bar{U}_{A_i}^m)\zeta_{A_i}(H)(U_{A_i}^{n-1-m}\otimes\bar{U}_{A_i}^{n-1-m})$ will be subsequently killed by $\Pi_{A_i\cap A_{i+1}}$. We thus again have that the evolution of G may be described fully by the dynamics of the diagonal of G. Furthermore, we may replace $\Pi_{A_i\cap A_{i+1}}$ in (3.87) with an operator that simply kills all correlations, namely $\sum_a P_a\otimes P_a$.

At this point in the analysis, there are two cases for the action of $(U_{A_i}\otimes\bar{U}_{A_i})$ which we will now consider. For sites in A_i^c and for sites in A_i without a neighboring site also in A_i (see Fig. 3.F.1), $(U_{A_i}\otimes\bar{U}_{A_i})$ simply acts as an identity. On the other hand, for sites in A_i with a neighboring site also in A_i, $(U_{A_i}\otimes\bar{U}_{A_i})$ will induce Rabi oscillations within the neighboring pair inside of A_i.

We further note that, for any given site b, the near-Zeno term in (3.87) only induces an interaction between b, the closest element or pair in A_i to b, and other nearest neighbors to this element/pair in A_i (see Fig. 3.F.1). This is by nature of the fact that the

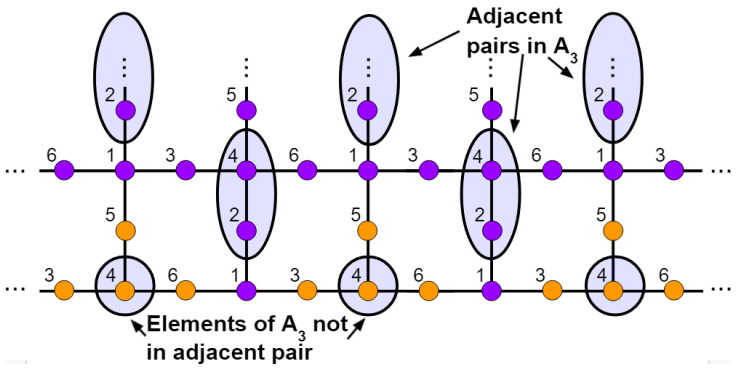

FIGURE 3.F.1: For any given A_i, here we take without loss of generality $i = 3$, some elements of A_i have a neighbor also in A_i. Other sites in A_i have no such nearest neighbor. As described in Appendix 3.F, all sites evolve in the near-Zeno approximation in one of two ways. Lone sites in A_i and nearest neighbors to lone sites in A_i (as shown in orange) exhibit an evolution given by case 1 of the near-Zeno term of (3.87). However, the evolution for sites that are in an adjacent pair in A_i or neighboring an adjacent pair in A_i (shown in purple), are governed by case 2.

$H^2 \otimes I$ and $I \otimes H^2$ terms (the only terms that act non-trivially on sites outside of A_i) in $\zeta_{A_i}(H)$ are sandwiched by Π_{A_i}, and so can only affect nearest neighbors to any given element of A_i. We therefore find that we have two disjoint sets of sites, as given in Fig. 3.F.1, that are affected by the near-Zeno term in (3.87) differently.

Case 1: Here (Orange Sites in Fig. 3.F.1), the second term in Eq. (3.87) becomes

$$\begin{aligned} &-\tau^2 \sum_a (P_a \otimes P_a) \sum_{m=0}^{n-1} \zeta_{A_i}(H) \sum_b (P_b \otimes P_b) \\ &= -n\tau^2 \sum_{a,b} (P_a \otimes P_a)\, \zeta_{A_i}(H)\, (P_b \otimes P_b) \end{aligned} \tag{3.88}$$

We now simplify to find

$$\begin{aligned}
&\sum_{a,b} (P_a \otimes P_a)\, \zeta_{A_i}(H)\, (P_b \otimes P_b) \\
&= \sum_{a,b} (P_a \otimes P_a) \left\{ \frac{1}{2} \Pi_{A_i} \left[H^2 \otimes I + I \otimes H^2 - 2H \otimes H \right] \Pi_{A_i} \right. \\
&\left. -\frac{1}{2} \left[H_{A_i}^2 \otimes P_{A_i} + P_{A_i} \otimes H_{A_i}^2 - 2H_{A_i} \otimes H_{A_i} \right] \right\} (P_b \otimes P_b) \\
&= \sum_a \deg(a)\, (P_a \otimes P_a) - \sum_{a,b} P_a H P_b \otimes P_a H P_b
\end{aligned} \tag{3.89}$$

where we have used the fact that $H_{A_i} = P_{A_i} H P_{A_i} = 0$ since in case 1 no element of A_i has a nearest neighbor also in A_i.

This implies that $\tilde{R}_i$ is given by

$$\textbf{Case 1: } \left[\tilde{R}_i\right]_{ab} = \begin{cases} deg(a) & \text{for } a = b \\ -1 & \text{for } a, b \text{ nearest neighbors} \\ 0 & \text{Otherwise} \end{cases} \tag{3.90}$$

Case 2: Here (purple sites in Fig. 3.F.1), note that $U_{A_i} \otimes \bar{U}_{A_i} = e^{-i\tau O}$ where we have defined

$$O \equiv H_{A_i} \otimes P_{A_i} - P_{A_i} \otimes H_{A_i}. \tag{3.91}$$

Furthermore, the following relations hold

$$O^2 = 2(P_{A_i} \otimes P_{A_i} - H_{A_i} \otimes H_{A_i}) \equiv 2E, \tag{3.92}$$

$$OE = 2O, \tag{3.93}$$

where we have defined E in the first line and used the fact that H_{A_i} simply acts like the pauli matrix σ_x for nearest neighbors in the subspace A_i, i.e. $H_{A_i}^2 = P_A$.

It then follows that

$$U_{A_i} \otimes \bar{U}_{A_i} = e^{-i\tau O} = \left(\frac{E}{2} - \frac{E}{2}\right) + 1 - 2i\tau\frac{O}{2} - (2\tau)^2\frac{E}{2} + \frac{i}{3!}(2\tau)^3\frac{O}{2} + \ldots$$
$$= \left(1 - \frac{E}{2}\right) + \frac{E}{2}\cos 2\tau - i\frac{O}{2}\sin 2\tau \tag{3.94}$$

We therefore find

$$\sum_{m=0}^{n-1}(U_{A_i}^m \otimes \bar{U}_{A_i}^m)\zeta_{A_i}(H)(U_{A_i}^{n-1-m} \otimes \bar{U}_{A_i}^{n-1-m})$$
$$= \sum_{m=0}^{n-1}\left[\left(1 - \frac{E}{2}\right) + \frac{E}{2}\cos 2m\tau - i\frac{O}{2}\sin 2m\tau\right]\zeta_{A_i}(H)$$
$$\times \left[\left(1 - \frac{E}{2}\right) + \frac{E}{2}\cos 2m\tau + i\frac{O}{2}\sin 2m\tau\right]\left(U_{A_i}^{n-1} \otimes \bar{U}_{A_i}^{n-1}\right)$$
$$= \left[n\left(1 - \frac{E}{2}\right)\zeta_{A_i}(H)\left(1 - \frac{E}{2}\right) + \frac{n}{2}\frac{E}{2}\zeta_{A_i}(H)\frac{E}{2} + \frac{n}{2}\frac{O}{2}\zeta_{A_i}(H)\frac{O}{2}\right](1 - E) + O(1) \tag{3.95}$$

where in the last line we have restricted ourselves to the perfect switching cycle, i.e. $n\tau = \frac{\pi}{2}$, and neglected any terms in the sum that are not at least $O(n)$.

It is now convenient to rewrite $\zeta_{A_i}(H)$:

$$\zeta_{A_i}(H) = \frac{1}{2}\Pi_{A_i}\left[H^2 \otimes I + I \otimes H^2 - 2H \otimes H\right]\Pi_{A_i} - \frac{1}{2}\left[H_{A_i}^2 \otimes P_{A_i} + P_{A_i} \otimes H_{A_i}^2 - 2H_{A_i} \otimes H_{A_i}\right]$$
$$= \frac{1}{2}\Pi_{A_i}\left[H^2 \otimes I + I \otimes H^2 - 2H \otimes H\right]\Pi_A - E \equiv Z - E \tag{3.96}$$

where Z has been defined in the last line. We may now combine Eqs. (3.95) and (3.96) to find

$$\sum_{m=0}^{n-1}(U_A^m \otimes \bar{U}_A^m)\zeta(H)(U_A^{n-1-m} \otimes \bar{U}_A^{n-1-m})$$

$$= \left[n\left(1-\frac{E}{2}\right)(Z-E)\left(1-\frac{E}{2}\right) + \frac{n}{2}\frac{E}{2}(Z-E)\frac{E}{2} + \frac{n}{2}\frac{O}{2}(Z-E)\frac{O}{2}\right](1-E) + O(1)$$

$$= n\left[Z - \frac{EZ}{2} - \frac{ZE}{2} + \frac{3}{8}EZE + \frac{1}{8}OZO - E\right](1-E) + O(1)$$

$$= n\left[Z + E - \frac{1}{2}\{E,Z\} + \frac{1}{8}EZE - \frac{1}{8}OZO\right] + O(1) \tag{3.97}$$

where $\{E,Z\} = EZ + ZE$ is the anti-commutator.

Now, combining Eqs. (3.87) and (3.97), we find that the near-Zeno term in (3.87) becomes

$$-n\tau^2 \sum_{a,b}(P_a \otimes P_a)\left[Z + E - \frac{1}{2}\{E,Z\} + \frac{1}{8}EZE - \frac{1}{8}OZO\right](P_b \otimes P_b) \tag{3.98}$$

Considering each of the terms in (3.98), we have

$$\sum_{a,b}(P_a\otimes P_a)\,Z\,(P_b\otimes P_b)=\sum_a \deg(a)\,(P_a\otimes P_a)-\sum_{a,b}P_aHP_b\otimes P_aHP_b \tag{3.99}$$

$$\sum_{a,b}(P_a\otimes P_a)\,E\,(P_b\otimes P_b)=\sum_{a\in A_i}P_a\otimes P_a-\sum_{a,b\in A_i}P_aHP_b\otimes P_aHP_b \tag{3.100}$$

$$\begin{aligned}\sum_{a,b}(P_a\otimes P_a)\left[-\frac{1}{2}\{E,Z\}\right](P_b\otimes P_b)&=-\sum_{a\in A_i}[\deg(a)+1]\,(P_a\otimes P_a)\\&+\sum_{a,b\in A_i}\left(2+\frac{\deg(a)+\deg(b)}{2}\right)P_aHP_b\otimes P_aHP_b\\&+\frac{1}{2}\sum_{a\in A_i^c,b\in A_i}(P_aHP_b\otimes P_aHP_b+h.c.)\\&-\frac{1}{2}\sum_{a\in A_i^c,b\in A_i}\left(P_aHH_{A_i}P_b\otimes P_aHH_{A_i}P_b+h.c.\right)\end{aligned} \tag{3.101}$$

$$\sum_{a,b}(P_a\otimes P_a)\left[\frac{1}{8}EZE\right](P_b\otimes P_b)=2\sum_{a\in A_i}P_a\otimes P_a-2\sum_{a,b\in A_i}P_aHP_b\otimes P_aHP_b \tag{3.102}$$

$$\sum_{a,b}(P_a\otimes P_a)\left[-\frac{1}{8}OZO\right](P_b\otimes P_b)=-2\sum_{a\in A_i}P_a\otimes P_a+2\sum_{a,b\in A_i}P_aHP_b\otimes P_aHP_b \tag{3.103}$$

Finally, we therefore have that $\tilde{R}_i$ becomes

$$\textbf{Case 2: }\left[\tilde{R}_i\right]_{ab}=\begin{cases}deg(a) & \text{for } a=b\in A_i^c\\ -1 & \text{for } a,b\in A_i^c \text{ and nearest neighbors}\\ -\frac{1}{2} & \text{for } \left(a\in A_i \text{ and } b \text{ neighbors the adjacent pair in } A_i\right.\\ & \left.\text{ that includes } a\right) \text{ or vice versa}\\ \frac{\deg(a)+\deg(b)}{2} & \text{for } a,b\in A_i \text{ and nearest neighbors}\\ 0 & \text{Otherwise}\end{cases} \tag{3.104}$$

Now, Eqs. (3.90) and (3.104) may be combined to find the full $\tilde{R}_i$. Note, on the seem between case 1 and case 2, for example the element $\left[\tilde{R}_i\right]_{ab}$ with a as an orange site in Fig. 3.F.1 and b as a blue site, case 1 and case 2 match as required for consistency. Namely, the element $\left[\tilde{R}_i\right]_{ab}=-1$ if a,b are nearest neighbors, and 0 otherwise.

Furthermore, note that $\tilde{R}_i$ is a Zero Line-Sum matrix. Hence, the rows and columns of $R_{nz,i} = R_i - n\tau^2\tilde{R}_i$ sum to 1. Furthermore, this implies the rows and columns of R_{nz} also sum to 1 as required for the usage of Eq. (3.30).

3.G Deterministic Hopping

Evolution in the Zeno Limit with perfect swapping is deterministic. Thus edge transport and bulk localization can be seen directly.

Figure 3.G.1 shows a Lieb lattice with two layers of dynamical unit cells in the y direction and infinitely many in the x direction. The following gives the transport of a particle beginning at any given site after one complete measurement cycle (represented by arrows). Note, after no more than 5 measurement cycles, each particle returns to either its initial position or its initial position shifted by one dynamical unit cell to the right or left.

Periodic Boundary Conditions:

- $1 \to 1$
- $2 \to 12e^{ik_x} \to 5 \to 4 \to 3 \to 2$
- $6 \to 11 \to 10 \to 9 \to 8 \to 6$
- $7 \to 7$

where e^{-ik_x} indicates a shift by one unit cell to the right. Note that after 5 measurement cycles every particle returns to its initial position in agreement with $R_{cyc}(k,\theta)^5 = I$ as described below Eq. (3.28). Now turning to open boundary conditions.

Open Boundary Conditions:

- $1 \to 6 \to 1e^{-ik_x}$
- $2 \to 12e^{ik_x} \to 5 \to 4 \to 3 \to 2$

- $7 \to 7$
- $8 \to 11e^{ik_x} \to 10e^{ik_x} \to 9e^{ik_x} \to 8e^{ik_x}$

Note here that, in contrast to the periodic boundary conditions, there is particle transport in the x direction. Namely, particles at sites 1 and 6 shift to the right by one unit cell every 2 measurement cycles, and particles at 8, 9, 10, and 11 shift to the left one unit cell every 4 measurement cycles.

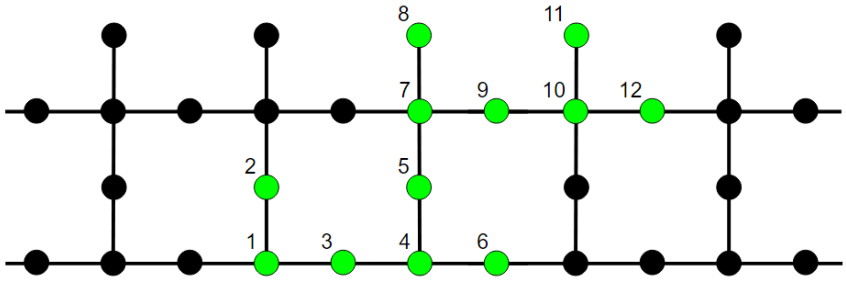

FIGURE 3.G.1: Lieb lattice with two layers of dynamical unit cells in the y-direction. The bottom and top of the lattice represent a "flat" and "jagged" edge configuration respectively.

Chapter 4

Arrested Development and Fragmentation in Strongly-Interacting Floquet Systems

4.1 Introduction

As experimental tools have progressed (e.g. [142, 143]), the microscopic control of quantum systems has become increasingly accessible. These advancements, along with a correlated increase in theoretical interest, have led to the discovery of many new and surprising phenomena that emerge when periodic driving, interactions, and their interplay are considered.

For example, periodically driven systems can be used to stabilize otherwise unusual behavior. A recent important example is topological Floquet insulators [14, 86, 144], where novel topological features of the band structure may emerge due to inherent periodicity of the non-interacting quasi- energy spectrum. Furthermore, it was shown in [15] that, by combining spatial disorder with a topological Floquet insulator model introduced by Rudner-Lindner-Berg-Levin (RLBL) [20], a new topological phase may be realized called the anomalous Floquet-Anderson insulator (AFAI). Discrete time crystals [12, 13, 145, 146] are another important example of behavior that may occur in periodically driven, but not static [147], systems. Namely, a time crystal is a system where time-translation symmetry is spontaneously broken (in analogy to spatial translation symmetry spontaneously breaking to form ordinary crystals).

Combining periodic driving with interactions, however, can often be problematic as generic, clean, interacting Floquet system are expected to indefinitely absorb energy

from their drive and thus quickly converge to a featureless infinite temperature state [148–150]. This problem may be side-stepped by considering Many-Body Localization (MBL) [27, 145, 150–154], in which strong disorder is utilized to help stave off thermalization, by considering the effective evolution of pre-thermal states [26, 28, 155–158] that, in the best cases, take exponentially long to thermalize, or by connecting the system to a bath to facilitate cooling and arrive at interesting, non- equilibrium steady-states [29, 159–161].

Yet another route for realizing non-trivial dynamics despite the expected runaway heating from interacting, Floquet drives is to consider systems where the ergodicity is weakly broken, i.e. where there are subspaces (whose size scales only polynomially in the system size) of the Hilbert space that do not thermalize despite the fact that the rest of the Hilbert space does. These non-thermal states are called quantum many-body scars [162–164] and have been shown to support many interesting phenomena including, for example, discrete time crystals [165]. Furthermore, in constrained systems, the full Hilbert space may fragment into subspaces where some of the subspaces thermalize while others do not [164, 166, 167]. When the fraction of non-thermal states are a set of measure zero in the thermodynamic limit, the system is an example of quantum many-body scarring. However, in other cases, the non-thermal subspaces form a finite fraction of the full Hilbert space and therefore correspond to a distinct form of ergodicity breaking.

In addition to leading to heating, interactions are also often responsible for our inability to efficiently study or describe many body quantum states in both Floquet and static Hamiltonian systems. However, there are situations when interactions play the opposite role in creating specialized states of particular simplicity or utility. For example, systems with interactions can exhibit counter-intuitive bound states due to coherent blocking of evolution. A nice class of such systems are the edge-locked few particle systems studied in [168, 169].

In this work, we consider Floquet drives where hopping between neighboring pairs of sites are sequentially activated. The theoretical and experimental tractability of such models have made them a popular workhorse for fleshing out a broad range of the exciting properties of periodically driven systems (e.g. [20, 170–174]). We find that, when interactions are added to such systems, there exist special values of interaction strength and driving frequency where the dynamics becomes exactly solvable. Furthermore, the complete set of these special parameter values may be determined via

emergent Diophantine equations [175]. At other parameter values, the Hilbert space is fragmented. Initial states contained within some, thermal, subspaces will ergodically explore the subspace (though not the entire Hilbert space), while other initial states contained within other, non-thermal, subspaces will evolve according to a classical cellular automation (CA) [176, 177], i.e. the system evolves in discrete time steps where after each step the occupancy of any given site is updated deterministically based on a small set of rules determined by the occupancy of neighboring sites.

As examples, we consider RLBL(-like) models with added nearest neighbor (NN) or Hubbard interactions as well as an even-odd Floquet drive in one dimension with NN interactions (more detailed descriptions of these models given below). We note that some work has been done in the first two cases [42, 43] where it was argued that novel, MBL anomalous Floquet insulating phases emmerged when a disorder potential was added. We will discuss how our focus on special parameter values leads to new insights into these models and how it suggests a possible route towards other exciting phenomena such as the support of discrete time crystals within fragments of the Hilbert space.

4.2 Conditions for evolution by Fock state permutations

In this section, we examine conditions for deterministic evolution of Fock states into Fock states in fermion models. Here we consider real space Fock states, which have a well defined fermion occupation on each lattice site (We will also refer to such states as fermion product states). We consider models where hopping between non-overlapping selected pairs of sites is sequentially activated. Two models of this type, discussed in detail below, deal with Hubbard and nearest neighbour interactions. The approach can be naturally extended to deal with more general interactions in sequentially applied evolution models.

4.2.1 Example 1: Hubbard-RLBL

As a particularly illuminating example, consider the Rudner-Lindner-Berg-Levin model [20]. This model is an exact toy model for a topological Floquet insulator and has been very useful in flushing out some of their salient properties. In addition, it provides the starting point for other states, such as the anomalous Floquet-Anderson insulators [15].

The model is two dimensional, however, it's simplicity lies in its similarity to even-odd type models, [170, 172–174], in that the evolution activates disjoint pairs of sites at each stage. The model can be tuned to a particular point where the stroboscopic evolution of product states is deterministic exhibiting bulk periodic motion and edge propagation. Similarly, one can tune the driving frequency to completely freeze the stroboscopic evolution. Here, we add interactions to the model and ask when we can make the evolution a product state permutation, at least in some sectors. The Hubbard-RLBL evolution is written as

$$U = U_{wait} U_4 U_3 U_2 U_1 \tag{4.1}$$

where $U_i(V, \tau) = e^{-i\tau H_i}$. For $i = 1, ..4$,

$$\mathcal{H}_i = -t_{hop} \sum_{(i,j)\in A_i;\sigma} (a^\dagger_{i,\sigma} a_{j,\sigma} + h.c.) + V \sum_{i\in A_i} n_{i,\uparrow} n_{i,\downarrow} \tag{4.2}$$

where $n_{i,\sigma} = a^\dagger_{i,\sigma} a_{i,\sigma}$ and the sets A_i are described in Fig. 1. Throughout the rest of the paper we will work in units where $t_{hop} = 1$ and $\hbar = 1$.

Above, U_{wait} is any unitary diagonal in number state basis. For example, the model investigated in [43] has $U_{wait} \to U_{dis}$ where U_{dis} corresponds to evolution under the Hamiltonian $\mathcal{H}_{dis} = \sum_i v_i (n_{i,\uparrow} + n_{i,\downarrow})$ with v_i a vector of uniformly distributed random real numbers within the bounded interval $[-W, W]$, i.e. the waiting period corresponds to evolution with a disordered on-site potential and no hopping [1]. In that work, it was shown that this model supports a new family of few-body topological phases characterized by a hierarchy of topological invariants. These results may be viewed from the following perspective. First, finely-tuned points where the dynamics is exactly solvable were studied (namely, $\tau = \frac{\pi}{2}$ and $V = 0$ or $V \to \infty$). Second, it is argued that regions near these special points are stabilized (i.e. localized, at least for finite particle number cases) by disorder leading to robust phases. Finally, topological invariants characterizing these phases (V small vs. V large) can be found and shown to be distinct implying two differing topological phases. An application of the methods we propose in this work will allow us to generalize the first step above and find families of these exactly solvable points. We leave discussions of when regions in parameter

[1] Technically, in [43] a weak disorder potential is added during the U_i steps and then the disorder strength during the wait step is effectively made stronger by increasing the length of time the wait step is applied. However, this slight difference in how the disorder potential is applied does not seriously alter the dynamics and so we will not make a hard distinction between the two.

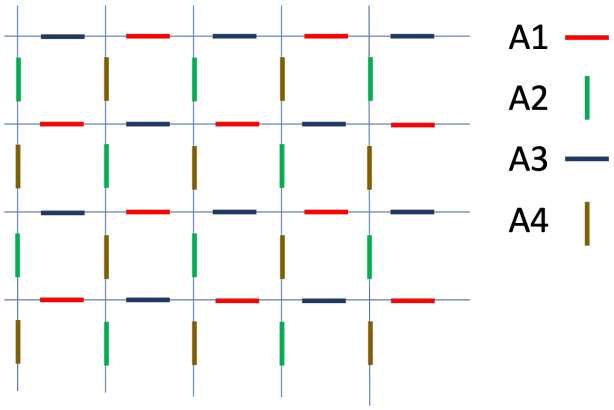

FIGURE 1: The RLBL model. Hopping is sequentially activated among neighbouring sites connected in the set A_i, $i = 1, ..., 4$.

space near these points may or may not be stabilized by disorder to future work. Since, at these exactly solvable points, we will be mapping product states to product states, U_{dis} will only act as an unobservable global phase and thus for the rest of our analysis we will set $U_{wait} = I$.

We now look for conditions to simplify the evolution (4.1) in such a way that the total evolution reduces to a permutation on the set of product states, i.e. when an initial configuration of fermions is placed at a selection of locations it will evolve into a different assignment of locations without generating entanglement.

To do so, we note that the evolution of each pair of sites, may be considered separately due to the disjoint nature of the set of pairs A_i. Thus, we consider the evolution on a pair of sites i, j

$$U_{(i,j)}(V, \tau) = e^{-i\tau(a^\dagger_{i,\sigma}a_{j,\sigma} + h.c.) + \tau V(n_{i,\uparrow}n_{i,\downarrow} + n_{j,\uparrow}n_{j,\downarrow})}. \tag{4.3}$$

Since the evolution preserves particle number, we can treat the sub-spaces of $0, 1, 2, 3$, and 4 particles in each neighboring pair of sites separately. In the case of 0 or 4 particles, evolution is trivially the identity (due to Pauli blocking in the 4 particle case). For 1 or 3 particles, one of the two sites is always doubly occupied, and thus the interaction term in (4.2) is a constant and does not affect evolution. In this case, solving the two site non-interacting evolution we see that in the one-particle sector, a fermion starting initially at site i has a probability $p = \sin^2 \tau$ to hop to the other site in pair j and probability $1 - p$ to stay. Similarly, in the 3-particle sector, an initially placed hole in site i has the

same probability, p to hop to the other site j. Thus, when

$$\tau = \frac{\pi}{2}\ell \tag{4.4}$$

for some integer ℓ, evolution for initial product states in the 1,3 particle subspace is completely deterministic with trivial evolution for even ℓ and the particle hopping to the other site in the pair with probability 1 (henceforth referred to as perfect swapping) when ℓ is odd. Clearly, for these values of τ (and independently of V), no new entanglement is created in any pairs with 1 or 3 particles. To render the evolution in the 2 particle pair subspace simple, it is shown in appendix 4.A.1 that deterministic evolution occurs when the two conditions below are simultaneously satisfied:

$$\tau\sqrt{4^2 + V^2} = 2\pi m \tag{4.5}$$

and

$$\frac{1}{2}\tau V + \pi m = \pi n \tag{4.6}$$

with $n, m \in \mathbb{Z}$. Note that (4.5) guarantees the preservation of the number of doubly occupied sites (doublons). When n is even, the sub-system will return to its initial state. On the other hand, if n is odd, the system will exhibit perfect swapping i.e. each particle will hop to the other site in the pair. By solving for τ and V in terms of n and m, we may now summarize when evolution is deterministic in each of the particle number sub-spaces:

particles	τ	V
1 or 3	$\tau = \frac{\pi}{2}\ell$	V arbitrary
2, opposite spins	$\tau = \frac{\pi}{2}\sqrt{2mn - n^2}$	$V = \frac{4(n-m)}{\sqrt{2mn-n^2}}$
otherwise	any	any

(4.7)

when n or ℓ are even (odd) evolution is frozen (perfect swapping). To keep the solutions real, Eq. 4.7 also implies we must take $2mn - n^2 > 0$.

Can all the conditions (4.4), (4.5), and (4.6) be simultaneously satisfied? In such a case the evolution of $\mathcal{U}$ is simply a permutation (being a product of identities and site swaps) and generates no new entanglement in any of the sectors.

4.2.2 The Diophantine Equation

Combining the conditions (4.4), (4.5), and (4.6) together yields the following equation:

$$\ell^2 + n^2 = 2mn.\ \ell, n, m \in \mathbb{Z} \tag{4.8}$$

Eq. (4.8) is a homogeneous Diophantine equation of degree 2 and can be solved.

We now give a brief review of Diophantine equations and the strategy for solving homogeneous quadratic equations. A reader familiar with Diophantine equations or interested only in the concrete results may skip to the next subsection.

Diophantine equations are algebraic (often polynomial) equations of several unknowns where only integer or rational solutions are of interest. They are named in honor of Diophantus of Alexandria for his famous treatise on the subject written in the 3rd century though the origins of Diophantine equations can be found across ancient Babylonian, Egyptian, Chinese, and Greek texts [175]. Despite their often innocuous appearance, they are an active area of research with solutions frequently requiring surprisingly sophisticated mathematical techniques and have been the centerpiece of several famous, long-standing mathematical problems that have only been (relatively) recently resolved, including Fermat's Last Theorem [178] and Hilbert's Tenth Problem [179].

In this section, we are interested in the relatively simple case of a homogeneous quadratic Diophantine equation, i.e. equation of the form

$$X^T Q X = 0 \tag{4.9}$$

with variables $X^T = (x_0, x_1, ..., x_n)$ and coefficients given by the $n \times n$ symmetric matrix Q with integral diagonal entries and half integral off-diagonal entries. As we shall see, however, for interactions beyond Hubbard a broader class of Diophantine equations may need to be considered. For information on broader classes of Diophantine equations and for more information on the derivation to follow, see, for example, [175].

The general strategy for finding rational (we will specialize to integer solutions for our cases of interest at the end) solutions to (4.9) is to first find a particular solution and then generate all other rational solutions from the particular solution. Particular solutions can be found simply by inspection or through existing efficient algorithms

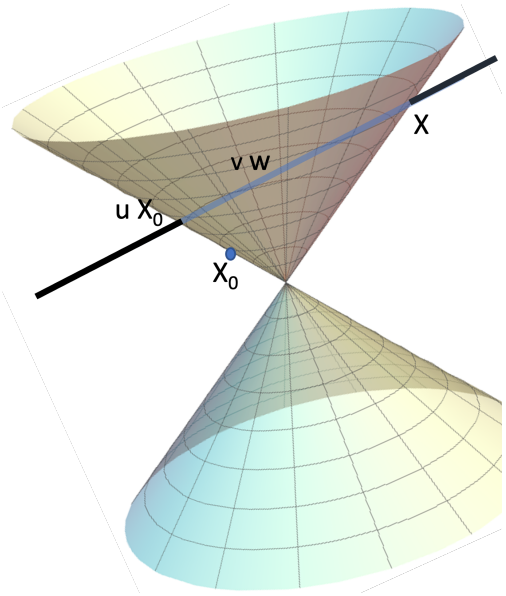

FIGURE 2: Any line passing through the null surface has two points of intersection. Given a particular solution X_0 of the homogeneous Diophantine eq (4.10), other rational solutions are found by looking at lines emanating from uX_0 with rational slopes .

[175]. The main task is then to generate all other rational solutions from a given particular solution.

Take $X_0^T = (x_{0,0}, x_{1,0}, ..., x_{n,0})$ to be a particular solution, i.e.

$$X_0^T Q X_0 = 0. \tag{4.10}$$

Since (4.9) is quadratic, any line through X_0 will intersect the hypersurface defined by (4.9) at a single other point (see Fig. 2). Furthermore, if the line through X_0 is rational (i.e. has rational coefficients), as we see below, this implies that the second intersection point must also be rational. Therefore, it is possible to generate every rational solution to (4.9) by finding the second intersection point of every rational line through uX_0, where u is rational.

Here, since (4.9) is homogeneous, it is convenient to work in projective space $\mathbb{P}_n(\mathbb{Q})$ where a general line passing through X_0 is parameterized by

$$X = uX_0 + vW \tag{4.11}$$

with $(u, v) \in \mathbb{P}_2(\mathbb{Q})$ and any $W = (w_1, .., w_n) \in \mathbb{P}_n(\mathbb{Q})$ not equal to X_0. Combining (4.11) and (4.9),

$$0 = (uX_0 + vW)^T Q(uX_0 + vW) \tag{4.12}$$

$$= v\left(2uW^T QX_0 + vW^T QW\right) \tag{4.13}$$

where we have simplified using (4.10). We may thus take as the solution $(u, v) = \left(W^T QW, -2W^T QX_0\right)$. Combining with Eq (4.11) and multiplying by a general $d \in \mathbb{Q}$ to restore full solutions (since we considered X as an element of a projective space), we find

$$X = d\left[(W^T QW)X_0 - 2(W^T QX_0)W\right]. \tag{4.14}$$

For integer solutions, we need simply to rescale $W \to \frac{W}{\zeta}$ and $d \to d\zeta^2$ where $\zeta = \gcd(w_i)$. After rescaling, the only non-integer information is coming from d, so all integer solutions may be found simply by considering $d \in \frac{1}{\xi}\mathbb{Z}$ with $\xi = gcd((W^T QW)X_0 - 2(W^T QX_0)W)$.

For the relevant case of $n = 3$, let us, without loss of generality, diagonalize $Q = diag(A, B, C)$ and let $W^T = (w_1, w_2, 0)$ where (after rescaling with ζ) w_1 and w_2 are coprime integers and the final element of W may be set to 0 due to the required linear independence with X_0. Simplifying (4.14) then becomes

$$X = d(Aw_1^2 + Bw_2^2)\begin{pmatrix} x_{0,0} \\ x_{1,0} \\ x_{2,0} \end{pmatrix} - 2d(w_1 Ax_{0,0} + w_2 Bx_{1,0})\begin{pmatrix} w_1 \\ w_2 \\ 0 \end{pmatrix} \tag{4.15}$$

$$= d\begin{pmatrix} -(Aw_1^2 - Bw_2^2)x_{0,0} - 2Bw_1 w_2 x_{1,0} \\ (Aw_1^2 - Bw_2^2)x_{1,0} - 2Aw_1 w_2 x_{0,0} \\ (Aw_1^2 + Bw_2^2)x_{2,0} \end{pmatrix} \tag{4.16}$$

4.2.3 Solution for product state permutation dynamics with Hubbard interaction

Following the previous section, we write our Diophantine eq. (4.8) in a diagonal form:

$$\ell^2 + n^2 = 2mn \tag{4.17}$$

$$\implies \begin{pmatrix} \ell & \tilde{n} & m \end{pmatrix} \begin{pmatrix} 1 & 0 & 0 \\ 0 & 1 & 0 \\ 0 & 0 & -1 \end{pmatrix} \begin{pmatrix} \ell \\ \tilde{n} \\ m \end{pmatrix} = 0, \tag{4.18}$$

where we have defined $\tilde{n} \equiv n - m$. Note, this is the famous Diophantine equation for Pythagorean triples.

By inspection, a non-trivial solution is $\ell = -1, \tilde{n} = 0, m = 1$. Utilizing Eq. (4.16) we find

$$\begin{pmatrix} \ell \\ \tilde{n} \\ m \end{pmatrix} = d \begin{pmatrix} w_1^2 - w_2^2 \\ 2w_1 w_2 \\ w_1^2 + w_2^2 \end{pmatrix} \tag{4.19}$$

$$\implies \begin{pmatrix} \ell \\ n \\ m \end{pmatrix} = d \begin{pmatrix} w_1^2 - w_2^2 \\ [w_1 + w_2]^2 \\ w_1^2 + w_2^2 \end{pmatrix} \tag{4.20}$$

Note, Eq. (4.19) is the standard solution for Pythagorean triples.

We thus found that the set of n, m, and ℓ simultaneously satisfying the conditions for simple dynamics can be written as:

$$\ell = d(w_1^2 - w_2^2) \tag{4.21a}$$

$$m = d(w_1^2 + w_2^2) \tag{4.21b}$$

$$n = d(w_1 + w_2)^2 \tag{4.21c}$$

where $w_1, w_2 \in \mathbb{Z}$, w_1, w_2 are coprime, and $d \in \frac{1}{\xi}\mathbb{Z}$ with $\xi = gcd((w_1^2 - w_2^2), (w_1^2 + w_2^2), (w_1 + w_2)^2)$. Note, in (4.21), if ℓ is even (odd) then so is n. This implies that the only way to completely satisfy the conditions in Eq. (4.7) is if all motion is frozen or all motion (not constrained by Pauli exclusion) becomes perfect swapping.

Inspecting the above solutions, we see that $2mn - n^2 = (w_1^2 - w_2^2)^2$, automatically satisfying the condition $2mn - n^2 > 0$ for V and τ to be real. Finally our solution is summarized by

$$\tau = \frac{\pi}{2} d(w_1^2 - w_2^2) \; ; \; V = \frac{8 w_1 w_2}{|w_1^2 - w_2^2|}. \tag{4.22}$$

Note that V doesn't depend on the choice of d, and that any choice involving $w_1 = 0$ or $w_2 = 0$ will yield a non-interacting model. As an illustration, consider the following example choices:
1. Taking $w_1 = 1, w_2 = 0, d = 1$ yields $\tau = \frac{\pi}{2}, V = 0$, which is the non-interacting dynamics considered in the original RLBL model, with perfect swapping.
2. Taking $w_1 = 3, w_2 = 1, d = 1$ yields $\tau = 4\pi, V = 3$. Since ℓ is even in this case, the dynamics is completely frozen.
3. Taking $w_1 = 3, w_2 = -1, d = 1$ yields $\tau = 4\pi, V = -3$, i.e. frozen dynamics in a model with an attractive Hubbard interaction.

It is important to note that the special values of interaction strength and driving frequency in Eq. (4.22) hold for any Hubbard-Floquet procedure where hopping between pairs of sites is sequentially activated. This is the case for such systems on any lattice and in any dimension. We also note, that the Diophantine solution is ill suited to describe the singular case of infinite V and finite τ and therefore this situation must be handled separately. In the limit of large V, the interaction strength overpowers the hopping strength and all evolution is frozen in the 2-particle sector. On the other hand, evolution in the 1,3 particle sector is independent of V and therefore may exhibit perfect swapping or freezing. Thus, in this case, it is possible to have one sector (the 2-particle sector) frozen while the other (the 1,3 particle sector) exhibits perfect swapping.

To visually represent the position of our special points we introduce the following function as a qualitative estimate for how far a given evolution U is from being a permutation of basis states:

$$F_{p,q}(U) = -\log \frac{||U||_{p,q}}{dim(U)^{1/q}} = -\frac{1}{q} \log \frac{\sum_{n,m} |U_{n,m}|^p}{dim(U)} \tag{4.23}$$

where $dim(U)$ is the dimensionality, and $||U||_{p,q} = (\sum_{n,m} |U_{n,m}|^p)^{1/q}$ is the p,q matrix entry-wise norm. Note that for a complex permutation, each row has a single non zero

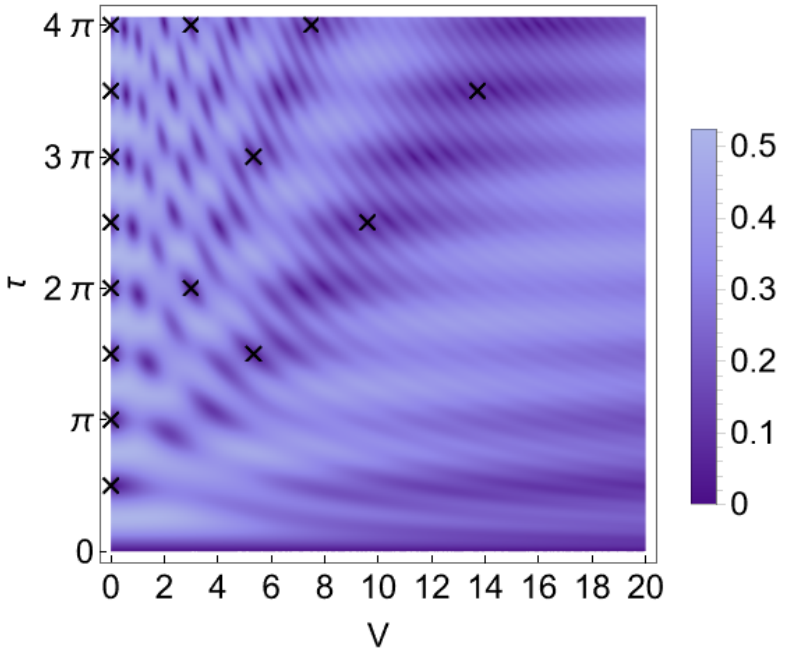

FIGURE 3: Special Diophantine points in the Hubbard-RLBL model and 'distance' of the two-site evolution from being a permutation of number states. Here we plot $\sqrt{F_{4,4}(U)}$ as function of V, τ. The darker regions indicate regions where the two-site evolution is close to pure number state permutation.

entry of absolute magnitude 1, therefore, for any $p, q > 0$,

$$F_{p,q}(\text{complex permutation}) = 0.$$

Note that for any unitary matrix U, $F_{2,q}(U) = 0$. However, for $p > 2, q > 0$ we have that $F_{p,q}(U) > 0$ whenever U is a unitary that is not a complex permutation. The following extensivity property is straightforward to verify:

$$F_{p,q}(U_1 \otimes U_2) = F_{p,q}(U_1) + F_{p,q}(U_2). \tag{4.24}$$

In figure Fig. 3, we plot $F_{4,4}$ for the two site Hubbard evolution showing regions where the two-site evolution is close to permutative and marking the Diophantine spots where it is exact. Interestingly, while the special points admit exact evolution, the plot shows many regions where the evolution is close to perfectly permutative. Exploration of what happens when the evolution is not exact, but perturbatively close to it is out of the scope of the present chapter, but will be initiated in chapter 5 (see also [4]).

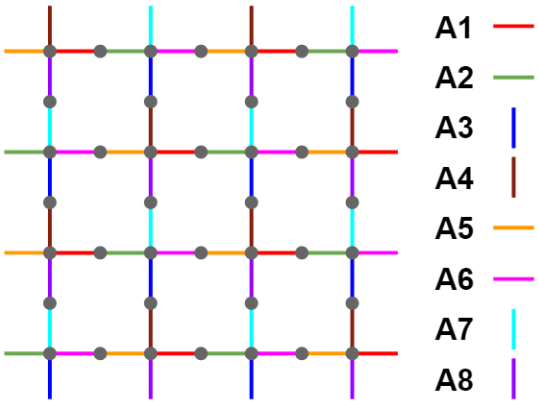

FIGURE 4: RLBL-like model on a Lieb lattice. Hopping between neighboring pairs of sites within A_i is activated during step i of the Floquet drive. The same sequence of activated site pairs is achieved with the chiral measurement scheme introduced in chapter 3. During each step i, evolution is confined between neighboring sites in A_i by rapidly measuring (in the Zeno limit) all sites in the complimentary set A_i^c. Both models, with NN interactions, will share the same conditions (Eqs. (4.29) and (4.30)) for number state to number state evolution.

4.2.4 Example 2: Nearest neighbour interactions on a Lieb lattice.

In the next two examples, we consider interactions involving nearest neighbours. Unfortunately, adding nearest neighbour interactions to the RLBL model directly destroys an essential feature for the solvability of the problem: that the evolution operators of different pairs of sites are not directly coupled (and therefore commute). Here, instead, we choose to work with RLBL-like dynamics on a Lieb lattice as described in chapter 3. A Lieb lattice is a decorated square lattice as shown in Fig. 4. The dynamics we consider here essentially activates pairs that are separated by several lattice sites at each step. The sequence of activations is described in Fig 4.

Here, we consider spinless fermions on the Lieb lattice. There are 8 steps. At step i we activate hopping between sites that are nearest neighbours that belong to the set A_i. The evolution is given by:

$$U = U_8 U_7 U_6 U_5 U_4 U_3 U_2 U_1 \tag{4.25}$$

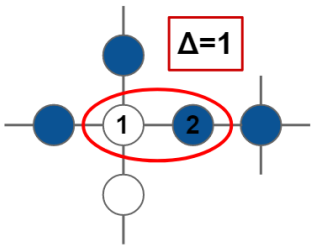

FIGURE 5: Evolution of a 2-site pair in the NN-RLBL model on a Lieb lattice. All evolution is restricted to the red ellipse above. Evolution within the red ellipse (i.e. between site 1 and site 2) is determined by τ, V, and the neighboring particle number difference $\Delta = |N_1 - N_2|$. In this case, $N_1 = 2$ and $N_2 = 1$, so $\Delta = 1$. If the $\Delta = 1$ condition on V and τ in Eq. (4.29) is satisfied, then the particle at site 2 will exactly return to site 2 after a time τ (at intermediate times, the particle may be in a generic superposition of being located at site 1 and site 2).

where $U_i = e^{-i\mathcal{H}_i\tau}$, and

$$\mathcal{H}_i = -t_{hop} \sum_{(i,j)\in A_i} (a_i^\dagger a_j + h.c.) + V \sum_{<i,j>} n_i n_j \tag{4.26}$$

We proceed, as in Section 4.2.1, by considering the evolution of a single connected pair during step i and exactly solving for values of V and τ where the pair exhibits freezing or perfect swapping. The evolution of a 2-site pair of sites i, j for one step is given by

$$U_{(i,j)} = e^{-i\tau[-t_{hop}(a_i^\dagger a_j + h.c.) + V n_i \sum_{k:\langle i,k\rangle} n_k + V n_j \sum_{k:\langle j,k\rangle} n_k]}. \tag{4.27}$$

Note that the number operators on neighbours of i, j commute with the evolution. Let the initial number of occupied neighbours of the sites i and j be N_i and N_j respectively (not counting i, j themselves). Evolution of the 2-site pair is now exactly solvable in terms of $\Delta = N_i - N_j$, the difference in the number of particles neighboring sites i and j in the 2-site pair respectively (see Figure 5).

Solving the two site evolution, we find that evolution is frozen when

$$\sqrt{4 + \Delta^2 V^2}\tau = 2\pi m \tag{4.28}$$

for some $m \in \mathbb{Z}$. We find that the evolution may only be perfect swapping when $\Delta = N_i - N_j = 0$ or when $V = 0$ and occurs when $\tau = \frac{\pi}{2} + \pi m$ for $m \in \mathbb{Z}$ (see appendix 4.A.2 for details).

In the rest of the paper, whenever considering the evolution on a pair of sites, we will denote Δ as the difference in the number of (static) particles that are nearest neighbours of the two sites during the relevant evolution step.

4.2.5 A coupled set of Diophantine Equations

For a generic initial position of the particles, $N_i - N_j$ will not be uniform across the sample. Thus, for proper particle permutation dynamics, we must simultaneously find a solution of (4.28) for all possible values of $|N_i - N_j|$. As we have seen for $V = 0$ there is no dependence on neighbour occupation and evolution will be frozen or perfect swapping if $\tau = \frac{\pi}{2}m$ with m, correspondingly, even or odd. In the rest of the section we concentrate on $V \neq 0$.

Note that N_i takes the values $0, .., D_i - 1$, where D_i is the degree (number of neighbours) of lattice site i. It follows that $|N_i - N_j| \in \{0, .., max(D_i, D_j) - 1\}$. Thus, if D_{max} is the maximum degree of the lattice, we have the simultaneous conditions:

$$\sqrt{4 + \Delta^2 V^2}\tau = 2\pi m_\Delta \; \forall \; \Delta = 1, ..., (D_{max} - 1) \tag{4.29}$$

$$\tau = \frac{\pi}{2}m_0 \text{ corresponds to } \Delta = 0 \; (N_i = N_j) \tag{4.30}$$

with all $m_i \in \mathbb{Z}$.

Equations (4.29) and (4.30) provide D_{max} equations that must be solved simultaneously. The first two equations set the values for τ and V in terms of m_0, m_1:

$$\tau = \frac{\pi}{2}m_0 \; ; \; V^2 = 4(\frac{4m_1^2}{m_0^2} - 1). \tag{4.31}$$

However, the rest of the equations for m_i, with $i > 1$, must be simultaneously solved with these values for τ and V yielding the coupled equations:

$$4m_l^2 = (1 - l^2)m_0^2 + 4l^2 m_1^2 \tag{4.32}$$

$$m_l \in \mathbb{Z} \, , \; l = 2, 3, ..., (D_{max} - 1) \tag{4.33}$$

A first solution to this system may be obtained by taking $m_0 = 2m_1 = 2m_2 = ... = 2m_{D_{max}-1}$, which, by (4.31), turns out to be the same as the non-interacting frozen case $V = 0$. We now search for other solutions, with $V \neq 0$.

Solution for $D_{max} = 3$. For $D_{max} = 3$, we describe a general solution in appendix 4.A.2 that yields non-trivial solutions. The result:

$$\begin{pmatrix} m_0 \\ m_1 \\ m_2 \end{pmatrix} = d \begin{pmatrix} -32w_1w_2 \\ -3w_1^2 - 16w_2^2 \\ 2\left[-3w_1^2 + 16w_2^2\right] \end{pmatrix}. \tag{4.34}$$

We note that m_0 resulting from (4.34) is always even (see the end of Appendix 4.A.2) and thus can only yield frozen evolution when $V \neq 0$. Due to the hierarchy of the equations, total freezing must then occur for any solutions with $D_{max} \geq 3$.

Solution for $D_{max} = 4$. We combine equations (4.34) and the $\Delta = 3$ equation from (4.29) to find a new Diophantine equation for the case $D_{max} = 4$:

$$\frac{1}{d^2} m_3^2 = 81w_1^4 + 2304w_2^4 - 1184w_1^2w_2^2 \tag{4.35}$$

The Diophantine equation (4.35) is harder to solve. However, a numerical search does find non-trivial ($V \neq 0$) solutions. For example, $(w_1; w_2; m_3) = (3; 9471; 4305592257)$ and $d = 1$ is a solution with $V \approx 6,394$ and $\tau = 454,608\pi$. Whether there exist V, τ such that lattices with a maximum degree larger than 4 may exhibit fully product state permutation evolution is an open question.

The result for $D_{max} = 4$ required simultaneous solution of the equations for two different primes ($l = 2$ and $l = 3$) which suggests the conjecture that there are solutions to the system of equations for any D_{max}. Similar to the strategy above, by solving for $D_{max} = k$, it is possible to construct a new Diophantine equation for $D_{max} = k + 1$. Determining whether this tower of equations is solvable is outside the scope of the present paper. On the other hand, as can already be seen in the case of $D_{max} = 4$, the values of V, τ for which the system exhibit such freezing for any initial number state quickly become prohibitively large for typical physical systems as the maximum lattice degree increases.

Remark. It is straightforward to generalize the Hamiltonian (4.26) to include more elaborate interactions as long as at each step the number operators associated with the neighbourhood of each evolving pair is constant. For example, we can write

$$\mathcal{H}_i = -t_{hop} \sum_{(i,j)\in A_i} (a_i^\dagger a_j + h.c.) + \sum_{i\in A_i} V_{ij} n_i n_j, \tag{4.36}$$

Given the number of particles in the neighborhood of each 2-site pair, we write (note here we include the potentials V in the the definition of Δ):

$$\Delta_{ij} = \sum_{k:\langle i,k\rangle} V_{ik} n_k - \sum_{k:\langle j,k\rangle} V_{jk} n_k \tag{4.37}$$

and the freezing condition becomes:

$$\tau\sqrt{4+\Delta_{ij}^2} = 2\pi m_{ij},\ m_{ij} \in \mathbb{Z} \tag{4.38}$$

for all Δ_{ij} of the form (4.37).

4.2.6 Example 3: Deterministic evolution in the measurement induced chirality model on a Lieb lattice.

As another example, we consider the measurement induced chirality protocol of chapter 3 with added nearest neighbour interactions and in the Zeno limit. In that work, a simple hopping Lieb lattice model of fermions was subjected to repeated measurements changing according to a prescribed chiral protocol. In contrast to the previous models, the Hamiltonian is not time dependent and all hopping terms in the Hamiltonian remain activated throughout the process.

It was shown in chapter 3 that in the limit of rapid measurements, the so called the Zeno limit, the resulting dynamics is a classical stochastic process of permuting Fock states. We will see that, in this case too, we can find special values of interaction strength and protocol duration where the dynamics becomes deterministic. In fact, we will see the dynamics is governed by the same Diophantine equation as in example 2.

Specifically, we consider fermions hopping on a Lieb lattice with nearest-neighbor interactions given by

$$\mathcal{H} = -t_{\text{hop}} \sum_{<i,j>} a_i^\dagger a_j + V \sum_{<i,j>} n_i n_j. \tag{4.39}$$

We now apply the measurement protocol introduced in chapter 3 to the system. Namely, we consider an 8 step measurement protocol in which, during the i^{th} step that runs for a time τ, the local particle density in all sites in a set A_i^c of sites are measured. In the Zeno limit, all evolution during a step is restricted to neighboring sites in the subspace

A_i (See figure 4 for details), while the rest of the sites are kept frozen. Thus, in the Zeno limit, the evolution is effectively split into 8 steps evolved by the Hamiltonian (4.26), interspersed by an additional measurement. The measurements keep projecting the system onto Fock states, however, the particular states at hand are statistically distributed. However, if the step evolution (4.27) maps Fock states into Fock states, the whole procedure yields a deterministic evolution of an initial Fock state into another. In other words, the conditions for permutative evolution (and the corresponding set of Diophantine equations) for this model are equivalent to those found in the interacting Floquet model investigated in example 2. This implies that the dynamics of the measurement induced chirality model and unitary Floquet evolution are equivalent at the special points in parameter space where Fock states are mapped to Fock states. However, if parameters are perturbed away from these special points, the dynamics of the two examples quickly begin to differ. This is due to the non-unitary nature of the measurements as opposed to the completely unitary evolution in the unitary Floquet case.

4.3 Hilbert Space Fragmentation

In Section 4.2.5, we gave $D_{\max}$ conditions that must be simultaneously satisfied for Fock state permutative dynamics in models on a Lieb lattice with NN interactions. Similarly, in Section 4.2.1 we gave conditions for permutative evolution in the Floquet-Hubbard RLBL model. If in these models not all of these conditions are satisfied, then the evolution of a general initial state will require consideration of the full quantum many-body Floquet Hamiltonian.

However, evolution for certain initial states may still be deterministic even if only one or a few of the conditions for Fock state to Fock state evolution are met. This fragments [164] the Hilbert space, $\mathcal{H}$, into disconnected Krylov supspaces, $\mathcal{K}_i$, i.e.

$$\mathcal{H} = \bigoplus_i \mathcal{K}_i,\ \mathcal{K}_i = span_n\{\mathcal{U}^n|\psi_i\rangle\} \tag{4.40}$$

where we have chosen a states $|\psi_i\rangle$ that are number local states in such a way that $\mathcal{K}_i$ are unique. In the rest of this section, we will explore the nature of the Hilbert space fragmentation in the example interacting Floquet and measurement induced models

discussed in the previous section. Namely, we will see how the Hilbert spaces in these systems simultaneously support Krylov subspaces that are one-dimensional and correspond to frozen product states, few dimensional and correspond to states that evolve according to a classical cellular automation [176, 177], and exponentially large subspaces that may evolve with more generic quantum many-body evolution.

4.3.1 Arrested development

Let us take as an example the NN-RLBL model on a Lieb lattice considered in Section 4.2.4. There, it was shown that when the parameters V, τ satisfy the conditions (4.29) and (4.30) with m_0 even, then the evolution of each step in the Floquet drive is given by the identity. However, certain initial states do not require all of the conditions (4.29) and (4.30) to be satisfied in order for this freezing of the dynamics to occur. For example, initial Fock states where $\Delta = 1$ for every activated 2-site pair only require $\sqrt{4+V^2}\tau = 2\pi m_1$ with $m_1 \in \mathbb{Z}$ to be satisfied in order to exhibit frozen dynamics. Even if every other condition (4.29) and (4.30) with $\Delta \neq 1$ fails to be satisfied, such states will still be frozen under the NN-RLBL evolution. However, in this case, initial states containing at least one 2-site pair with $\Delta \neq 1$ may evolve into a superposition of Fock states. Therefore, the Hilbert space has been split (fragmented) into subspaces of Fock states that are frozen and a subspace of states which are not frozen.

In Fig. 6 we give examples of frozen particle configurations. At the top of the figure are configurations that require the satisfaction of only the $\Delta = 0$ condition (4.30) to be frozen, configurations in the middle of the figure require only the $\Delta = 1$ condition, and at the bottom of the figure is a particle configuration that will be frozen so long as both the $\Delta = 1$ and $\Delta = 3$ conditions (4.29) are satisfied. If the conditions for $\Delta = 0$, $\Delta = 1$, and $\Delta = 3$ are all satisfied then the entire Fig. 6 represents a frozen particle configuration. We emphasize here that, even if only one of the conditions (4.30), (4.29) are satisfied, that the number of frozen particle configurations grows exponentially in system size.

Additionally, we note here that the chiral nature of the Floquet procedure played no role in the emergence of these frozen states. In fact, any procedure that sequentially activates hopping between neighboring pairs of sites (suitably spaced to keep evolution disjoint after adding NN interactions) will exhibit the exact same frozen states. For example, even if we consider a new procedure where, at each step in the evolution, the

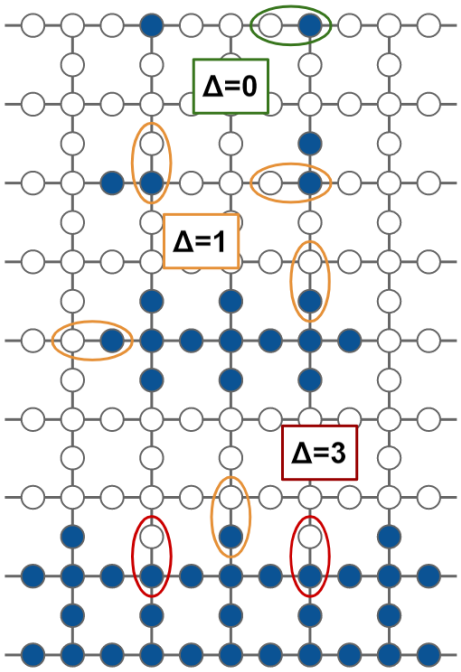

FIGURE 6: A Zoo of frozen particle configurations when only some of the conditions in (4.29) and (4.30) are satisfied on a nearest neighbour interacting Lieb-RLBL model. At the top, a particle configuration that requires only that the $\Delta = 0$ condition (and m_0 even) be satisfied for frozen evolution. In the bulk of the system are particle configurations that will be frozen so long as the $\Delta = 1$ condition is satisfied. The lower edge of the system provides an example of a particle configuration that will be frozen so long as both the $\Delta = 1$ and $\Delta = 3$ conditions are satisfied. Since all the particle configurations above are disconnected, the simultaneous satisfaction of the $\Delta = 0$, $\Delta = 1$, and $\Delta = 3$ conditions implies that the entire system above will be frozen.

system is evolved with a U_i from equation (4.25) chosen at random (uniformly), i.e. an example realization of this aperiodic, random evolution is given by

$$U = ...U_4U_5U_3U_3U_1U_2U_7U_3. \tag{4.41}$$

The exact same states will be frozen in this model as in the NN-RLBL model on a Lieb lattice.

Therefore, for any model of the form (4.41) we have the following situation. The Hilbert space is fragmented into a (exponentially large) non-frozen subspace and an

exponential number of subspaces corresponding to frozen states. In general cases, initial states in the non-frozen subspace are free to ergodically explore their Krylov subspace leading to chaotic dynamics. Such behavior is referred to as Krylov-restricted thermalization [180]. However, if additional symmetries and structure are present, the non-frozen subspace may be further split into additional subspaces (see Sec. 4.3.4).

4.3.2 Krylov Subspaces of Cellular Automation

Since the dynamics of a particle configuration that obey the Diophantine conditions depends crucially on particles on the neighbouring sites, it can be naturally encoded as a cellular automation step. We will now see how Krylov subspaces supporting classical CA [176, 177] at each evolution step may emerge in interacting Floquet and measurement-induced systems when a few of the conditions for number state to number state evolution are satisfied.

To elucidate this effect, we consider again the NN-RLBL model on the Lieb lattice. In this case, we take the $\Delta = 0$ and the $\Delta = 1$ conditions for number state to number state evolution to both be satisfied, but this time the $\Delta = 0$ condition is satisfied for perfect swapping while the $\Delta = 1$ condition is satisfied for freezing. This may happen at, for example, $\tau = \frac{\pi}{2}$ and $V = \sqrt{12}$.

It is now possible to find number states such that the initial particle configuration, $|\Psi_{init}\rangle$, and the resulting states after evolution of each step in the Floquet drive, all satisfy either $\Delta = 0$ or $\Delta = 1$ for every activated two-site pair in the system with a single particle. We give an example particle configuration where this may occur in Figure 7. Here, the space of states $span_n\{U^n|\Psi_{init}\rangle\}$ defines a Krylov subspace where evolution is completely given by a CA since at each step in the Floquet drive the local particle densities are updated deterministically based on the neighboring particle densities (i.e. if $\Delta = 0$ or 1).

Similarly to the case of frozen initial particle configurations, disjoint unions of particle configurations that evolve as a CA will also evolve as a CA. For particle configurations whose CA evolution leaves all particles contained in a volume that does not scale with system size (for example, the evolution of the configuration in Figure 7 remains contained within the 5×5 site square), the number of CA Krylov subspaces will grow exponentially with the system size (since there are exponentially many disjoint unions of such particle configurations). These CA subspaces may coexist with

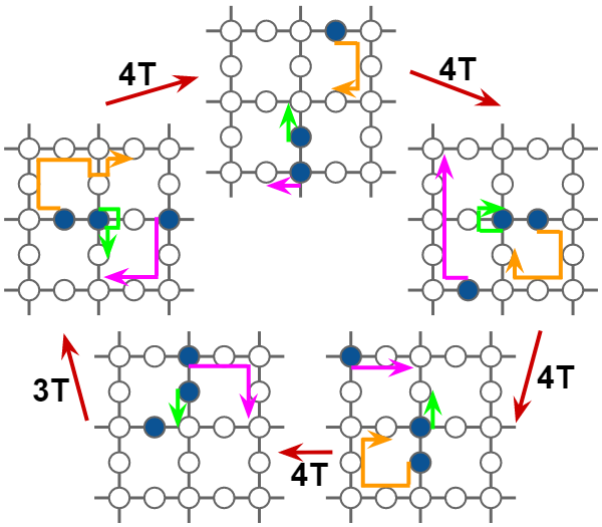

FIGURE 7: Example evolution within a cellular automation Krylov subspace set by the simultaneous satisfaction of the $\Delta = 0$ and $\Delta = 1$ conditions in equations (4.29) and (4.30). In this case, 2-site pairs with $\Delta = 0$ evolve with perfect swapping while 2-site pairs with $\Delta = 1$ are frozen. The resulting cellular automation for this example initial particle configuration results in the particles returning to their initial sites after $19T$. Example values of V, τ that achieve this evolution are $V = \sqrt{12}$ and $\tau = \frac{\pi}{2}$. Particle trajectories are drawn with orange, green, and magenta arrows.

frozen Krylov subspaces as well as with exponentially large subspaces with more general quantum evolution.

It is important to note that these CA subspaces break the underlying T time translation symmetry of the evolution operator. For example, the particle configuration in Fig. 7 returns to its initial configuration after $19T$. However, the exact realization of this Krylov subspace requires fine-tuning in parameter space. If an alteration of this model was possible such that the realization of these Krylov subspaces did not require fine-tuning, then such a model would be a realization of a time-crystal. In fact, since the systems we've considered may simultaneously support Krylov supspaces that break the T time translation symmetry in different ways, such a stabilized system would simultaneously support several different time crystals depending on which Krylov subspace contains the initial state. Recent works [42, 43] have argued that disorder may stabilize dynamics for regions in parameter space near similarly fine-tuned points in an interacting, RLBL model to achieve anomalous Floquet insulating phases. The basic idea is to consider a high frequency regime, where the expansion studied in e.g. [28, 38] shows that the effective evolution in the high frequency limit only acts non-trivially on

small resonant spots that take an exponentially long time to destroy localization. This in turn is associated with the robustness of prethermal phases and localization when an MBL Floquet system is perturbed. In the RLBL system our special points for the model require, for example, $\tau \sim \frac{\pi}{2}$ which is not a high frequency drive. However, if the system is instead viewed in the rotating frame of the chiral RLBL drive, the evolution can be effectively presented as a high frequency drive, related to the inverse of the parameter offsets between τ, V and the perfect point (see [42] for details). It is thus possible to show that disorder stabilizes the evolution. In chapter 5 we extend this treatment to address when disorder may stabilize dynamics for the entire system or for specific Krylov subspaces in a more general set of models.

4.3.3 Frozen states of Floquet evolution on a chain with nearest neighbour interactions

A major tool used in the analysis of the interacting Floquet and measurement models above was that the interactions preserved the disjoint nature of the steps of the periodic drive. However, using the same tools as in the disjoint case, it is possible to find frozen states even when the activated neighboring pairs interact (i.e. do not commute).

Here, we investigate an example model where the interactions ruin the disjoint nature of the Floquet drive and show how, at special values of interaction strength and driving frequency, it is still possible to find states that are frozen. Namely, we take as an example a 1D, NN interacting Hamiltonian of the form

$$\mathcal{H}(t) = H_0(t) + V \sum_{i=0}^{N-2} n_i n_{i+1} \tag{4.42}$$

where

$$H_0(t) = \begin{cases} \sum_{i \text{ even}} (a_i^\dagger a_{i+1} + h.c.) & 0 \leq t < \frac{T}{2} \equiv \tau \\ \sum_{i \text{ odd}} (a_i^\dagger a_{i+1} + h.c.) & \frac{T}{2} \leq t < T. \end{cases} \tag{4.43}$$

Similarly to the previous cases, let us again consider a single 2-site pair where hopping is activated. If the occupancy of the sites neighboring the pair happen to be static, then the conditions for frozen or perfect swapping (4.29) and (4.30) will still hold

(except here with $D_{max} = 2$). However, this is, of course, not generally the case. Even if a neighboring pair is stroboscopically frozen, the number of particles at neighbouring sites may change during the evolution and ruin the conditions (4.29) and (4.30).

However, if every 2-site pair with a single particle is located on the edge of a domain wall in the system, then Δ will again be well defined (since any neighboring particles will be stationary due to Pauli exclusion) and the conditions (4.29) and (4.30) will hold for these particle configurations. In Figure 8, we give examples of such states that will be stroboscopically frozen when the $\Delta = 1$ condition is satisfied, i.e. all these states are eigenstates to the evolution operator $\mathcal{U}(T) = \mathcal{T} e^{-i \int_0^T \mathcal{H}(t)}$.

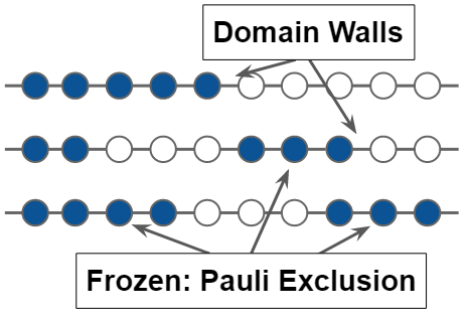

FIGURE 8: Particle configurations frozen in the Even-Odd NN model at values of V, τ that satisfy the $\Delta = 1$ condition in (4.29). The only 2-site pairs with a single particle are located on the domain walls. Since, within the uniform domain, particles are frozen at all times due to Pauli exclusion, the neighboring particle number difference for 2-site pairs on the domain wall is constant and given by $\Delta = 1$.

We now turn to numerically investigating the emergence of these frozen states and the Hilbert space fragmentation in this system. We exactly diagonalize $\mathcal{U}(T)$ at the special points $V = \sqrt{12}$, $\tau = \frac{\pi}{2}$ and $\tau = \pi$ [2]. Here, the condition for frozen $\Delta = 1$ is satisfied, while $\Delta = 0$ is perfect swapping or frozen respectively. If the activated neighboring pairs were disjoint, evolution at these parameter values would be exactly solvable (with dynamics either being a CA or stroboscopically frozen). As we will see, however, this is not the case here. The Hilbert space instead fragments into exponentially many subspaces of frozen domain wall states and a single, exponentially large, ergodic subspace.

[2] As a technical note, the frozen domain wall states will be highly degenerate and numerical diagonalization will give a random basis of eigenstates within the degenerate subspace. To find the frozen states within this basis, we apply a small disorder potential during the wait step in the evolution to split the energy levels. This disorder potential will add only a global phase to the frozen states and thus allows a direct numerical route to finding them.

To seperate the two classes of subspaces, we calculate the half-chain entanglement entropy of the eigenstates (shown in Figure 9). The frozen eigenstates have zero entanglement entropy while the other eigenstates have finite (and as can be seen from Fig. 9, large) entanglement entropy. Upon plotting the average local particle densities of a sample of the zero entanglement entropy eigenstates, we find that they do indeed correspond to the expected frozen domain wall states.

While the number of domain wall states n_{Froz} grows exponentially with system size, their fraction of the total Hilbert space dimension goes to zero. To see this, consider e.g. states that satisfy the $\Delta = 1$ condition (with similar consideration applying to $\Delta = 0$ situations). Such states are characterized by occupied domains that are separated from each other by at least 3 sites (see Fig (8)) so that particles on the edges of separate domains do not interact with each other at any stage of the evolution. A rough lower bound on the number of such states is $2^{\lfloor N/3 \rfloor}$, if we only look at domains whose length is a multiple of 3 starting at sites $3, 6, ..., \lfloor N/3 \rfloor$. An upper bound can easily be obtained by noticing that the total number of domains cannot exceed $\lfloor N/3 \rfloor$, thus we have an upper bound by considering the entropy of the positions of domain wall boundaries $\sum_{k=0}^{\lfloor N/3 \rfloor} \binom{N}{k}$. In the large N limit, this is dominated by the term $\binom{N}{N/3}$ which scales as $2^{NS_{\text{bi}}(1/3)} \approx 2^{0.92N}$, by Stirlings approximation, with the entropy function $S_{\text{bi}}(a) = a \log_2(\frac{1}{a}) + (1-a)\log_2(\frac{1}{1-a})$. In summary, we see that n_{Froz} grows exponentially in system size but the fraction of frozen states compared to the full Hilbert space dimension (which scales as 2^N) is zero in the thermodynamic limit.

The large half-chain entanglement entropy of non-domain wall states suggests that the rest of the Hilbert space might be thermalized. To provide further evidence to this claim, we analyze an indicator often used to differentiate between ergodic and integrable systems: the statistics of level spacing ratios.

For thermalizing systems, it is expected [149] that the evolution operator $\mathcal{U}$ resembles random matrices drawn from a circular ensemble (the analog of gaussian ensembles for unitary matrices). Unlike the evolution operators for integrable systems, eigenstates of circular ensembles are random vectors and the spectrum exhibits level repulsion. Thus, it is possible to argue whether a system is ergodic by analyzing the statistics of the spacing of energy levels to see if the distribution is Poissonian (corresponding to no level repulsion) or if it corresponds to the expected level spacing distribution of circular ensembles (see [149] for explicit formulas).

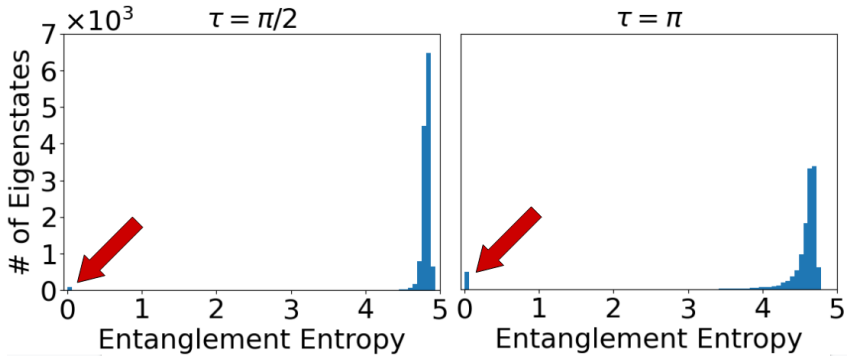

FIGURE 9: Half-chain entanglement entropy of all eigenstates of the evolution in the even-odd NN Floquet model. Eigenstates were found by exactly diagonalizing a 16 site chain. The parameter values were chosen such that both the $\Delta = 0$ and $\Delta = 1$ conditions in (4.29) and (4.30) are satisfied: $V = \sqrt{12}$, $\tau = \frac{\pi}{2}$ (left) and $\tau = \pi$ (right). Despite the non-disjoint nature of the activated hopping site pairs, the conditions (4.29) and (4.30) will still be valid for domain wall states that will, therefore, be frozen under the dynamics. These number states have no entanglement entropy and are indicated with red arrows in the figure above. The other eigenstates exhibit near-maximal entanglement entropy. This is a signature of the fragmentation of the Hilbert space into frozen Krylov subspaces and a ergodic Krylov subspace.

Namely, consider the level spacings between two neighboring eigen-quasienergies ε (i.e. ε's are the phases of the eigenvalues of $\mathcal{U}$),

$$\delta_n = \varepsilon_{n+1} - \varepsilon_n. \tag{4.44}$$

The ratio of level spacings is given by

$$r_n = \frac{min\{\delta_n, \delta_{n+1}\}}{max\{\delta_n, \delta_{n+1}\}}. \tag{4.45}$$

We then expect the statistics of r to match that of the circular ensembles instead of yielding a Poissonian distribution if the system is ergodic.

In our case, however, the system is not completely ergodic since the domain wall number states are eigenstates of the evolution. We instead wish to study the nature of the subspace which is the compliment of the set of all frozen Krylov subspaces within

the Hilbert space. We thus will only consider δ_n in (4.44) if the corresponding eigenstates of ε_{n+1} and ε_n have non-zero half-chain entanglement entropy. The results of this analysis are shown in Fig. 10. As can be seen in the figure, the probability distribution is in good agreement with that of the circular orthogonal ensemble (COE) suggesting that the Krylov subspace is thermal.

In summary, we have shown that the Hilbert space of the even-odd NN Floquet model is fragmented at special values of interaction strength and driving frequency. The fragmented Hilbert space simultaneously supports exponentially many (in system size) frozen Krylov subspaces and a single, exponentially large ergodic Krylov subspace. In this model, we did not find evidence of CA subspaces. Whether these subspaces are realizable in other non-disjoint models is an open question. Furthermore, for neighboring two-site pairs each with a single particle, the interactions between the pairs could conspire to produce special values of V, τ not given by equations (4.29) and (4.30) where evolution is stroboscopically frozen. We leave both these open questions for future work.

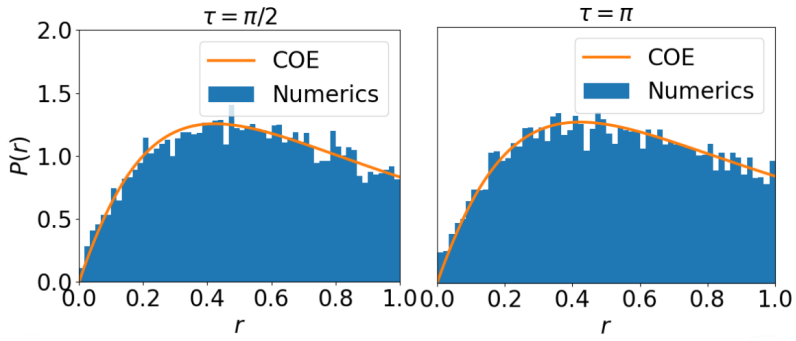

FIGURE 10: Level spacing statistics in the non-frozen Krylov subspace for evolution in the even-odd NN Floquet model. As in Fig. 9, parameter values are chosen as $V = \sqrt{12}$, $\tau = \frac{\pi}{2}$ (left) and $\tau = \pi$ (right). The probability distribution, $P(r)$, of the level spacing ratios, r, for quasi-energy levels not corresponding to frozen eigenstates provides good agreement with the level spacing probability distribution of random matrices in the circular orthogonal ensemble (COE). This suggests that the Krylov subspace is ergodic.

4.3.4 Remarks on Fragmentation and Ergodicity in NN-RLBL

In this section, we study numerically the entanglement entropy of eigenstates and level statistics in the NN-RLBL model with the Diophantine conditions only partly satisfied.

We show that the fragmentation seems to allow for a yet richer structure than shown in the 1D example above. In particular, we consider the NN-RLBL model with parameters $\tau = \frac{2\pi}{\sqrt{7}}$ and $V = \sqrt{3}$. Here, activated hopping pairs with $\Delta = 1$ are frozen, but none of the other conditions (4.29) or (4.30) are satisfied. We plot the entanglement entropy of the eigenstates of the evolution in Fig. 11.

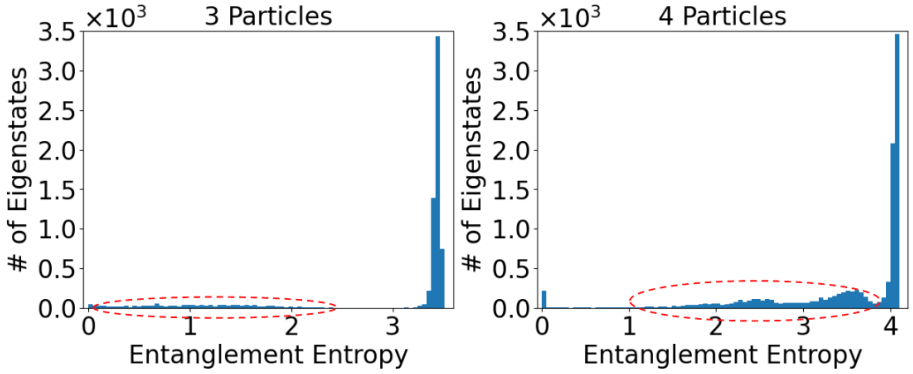

FIGURE 11: Entanglement entropy for eigenstates of the evolution in the NN-RLBL model. Parameters are given by $\tau = \frac{2\pi}{\sqrt{7}}$ and $V = \sqrt{3}$ which corresponds to activated hopping pairs with $\Delta = 1$ frozen and none of the other Δ conditions satisfied. On the left we consider evolution of 3 particles in an 8×6 lattice and on the right the evolution of 4 particles in an 8×4 lattice. In both cases, $\Delta = 1$ frozen yields frozen particle configurations leading to a set of zero entanglement entropy eigenstates. Additionally, there is a subspace of near-maximal entanglement entropy eigenstates. However, circled in red, there are eigenstates with entanglement entropy in-between the two extreme values. The span of these eigenstates forms another non-ergodic subspace of the Hilbert space that is distinct from frozen or cellular automation subspaces.

Examining Fig. 11 we find that there are frozen particle configurations leading to eigenstates with no entanglement entropy. There are no cellular automation subspaces since only a Diophantine condition for freezing has been satisfied. Additionally, there is a subspace containing eigenstates with near-maximal entanglement entropy suggesting ergodicity. However, there is also a subspace of eigenstates with entanglement entropy that is neither zero nor maximal. This suggests that the subspace compliment to the frozen and cellular automation subspaces has been further fragmented into ergodic and non-ergodic subspaces.

We further investigate this phenomena by examining the level spacing statistics for the non-frozen subspace in Fig. 12. The statistics show some level repulsion as they do not match that of the Poisson distribution, but the sampled ratios also do not align

with the distribution associated with the relevant ensemble of random matrices, the circular unitary ensamble (CUE).

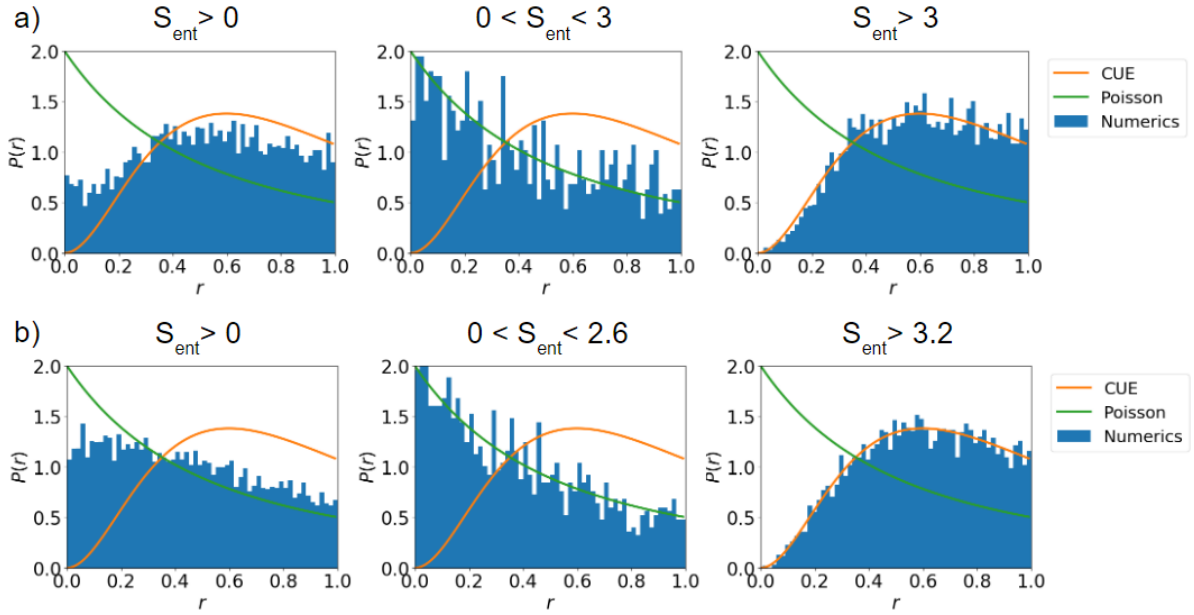

FIGURE 12: Level spacing statistics in the NN-RLBL model. Similar to Fig. 11, we consider evolution at $\tau = \frac{2\pi}{\sqrt{7}}$ and $V = \sqrt{3}$ with two different lattice sizes and fillings: a) 3 particles in an 8×6 lattice, b) 4 particles in an 8×4 lattice. In both cases, we have, from left to right: level spacing statistics of the full Hilbert space minus the frozen subspace, statistics for non-frozen eigenstates with entanglement entropy, S_{ent}, less than a cutoff value [3 for a) and 2.6 for b)], and statistics for eigenstates with entanglement entropy greater than a cutoff [3 for a) and 3.2 for b)]. The level spacing statistics for all non-frozen eigenstates is a mixture of Poisson statistics (corresponding to the subspace spanned by the eigenstates with S_{ent} less than a given cutoff) and circular unitary ensemble (CUE) statistics (corresponding to the subspace spanned by the eigenstates with S_{ent} more than a given cutoff). In the 4 particle case, the entanglement entropy range between 2.6 and 3.2 contains a mixture of Poisson and CUE statistics, so we focus on the eigenstates with S_{ent} less than 2.6 or more than 3.2 where the Poisson and CUE subspaces may be easily distinguished.

We now further separate the non-frozen subspace into the subspace spanned by the eigenstates with near-maximal entanglement entropy and the subspace spanned by the eigenstates without near-maximal entanglement entropy. Fig. 12 shows that the level spacing statistics corresponding to the near-maximal states agrees with the distribution for the associated random matrix ensemble, while the level spacing statistics associated with the eigenstates without near-maximal entanglement entropy seems to

exhibit Poisson statistics. This, therefore, provides evidence to suggest that the non-frozen subspace has fragmented into a subspace exhibiting chaotic dynamics and a subspace exhibiting integrable dynamics.

We suspect that the splitting of the non-frozen subspace may be further understood via a close consideration of the symmetries of the Floquet model, the satisfied Diophantine conditions, and their interplay. Similarly, it may be possible to describe in more detail the dynamics of the putative integrable subspace. However, we leave such investigations for future work.

4.4 Summary and discussion

In recent years the study of quantum many body states that break ergodicity has been an active field of research. Here, we considered conditions for dynamics in interacting systems that takes initial local number states to local number states. We have found such conditions for systems with sequentially activated hopping involving interactions such as Hubbard and nearest neighbour density interactions. Studying the resultant Diophantine relations between interaction strength, hopping energy, and hopping activation time, we discovered solutions to a variety of such systems. The resultant dynamics can be cast into two types: (1) Evolution that is deterministic for any initial Fock state (2) Fragmentation of the Hilbert space into deterministic sub-spaces and non-deterministic ones.

Our results introduce new sets of dynamically tractable interacting systems, with an emphasis on 2d where such results are scarce. Furthermore, the approach is applicable to similar systems in other dimensions. At the special solvable points, we get a variaty of behaviors from frozen dynamics of Fock states to cellular automata like evolution of selected subspaces. In cases where only some of the Diophantine conditions are met, we have shown that the special subspaces can exist simultaneously with states that possess volume law entanglement entropy and level statistics suggesting thermalizing behavior.

As discussed in section 4.3.2, although the ratios of Hamiltonian parameters (interaction strength, evolution time etc) considered here are finely tuned, previous work suggests that similarly finely tuned points may be stabilized by disorder to realize novel dynamical phases. In particular, periodic celullar automata evolution in our models

may lead to new classes of time crystals.

The problem of finding complete freezing of Fock states also led us to an interesting number theoretic problem involving the solution of a tower of Diophantine equations described in (4.29) and (4.30). We have shown explicitly solutions for dynamics on lattices with maximal degree of up to 4 nearest neighbours and conjecture a solution can be found for arbitrary maximal degree.

Another interesting question is that of the effect of long range interactions. We expect that two main consequences may arise: (1) The removal of all exactly solvable points, possibly destroying classical cellular automata like behavior in the system and (2) The long-range interactions may act as an effective disorder (due to the many possible configurations of particles away from particular activated sites where the dynamics occurs) stabilizing the classical like dynamics. A further possibility is that interactions with finely tuned decay properties may facilitate additional Diophantine conditions. However, except in rare cases, we do not expect that the new equations will combine into a solvable system.

Finally, we remark that the Diophantine methods utilized in this work may be applicable to bosonic systems, and systems with pairing terms where resultant cellular automata may not be of the number preserving type.

Appendix

4.A Solutions for subspaces of two sites

4.A.1 Hubbard Floquet Evolution of 2-site Pair in the 2-particle Sector

We index the 4-particle configurations of the subspace as follows:

$$0 \rightarrow \ \uparrow\downarrow \ \ \_\_ \tag{4.46a}$$
$$1 \rightarrow \ \_\_ \ \ \uparrow\downarrow \tag{4.46b}$$
$$2 \rightarrow \ \uparrow\_ \ \ \_\downarrow \tag{4.46c}$$
$$3 \rightarrow \ \_\downarrow \ \ \uparrow\_ \tag{4.46d}$$

We therefore have that the representation of the Hubbard Hamiltonian (4.2) in this subspace is given by

$$\mathcal{H} = \begin{pmatrix} V & 0 & -1 & -1 \\ 0 & V & -1 & -1 \\ -1 & -1 & 0 & 0 \\ -1 & -1 & 0 & 0 \end{pmatrix} \tag{4.47}$$

Hence, the evolution, $\mathcal{U} = e^{-i\mathcal{H}\tau}$, is given by

$$\mathcal{U} = e^{-\frac{1}{2}iV\tau}\begin{pmatrix} e^{-\frac{1}{2}iV\tau}\left[\frac{1}{2}+A\right] & e^{-\frac{1}{2}iV\tau}\left[-\frac{1}{2}+A\right] & B & B \\ e^{-\frac{1}{2}iV\tau}\left[-\frac{1}{2}+A\right] & e^{-\frac{1}{2}iV\tau}\left[\frac{1}{2}+A\right] & B & B \\ B & B & e^{\frac{1}{2}iV\tau}\left[\frac{1}{2}+\bar{A}\right] & e^{\frac{1}{2}iV\tau}\left[-\frac{1}{2}+\bar{A}\right] \\ B & B & e^{\frac{1}{2}iV\tau}\left[-\frac{1}{2}+\bar{A}\right] & e^{\frac{1}{2}iV\tau}\left[\frac{1}{2}+\bar{A}\right] \end{pmatrix} \tag{4.48}$$

where

$$A(V,\tau) = \frac{e^{\frac{1}{2}iV\tau}}{2}\left[\cos\left(\frac{1}{2}\tau\sqrt{16+V^2}\right) - i\frac{V}{\sqrt{16+V^2}}\sin\left(\frac{1}{2}\tau\sqrt{16+V^2}\right)\right] \tag{4.49}$$

$$B(V,\tau) = 2i\frac{\sin\left(\frac{1}{2}\tau\sqrt{16+V^2}\right)}{\sqrt{16+V^2}}. \tag{4.50}$$

and $\bar{A}$ is the complex conjugate.

We are now interested in finding when (4.48) is a permutation matrix. Note, for non-zero V, $|B| < 1$. Thus, our only hope for a permutation matrix is if $B = 0$. This occurs when $\frac{1}{2}\tau\sqrt{16+V^2} = \pi m$ for some $m \in \mathbb{Z}$, i.e. the condition given in (4.5).

Solving for $A(V,\tau)$ at condition (4.5) yields

$$A(V,\tau)|_{Condition:(4.5)} = \frac{1}{2}e^{i[\pi m + \frac{1}{2}V\tau]} \tag{4.51}$$

In (4.48), $\mathcal{U}$ is a permutation matrix when, in addition to the requirement $B = 0$, $|A| = \frac{1}{2}$ and $\frac{V\tau}{\pi} \in \mathbb{Z}$. These 2 conditions are uniquely met when, using (4.51), $\pi m + \frac{1}{2}V\tau = \pi n$ for some $n \in \mathbb{Z}$. Thus, we have arrived at the condition given in (4.6). When (4.5) and (4.6) are satisfied, $\mathcal{U}$ then becomes

$$\mathcal{U}|_{\text{Conditions: (4.5) and (4.6)}} = \begin{pmatrix} n-1 & n & 0 & 0 \\ n & n-1 & 0 & 0 \\ 0 & 0 & n-1 & n \\ 0 & 0 & n & n-1 \end{pmatrix} \mod 2 \tag{4.52}$$

i.e. yielding the result that when n is even (odd) evolution is the identity (perfect swapping).

4.A.2 Nearest Neighbor Floquet Evolution of 2-site Pair in 1-particle Sector

The Hamiltonian of the j^{th} 2-site pair is

$$\mathcal{H}_j = -(a_{j1}^\dagger a_{j2} + h.c.) + V n_{j1} n_{j2} + V N_1 n_{j1} + V N_2 n_{j2} \tag{4.53}$$

where N_1, N_2 correspond to the number of particles (outside the j^{th} pair) neighboring site 1 and site 2 in pair j respectively. Note, $[N_1, \mathcal{H}_j] = [N_2, \mathcal{H}_j] = 0$.

The representation of the Nearest Neighbor Hamiltonian in the 1-particle sector is given by

$$\mathcal{H} = \begin{pmatrix} N_1 V & -1 \\ -1 & N_2 V \end{pmatrix} \tag{4.54}$$

Hence, the evolution, $\mathcal{U} = e^{-i\mathcal{H}\tau}$, is given by

$$\mathcal{U} = \frac{e^{-\frac{1}{2}i(N_1+N_2)V\tau}}{C} \begin{pmatrix} C\cos\left[\frac{C}{2}\tau\right] - i\Delta V \sin\left[\frac{C}{2}\tau\right] & 2i\sin\left[\frac{C}{2}\tau\right] \\ 2i\sin\left[\frac{C}{2}\tau\right] & C\cos\left[\frac{C}{2}\tau\right] + i\Delta V \sin\left[\frac{C}{2}\tau\right] \end{pmatrix} \tag{4.55}$$

where

$$C(\Delta, V) \equiv \sqrt{4 + \Delta^2 V^2} \tag{4.56}$$

$$\Delta \equiv N_1 - N_2. \tag{4.57}$$

For perfect swapping to occur, we must have that the diagonal elements of (4.55) go to zero. This may only occur when

$$\frac{C}{2}\tau = \pi(m + \frac{1}{2}) \text{ for } m \in \mathbb{Z}\,; \Delta = 0 \tag{4.58}$$

For freezing to occur, we must have that the off-diagonal elements of (4.55) are zero. Note, depending on the particle configuration, Δ may take any value such that

$$\Delta \in \mathbb{Z}, \text{ and } |\Delta| < \max[\deg(\text{site } 1), \deg(\text{site } 2)].$$

where deg is the degree of the vertex. We must therefore have that $\frac{C}{2}\tau = \pi m$ for all possible values of Δ and with $m \in \mathbb{Z}$, i.e. letting $\Delta_i \in \{0, 1, ..., \max[\deg(\text{site } 1), \deg(\text{site } 2)] - 1\}$ such that $\Delta_i = \Delta_j$ iff $i = j$, we require

$$\frac{C(\Delta_i, V)}{2}\tau = \pi m_i \; \forall \; i \tag{4.59}$$

where $m_i \in \mathbb{Z}$.

Combining Equations (4.58) and (4.59) yields (4.29) and (4.30) in the main text.

We may now proceed by solving one value of Δ_i at a time. We start with Δ_0 and, without loss of generality, let $\Delta_0 \neq 0$ (if $\Delta_0 = 0$, we may simply replace $m_0 \to \frac{m_0}{2}$ in the final result), we have from (4.59) that

$$\tau = \frac{2\pi m_0}{\sqrt{4 + \Delta_0^2 V^2}} \tag{4.60}$$

Now, looking next at $\Delta_1 \neq 0$ (again, we may set $m_1 \to \frac{m_1}{2}$ if $\Delta_1 = 0$), we use Eqs. (4.59) and (4.60) to find

$$\frac{\sqrt{4+\Delta_1^2 V^2}}{\sqrt{4+\Delta_0^2 V^2}}\pi m_0 = \pi m_1 \tag{4.61}$$

$$\implies V = 2\sqrt{\frac{m_1^2 - m_0^2}{\Delta_1^2 m_0^2 - \Delta_0^2 m_1^2}} \tag{4.62}$$

Now, taking any Δ_j such that $j \geq 2$ and combining Eqs. (4.59), (4.60), and (4.62) and simplifying we find

$$m_0^2(\Delta_1^2 - \Delta_j^2) + m_1^2(\Delta_j^2 - \Delta_0^2) + m_j^2(\Delta_0^2 - \Delta_1^2) = 0 \,;\, m_i \to \frac{m_i}{2} \text{ if } \Delta_i = 0 \tag{4.63}$$

Equation (4.63) therefore corresponds to a set of $\max\left[\deg(\text{site } 1), \deg(\text{site } 2)\right] - 3$ Diophantine equations that must be solved simultaneously to find the values of m_i (and thus V, τ) that correspond to CA dynamics. Note, also, that in (4.63) we must replace $m_i \to \frac{m_i}{2}$ for whichever $\Delta_i = 0$.

Note, a particular solution for the first equation in (4.63) when $\Delta_0, \Delta_1, \Delta_2 \neq 0$ is $m_0 = \Delta_0, m_1 = \Delta_1, m_2 = \Delta_2$. Hence, using (4.16), the solution to (4.63) for $j = 2$ is given by

$$\begin{pmatrix} m_0 \\ m_1 \\ m_2 \end{pmatrix} = d \begin{pmatrix} -\left[(\Delta_1^2 - \Delta_2^2)w_1^2 - (\Delta_2^2 - \Delta_0^2)w_2^2\right]\Delta_0 - 2(\Delta_2^2 - \Delta_0^2)w_1 w_2 \Delta_1 \\ \left[(\Delta_1^2 - \Delta_2^2)w_1^2 - (\Delta_2^2 - \Delta_0^2)w_2^2\right]\Delta_1 - 2(\Delta_1^2 - \Delta_2^2)w_1 w_2 \Delta_0 \\ \left[(\Delta_1^2 - \Delta_2^2)w_1^2 + (\Delta_2^2 - \Delta_0^2)w_2^2\right]\Delta_2 \end{pmatrix} \tag{4.64}$$

To obtain the equivalent of (4.64) when, for example, $\Delta_0 = 0$, we must take $m_0 = 2\Delta_0$ instead of $m_0 = \Delta_0$ in the particular solution of (4.63) and relatedly must use $A = \frac{\Delta_1^2 - \Delta_2^2}{4}$ instead of $A = \Delta_1^2 - \Delta_2^2$ in (4.16). Similar adjustments must be made to B, m_1 or C, m_2 if $\Delta_1 = 0$ or $\Delta_2 = 0$ respectively.

Equation (4.64) provides all possible solutions for m_0, m_1, m_2 (and thus V, τ) that yield classical dynamics for any two site pair with $\Delta = \Delta_0, \Delta_1$, or Δ_2. As a corollary, this implies that there exist values of V, τ (beyond the trivial $V = 0$ or $\tau = 0$ solutions) for any measurement protocol that sequentially isolates pairs of sites on a lattice such

that all dynamics is a CA so long as the maximum degree of the lattice is at most 3. In other words, in this case, we may choose $\Delta_0 = 0$, $\Delta_1 = 1$, and $\Delta_2 = 2$ and (remembering to make the appropriate substitutions since $\Delta_0 = 0$) we find (4.64) becomes (4.34). As discussed in the main text, combining (4.34) with the $\Delta = 3$ condition yields a new Diophantine equation that may be solved numerically to find non-trivial solutions. For arbitrary maximal degree, a tower of Diophantine equations emerges. Whether solutions exist to these Diophantine equations for arbitrary maximal degree (and, if they exist, what they are) we leave as an open problem.

Below Eq. (4.34) we also made the comment that, in this case, m_0 is always even implying frozen dynamics. We here show that this is the case by way of contradiction. If m_0 is odd, then (4.34) implies

$$\frac{-32w_1w_2}{\gcd[-32w_1w_2, -3w_1^2 - 16w_2^2, -6w_1^2 + 32w_2^2]} \in 2\mathbb{Z} + 1 \tag{4.65}$$

i.e. an odd number. Hence, the gcd in the denominator must cancel all the powers of 2 in $-32w_1w_2$. This implies w_1 must be even, since otherwise $-3w_1^2 - 16w_2^2$ would be odd leaving the gcd in the denominator odd. Since w_1 and w_2 are coprime, w_2 must be odd. We factor out the powers of 2 from w_1 leaving $w_1 = 2^{a_1}w_1'$ where w_1' is odd. In the following, we will use two properties of the gcd:

$$\gcd(A, B) = \gcd(A, B + mA) \tag{4.66}$$
$$\gcd(A_1A_2, B) = \gcd(A_1, B)\gcd(A_2, B) \tag{4.67}$$

for $m \in \mathbb{Z}$ and A_1, A_2 coprime. We now get

$$\gcd[-32w_1w_2, -3w_1^2 - 16w_2^2, -6w_1^2 + 32w_2^2] \tag{4.68}$$
$$= \gcd[-(2^{5+a_1})w_1'w_2, -3(2^{2a_1})w_1'^2 - 2^4w_2^2, -3(2^{2a_1+1})w_1'^2 + 2^5w_2^2] \tag{4.69}$$
$$= \gcd[-(2^{5+a_1})w_1'w_2, -3(2^{2a_1})w_1'^2 - 2^4w_2^2, -3(2^{2a_1+2})w_1'^2] \tag{4.70}$$
$$= \gcd[(2^{5+a_1}), -3(2^{2a_1})w_1'^2 - 2^4w_2^2, (2^{2a_1+2})]A \tag{4.71}$$

where in the third line we have added twice the second term in (4.69) to the third term

using (4.66) and in the fourth line we focus only on terms in the gcd that may contribute a factor of 2, compiling the rest of the terms (through the use of (4.67)) in A given by

$$A = \gcd[-w_1' w_2, -3(2^{2a_1})w_1'^2 - 2^4 w_2^2, -3(2^{2a_1+2})w_1'^2] \gcd[(2^{5+a_1}), -3(2^{2a_1})w_1'^2 - 2^4 w_2^2, -3w_1'^2].$$

For the gcd (4.71) to cancel all the powers of 2 in $-32w_1w_2$ (thus making (4.65) odd), we therefore must have that

$$2^{5+a_1} = \gcd[(2^{5+a_1}), -3(2^{2a_1})w_1'^2 - 2^4 w_2^2, (2^{2a_1+2})] \tag{4.72}$$

This, however, is a contradiction since for $\gcd[(2^{5+a_1}), (2^{2a_1+2})] = 2^{5+a_1}$ we must have $a_1 \geq 3$, but then we have

$$\gcd[(2^{5+a_1}), -3(2^{2a_1})w_1'^2 - 2^4 w_2^2, (2^{2a_1+2})] \tag{4.73}$$

$$= 2^4 \neq 2^{5+a_1}. \tag{4.74}$$

Chapter 5

Fragmentation and Novel Prethermal Dynamical Phases in Disordered, Strongly-Interacting Floquet Systems

5.1 Introduction

Periodic driving of quantum systems has emerged as an exciting tool that may be used to engineer otherwise exotic behavior [144]. Furthermore, periodically driven (Floquet) systems may support phases that are forbidden in systems evolving under static Hamiltonians. Two prominent examples are Discrete Time Crystals [12, 13] and anomalous Floquet topological insulators [15, 42, 43]. Time Crystals are a proposed phase [181] in which continuous time translation symmetry of a system is spontaneously broken (in analogy with the spontaneous breaking of spatial translation symmetry in the formation of crystal lattices). Following a No-Go theorem for time crystals in static systems [147], it was discovered that it is possible for the discrete time translation symmetry in periodically driven systems to be spontaneously broken forming Discrete Time Crystals [146]. Anomalous Floquet topological insulators take advantage of the inherently periodic nature of the non-interacting quasi-energy spectrum of periodically driven systems to exhibit novel topological features in the band structure that are impossible for static systems. This anomalous band structure was realized in a model by Rudner-Lindner-Berg-Levin (RLBL) [20]. By adding a disordered on-site potential to the RLBL model, it was then found that the system supports a robust, new topological phase called the anomalous Floquet-Anderson topological insulator [15]. The physical manifestation of this exotic, topological band structure is the emergence of chiral edge modes

existing alongside a fully localized bulk. Both Discrete Time Crystals and the anomalous topological edge behavior of anomalous Floquet topological insulators have been realized across a variety of physical platforms [182–187].

A priori, it may be surprising that Floquet systems may exhibit robust phases since energy may be indefinitely absorbed from the drive, eventually leading to a featureless, infinite temperature state [148–150]. However, this thermalization may be combated using three main mechanisms: 1) The driven system is connected to a reservoir, which acts as a heat sink, leading to non-trivial non-equilibrium steady states [29, 159–161]. 2) Only systems where energy is absorbed exponentially slowly from the drive are considered, leading to a pseudo-stable "prethermal" phase [26, 28, 188–190]. 3) Disorder is added to the system, resulting in a localizing effect, that prevents thermalization. This phenomena is referred to as many-body localization (MBL) [27, 35, 38, 145, 150–154, 191] and is an interacting generalization of Anderson localization [30].

In constrained systems, there exists yet another route towards ergodicity breaking - Hilbert Space Fragmentation [164, 166, 167, 192]. In this case, the full Hilbert space is broken into subspaces that evolve independently. This leads to cases where a system may have some Krylov subspaces that thermalize while others do not. When the size of the non-thermal Krylov subspaces scales polynomially with system size (i.e. only representing a measure zero portion of the full Hilbert space), the states in these subspaces are referred to as quantum many-body scars [162–164].

In this work, we consider a broad class of Floquet models where hoppings between neighboring pairs of sites are sequentially activated. A large number of Floquet systems that have received theoretical and/or experimental attention are contained within this class of models (e.g. [15, 20, 42, 43, 170–174]). In chapter 4 it was shown that the dynamics of clean, interacting systems in this class of models may become exactly solvable for certain driving frequencies and interaction strengths. Specifically, these parameter values lead to evolution of Fock states into Fock states. The special points in parameter space where this occurs are found by solving an emergent set of Diophantine equations [175]. At other points in parameter space (also found via a set of Diophantine equations), the Hilbert space is fragmented into subspaces supporting either Frozen dynamics, classical cellular automation [176], or ergodic behavior.

Here, we add a disordered potential to the class of interacting, Floquet systems considered in chapter 4. We find that the disorder stabilizes, via K-body localization

(described below) [40], the dynamics of systems perturbed away from the special, Diophantine points in parameter space, leading to novel, robust phases. The exotic dynamics of these phases may include, for example, the spontaneous breaking of time translation symmetry to form Discrete Time Crystals.

Furthermore, we find that there are other regions in parameter space, away from any special, Diophantine points, that also represent K-body localized phases. These regions are given by values of interaction strength and driving frequency that 'almost' (see Sec. 5.3) satisfy Diophantine conditions. In addition, at the points in the clean model where Hilbert space fragmentation occurs, the added disorder ensures that the frozen and cellular automation Krylov subspaces are stable to perturbations (in driving frequency and interaction strength) away from the special points in parameter space. In some cases the subspace is localized by the disorder. In other cases, the cellular automation dynamics of the subspace is stabilized over long time scales but is eventually expected to thermalize.

Note, the stability of our results hinge on K-body localization instead of the full many-body localization. K-body localization is a generalization of MBL where a system containing up to a maximum number of particles, K, is localized by disorder (thus MBL is given in the limit of $K \to \infty$). Unlike MBL, which has only been rigorously established in one dimension, K-body localization is established in generic dimensional systems [40]. However, K-body localized systems containing more then K particles will eventually be thermalized via $K+1$ particle correlations. Thus, in the thermodynamic limit, we expect our results describe the system prethermally (except for cases, especially in 1D, where full MBL may occur).

To help illustrate our results throughout this work, we will use a Hubbard interacting RLBL-like model on a square lattice. In addition to the model being particularly clear for expository purposes, it has also been the center of recent interest in [43] where it was found that the model supports a novel topological phase called a correlation-induced anomalous Floquet insulator (CIAFI). The phase is characterized by a Hierarchy of topological invariants and supports quantized magnetization density. We describe how these results may be viewed from the perspective of this work and describe new insights into the system that the Diophantine framework provides.

The rest of this paper is structured as follows. In Section 5.2, we briefly review how Diophantine equations emerge in clean, periodically driven systems and their implications for the dynamics at special driving frequencies and interaction strengths (as

described in chapter 4). In Section 5.3, we perturbatively describe the evolution of these (so far clean) systems with parameter values close to the special, Diophantine points. Section 5.4 describes how, once disorder is added, the evolution in this perturbative regime becomes K-body localized. For the example case of the Hubbard-RLBL model, we provide a phase diagram for where this localization occurs. Section 5.5 describes the stability of subspaces when Hilbert space fragmentation is weakly broken by perturbing away from points where a few (but not all) of the conditions for Fock state to Fock state evolution are satisfied. In Section 5.6, we corroborate the above results with numerical evidence. Finally, in Section 5.7 we provide concluding remarks.

5.2 Interacting Floquet models, Diophantine Equations, and Hilbert Space Fragmentation

Here, we briefly review the identification of special evolution points following [3]. We look for conditions on fermion models to evolve Fock states into Fock states deterministically. We consider periodically-driven models where hopping between neighboring sites are sequentially activated. Namely, we divide the period, T, of the Floquet drive into M steps where, during step m, particles are only allowed to hop between pairs of sites given by a set A_m. Interactions are then added to this free-hopping evolution, but we restrict ourselves to interactions that do not contain terms connecting two (or more) of the otherwise disjoint pairs with activated hopping. Specifically, evolution during the Floquet period, $U(T)$, is given by

$$U(T) = U_M ... U_2 U_1 \tag{5.1}$$

where $U_m = e^{-i\tau \mathcal{H}_m}$, $\tau = \frac{T}{M}$, and

$$\mathcal{H}_m = -t_{hop} \sum_{(i,j)\in A_m;\sigma} (a^\dagger_{i,\sigma} a_{j,\sigma} + h.c.) + \mathcal{H}_{\text{int}}(\mathbf{V}_m). \tag{5.2}$$

where $\mathbf{V}_m$ is a set of interaction parameters. For the rest of this work, we will set $t_{\text{hop}} = 1$ unless otherwise noted.

As an example, consider the case of the RLBL model with Hubbard interactions. In this case, we set $M = 4$, choose A_m as given in Fig. 1, and set

$$\mathcal{H}_{\text{int}}^{\text{Hubbard}}(V) = V \sum_i n_{i,\uparrow} n_{i,\downarrow} \tag{5.3}$$

with $n_{i,\sigma} = a_{i,\sigma}^\dagger a_{i,\sigma}$. Note, the Hubbard interaction is on-site and thus leaves the pairs connected by A_m disjoint.

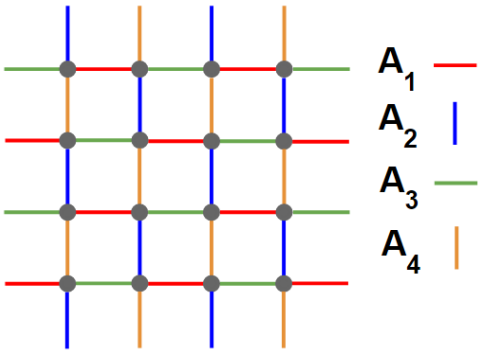

FIGURE 1: The RLBL model. Hopping is sequentially activated among neighbouring sites connected by the set A_m, $m = 1, ..., 4$.

The next step is to find conditions for when individual, activated hopping pairs map Fock states into Fock states. Since the site pairs are disjoint, we may do this individually for each pair during each step m of the evolution.

In the Hubbard-RLBL model a 2-site pair has 16 possible initial Fock states. Let us first consider the case of a single spin up at one site with an empty neighbor. We can ignore the interacting term, and compute directly the probability, p, for the particle to hop to site 2. We have

$$p = |\langle vac| a_2 e^{i\tau(a_1^\dagger a_2 + a_2^\dagger a_1)} a_1^\dagger |vac\rangle|^2 = \sin^2 \tau,$$

showing that when $\tau = \frac{\pi}{2}\ell$ with $\ell \in \mathbb{Z}$, the evolution maps this particular Fock state to a Fock state. Namely, the particle will remain at its initial site for τ with ℓ even and hop to the neighboring site when ℓ is odd. We repeat this procedure for the other 15 possible initial Fock states. The lines in the following table summarize the conditions

we find on τ and V and the resulting type of evolution:

particles	τ	V
1 or 3, frozen	$\frac{\pi}{2}\ell$, ℓ even	arbitrary
1 or 3, swap	$\frac{\pi}{2}\ell$, ℓ odd	arbitrary
2, opposite spins, frozen	$\frac{\pi}{2}\sqrt{2mn-n^2}$, n even	$\frac{4(n-m)}{\sqrt{2mn-n^2}}$
2, opposite spins, swap	$\frac{\pi}{2}\sqrt{2mn-n^2}$, n odd	$\frac{4(n-m)}{\sqrt{2mn-n^2}}$
otherwise	any	any

(5.4)

where $\ell, m, n \in \mathbb{Z}$, and $2mn - n^2 > 0$. The left column refers to the number of particles in the initial state of the 2-site pair (spin-up + spin-down) and the type of evolution we get. Thus, for example, if n is odd, and we start with a an up/down pair (a doublon) sitting at site 1, the doublon will hop to site 2. On the other hand, if n is even, the doublon will stay at site 1.

For a generic Fock state in the full system to evolve to another Fock state, we need every 2-site activated pair to evolve deterministically. Hence, we require all the conditions in Eq. (5.4) to be satisfied simultaneously. This leads to the following restriction on ℓ, m, n

$$\ell^2 + n^2 = 2mn. \tag{5.5}$$

The equation (5.5), where we are only interested in integer solutions for ℓ, m, n, is a Diophantine equation [175]. Diophantine equations are an active area of mathematical research and, contrary to their often innocuous appeareance, there only exists general solution methods for a few special classes of equations.

For the class of interacting Floquet models considered in this work, the Diophantine equations that emerge from the conditions of Fock state to Fock state evolution may not, in general, be solvable. Fortunately, in the Hubbard-RLBL case, Eq. (5.5) is a polynomial Diophantine equation of degree 2 for which general solution methods exist. The solutions can be parameterized as

$$\ell = d(w_1^2 - w_2^2) \tag{5.6a}$$
$$m = d(w_1^2 + w_2^2) \tag{5.6b}$$
$$n = d(w_1 + w_2)^2 \tag{5.6c}$$

where $w_1, w_2 \in \mathbb{Z}$, w_1, w_2 are coprime, and $d \in \frac{1}{\xi}\mathbb{Z}$ with $\xi = gcd((w_1^2 - w_2^2), (w_1^2 + w_2^2), (w_1 + w_2)^2)$.

Thus, the following values of τ, V yield deterministic Fock state to Fock state evolution in the Hubbard-RLBL model

$$\tau = \frac{\pi}{2} d(w_1^2 - w_2^2) \; ; \; V = \frac{8 w_1 w_2}{|w_1^2 - w_2^2|}. \tag{5.7}$$

Importantly, note that the analysis leading to Eq. (5.7) was independent of the fact that the driving procedure was RLBL. Thus, any periodic drive with sequentially activated hopping pairs, in any dimension, with Hubbard interactions will also exhibit deterministic Fock state to Fock state evolution at the special points in parameter space given by Eq. (5.7).

In summary, for each step m in the Floquet evolution, the evolution of a special, Diophantine point given by an evolution time τ_0 and a set of interaction parameters $\mathbf{V}_{0,m}$ is given by

$$U_m(\mathbf{V}_{0,m}, \tau_0) = \mathcal{P}_m \tag{5.8}$$

where $\mathcal{P}_m$ is a (complex) permutation matrix on Fock states [1]. Furthermore, for local interactions, $\mathcal{P}_m$ deterministically updates the occupation of individual sites based on the occupation of neighboring sites. Starting from a product state, the evolution under an operator such as this, up to a phase, can be thought of as a classical cellular automation. It is for this reason that evolution such as this is sometimes referred to as "automation" dynamics [177].

[1] A complex permutation matrix is a matrix where every row and column has a single non-zero element whose modulus is 1.

What happens if only some of the conditions for Fock state to Fock state evolution are satisfied? In this case, the Hilbert space will fragment into subspaces. States in some subspaces will still evolve under cellular automation, while states in other subspaces are, in general, expected to ergodically explore their subspace.

For example, consider a Hubbard-Floquet model with a generic sequentially activated hopping. Like the Hubbard-RLBL model, the conditions for Fock state to Fock state evolution in this model are given by (5.4) (see discussion after Eq. (5.7)). Now suppose only the fourth condition in (5.4) is satisfied (for example $n = 3, m = 2$ with $\tau = \frac{\sqrt{3}}{2}\pi$ and $V = \frac{4\sqrt{3}}{3}$). This condition will state that an up down pair at neighbouring sites will swap spins. Therefore, the subspace of states with exactly one particle on each site (though the spin of each particle is left generic) is invariant under the evolution. Evolving any state in this subspace by U_m will still be equivalent to evolving it by $\mathcal{P}_m$ since there are no 2-site activated pairs with 1 or 3 particles in the system. This implies that this exponentially large subspace will evolve as a classical process of spin swaps. On the other hand, Fock states that do have 2-site pairs with 1 or 3 particles will evolve into superpositions of Fock states under U. For general hopping activation sequences, this leads to an ergodic exploration of the complimentary subspace. The full Hilbert space is thus fragmented into independent subspaces exhibiting either cellular automation or ergodic evolution.

5.3 Quantum dynamics in slow motion

We now investigate how the systems considered in the previous section evolve when parameter values are perturbed away from the special, Diophantine points. Now the evolution generates super-positions of Fock states and therefore entanglement. In this case, the evolution during each Floquet period is given by the cellular automation of the special point times an evolution with an effective local Hamiltonian during a reduced time compared with the original evolution period. In other words, the correction to the classical cellular automation is a 'slow motion' quantum dynamics.

5.3.1 Perturbation in Time

We first consider a perturbation in the evolution time $\tau = \tau_0 + \delta\tau$. We therefore have that evolution of a step m is given by

$$U_m(\mathbf{V}_{0,m}, \tau_0 + \delta\tau) = U_m(\mathbf{V}_{0,m}, \tau_0) U_m(\mathbf{V}_{0,m}, \delta\tau) \tag{5.9}$$
$$= \mathcal{P}_m e^{-i\delta\tau\mathcal{H}_m} \tag{5.10}$$

Combining this with Eq. (5.1) we have that the evolution of the full Floquet period is given by

$$U = \mathcal{P}_M e^{-i\delta\tau\mathcal{H}_M} ... \mathcal{P}_2 e^{-i\delta\tau\mathcal{H}_2} \mathcal{P}_1 e^{-i\delta\tau\mathcal{H}_1} \tag{5.11}$$
$$\equiv \mathcal{P} U_{quantum} \tag{5.12}$$

where $\mathcal{P} = \mathcal{P}_M ... \mathcal{P}_2 \mathcal{P}_1$ is the unperturbed permutation, and the $U_{quantum}$ is the quantum correction to the dynamics:

$$U_{quantum} = \tag{5.13}$$
$$= e^{-i\delta\tau\mathcal{P}_1^\dagger \mathcal{P}_2^\dagger \mathcal{P}_{M-1}^\dagger \mathcal{H}_M \mathcal{P}_{M-1} .. \mathcal{P}_2 \mathcal{P}_1} ... e^{-i\delta\tau\mathcal{P}_1^\dagger \mathcal{H}_2 \mathcal{P}_1} e^{-i\delta\tau\mathcal{H}_1}.$$

We note that the as long as the range of the permutations $\mathcal{P}$ is finite, the dynamics $U_{quantum}$ cannot build correlations further away from the range of allowed classical dynamics. Moreover, the generation of super-positions of states is now governed by the slow time scale $\delta\tau$.

When tracking the evolution of a cluster of initial particles when the perturbation is small ($\delta\tau t_{\text{hop}}, \delta\tau V_{0,m} \ll 1$), it is convenient to think of the quantum correction as $U_{quantum} = e^{-i\delta\tau\mathcal{H}_{\text{eff}}}$ where $\mathcal{H}_{\text{eff}}$ is given to lowest order in $\delta\tau$ as

$$\mathcal{H}_{\text{eff}} \simeq \sum_{m=1}^{M} \mathcal{P}_1^\dagger \mathcal{P}_2^\dagger ... \mathcal{P}_{m-1}^\dagger \mathcal{H}_m \mathcal{P}_{m-1} ... \mathcal{P}_2 \mathcal{P}_1. \tag{5.14}$$

Let us again take as an example the Hubbard-RLBL model. In this case, the vicinity of frozen dynamics is particularly appealing. For frozen dynamics, $\mathcal{P}_m = I$ and thus $H_{\text{eff}} \simeq H_4 + H_3 + H_2 + H_1$ simply becomes the static Hubbard Hamiltonian on the square lattice with $V \to 4V_0$. This means that, to a good approximation, $\mathcal{H}_{Floquet} \simeq \frac{\delta\tau}{T}\mathcal{H}_{Hubbard}(4V_0)$ with $\mathcal{H}_{Floquet}$ the usual Floquet Hamiltonian defined by $U(T) = e^{-iT\mathcal{H}_{Floquet}}$. In other words, the stroboscopic evolution in the system is that of a slow-motion static Hubbard evolution, i.e. after N evolution cycles, at time TN, the system will have

evolved under a static Hubbard Hamiltonian (with interaction $4V_0$) for a reduced time $\delta\tau N$. When $\mathcal{P}_m \neq \mathbb{I}$, the evolution is a sequence of permutations followed by slowed, modified Hubbard evolution. Note, the modified Hubbard evolution (given by specializing (5.14) to the Hubbard-RLBL case) includes hopping terms that are modified by the permutations of lattice sites while the interaction terms are unaffected (since $\mathcal{H}_{\text{int}}^{\text{Hubbard}}$ counts the number of doublons, which is preserved under the freezing and swapping operations generating the dynamics at the special Diophantine points).

5.3.2 Perturbation in Interaction Strength

Now, suppose instead that we consider a perturbation in interaction parameters $\mathbf{V}_m = \mathbf{V}_{0,m} + \delta\mathbf{V}_m$. In the case that $\tau_0 \delta V_m \ll 1$ for all $\delta V_m \in \delta\mathbf{V}_m$, we expand

$$\begin{aligned} &U_m(\mathbf{V}_{0,m} + \delta\mathbf{V}_m, \tau_0) \\ &\approx \mathcal{P}_m \left(1 - i\int_0^{\tau_0} ds e^{is\mathcal{H}_m(\mathbf{V}_{0,m})} \delta\mathcal{H}_{\text{int}} e^{-is\mathcal{H}_m(\mathbf{V}_{0,m})}\right) \\ &\equiv \mathcal{P}_m e^{-i\tau_0 \mathcal{H}_{\text{eff},m}} \end{aligned} \tag{5.15}$$

with $\mathcal{H}_{\text{eff},m}$ defined in the last line. Thus, in a similar fashion to the perturbation in τ case, we find that

$$U = \mathcal{P}_M ... \mathcal{P}_2 \mathcal{P}_1 e^{-i\tau_0 \mathcal{H}_{\text{eff}}} \tag{5.16}$$

with

$$\mathcal{H}_{\text{eff}} \simeq \sum_{m=1}^{M} \mathcal{P}_1^\dagger \mathcal{P}_2^\dagger ... \mathcal{P}_{m-1}^\dagger \mathcal{H}_{\text{eff},m} \mathcal{P}_{m-1} ... \mathcal{P}_2 \mathcal{P}_1. \tag{5.17}$$

Illustrating again with the Hubbard-RLBL model, $H_{\text{eff},m}$ may be written explicitly in terms of creation and annihilation operators by solving each disjoint 2-site pair in $\int_0^{\tau_0} ds e^{is\mathcal{H}_m(\mathbf{V}_{0,m})} \delta\mathcal{H}_{\text{int}} e^{-is\mathcal{H}_m(\mathbf{V}_{0,m})}$ separately and then summing. We find, to lowest order in $\tau_0 \delta V$, that

$$H_{\text{eff},m} = \delta V \sum_{i \in \text{2-site pairs}} n_{\leq \text{2-part},i} \mathbf{a}_i^\dagger \mathcal{T} \mathbf{a}_i n_{\leq \text{2-part},i} + n_{>\text{2-part},i} \tag{5.18}$$

where we have defined

$$\mathcal{T} = \frac{-1}{16+V_0^2}\begin{pmatrix} 12-V_0^2 & -4 & V_0 & V_0 \\ -4 & 12-V_0^2 & V_0 & V_0 \\ V_0 & V_0 & 4 & 4 \\ V_0 & V_0 & 4 & 4 \end{pmatrix} \tag{5.19}$$

$$\mathbf{a}_i = \begin{pmatrix} a_{2\uparrow}a_{2\downarrow} & a_{1\uparrow}a_{1\downarrow} & a_{1\uparrow}a_{2\downarrow} & a_{2\uparrow}a_{1\downarrow} \end{pmatrix}^T \tag{5.20}$$

and $n_{>2\text{-part},i}$ projects onto the subspace with the ith 2-site pair having more than 2 particles, i.e.

$$\begin{aligned} n_{>2\text{-part}} &= 1 - n_{\leq 2\text{-part}} \\ &= \sum_{\substack{a,b,c \in \{1\uparrow, 1\downarrow, 2\uparrow, 2\downarrow\} \\ a \neq b \neq c}} n_a n_b n_c. \end{aligned} \tag{5.21}$$

In other words, evolution under $H_{\text{eff},m}$ corresponds to correlated hopping for any 2-site pairs containing 2 particles and a δV energy cost of having a two-site pair with 3 or more particles.

5.3.3 Away From Special Points

Slowed effective quantum dynamics corrections to classical Fock state permutations may occur away from the vicinity of the special Diophantine points. Here we explore other regions in parameter space, far from special points, where the conditions for Fock state to Fock state evolution are approximately satisfied. Specifically, consider the evolution at step m consisting of the set A_m of the activated two site pairs, and let $\mathcal{H}_{(i,j)}$ be the Hamiltonian for $(i,j) \in A_m$.

Let us define:

$$D_{(i,j)} = \inf_{\mathcal{P}_{(i,j)}} ||e^{-i\tau\mathcal{H}_{(i,j)}} - \mathcal{P}_{(i,j)}||_{HS} \; ; \; D = \max_{(i,j)} D_{(i,j)} \tag{5.22}$$

where $||\cdot||_{HS}$ is the Hilbert-Schmidt norm of the (i,j) subspace. When $D_{(i,j)} \ll 1$ we can say that the conditions for Fock state to Fock state evolution are approximately satisfied for $\mathcal{H}_m$ and τ.

We may now choose a $\mathcal{P}_{(i,j)}$ that minimizes $D_{(i,j)}$ and write

$$e^{-i\tau\mathcal{H}_{(i,j)}} \equiv \mathcal{P}_{(i,j)} e^{-i\tau\mathcal{H}_{eff,(i,j)}}. \tag{5.23}$$

As before, $e^{-i\tau\mathcal{H}_{eff,(i,j)}}$ is close to the identity matrix when D is small, therefore the evolution corresponds to a permutation augmented with slowed quantum dynamics. Using Eq. (5.23) the evolution of the full system for step m is

$$U_m = \bigotimes_{(i,j)\in A_m} e^{-i\tau\mathcal{H}_{(i,j)}} = \mathcal{P}_m e^{-i\tau\mathcal{H}_{eff,m}} \tag{5.24}$$

where we have defined

$$\mathcal{P}_m = \bigotimes_{(i,j)\in A_m} \mathcal{P}_{(i,j)} \tag{5.25}$$

$$\mathcal{H}_{eff,m} = \sum_{(i,j)\in A_m} \mathcal{H}_{eff,(i,j)}. \tag{5.26}$$

Equation (5.24) is of the general form of equations (5.15) and (5.10), and we find analogously that the evolution of the full Floquet period is given by (5.16) and (5.17).

To illustrate the appearance of slow dynamics parameter space regions away from special points, in Fig. 2 we plot regions where the Diophantine conditions are approximately satisfied in the Hubbard-RLBL model. Namely, we plot regions where the Hilbert-Schmidt norm of the difference between the evolution of an activated pair and a SWAP or Identity permutation is less than some small cutoff. In the figure, we consider separately when 2 site pairs with 1 or 3 particles evolve approximately as a permutation and when 2 site pairs with 2 particles of opposite spin evolve approximately as a permutation. Parameters where pairs with 1 or 3 particles are approximately frozen (perfect swapping) are colored green (yellow) while parameters where pairs with 2 particles of opposite spin are approximately frozen (perfect swapping) are colored blue (red). Thus, D is small only in regions of overlapping colors. Note that each special, Diophantine point is surrounded by a region of overlapping colors, but not all regions of overlapping colors contain a special point.

A couple of remarks are in order. Note that in the Hubbard-RLBL model, special points are only found when all activated 2-site pairs are frozen or when all the pairs are perfect swapping. This can be seen from Eq. (5.6) by verifying that the parity of ℓ and n

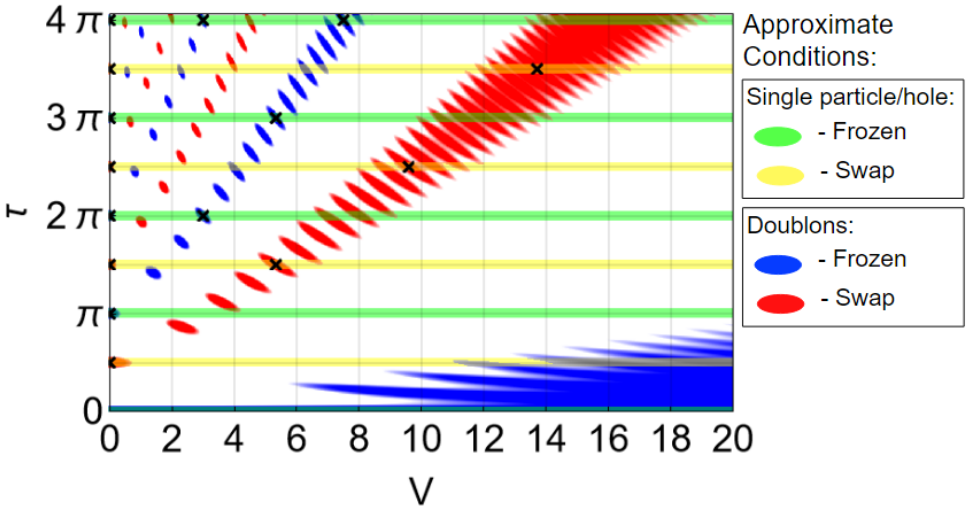

FIGURE 2: Parameter space regions where the Diophantine conditions (5.4) are approximately satisfied. Specifically, regions where the Hilbert-Schmidt norm of the difference between the evolution of a step for an activated 2-site pair and the Fock state permutation corresponding to the satisfaction of the i^{th} condition in (5.4) is less than $\epsilon = 0.1$ are filled with color i (as given in the legend). The special, Diophantine points where evolution is exactly a Fock state permutation are marked with a black "X."

come out the same for any choice of d, w_1, w_2 (see chapter 4). Indeed, in Fig. 2 the special points (represented by x) appear only when both single particle and doublon sectors are simultaneously perfectly swapping (or simultaneously perfectly frozen). However, Fig. 2 also shows that it is possible to approximately have perfect swapping in the 1 and 3 particle sector while pairs with 2 particles are approximately frozen (and vice versa). Another thing to note is that when only some of the Diophantine conditions are approximately satisfied, the fragmented Krylov subspaces that would emerge if the conditions were perfectly satisfied may become connected by the slowed dynamics $\mathcal{H}_{eff}$.

We note that an alternative measure for how far the evolution is from permutative was presented in chapter 4, based on the function

$$F_{p,q}(U) = -\log \frac{||U||_{p,q}}{dim(U)^{1/q}} = -\frac{1}{q} \log \frac{\sum_{n,m} |U_{n,m}|^p}{dim(U)} \tag{5.27}$$

defined on unitary matrices where $dim(U)$ is the dimensionality, and $||U||_{p,q} = (\sum_{n,m} |U_{n,m}|^p)^{1/q}$ is the p, q matrix entry-wise norm. It is straightforward to check that for $p > 2, q > 0$,

the function F reaches its minimum $F_{p,q}(U) = 0$ if an and only if U is a complex permutation matrix. However in figure 2 we wanted to distinguish between the different types of permutative behavior (frozen vs perfect swapping) and so instead focused on using (5.22).

In the next section, we add disorder to the system and find that the slowed dynamics is (in some cases) either K-body or many-body localized by the disorder. This then stabilizes the cellular automation dynamics in regions where the conditions for Fock state to Fock state evolution are approximately satisfied leading to robust phases.

5.4 Stabilizing Classical Evolution with Disorder

We now add disorder to the periodically driven, interacting models considered above. Specifically, we investigate Floquet drives of the form

$$U(T) = U_{\text{dis}} U_M ... U_2 U_1 \tag{5.28}$$

where we take U_{dis} to be evolution under a disordered on-site potential with no hopping, i.e.

$$U_{dis} = e^{-i\tau \mathcal{H}_{dis}} \tag{5.29}$$

where

$$\mathcal{H}_{dis} = \sum_{i,\sigma} v_i n_{i,\sigma} \tag{5.30}$$

with v_i uniformly distributed in $[-W, W]$. However, the exact form of disorder doesn't play a role in the argument [2].

For Floquet systems of this type, sufficiently strong disorder will (either K-body or many-body) localize the slowed dynamics but leave the cellular automation dynamics unaffected. This happens when the cellular automation has a finite order and when

[2] Note, for example, if H_{dis} is included as a constant term throughout the evolution instead of only being applied during the U_{dis} portion of the drive, then all our results still hold [43]. In this case, the strength of the disorder during the first 4 steps of the floquet drive must be kept small. The strength during the 5^{th}, disorder only, step may be made large by lengthening the time that U_{dis} is applied.

the disorder is large compared to the slowed evolution. This leads to the emergence of robust phases with stabilized cellular automation dynamics.

5.4.1 Dynamics with disorder close to $\mathcal{P} = I$

To illustrate how this occurs, we begin with the simpler case of when the cellular automation of the full Floquet period (though not necessarily each step m of the drive) is the identity, i.e.

$$\mathcal{P}_M ... \mathcal{P}_2 \mathcal{P}_1 \equiv \mathcal{P} = I \tag{5.31}$$

where we have defined $\mathcal{P}$ as the full cellular automation. Examples of cellular automata of this type include frozen dynamics and the perfect swapping Hubbard-RLBL model with periodic boundary conditions (e.g. $\tau = \frac{\pi}{2}$, $V = 0$ or $\tau = \frac{3\pi}{2}$, $V = \frac{16}{3}$).

Using (5.16) we find that, for parameters where the Diophantine conditions are approximately satisfied, the evolution of one Floquet period T may be written

$$\begin{aligned} U &= U_{\text{dis}} \mathcal{P} e^{-i\tau \mathcal{H}_{\text{eff}}} && (5.32)\\ &= U_{\text{dis}} e^{-i\tau \mathcal{H}_{\text{eff}}} && (5.33)\\ &\approx U_{\text{dis}} \left(1 - i \int_0^\tau dt e^{it\mathcal{H}_{\text{dis}}} \mathcal{H}_{\text{eff}}(t) e^{-it\mathcal{H}_{\text{dis}}}\right) && (5.34)\\ &= \mathcal{T} e^{-i\int_0^\tau dt \mathcal{H}(t)} && (5.35) \end{aligned}$$

where

$$\begin{aligned} \mathcal{H}_{\text{eff}}(t) &= e^{-it\mathcal{H}_{\text{dis}}} \mathcal{H}_{\text{eff}} e^{it\mathcal{H}_{\text{dis}}} && (5.36)\\ \mathcal{H}(t) &= \mathcal{H}_{\text{dis}} + \mathcal{H}_{\text{eff}}(t) && (5.37) \end{aligned}$$

We therefore have that the cellular automation evolution will be stable if the Hamiltonian (5.37) is localized.

To see when this is the case, we rewrite (5.37) as

$$\mathcal{H}(t) = \mathcal{H}^{(0)} + V(t) \tag{5.38}$$

where

$$\mathcal{H}^{(0)} = \mathcal{H}_{\text{dis}} + \overline{\mathcal{H}_{\text{eff}}(t)} \tag{5.39}$$

$$V(t) = \mathcal{H}_{\text{eff}}(t) - \overline{\mathcal{H}_{\text{eff}}(t)};\ \overline{V(t)} = 0. \tag{5.40}$$

with $\overline{f(t)} = \frac{1}{\tau}\int_0^\tau ds f(s)$ the time average and $V(t)$ is the strictly time-dependent part of $\mathcal{H}(t)$.

We note that $\mathcal{H}_{\text{eff}}$ is a sum of local Hamiltonians sandwiched by $\mathcal{P}_m$ (5.17) and is thus also local. This implies that $V(t)$ is local as well and may be written

$$V(t) = \sum_i V_i(t). \tag{5.41}$$

Whenever $\mathcal{H}^{(0)}$ is MBL, we may use a theorem by Abanin, De Roeck, and Huveneers [38] to show that the weak, local drive $V(t)$ will not ruin the localization of $\mathcal{H}^{(0)}$. Namely, that the Hamiltonian (5.37) will be MBL whenever

$$\tau||V_i(t)||_{HS} \ll 1 \text{ and } \frac{\tau||V_i(t)||_{HS}^2}{W} \ll 1 \tag{5.42}$$

Note that $\tau||\mathcal{H}_{\text{eff}}||_{HS} \ll 1$ implies $\tau||V_i(t)||_{HS} \ll 1$. Hence, for sufficiently strong disorder, the Hamiltonian (5.37) will be MBL so long as $\mathcal{H}^{(0)}$ is MBL. A corrollary of this result is that (5.37) will be K-body localized so long as $\mathcal{H}^{(0)}$ is K-body localized [3].

We have thus reduced the problem to asking whether the static Hamiltonian $\mathcal{H}^{(0)}$ is localized. For 1D systems, we expect $\mathcal{H}^{(0)}$ to be MBL. This is because, using a KAM type scheme, it has been shown that models of this type (i.e. Hamiltonians with a

[3] This is because [38] uses a KAM type scheme to, order by order, find exactly the dressed ℓ-bits of the Hamiltonian and thus prove it is MBL. This procedure may thus be stopped at some order K to show K-body localization.

disordered term plus a weak, local interacting term) are MBL in 1D under the weak assumption of Limited Level Attraction (see [35]). In higher dimensions, rare regions of weak disorder can cause an avalanche effect that ruins the MBL [36, 37, 41, 193]. This delocalization, however, happens on exponentially long time scales and thus the system is prethermally localized. Furthermore, these systems are expected to be K-body localized. This is because the probability that the K-particle energy spectrum features the accidental resonances that ruin localization goes to zero in the thermodynamic limit [40].

In summary, we have shown that when disorder is added to a Floquet system near a special point with $\mathcal{P} = I$, then the dynamics is stabilized by (many-body or K-body) localization and thus corresponds to a robust prethermal phase. We expect that as we move further away from special points, the effective evolution would resemble that of random local unitaries in which spreading has been studied in e.g. [194].

5.4.2 Discrete Time Crystals

We now consider a Floquet drive that corresponds to a perfect cellular automation with some finite order ≥ 1, i.e.

$$\mathcal{P}^{\mathcal{O}} = I; \ \mathcal{O} \in \mathbb{N}. \tag{5.43}$$

Such dynamics, when stable to disorder and $\mathcal{O} > 1$, is often called a discrete time crystal. Indeed, the original time translation symmetry of the Floquet drive, T, has been spontaneously broken in these interacting, localized Floquet phases that now have $\mathcal{O}T$ time translation symmetry. Let us consider the evolution after $\mathcal{O}$ Floquet periods given by

$$U^{\mathcal{O}} = \left[U_{\text{dis}}\mathcal{P}e^{-i\tau\mathcal{H}_{\text{eff}}}\right]^{\mathcal{O}} \tag{5.44}$$

$$= \left[U_{\text{dis}}\mathcal{P}\right]^{\mathcal{O}} e^{-i\tau\mathcal{H}_{\mathcal{O},\text{eff}}} \tag{5.45}$$

where, to first order in $\tau||\mathcal{H}_{eff,(i,j)}||_{HS}$,

$$\mathcal{H}_{\mathcal{O},\text{eff}} = \sum_{a=0}^{\mathcal{O}-1} \left(\mathcal{P}^{\dagger}U_{\text{dis}}^{\dagger}\right)^{a} \mathcal{H}_{\text{eff}} \left(U_{\text{dis}}\mathcal{P}\right)^{a}. \tag{5.46}$$

Now, note that since $\mathcal{P}$ is a cellular automation (and thus updates the occupancy of sites based on the occupancy of nearby sites), it transforms the number operator of a site i in the following way

$$\begin{aligned}\mathcal{P}^\dagger n_i \mathcal{P} = \sum_{i_1} P_{i_1} n_{i_1} + \sum_{i_1,i_2} P_{i_1 i_2} n_{i_1} n_{i_2} \\ + ... + \sum_{i_1,i_2,...,i_\lambda} P_{i_1 i_2 ... i_\lambda} n_{i_1} n_{i_2} ... n_{i_\lambda}\end{aligned} \tag{5.47}$$

where the coefficients $P_{i_1}, P_{i_1 i_2}, ..., P_{i_1 i_2 ... i_\lambda}$ are only non-zero when all the sites $i_1, i_2, ..., i_\lambda$ are within some finite region surrounding site i. This implies that

$$\begin{aligned}&[U_{\text{dis}}\mathcal{P}]^{\mathcal{O}} e^{-i\tau\mathcal{H}_{\mathcal{O},\text{eff}}} \\ &= \mathcal{P}^{\mathcal{O}} e^{-i\tau\mathcal{H}_{\text{loc}}} e^{-i\tau\mathcal{H}_{\mathcal{O},\text{eff}}} \\ &= e^{-i\tau\mathcal{H}_{\text{loc}}} e^{-i\tau\mathcal{H}_{\mathcal{O},\text{eff}}}\end{aligned} \tag{5.48}$$

where

$$\mathcal{H}_{\text{loc}} = \sum_{a=0}^{\mathcal{O}-1} \mathcal{P}^a \mathcal{H}_{\text{dis}} \mathcal{P}^a. \tag{5.49}$$

Note that $\mathcal{H}_{\text{loc}}$ is a sum of local terms as in (5.47). We now repeat the steps (5.33) to (5.38) to find that

$$U^{\mathcal{O}} = \mathcal{T} e^{-i\int_0^\tau dt \mathcal{H}(t)} \tag{5.50}$$

with

$$\mathcal{H}(t) = \mathcal{H}^{(0)} + V(t) \tag{5.51}$$

and

$$\mathcal{H}^{(0)} = \mathcal{H}_{\text{loc}} + \overline{\mathcal{H}_{\mathcal{O},\text{eff}}(t)} \tag{5.52}$$

$$V(t) = \mathcal{H}_{\mathcal{O},\text{eff}}(t) - \overline{\mathcal{H}_{\mathcal{O},\text{eff}}(t)} \tag{5.53}$$

$$\mathcal{H}_{\mathcal{O},\text{eff}}(t) = e^{-it\mathcal{H}_{\text{loc}}} \mathcal{H}_{\mathcal{O},\text{eff}} e^{it\mathcal{H}_{\text{loc}}} \tag{5.54}$$

Again using [38], we find that (5.51) is k-body (many-body) localized whenever $\mathcal{H}^{(0)}$ is k-body (many-body) localized and (5.42) are satisfied. Again, since $\mathcal{H}^{(0)}$ is a fully MBL term plus a weak, local interacting term, we expect it to be k-body (many-body) localized as discussed in the paragraph following (5.42).

We remark that the range of $\mathcal{H}_{\mathcal{O},\text{eff}}$, and thus $||V_i(t)||_{HS}$, increases with increasing $\mathcal{O}$. By (5.42), this implies that the region in parameter space where the system is localized will shrink rapidly for increasing $\mathcal{O}$, however the region will remain finite so long as $\mathcal{O}$ is finite. This also suggests that general cellular automations without finite order are not likely to be stabilized by the disorder. For example, for the perfect swapping RLBL model, the bulk cellular automation has order 1 while the cellular automation at the edge has infinite order (since particles are transported chirally along the edge). This is another way of viewing why the edge modes of an interacting, perfect-swapping RLBL model thermalize [42, 43] even while the system with periodic boundary conditions does not.

5.5 Stabilized Subspaces

We now investigate when interacting models with sequentially activated hopping may exhibit stabilized cellular automation dynamics in Krylov subspaces even when the full Hilbert space does not support such dynamics. Namely, we consider two main situations where this may occur.

First, we can have all the Diophantine conditions approximately satisfied, but the corresponding cellular automation has infinite order when acting on some states (e.g edge states in the RLBL model). However, some initial Fock states may exhibit finite orbits under the cellular automation. These orbits may then be stabilized by disorder.

Another possibility is when only some of the Diophantine conditions are approximately satisfied. Here, the Hilbert space fragmentation (that occurs when a few of the Diophantine conditions are perfectly satisfied, see Ch. 4) may be stabilized by the disorder.

In both these cases, we are thus interested in Floquet evolution that may be written

$$U(T) = U_{\text{dis}} U_{\mathcal{P}} e^{-i\tau \mathcal{H}_{\text{eff}}}. \tag{5.55}$$

Here $U_{\mathcal{P}}$ maps number states to number states only in a subspace n associated with satisfied conditions. Let us consider cases where

$$U_{\mathcal{P}}^{\mathcal{O}}|n\rangle = |n\rangle \tag{5.56}$$

for some finite $\mathcal{O} \in \mathbb{N}$.

We now ask whether the subspace n is localized under the evolution $U(T)$.

We first specialize to the situation where the subspace n is closed under the evolution of $U(T)$, i.e.

$$U(T)|n\rangle = |n'\rangle \ \ \forall \ \ |n\rangle \in n \tag{5.57}$$

where $|n'\rangle \in n$. A simple example when this (approximately) happens is when starting with a few particles far away from the edge in the RLBL model. A more elaborate example will be discussed below.

In this case, $U(T)$ is therefore block diagonal with

$$U(T) = \begin{pmatrix} U_{n^c} & 0 \\ 0 & U_n \end{pmatrix} \tag{5.58}$$

where U_n acts on the space n and U_{n^c} acts on its compliment n^c.

Now, using (5.55) and (5.56) and repeating the steps (5.44) through (5.50), we have that $U_n^{\mathcal{O}}$ is localized.

We again illustrate our point using the Hubbard-RLBL model. Consider the case where activated pairs with 1 or 3 particles are approximately perfect swapping while pairs with 2 particles of opposite spin are approximately frozen (i.e. regions in Fig, 2 where yellow and blue overlap). Here, the corresponding cellular automation has infinite order. However, the cellular automation does have finite order when acting on subspaces with a fixed, finite number of particles. Furthermore, note that the Hubbard-RLBL evolution is $U(1)$ symmetric, thus the finite particle number subspaces are closed under $U(T)$. Therefore, by the arguments of this section, we have that the cellular automation will be stabilized by disorder for any initial state with a fixed, finite number of particles.

For cases where the subspace n is not closed under the evolution $U(T)$ it might be expected, in general, that the system will fail to localize. This is because, as soon as

the initial state evolves outside the subspace $\mathcal{N}$, the operator $U_{\mathcal{P}}$ will act to delocalize the state. However, we investigate such cases numerically in the next section and find that initial states within $\mathcal{N}$ may still remain localized on prethermal time scales.

5.6 Numerical results

In this section, we numerically investigate the evolution of several example interacting Floquet systems both with and without disorder. Namely, we investigate the stabilizing effect when disorder is added and if the evolution is consistent with localization dynamics.

As a measure of localization, we use the Inverse Participation Ratio (IPR). Given any state $|\Psi\rangle$, and letting $|\mathbf{n}\rangle$ be the number state basis in real space, the IPR is defined as

$$\text{IPR} = \sum_{\mathbf{n}} |\langle \Psi | \mathbf{n} \rangle|^4 \tag{5.59}$$

The IPR is 1 for any $|\Psi\rangle$ that is a Fock state and goes as $\frac{1}{N^2}$ (where N is the dimension of the Hilbert space) for an equal superposition of number states.

In Figure 3a, we plot the IPR as a function of time for three example values of V, τ in the Hubbard-RLBL model starting from the initial Fock state of a doublon localized in the center of the system.

In the first case, the second and fourth conditions in (5.4) are approximately satisfied with $V = \frac{16}{3} - 0.05$, $\tau = \frac{3\pi}{2} + 0.05$, i.e. we have perturbed both V, τ away from the special point $V = \frac{16}{3}, \tau = \frac{3\pi}{2}$ where both single particles and doublons evolve with swapping. Without disorder, the system will evolve with the effective slowed, interacting dynamics as discussed in Section 5.3 since it is near a special point. However, the doublon under this dynamics may still generate superpositions and spread throughout the system. Thus, the IPR decreases. Note, however, that the Fock state permutation at the special, Diophantine point has finite order (namely, order 1 since the perfect swapping RLBL model acts as the identity in the bulk of the system). Therefore, by the analysis of Section 5.4, it is expected that disorder will K-body (in this case, 2-body) localize the evolution. Consistent with this result, it can be seen in Fig. 3a that the IPR

approaches a constant value (~ 0.8) when disorder is included. In Fig. 3b, the average density of spin-up particles [4] at each site is plotted after $10,000$ Floquet periods. Without disorder, the particle spreads throughout the entire system. With disorder, it remains localized around its initial location.

In the second case, we evolve under Hubbard-RLBL with the parameters $V = 7.9$, $\tau = 2\pi + 0.1$. This point in parameter space is not in the vicinity of any Diophantine points, but, nonetheless, the first and fourth conditions (single particles frozen, doublons swapping) in (5.4) are approximately satisfied (since the point is in an overlapping red and green region in Fig. 2). Similar to the first case, the evolution without disorder exhibits slowed, effective dynamics with the IPR decreasing over time (Fig. 3a). When disorder is added, the IPR again converges to a constant value (~ 0.8). Note, the Fock state permutation corresponding to single particles frozen and doublons swapping does not have finite order. However, it does have finite orbits in the two particle subspace, and, furthermore, the evolution is $U(1)$ symmetric. Thus, evolution is confined to the two particle subspace. This implies that, consistent with the numerics, disorder is again expected to localize the system by the arguments of Section 5.5.

In the third case, we consider evolution at $V = \sqrt{2} - 0.01$, $\tau = \sqrt{2}\pi + 0.01$. Here, only the third condition in (5.4) is approximately satisfied (doublons frozen). The exact satisfaction of the third condition fragments the Hilbert space leaving any configuration of doublons frozen while other particle configurations may thermalize. Since, in this case, the third condition is only approximately satisfied, doublons may separate into a spin-up and spin-down particle. This means that, unlike case 2, the perturbation allows the system to evolve out of the Fock state permutation subspace and, as discussed at the end of Section 5.5, disorder is not guaranteed to localize the evolution. This is reflected in Fig. 3a where the IPR no longer converges once disorder is added. However, the disorder does help to stabilize the frozen dynamics of the doublon over long time scales. The difference from the first two cases is also apparent when considering the average particle density Fig. 3b. Here, the doublon is still with high probability localized near its initial location, but once it splits (thereby leaving the frozen subspace) the single particles may travel throughout the system. This creates a non-zero background in the average particle density even far from the initial doublon location.

[4] Due to the up-down symmetry of the evolution, the average density of spin-down particles is equivalent to the average density of spin-up particles and thus the spin-down density plots are not included.

5.7 Summary and discussion

In this chapter, we have shown that interacting Floquet models with periodically activated pairs exhibit classical cellular automation dynamics corrected by a slowed, effective interacting evolution when a given set of conditions (e.g. (5.4)) are approximately satisfied. Furthermore, when disorder is added to the system, these regions with approximately satisfied conditions become robust prethermal phases. If only a few of the Diophantine conditions are satisfied, the Hilbert space fragments into cellular automation subspaces and ergodic subspaces. When the same conditions are instead approximately satisfied, the disorder stabilizes the dynamics in the cellular automation subspace for long, but not infinite, time scales. On the other hand, these subspaces may still support localization if the subspace is closed under the evolution.

The existence of these stabilized cellular automation phases opens the door to a systematic investigation into their properties. For example, in [43] the disordered Hubbard-RLBL model was investigated at $\tau = \frac{\pi}{2}$ with V approaching 0 and V approaching infinity. It was found that, in this regime, the system belongs to a class of anomalous Floquet topological insulators, called correlation-induced anomalous Floquet insulators (CIAFI), labeled by a hierarchy of topological invariants. The two different values of V correspond to topological insulators with two differing topological invariants. From the perspective of our work, this corresponds to the cases where single particles and doublons are approximately swapping (conditions two and four approximately satisfied) for V near 0 and corresponds to single particles swapping and doublons frozen (conditions two and three approximately satisfied) for V large. Thus, any parameter space region with those Diophantine conditions approximately satisfied will also correspond to a CIAFI with the corresponding topological invariants. Similarly, when other Diophantine conditions are approximately satisfied, we expect the system to again correspond to a CIAFI with different topological invariants. This is just one example of the interesting phenomena that may occur in systems with stabilized cellular automation dynamics and an exciting direction for future work is the investigation of possible exotic behavior found in systems stabilizing other cellular automata. For example, it would be interesting to consider interacting Floquet drives without $U(1)$ symmetry such that the corresponding cellular automation may not preserve particle number.

One restriction used in this work to show localization was the finite order of the cellular automation. It is an open question whether there are any systems where

this constraint may be relaxed. Another interesting possibility is the generalization of the models discussed in this work to aperiodically driven systems. If this is possible, the prospective stabilized cellular automation corresponding to the evolution of such a drive would necessarily be aperiodic as well and therefore allow for more general stabilized cellular automata. Recent work has suggested the existence of prethermal phases for aperiodically driven systems [195, 196].

Instead of periodic drives, it is also possible to restrict hopping to between pairs of sites via measurements. Recently it was shown that, in this way, it is possible to mimic the RLBL procedure to produce protected edge transport alongside a local bulk via measurements alone [2]. Due to the non-unitary nature of the measurements, the analysis in this paper does not directly apply in the measurement-induced setting. A possible avenue for future investigations is determining if the stabilized cellular automation dynamics is also possible for measurement-induced systems and, if so, what similarities and differences does the dynamics have with the Floquet systems considered here.

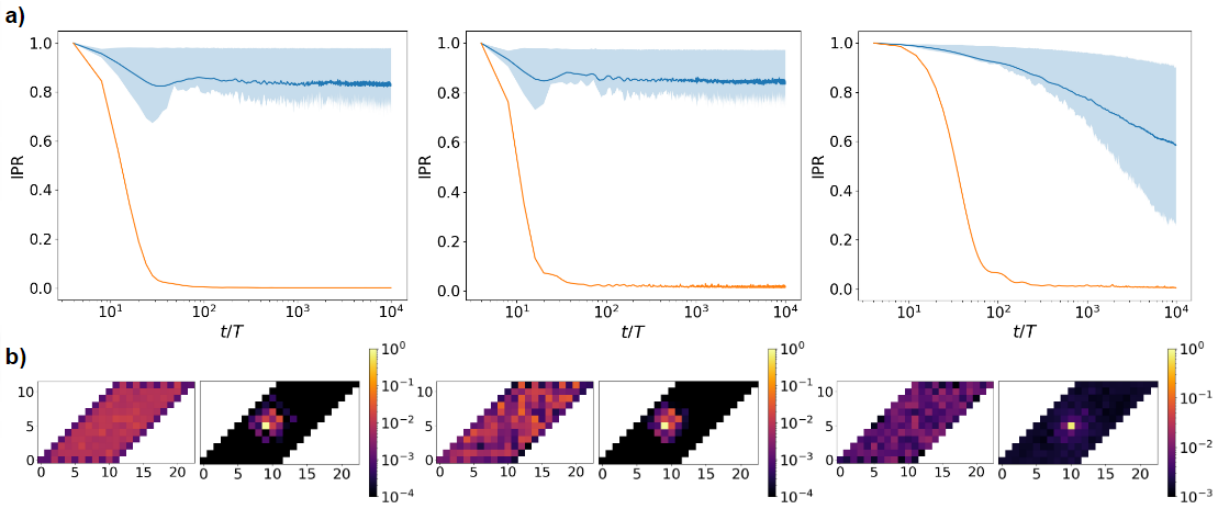

FIGURE 3: Localization in Hubbard-RLBL: a) Evolution of the Inverse Participation Ratio (IPR) in the Hubbard-RLBL model for a doublon initially localized in the center of the system. From left to right, the figures correspond to the second and fourth conditions in (5.4) being approximately satisfied (both particles and doublons are swapping, $V = \frac{16}{3} - 0.05$, $\tau = \frac{3\pi}{2} + 0.05$), the first and fourth conditions being approximately satisfied (particles are frozen and doublons are swapping, $V = 7.9$, $\tau = 2\pi + 0.1$), and solely the third condition being approximately satisfied (doublons are frozen, $V = \sqrt{2} - 0.01$, $\tau = \sqrt{2}\pi + 0.01$). The orange curve corresponds to the evolution without disorder, while the blue curve corresponds to the evolution with disorder. Disordered runs are averaged over 500 realizations of $W = 10$ with the range from the 25^{th} to the 75^{th} percentiles filled in with light blue. Consistent with the theoretical arguments of Sections 5.4 and 5.5, the numerics suggest that disorder fully localizes the evolution in the first two cases and stabilizes the classical dynamics over exponentially long time scales in the third case. b) Average density of spin-up particles per site after $10,000$ driving periods from an initial doublon localized in the center of the system. From left to right, the same three values for V, τ are used as in Fig. 3a. For each value of V, τ, the densities after evolution without disorder (left) and with disorder (right) are plotted.

Chapter 6

Conclusion

Experimental progress has allowed for unprecedented control of quantum systems in recent years. By probing, driving, and carefully connecting systems to external baths, it is possible to not only induce exotic equilibrium dynamics in a tunable fashion, but also realize novel phases of matter which are uniquely non-equilibrium in nature. In this thesis, we have introduced and analyzed several systems where the surprising behavior of non-equilibrium dynamics is showcased. Furthermore, through the usage and introduction of several new theoretical advancements, it was shown that the physical scenarios investigated in this work exhibit a variety of interesting, previously undiscovered behavior. We, therefore, hope that this work will provide a foundation upon which these appealing phenomena may be further explored, extended, and experimentally investigated.

Specifically, in chapter 2 we analyzed the behavior of wake patterns induced by disturbances moving through a sea of lattice fermions. The investigation of these problems, especially in regards to the disturbances with uniquely quantum characteristics (such as measurement), appears to be completely new. It was shown that the wake pattern may be described in terms of the velocity of the probe and its direction of motion in comparison to the lattice vectors. Furthermore, stark contrasts were found to exist between the wake patterns of the different varieties of probes. Surprising behavior emerged especially at half-filling where the wake in particle density behind a moving detector vanishes and where the wake behind a particle extractor becomes invariant of temperature. As the results for the geometry of a wake are essentially exact in the linear response regime, this work provides an essential point of comparison for both future experimental and theoretical studies into important extensions of the model (for example, the inclusion of interactions).

In chapter 3, we introduced a periodic sequence of measurements which showed that it is possible to induce protected chiral edge transport through measurements alone. In addition to the exciting similarities with other systems that exhibit protected transport (such as Floquet topological insulators), the non-unitary nature of the evolution provides key differences as well. The model we have here introduced therefore provides a gateway (as well as a foundation of theoretical tools) into the study of distinctive features in periodic, non-unitary non-equilibrium dynamics. This system is also intriguing due to the fact that it stands at an intersection point of several currently active fields of interest (including Floquet theory, dark-state engineering, and measurement-induced phase transitions).

Chapters 4 and 5 focus on a class of closed systems where periodic driving and interactions conspire to induce interesting phenomena and novel phases of matter. Namely, it was shown that Diophantine equations may be used to find sets of interaction strengths and driving frequencies where the dynamics is given exactly in terms of a complex permutation of number states. At other points in parameter space, an exponentially large subspace of the Hilbert space exhibits this dynamics. In addition, it was argued that when disorder is added this dynamics may be stabilized (prethermally or via MBL) within finite regions of parameter space to realize novel phases of matter. Our analysis therefore provides a tool to search for and describe exotic phenomena in a general class of Floquet models which, as we have shown using these Diophantine tools, include many of the uniquely non-equilibrium phases of matter which are the subject of much active interest (such as time crystals and anomalous Floquet insulators). An appealing direction for future work is to use the theoretical tools here developed to further investigate these interacting Floquet systems to see if there are other completely novel non-equilibrium phases of matter or interesting phenomena which exist as special cases within this class of models.

Overall, this dissertation has made theoretical pushes on a variety of fronts within non-equilibrium physics to help show that, by taking advantage of the precise control of quantum systems which is beginning to be experimentally achievable, it is possible to realize exciting phenomena which are either rare or completely forbidden in equilibrium systems. One of the major end goals and motivations for research in this direction is to engineer novel, non-equilibrium quantum devices which may act as tools with previously unheard of capabilities. Furthermore, the study of non-equilibrium dynamics is, in the end, the study of how we interact with and impact the physical systems around us. Research in this direction is thus important, at least on some foundational

level, as it is the rigorous study of the lens through which we observe the world.

Bibliography

[1]M. Wampler, P. Schauss, E. B. Kolomeisky, and I. Klich, "Quantum wakes in lattice fermions", Physical Review Research **3**, 033112 (2021).

[2]M. Wampler, B. J. J. Khor, G. Refael, and I. Klich, "Stirring by staring: measurement-induced chirality", Phys. Rev. X **12**, 031031 (2022).

[3]M. Wampler and I. Klich, "Arrested development and fragmentation in strongly-interacting floquet systems", Accepted at Scipost: scipost_202210_00045v2 (2023).

[4]M. Wampler and I. Klich, "Fragmentation and novel prethermal dynamical phases in disordered, strongly-interacting floquet systems", arXiv preprint arXiv:2212.09678 (2022).

[5]B. Keimer, S. A. Kivelson, M. R. Norman, S. Uchida, and J. Zaanen, "From quantum matter to high-temperature superconductivity in copper oxides", Nature **518**, 179–186 (2015).

[6]M. H. Anderson, J. R. Ensher, M. R. Matthews, C. E. Wieman, and E. A. Cornell, "Observation of bose-einstein condensation in a dilute atomic vapor", Science **269**, 198–201 (1995).

[7]Y. Ando, "Topological insulator materials", Journal of the Physical Society of Japan **82**, 102001 (2013).

[8]T. Senthil, "Symmetry-protected topological phases of quantum matter", Annual Review of Condensed Matter Physics **6**, 299–324 (2015).

[9]N. R. Cooper, J. Dalibard, and I. B. Spielman, "Topological bands for ultracold atoms", Rev. Mod. Phys. **91**, 015005 (2019).

[10]G. Mahan, Many-particle physics, 3rd ed. (Springer, New York, NY, 2000).

[11]T. Oka and S. Kitamura, "Floquet engineering of quantum materials", Annual Review of Condensed Matter Physics **10**, 387–408 (2019).

[12]K. Sacha, Time crystals, 1st ed., Springer Series on Atomic, Optical, and Plasma Physics (Springer Cham, Switzerland, 2020).

[13]D. V. Else, C. Monroe, C. Nayak, and N. Y. Yao, "Discrete time crystals", Annual Review of Condensed Matter Physics **11**, 467–499 (2020).

[14]T. Kitagawa, E. Berg, M. Rudner, and E. Demler, "Topological characterization of periodically driven quantum systems", Phys. Rev. B **82**, 235114 (2010).

[15]P. Titum, E. Berg, M. S. Rudner, G. Refael, and N. H. Lindner, "Anomalous floquet-anderson insulator as a nonadiabatic quantized charge pump", Physical Review X **6**, 021013 (2016).

[16]J. Preskill, "Quantum Computing in the NISQ era and beyond", Quantum **2**, 79 (2018).

[17]J. H. Shirley, "Solution of the schrödinger equation with a hamiltonian periodic in time", Phys. Rev. **138**, B979–B987 (1965).

[18]F. Casas, J. A. Oteo, and J. Ros, "Floquet theory: exponential perturbative treatment", **34**, 3379 (2001).

[19]R. Achilles and A. Bonfiglioli, "The early proofs of the theorem of campbell, baker, hausdorff, and dynkin", Archive for History of Exact Sciences **66**, 295–358 (2012).

[20]M. S. Rudner, N. H. Lindner, E. Berg, and M. Levin, "Anomalous edge states and the bulk-edge correspondence for periodically driven two-dimensional systems", Physical Review X **3**, 031005 (2013).

[21]C.-X. Liu, S.-C. Zhang, and X.-L. Qi, "The quantum anomalous hall effect: theory and experiment", Annual Review of Condensed Matter Physics **7**, 301–321 (2016).

[22]A. Kitaev, "Fault-tolerant quantum computation by anyons", Annals of Physics **303**, 2–30 (2003).

[23]M. Z. Hasan and C. L. Kane, "Colloquium: topological insulators", Rev. Mod. Phys. **82**, 3045–3067 (2010).

[24]C. Kittel, Introduction to solid state physics, 8th ed. (Wiley, 2004).

[25]R. Bott and R. Seeley, "Some remarks on the paper of callias", Communications in Mathematical Physics **62**, 235–245 (1978).

[26]T. Kuwahara, T. Mori, and K. Saito, "Floquet–magnus theory and generic transient dynamics in periodically driven many-body quantum systems", Annals of Physics **367**, 96–124 (2016).

[27]D. A. Abanin, E. Altman, I. Bloch, and M. Serbyn, "Colloquium: many-body localization, thermalization, and entanglement", Rev. Mod. Phys. **91**, 021001 (2019).

[28]D. Abanin, W. De Roeck, W. W. Ho, and F. Huveneers, "A rigorous theory of many-body prethermalization for periodically driven and closed quantum systems", Communications in Mathematical Physics **354**, 809–827 (2017).

[29]K. I. Seetharam, C.-E. Bardyn, N. H. Lindner, M. S. Rudner, and G. Refael, "Controlled population of floquet-bloch states via coupling to bose and fermi baths", Phys. Rev. X **5**, 041050 (2015).

[30]P. W. Anderson, "Absence of diffusion in certain random lattices", Phys. Rev. **109**, 1492–1505 (1958).

[31]L. Fleishman and P. W. Anderson, "Interactions and the anderson transition", Phys. Rev. B **21**, 2366–2377 (1980).

[32]T. V. Shahbazyan and M. E. Raikh, "Surface plasmon in a two-dimensional anderson insulator with interactions", Phys. Rev. B **53**, 7299–7307 (1996).

[33]D. Basko, I. Aleiner, and B. Altshuler, "Metal–insulator transition in a weakly interacting many-electron system with localized single-particle states", Annals of Physics **321**, 1126–1205 (2006).

[34]V. Oganesyan and D. A. Huse, "Localization of interacting fermions at high temperature", Phys. Rev. B **75**, 155111 (2007).

[35]J. Z. Imbrie, "On many-body localization for quantum spin chains", Journal of Statistical Physics **163**, 998–1048 (2016).

[36]W. De Roeck and F. ç. Huveneers, "Stability and instability towards delocalization in many-body localization systems", Phys. Rev. B **95**, 155129 (2017).

[37]W. De Roeck and J. Z. Imbrie, "Many-body localization: stability and instability", Philosophical Transactions of the Royal Society A: Mathematical, Physical and Engineering Sciences **375**, 20160422 (2017).

[38]D. A. Abanin, W. De Roeck, and F. Huveneers, "Theory of many-body localization in periodically driven systems", Annals of Physics **372**, 1–11 (2016).

[39]U. Agrawal, R. Vasseur, and S. Gopalakrishnan, "Quasiperiodic many-body localization transition in dimension $dgt;1$", Phys. Rev. B **106**, 094206 (2022).

[40]M. Aizenman and S. Warzel, "Localization bounds for multiparticle systems", Communications in Mathematical Physics **290**, 903–934 (2009).

[41]I.-D. Potirniche, S. Banerjee, and E. Altman, "Exploration of the stability of many-body localization in $d > 1$", Phys. Rev. B **99**, 205149 (2019).

[42]F. Nathan, D. Abanin, E. Berg, N. H. Lindner, and M. S. Rudner, "Anomalous floquet insulators", Phys. Rev. B **99**, 195133 (2019).

[43]F. Nathan, D. A. Abanin, N. H. Lindner, E. Berg, and M. S. Rudner, "Hierarchy of many-body invariants and quantized magnetization in anomalous floquet insulators", SciPost Phys. **10**, 128 (2021).

[44]T. Mori, "Floquet states in open quantum systems", Annual Review of Condensed Matter Physics **14**, 35–56 (2023).

[45]H. Dehghani, T. Oka, and A. Mitra, "Dissipative floquet topological systems", Phys. Rev. B **90**, 195429 (2014).

[46]T. Iadecola and C. Chamon, "Floquet systems coupled to particle reservoirs", Phys. Rev. B **91**, 184301 (2015).

[47]T. Iadecola, T. Neupert, and C. Chamon, "Occupation of topological floquet bands in open systems", Phys. Rev. B **91**, 235133 (2015).

[48]A. Schnell, A. Eckardt, and S. Denisov, "Is there a floquet lindbladian?", Phys. Rev. B **101**, 100301 (2020).

[49]T. N. Ikeda, K. Chinzei, and M. Sato, "Nonequilibrium steady states in the Floquet-Lindblad systems: van Vleck's high-frequency expansion approach", SciPost Phys. Core **4**, 033 (2021).

[50]A. Rivas and S. Huelga, Open quantum systems: an introduction, 1st ed. (Springer, Berlin, Heidelberg, 2012).

[51]J. Preskill, Lecture notes on quantum information and computation, `http://theory.caltech.edu/~preskill/ph229/`, [Online; accessed 11-April-2023], 2015.

[52]I. Klich, "Closed hierarchies and non-equilibrium steady states of driven systems", Annals of Physics **404**, 66–80 (2019).

[53]A. Jaiswal and V. Roy, "Relativistic hydrodynamics in heavy-ion collisions: general aspects and recent developments", Adv. High Energy Phys. **2016**, `10.1155/2016/9623034` (2016).

[54]H. Guo, E. Ilseven, G. Falkovich, and L. S. Levitov, "Higher-than-ballistic conduction of viscous electron flows", Proc. Natl. Acad. Sci. USA **114**, 3068–3073 (2017).

[55]J. Avron, B. Gutkin, and D. Oaknin, "Adiabatic swimming in an ideal quantum gas", Phys. Rev. Lett. **96**, 130602 (2006).

[56]E. B. Kolomeisky and J. P. Straley, "Kelvin-Mach wake in a two-dimensional Fermi sea", Phys. Rev. Lett. **120**, 226801 (2018).

[57]C. Luo, M. Ibanescu, S. G. Johnson, and J. Joannopoulos, "Cerenkov radiation in photonic crystals", Science **299**, 368–371 (2003).

[58]H. Chen and M. Chen, "Flipping photons backward: reversed cherenkov radiation", Mater. Today **14**, 34–41 (2011).

[59]G. Mazzucchi, W. Kozlowski, S. F. Caballero-Benitez, T. J. Elliott, and I. B. Mekhov, "Quantum measurement-induced dynamics of many-body ultracold bosonic and fermionic systems in optical lattices", Phys. Rev. A **93**, 023632 (2016).

[60]R. Blattmann and K. Mølmer, "Conditioned quantum motion of an atom in a continuously monitored one-dimensional lattice", Phys. Rev. A **93**, 052113 (2016).

[61]G. Mazzucchi, S. F. Caballero-Benitez, and I. B. Mekhov, "Quantum measurement-induced antiferromagnetic order and density modulations in ultracold Fermi gases in optical lattices", Sci. Rep. **6**, 1–10 (2016).

[62]Y. Fuji and Y. Ashida, "Measurement-induced quantum criticality under continuous monitoring", Phys. Rev. B **102**, 054302 (2020).

[63]D. A. Ivanov, T. Y. Ivanova, S. F. Caballero-Benitez, and I. B. Mekhov, "Feedback-induced quantum phase transitions using weak measurements", Phys. Rev. Lett. **124**, 010603 (2020).

[64]Y. Ashida and M. Ueda, "Multiparticle quantum dynamics under real-time observation", Phys. Rev. A **95**, 022124 (2017).

[65]H. Ritsch, P. Domokos, F. Brennecke, and T. Esslinger, "Cold atoms in cavity-generated dynamical optical potentials", Rev. Mod. Phys. **85**, 553–601 (2013).

[66]F. Schäfer, I. Herrera, S. Cherukattil, C. Lovecchio, F. S. Cataliotti, F. Caruso, and A. Smerzi, "Experimental realization of quantum Zeno dynamics", Nat. Commun. **5**, 3194 (2014).

[67]J. J. W. H. Sørensen, M. Dalgaard, A. H. Kiilerich, K. Mølmer, and J. F. Sherson, "Quantum control with measurements and quantum Zeno dynamics", Phys. Rev. A **98**, 062317 (2018).

[68]W. G. Unruh, "Notes on black-hole evaporation", Phys. Rev. D **14**, 870–892 (1976).

[69]C. Gross and I. Bloch, "Quantum simulations with ultracold atoms in optical lattices", en, Science **357**, 995–1001 (2017).

[70] A. Sommer, M. Ku, G. Roati, and M. W. Zwierlein, "Universal spin transport in a strongly interacting Fermi gas", Nature **472**, 201–204 (2011).

[71] M. Koschorreck, D. Pertot, E. Vogt, and M. Köhl, "Universal spin dynamics in two-dimensional Fermi gases", Nat. Phys. **9**, 405–409 (2013).

[72] S. Trotzky, S. Beattie, C. Luciuk, S. Smale, A. Bardon, T. Enss, E. Taylor, S. Zhang, and J. Thywissen, "Observation of the Leggett-Rice effect in a unitary Fermi gas", Phys. Rev. Lett. **114**, 10.1103/physrevlett.114.015301 (2015).

[73] S. Krinner, D. Stadler, D. Husmann, J.-P. Brantut, and T. Esslinger, "Observation of quantized conductance in neutral matter", Nature **517**, 64–67 (2014).

[74] R. Anderson, F. Wang, P. Xu, V. Venu, S. Trotzky, F. Chevy, and J. H. Thywissen, "Conductivity spectrum of ultracold atoms in an optical lattice", Phys. Rev. Lett. **122**, 153602 (2019).

[75] W. Xu, W. R. McGehee, W. N. Morong, and B. DeMarco, "Bad-metal relaxation dynamics in a Fermi lattice gas", Nat. Commun. **10**, 1588 (2019).

[76] J. Vijayan, P. Sompet, G. Salomon, J. Koepsell, S. Hirthe, A. Bohrdt, F. Grusdt, I. Bloch, and C. Gross, "Time-resolved observation of spin-charge deconfinement in fermionic Hubbard chains", en, Science **367**, 186–189 (2020).

[77] M. A. Nichols, L. W. Cheuk, M. Okan, T. R. Hartke, E. Mendez, T. Senthil, E. Khatami, H. Zhang, and M. W. Zwierlein, "Spin transport in a Mott insulator of ultracold fermions", Science **363**, 383–387 (2019).

[78] P. T. Brown, D. Mitra, E. Guardado-Sanchez, R. Nourafkan, A. Reymbaut, C.-D. Hébert, S. Bergeron, A.-M. S. Tremblay, J. Kokalj, D. A. Huse, P. Schauß, and W. S. Bakr, "Bad metallic transport in a cold atom Fermi-Hubbard system", Science **363**, 379–382 (2019).

[79] L. Kelvin, "On ship waves", Proc. Inst. Mech. Engrs **38**, 409–434 (1887).

[80] A. Darmon, M. Benzaquen, and E. Raphaël, "Kelvin wake pattern at large Froude numbers", J. Fluid Mech. **738** (2014).

[81] J. Colen and E. B. Kolomeisky, "Kelvin-froude wake patterns of a traveling pressure disturbance", European Journal of Mechanics / B Fluids **85**, 400–412 (2021).

[82] M. Bonitz, Quantum kinetic theory, Vol. 33 (B. G. Teubner, Stuttgart- Leipzig, 1998).

[83] K. Temme, M. M. Wolf, and F. Verstraete, "Stochastic exclusion processes versus coherent transport", New J. Phys. **14**, 075004 (2012).

[84]I. Carusotto and G. Rousseaux, "The Cěrenkov effect revisited: from swimming ducks to zero modes in gravitational analogues", in Analogue gravity phenomenology, edited by D. Faccio et al., Lecture Notes in Physics, and references therein (Springer International Publishing Switzerland, 2013) Chap. 6, p. 109.

[85]C. Weitenberg, M. Endres, J. F. Sherson, M. Cheneau, P. Schauss, T. Fukuhara, I. Bloch, and S. Kuhr, "Single-spin addressing in an atomic Mott insulator", Nature **471**, 319–324 (2011).

[86]N. H. Lindner, G. Refael, and V. Galitski, "Floquet topological insulator in semiconductor quantum wells", Nature Physics **7**, 490–495 (2011).

[87]J. W. McIver, B. Schulte, F.-U. Stein, T. Matsuyama, G. Jotzu, G. Meier, and A. Cavalleri, "Light-induced anomalous hall effect in graphene", Nature Physics **16**, 38–41 (2019).

[88]M. Nuske, L. Broers, B. Schulte, G. Jotzu, S. A. Sato, A. Cavalleri, A. Rubio, J. W. McIver, and L. Mathey, "Floquet dynamics in light-driven solids", Physical Review Research **2**, 10.1103/physrevresearch.2.043408 (2020).

[89]P. Titum, N. H. Lindner, M. C. Rechtsman, and G. Refael, "Disorder-induced floquet topological insulators", Physical Review Letters **114**, 10.1103/physrevlett.114.056801 (2015).

[90]A. Kundu, M. Rudner, E. Berg, and N. H. Lindner, "Quantized large-bias current in the anomalous Floquet-Anderson insulator", Physical Review B **101**, 041403, 041403 (2020).

[91]H. C. Po, L. Fidkowski, T. Morimoto, A. C. Potter, and A. Vishwanath, "Chiral floquet phases of many-body localized bosons", Physical Review X **6**, 10.1103/physrevx.6.041070 (2016).

[92]S. Roy, J. T. Chalker, I. V. Gornyi, and Y. Gefen, "Measurement-induced steering of quantum systems", Physical Review Research **2**, 033347, 033347 (2020).

[93]S. Lieu, M. McGinley, and N. R. Cooper, "Tenfold Way for Quadratic Lindbladians", Phys. Rev. Lett. **124**, 040401, 040401 (2020).

[94]T. Müller, S. Diehl, and M. Buchhold, "Measurement-induced dark state phase transitions in long-ranged fermion systems", Phys. Rev. Lett. **128**, 010605 (2022).

[95]S. Sang and T. H. Hsieh, "Measurement-protected quantum phases", Phys. Rev. Research **3**, 023200 (2021).

[96]J. C. Budich, P. Zoller, and S. Diehl, "Dissipative preparation of chern insulators", Physical Review A **91**, 10.1103/physreva.91.042117 (2015).

[97]C.-E. Bardyn, M. A. Baranov, C. V. Kraus, E. Rico, A. İmamoğlu, P. Zoller, and S. Diehl, "Topology by dissipation", New Journal of Physics **15**, 085001 (2013).

[98]A. Tomadin, S. Diehl, M. D. Lukin, P. Rabl, and P. Zoller, "Reservoir engineering and dynamical phase transitions in optomechanical arrays", Physical Review A **86**, 10.1103/physreva.86.033821 (2012).

[99]P. Sierant, G. Chiriacò, F. M. Surace, S. Sharma, X. Turkeshi, M. Dalmonte, R. Fazio, and G. Pagano, "Dissipative Floquet Dynamics: from Steady State to Measurement Induced Criticality in Trapped-ion Chains", Quantum **6**, 638 (2022).

[100]L. Zhou and J. Gong, "Non-Hermitian Floquet topological phases with arbitrarily many real-quasienergy edge states", Physical Review B **98**, 205417, 205417 (2018).

[101]Y. Li and M. P. A. Fisher, "Statistical mechanics of quantum error correcting codes", Physical Review B **103**, 104306, 104306 (2021).

[102]M. Buchhold, Y. Minoguchi, A. Altland, and S. Diehl, "Effective theory for the measurement-induced phase transition of dirac fermions", Phys. Rev. X **11**, 041004 (2021).

[103]Y. Bao, S. Choi, and E. Altman, "Theory of the phase transition in random unitary circuits with measurements", Phys. Rev. B **101**, 104301 (2020).

[104]A. Chan, R. M. Nandkishore, M. Pretko, and G. Smith, "Unitary-projective entanglement dynamics", Physical Review B **99**, 224307 (2019).

[105]M. J. Gullans and D. A. Huse, "Dynamical purification phase transition induced by quantum measurements", Phys. Rev. X **10**, 041020 (2020).

[106]C.-M. Jian, Y.-Z. You, R. Vasseur, and A. W. W. Ludwig, "Measurement-induced criticality in random quantum circuits", Phys. Rev. B **101**, 104302 (2020).

[107]M. Szyniszewski, A. Romito, and H. Schomerus, "Entanglement transition from variable-strength weak measurements", Physical Review B **100**, 064204, 064204 (2019).

[108]A. Zabalo, M. J. Gullans, J. H. Wilson, R. Vasseur, A. W. W. Ludwig, S. Gopalakrishnan, D. A. Huse, and J. H. Pixley, "Operator scaling dimensions and multifractality at measurement-induced transitions", Phys. Rev. Lett. **128**, 050602 (2022).

[109]B. Skinner, J. Ruhman, and A. Nahum, "Measurement-induced phase transitions in the dynamics of entanglement", Physical Review X **9**, 031009 (2019).

[110]A. Zabalo, M. J. Gullans, J. H. Wilson, S. Gopalakrishnan, D. A. Huse, and J. H. Pixley, "Critical properties of the measurement-induced transition in random quantum circuits", Phys. Rev. B **101**, 060301 (2020).

[111]R. Fan, S. Vijay, A. Vishwanath, and Y.-Z. You, "Self-organized error correction in random unitary circuits with measurement", Phys. Rev. B **103**, 174309 (2021).

[112]M. Ippoliti, M. J. Gullans, S. Gopalakrishnan, D. A. Huse, and V. Khemani, "Entanglement phase transitions in measurement-only dynamics", Physical Review X **11**, 011030 (2021).

[113]A. Lavasani, Y. Alavirad, and M. Barkeshli, "Measurement-induced topological entanglement transitions in symmetric random quantum circuits", Nature Physics, 1–6 (2021).

[114]S. Sang, Y. Li, T. Zhou, X. Chen, T. H. Hsieh, and M. Fisher, "Entanglement negativity at measurement-induced criticality", arXiv preprint arXiv:2012.00031 (2020).

[115]B. Shi, X. Dai, and Y.-M. Lu, "Entanglement negativity at the critical point of measurement-driven transition", arXiv preprint arXiv:2012.00040 (2020).

[116]Y. Li, X. Chen, and M. P. A. Fisher, "Quantum zeno effect and the many-body entanglement transition", Phys. Rev. B **98**, 205136 (2018).

[117]Y. Li, X. Chen, and M. P. Fisher, "Measurement-driven entanglement transition in hybrid quantum circuits", Physical Review B **100**, 134306 (2019).

[118]M. J. Gullans and D. A. Huse, "Scalable probes of measurement-induced criticality", Phys. Rev. Lett. **125**, 070606 (2020).

[119]S. Choi, Y. Bao, X.-L. Qi, and E. Altman, "Quantum error correction in scrambling dynamics and measurement-induced phase transition", Phys. Rev. Lett. **125**, 030505 (2020).

[120]R. Vasseur, A. C. Potter, Y.-Z. You, and A. W. W. Ludwig, "Entanglement transitions from holographic random tensor networks", Phys. Rev. B **100**, 134203 (2019).

[121]D. Rossini and E. Vicari, "Measurement-induced dynamics of many-body systems at quantum criticality", Phys. Rev. B **102**, 035119 (2020).

[122]V. Gebhart, K. Snizhko, T. Wellens, A. Buchleitner, A. Romito, and Y. Gefen, "Topological transition in measurement-induced geometric phases", Proceedings of the National Academy of Sciences **117**, 5706–5713 (2020).

[123]O. Lunt and A. Pal, "Measurement-induced entanglement transitions in many-body localized systems", Physical Review Research **2**, 043072 (2020).

[124]X. Cao, A. Tilloy, and A. D. Luca, "Entanglement in a fermion chain under continuous monitoring", SciPost Phys. **7**, 24 (2019).

[125]O. Alberton, M. Buchhold, and S. Diehl, "Entanglement transition in a monitored free-fermion chain: from extended criticality to area law", Phys. Rev. Lett. **126**, 170602 (2021).

[126]K. v. Klitzing, G. Dorda, and M. Pepper, "New method for high-accuracy determination of the fine-structure constant based on quantized hall resistance", Phys. Rev. Lett. **45**, 494–497 (1980).

[127]J. K. Jain, Composite fermions (Cambridge University Press, 2007).

[128]P. Facchi and S. Pascazio, "Quantum zeno dynamics: mathematical and physical aspects", Journal of Physics A: Mathematical and Theoretical **41**, 493001 (2008).

[129]O. Hosten, M. T. Rakher, J. T. Barreiro, N. A. Peters, and P. G. Kwiat, "Counterfactual quantum computation through quantum interrogation", Nature **439**, 949–952 (2006).

[130]Y. Cao, Y.-H. Li, Z. Cao, J. Yin, Y.-A. Chen, H.-L. Yin, T.-Y. Chen, X. Ma, C.-Z. Peng, and J.-W. Pan, "Direct counterfactual communication via quantum zeno effect", Proceedings of the National Academy of Sciences **114**, 4920–4924 (2017).

[131]B. Yan, S. A. Moses, B. Gadway, J. P. Covey, K. R. A. Hazzard, A. M. Rey, D. S. Jin, and J. Ye, "Observation of dipolar spin-exchange interactions with lattice-confined polar molecules", Nature **501**, 521–525 (2013).

[132]B. Zhu, B. Gadway, M. Foss-Feig, J. Schachenmayer, M. L. Wall, K. R. A. Hazzard, B. Yan, S. A. Moses, J. P. Covey, D. S. Jin, J. Ye, M. Holland, and A. M. Rey, "Suppressing the loss of ultracold molecules via the continuous quantum zeno effect", Phys. Rev. Lett. **112**, 070404 (2014).

[133]W. M. Itano, D. J. Heinzen, J. J. Bollinger, and D. J. Wineland, "Quantum zeno effect", Phys. Rev. A **41**, 2295–2300 (1990).

[134]M. C. Fischer, B. Gutiérrez-Medina, and M. G. Raizen, "Observation of the quantum zeno and anti-zeno effects in an unstable system", Phys. Rev. Lett. **87**, 040402 (2001).

[135]E. W. Streed, J. Mun, M. Boyd, G. K. Campbell, P. Medley, W. Ketterle, and D. E. Pritchard, "Continuous and pulsed quantum zeno effect", Phys. Rev. Lett. **97**, 260402 (2006).

[136]S. V. Kilina, A. J. Neukirch, B. F. Habenicht, D. S. Kilin, and O. V. Prezhdo, "Quantum zeno effect rationalizes the phonon bottleneck in semiconductor quantum dots", Phys. Rev. Lett. **110**, 180404 (2013).

[137]F. Schäfer, I. Herrera, S. Cherukattil, C. Lovecchio, F. S. Cataliotti, F. Caruso, and A. Smerzi, "Experimental realization of quantum zeno dynamics", Nature Communications **5**, 3194 (2014).

[138]A. Signoles, A. Facon, D. Grosso, I. Dotsenko, S. Haroche, J.-M. Raimond, M. Brune, and S. Gleyzes, "Confined quantum zeno dynamics of a watched atomic arrow", Nature Physics **10**, 715–719 (2014).

[139]P. M. Harrington, J. T. Monroe, and K. W. Murch, "Quantum zeno effects from measurement controlled qubit-bath interactions", Phys. Rev. Lett. **118**, 240401 (2017).

[140]C. R. Kagan, E. Lifshitz, E. H. Sargent, and D. V. Talapin, "Building devices from colloidal quantum dots", Science **353** (2016).

[141]M. F. Parsons, F. Huber, A. Mazurenko, C. S. Chiu, W. Setiawan, K. Wooley-Brown, S. Blatt, and M. Greiner, "Site-resolved imaging of fermionic li 6 in an optical lattice", Physical review letters **114**, 213002 (2015).

[142]I. Bloch, J. Dalibard, and W. Zwerger, "Many-body physics with ultracold gases", Rev. Mod. Phys. **80**, 885–964 (2008).

[143]R. Blatt and C. F. Roos, "Quantum simulations with trapped ions", Nature Physics **8**, 277–284 (2012).

[144]M. S. Rudner and N. H. Lindner, "Band structure engineering and non-equilibrium dynamics in floquet topological insulators", Nature Reviews Physics **2**, 229–244 (2020).

[145]V. Khemani, A. Lazarides, R. Moessner, and S. L. Sondhi, "Phase structure of driven quantum systems", Phys. Rev. Lett. **116**, 250401 (2016).

[146]D. V. Else, B. Bauer, and C. Nayak, "Floquet time crystals", Phys. Rev. Lett. **117**, 090402 (2016).

[147]H. Watanabe and M. Oshikawa, "Absence of quantum time crystals", Phys. Rev. Lett. **114**, 251603 (2015).

[148]A. Lazarides, A. Das, and R. Moessner, "Equilibrium states of generic quantum systems subject to periodic driving", Phys. Rev. E **90**, 012110 (2014).

[149]L. D'Alessio and M. Rigol, "Long-time behavior of isolated periodically driven interacting lattice systems", Phys. Rev. X **4**, 041048 (2014).

[150]P. Ponte, A. Chandran, Z. Papić, and D. A. Abanin, "Periodically driven ergodic and many-body localized quantum systems", Annals of Physics **353**, 196–204 (2015).

[151]L. D'Alessio and A. Polkovnikov, "Many-body energy localization transition in periodically driven systems", Annals of Physics **333**, 19–33 (2013).

[152]P. Ponte, Z. Papi ć, F. ç. Huveneers, and D. A. Abanin, "Many-body localization in periodically driven systems", Phys. Rev. Lett. **114**, 140401 (2015).

[153]A. Lazarides, A. Das, and R. Moessner, "Fate of many-body localization under periodic driving", Phys. Rev. Lett. **115**, 030402 (2015).

[154]A. Agarwala and D. Sen, "Effects of interactions on periodically driven dynamically localized systems", Phys. Rev. B **95**, 014305 (2017).

[155]M. Bukov, S. Gopalakrishnan, M. Knap, and E. Demler, "Prethermal floquet steady states and instabilities in the periodically driven, weakly interacting bose-hubbard model", Phys. Rev. Lett. **115**, 205301 (2015).

[156]D. V. Else, B. Bauer, and C. Nayak, "Prethermal phases of matter protected by time-translation symmetry", Phys. Rev. X **7**, 011026 (2017).

[157]T.-S. Zeng and D. N. Sheng, "Prethermal time crystals in a one-dimensional periodically driven floquet system", Phys. Rev. B **96**, 094202 (2017).

[158]F. Machado, G. D. Kahanamoku-Meyer, D. V. Else, C. Nayak, and N. Y. Yao, "Exponentially slow heating in short and long-range interacting floquet systems", Phys. Rev. Research **1**, 033202 (2019).

[159]H. Dehghani, T. Oka, and A. Mitra, "Dissipative floquet topological systems", Phys. Rev. B **90**, 195429 (2014).

[160]T. Iadecola and C. Chamon, "Floquet systems coupled to particle reservoirs", Phys. Rev. B **91**, 184301 (2015).

[161]T. Iadecola, T. Neupert, and C. Chamon, "Occupation of topological floquet bands in open systems", Phys. Rev. B **91**, 235133 (2015).

[162]C. J. Turner, A. A. Michailidis, D. A. Abanin, M. Serbyn, and Z. Papić, "Weak ergodicity breaking from quantum many-body scars", Nature Physics **14**, 745–749 (2018).

[163]W. W. Ho, S. Choi, H. Pichler, and M. D. Lukin, "Periodic orbits, entanglement, and quantum many-body scars in constrained models: matrix product state approach", Phys. Rev. Lett. **122**, 040603 (2019).

[164]S. Moudgalya, B. A. Bernevig, and N. Regnault, "Quantum many-body scars and hilbert space fragmentation: a review of exact results", Reports on Progress in Physics **85**, 086501 (2022).

[165]H. Yarloo, A. Emami Kopaei, and A. Langari, "Homogeneous floquet time crystal from weak ergodicity breaking", Phys. Rev. B **102**, 224309 (2020).

[166]P. Sala, T. Rakovszky, R. Verresen, M. Knap, and F. Pollmann, "Ergodicity breaking arising from hilbert space fragmentation in dipole-conserving hamiltonians", Phys. Rev. X **10**, 011047 (2020).

[167]V. Khemani, M. Hermele, and R. Nandkishore, "Localization from hilbert space shattering: from theory to physical realizations", Phys. Rev. B **101**, 174204 (2020).

[168]M. Haque, O. Zozulya, and K. Schoutens, "Entanglement entropy in fermionic laughlin states", Physical Review Letters **98**, 060401, 060401 (2007).

[169]M. Haque, "Self-similar spectral structures and edge-locking hierarchy in open-boundary spin chains", Physical Review A **82**, 012108 (2010).

[170]A. Kumar, P. T. Dumitrescu, and A. C. Potter, "String order parameters for one-dimensional floquet symmetry protected topological phases", Phys. Rev. B **97**, 224302 (2018).

[171]A. J. Friedman, S. Gopalakrishnan, and R. Vasseur, "Integrable many-body quantum floquet-thouless pumps", Physical review letters **123**, 170603 (2019).

[172]M. Ljubotina, L. Zadnik, and T. ž. Prosen, "Ballistic spin transport in a periodically driven integrable quantum system", Phys. Rev. Lett. **122**, 150605 (2019).

[173]L. Piroli, B. Bertini, J. I. Cirac, and T. ž. Prosen, "Exact dynamics in dual-unitary quantum circuits", Phys. Rev. B **101**, 094304 (2020).

[174]M. Lu, G. H. Reid, A. R. Fritsch, A. M. Piñeiro, and I. B. Spielman, "Floquet engineering topological dirac bands", Phys. Rev. Lett. **129**, 040402 (2022).

[175]H. Cohen, Number theory, Volume 1: tools and diophantine equations, 1st ed., Graduate Texts in Mathematics (Springer, New York, NY, 2007).

[176]S. Wolfram, "Statistical mechanics of cellular automata", Rev. Mod. Phys. **55**, 601–644 (1983).

[177]J. Iaconis, S. Vijay, and R. Nandkishore, "Anomalous subdiffusion from subsystem symmetries", Phys. Rev. B **100**, 214301 (2019).

[178] A. Wiles, "Modular elliptic curves and fermat's last theorem", Annals of Mathematics, 2nd ser. **141**, 443–551 (1995).

[179] Y. Matiyasevich, "Enumerable sets are diophantine", Doklady Akademii Nauk SSSR **191**, 279–282 (1970).

[180] S. Moudgalya, A. Prem, R. Nandkishore, N. Regnault, and B. A. Bernevig, "Thermalization and its absence within krylov subspaces of a constrained hamiltonian", in Memorial volume for shoucheng zhang (World Scientific, 2021) Chap. Chapter 7, pp. 147–209.

[181] F. Wilczek, "Quantum time crystals", Phys. Rev. Lett. **109**, 160401 (2012).

[182] J. Zhang, P. W. Hess, A. Kyprianidis, P. Becker, A. Lee, J. Smith, G. Pagano, I.-D. Potirniche, A. C. Potter, A. Vishwanath, N. Y. Yao, and C. Monroe, "Observation of a discrete time crystal", Nature **543**, 217–220 (2017).

[183] P. Frey and S. Rachel, "Realization of a discrete time crystal on 57 qubits of a quantum computer", Science Advances **8**, eabm7652 (2022).

[184] Y.-G. Peng, C.-Z. Qin, D.-G. Zhao, Y.-X. Shen, X.-Y. Xu, M. Bao, H. Jia, and X.-F. Zhu, "Experimental demonstration of anomalous floquet topological insulator for sound", Nature Communications **7**, 13368 (2016).

[185] L. J. Maczewsky, J. M. Zeuner, S. Nolte, and A. Szameit, "Observation of photonic anomalous floquet topological insulators", Nature Communications **8**, 13756 (2017).

[186] S. Mukherjee, A. Spracklen, M. Valiente, E. Andersson, P. Öhberg, N. Goldman, and R. R. Thomson, "Experimental observation of anomalous topological edge modes in a slowly driven photonic lattice", Nature Communications **8**, 13918 (2017).

[187] K. Wintersperger, C. Braun, F. N. Ünal, A. Eckardt, M. D. Liberto, N. Goldman, I. Bloch, and M. Aidelsburger, "Realization of an anomalous floquet topological system with ultracold atoms", Nature Physics **16**, 1058–1063 (2020).

[188] E. Canovi, M. Kollar, and M. Eckstein, "Stroboscopic prethermalization in weakly interacting periodically driven systems", Phys. Rev. E **93**, 012130 (2016).

[189] T. Mori, T. Kuwahara, and K. Saito, "Rigorous bound on energy absorption and generic relaxation in periodically driven quantum systems", Phys. Rev. Lett. **116**, 120401 (2016).

[190] D. A. Abanin, W. De Roeck, W. W. Ho, and F. ç. Huveneers, "Effective hamiltonians, prethermalization, and slow energy absorption in periodically driven many-body systems", Phys. Rev. B **95**, 014112 (2017).

[191]L. Fleishman and P. W. Anderson, "Interactions and the anderson transition", Phys. Rev. B **21**, 2366–2377 (1980).

[192]S. Moudgalya and O. I. Motrunich, "Hilbert space fragmentation and commutant algebras", Phys. Rev. X **12**, 011050 (2022).

[193]A. Morningstar, L. Colmenarez, V. Khemani, D. J. Luitz, and D. A. Huse, "Avalanches and many-body resonances in many-body localized systems", Phys. Rev. B **105**, 174205 (2022).

[194]A. Nahum, S. Vijay, and J. Haah, "Operator spreading in random unitary circuits", Physical Review X **8**, 021014 (2018).

[195]H. Zhao, F. Mintert, R. Moessner, and J. Knolle, "Random multipolar driving: tunably slow heating through spectral engineering", Phys. Rev. Lett. **126**, 040601 (2021).

[196]H. Zhao, M. S. Rudner, R. Moessner, and J. Knolle, "Anomalous random multipolar driven insulators", Phys. Rev. B **105**, 245119 (2022).